Diffusion in Minerals of the Earth's Lower Mantle: Constraining Rheology from First Principles

Ph.D.-Thesis

by

Michael W. Ammann

Supervised by

Prof. Dr. J. P. Brodholt and Dr. D. P. Dobson

University College London (UCL)

Department of Earth Sciences

January 17, 2011

I, Michael W. Ammann, confirm that the work presented in this thesis is my own. Where information has been derived from other sources, I confirm that this has been indicated in the thesis.

Abstract

Absolute diffusion rates in minerals of the Earth's lower mantle are calculated from first principles using density functional theory. The agreement with the available experimental data is excellent and provides confidence in predicting diffusivities in regions of the lower mantle inaccessible to current experimental techniques. I have calculated the diffusivity of all constituting species in ferro-periclase ((Fe,Mg)O), (Fe,Mg)SiO_3 perovskite and $MgSiO_3$ post-perovskite. This enables me to put tight constraints on the viscosity of the Earth's lower mantle, and, in particular, on the viscosity of post-perovskite for which no experimental data are available. I find that perovskite deforming in diffusion creep can readily reproduce the Earth's lower mantle viscosity profile that has been inferred from inversion modelling. I also show that post-perovskite is either much stiffer (if also deforming in diffusion creep) or up to four orders of magnitude weaker than perovskite (if deforming in dislocation creep). This leads to a new interpretation of the sharp seismic reflector in the lowermost lower mantle, known as D$''$, as the onset of a sudden rheological transition and the generation of a mineral texture therewith. Finally, I also find that the pressure induced high-to-low-spin transition of iron in ferro-periclase and perovskite has a negligible effect on the rheology of the lower mantle.

Contents

Outline

Let me first briefly outline the structure of this thesis. I will start with an introduction on why diffusion in minerals is one of the most important processes in geophysics, what we (believe to) know about the Earth's interior and why I applied first principles methods instead of carrying out experiments. This will be followed by an overview of the basic theory behind the used method, namely density functional theory. I will then introduce the reader to the theory of solid-state diffusion and how it can be calculated from first-principles - this will close the theoretical part of this thesis.

The next part is my actual work, where I present the results of my calculations, showing that it is indeed possible to calculated absolute diffusion rates from first principles that are in excellent agreement with the available experimental data. Each investigated phase (periclase, $MgSiO_3$-perovskite, $MgSiO_3$-post-perovskite and ferrous iron diffusion in periclase and $MgSiO_3$-perovskite) will have its own section including a discussion about the implications of my results for the lower mantle.

The thesis will be concluded in a discussion about assumptions that had to be made in order to explain the experiments and to draw my conclusions. I will try to point out the (hidden) unknowns in my results and give an outlook on what might be done next - be it continuing calculations on diffusion or improving the understanding of the unknowns and better constrain my assumptions.

Tables of the calculated diffusion-parameters and figures of migration pathways are collected in the appendix, where one also finds the acknowledgements, all references, a list of abbreviations and my four peer reviewed publications (Physics and Chemistry of Minerals 36 (2009), Reviews in Mineralogy and Geochemistry 71 (2010), Nature 465 (2010) and Earth and Planetary Science Letters (in press, 2011)).

Part I.
Introduction

Solid-State Diffusion in Geophysics

Diffusion is a fundamental physical process in which atoms migrate through matter by following the gradients of chemical potentials (often concentration gradients). It occurs in any material, be it gaseous, liquid or solid, and cannot be prevented, only slowed down. Diffusion rates thus are a direct measure of the mobility of atoms, which is why diffusion in solids is slowest. The slowness of solid-state diffusion limits its industrial applications to surface reactions such as semiconductor doping, carbonitration of steal surfaces or sintering. Hence, solid-state diffusion is limited to the microscopic regime, rarely observable on the macroscopic level. In our day to day life, the slowness of solid-state diffusion renders it, fortunately, generally irrelevant — which keeps everything stable.

Over large, geological time-scales, however, diffusion processes can readily reach the macroscopic level which makes it one of the most important processes in geophysics: solid-state diffusion allows crystals to chemically react or interact with each other as well as with gases and liquids and thus controls the degree of compositional zoning in minerals, the rate of transformation into new phases, the rate of crystal growth, its ability to couple with electromagnetic fields via ionic conduction, the attenuation of seismic waves via anelasticity and to yield plastically to stresses and thence deform. Thus, inside the Earth, solid-state diffusion enables minerals to change their chemical compositions and crystal-structures and, in particular, it controls the viscosity of the mineral aggregate. In diffusion creep, stress is accommodated through ions migrating from regions of high stress to regions of low stress. This is achieved either through bulk diffusion or grain boundary diffusion. In dislocation creep, the rate-limiting step is generally dislocation climb — the process where a dislocation has to migrate out of the dislocation plane to avoid an obstacle — and this requires ionic diffusion.

Viscosity, is arguably the most important parameter for understanding the thermochemical evolution of the Earth (see also below). The viscosity of the mineral-aggregate of the Earth's mantle controls the vigour of the convection which transports heat out of the core to the Earth's surface. The ratio of the viscosities of

the upper and lower mantle determines the speed of the plates and whether slabs can penetrate into the lower mantle and reach the core-mantle boundary. In short, the viscosity of the minerals inside the Earth control plate tectonics — and plate-tectonics is what makes our planet inhabitable. Mantle-viscosity also determines the topology of the core-mantle boundary and its physical coupling with the core. At the same time, diffusion limits the chemical interaction between the mantle and the core. Moreover, the formation and stability of plumes can be directly linked to the relative viscosities of the minerals in the plume, at the bottom of the plume and in its surrounding.

The multitude of geophysical phenomena controlled by viscosity and changes thereof demand for a better understanding of this quantity. However, our current knowledge of the Earth's mantle's viscosity is very limited as it is impossible to measure it directly. Indirect measurements (inversion modelling), in contrast, allow one to derive at least radial viscosity profiles from convection observables, post-glacial rebound and the geoid. However, the various viscosity models derived from different datasets, inversion techniques and observables vary over several orders of magnitude as shown in figure 1. Nevertheless, the models show a common trend starting with a stiff uppermost mantle, followed by a narrow low viscosity region near the transition zone and a viscosity peak in the second half of the lower mantle.

Viscosity depends on composition, crystal structure, mineral distribution within the aggregate and the physical conditions (pressure and temperature). Localised temperature anomalies can affect the viscosity as well as compositional (chemical) or crystal-structural and therewith viscous inhomogeneities, which all give rise to complex mantle dynamics, especially near the core-mantle boundary. At the same time, changes in viscosity do not need to reflect changes in composition or crystal structure but may result from changes of the aggregate structure itself, e.g. by phase separation or generation of lattice preferred orientation (LPO). Thus, understanding the rheology of lower mantle minerals will also allow a better interpretation of seismic signals with which one observes the complex structures at the core-mantle boundary.

Studying the movements of atoms in crystals is thus not only key to understand the movement of our continents but ultimately allows us to better understand the thermochemical evolution of the entire planet Earth. I will focus my work on diffusion in minerals in the Earth's lower mantle which is currently the least well understood part, mainly due to experimental difficulties.

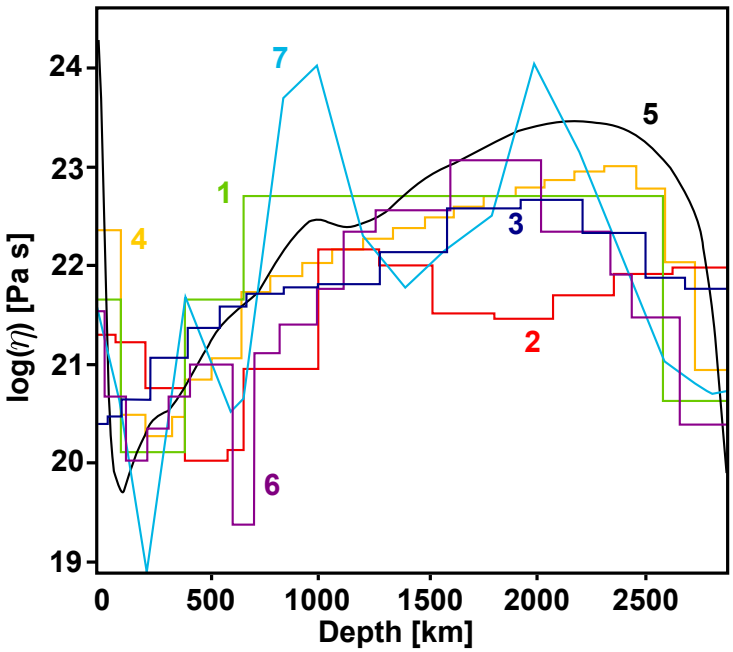

Figure 1: **Radial Mantle Viscosity Models** modified after[1]. (1)[2] (2)[3] (3)[4] (4)[5] (5)[6] (6)[7] (7)[8] : While the models vary over several orders of magnitude, a common trend can be seen with a stiff uppermost mantle, followed by a narrow low viscosity region near the transition zone and a viscosity peak in the second half of the lower mantle

The Earth's Lower Mantle

Most of what we know about the Earth internal structure was observed with seismic waves that are generated in earthquakes. These waves travel through the Earth reflecting and deflecting at structures with varying wave-speeds. While the interpretation of what exactly is seen is complicated, they readily reveal the layered structure of the Earth (now called transition zone, lower mantle, D″, outer and inner core). The interpretation of what causes these structures and their geophysical significance need to be clarified by investigating the physical properties of the minerals forming the Earth. I will work on the rheological properties of the minerals in the lower mantle.

The Earth's lower mantle reaches from the lower end of the transition zone at 660 km down to the core-mantle boundary at 2900 km (see figure 2). Simply by its shear size, comprising more than 50 % of Earth by volume, it takes a up fundamentally important role in the thermochemical evolution of the Earth. The physical conditions in this region of the Earth are extreme: pressure increases from 25 GPa to 135 GPa, temperature rises from 1600 K up to 3000 - 4000 K.

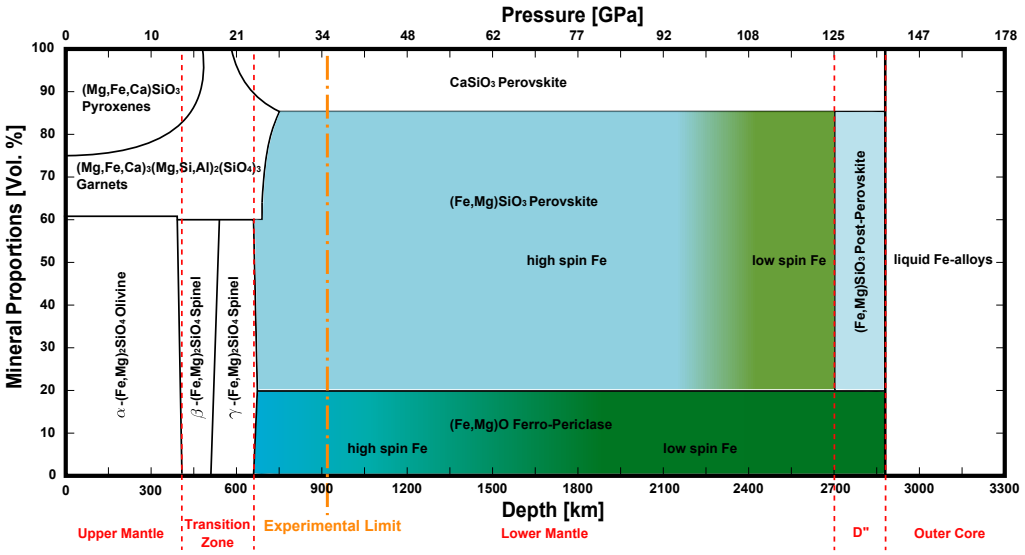

Figure 2: **Pyrolite Mantle Composition** modified after[9]. Changes of the volume proportions in mantle minerals along a Brown-Shankland geotherm[10]. The coloured region is the one investigated in this work. Also shown are the high to low spin iron transitions in ferro-periclase and perovskite. The current limit for diffusion experiments is 35 GPa[11]

The Earth's interior consists of solid rocks that over geological time-scales behave like a viscous fluid. The exact chemical composition and crystallographic structure of the minerals of the Earth's mantle are unknown and several models exist[9]. A widely used and accepted model is the pyrolite composition[12,13]. The volume fractions of the various phases along a Brown-Shankland geotherm[10] of this model are shown in figure 2(modified after[9]). The pyrolite model reproduces seismic features of the upper mantle and transition zone fairly well. The major seismic discontinuities at 410 km and 660 km are explained as phase transitions of $(Fe,Mg)_2SiO_4$ olivine to β-spinel and of γ-spinel to $(Fe,Mg)SiO_3$ perovskite plus (Fe,Mg)O ferro-periclase respectively. Luckily, the phase fractions of the lower mantle are fairly independent of the used compositional model. It is believed that the lower mantle is composed of about 70 % $(Fe,Mg)SiO_3$ perovskite, 20 % (Fe,Mg)O ferro-periclase and 10 % $CaSiO_3$ perovskite with an iron content up to 20 %, and all phases incorporate traces of other chemical species of which aluminum is the most abundant.

Within the Earth's mantle, heat is generated from radioactive decay, gravitation and as a leftover from accretion. It is transported from the core to the surface via convection (see figure 3): hot material rises up while cold material sinks down. This gives rise to plate-tectonics, volcanism and earthquakes. The exact mode of

convection is not yet fully understood, partly because the viscosities of the mantle minerals are not well constrained. In either case, the base of the lower mantle, the core-mantle boundary, plays a key role as it transfers the heat from the core into the convection cycles. Part of the heat is transferred to the surface via plumes that are formed in this region and manifest themselves in hot-spot volcanism such as Hawaii. These plumes originate in the edges of the large, low-shear velocity provinces (LLSVPs) underneath Africa and the Pacific. These regions are thought to be hot, chemical piles. On the other hand, down-welling slabs may accumulate in this region as they cannot penetrate into the much denser, liquid iron outer core. Moreover, chemical exchange between the mantle and the core will be controlled by this region.

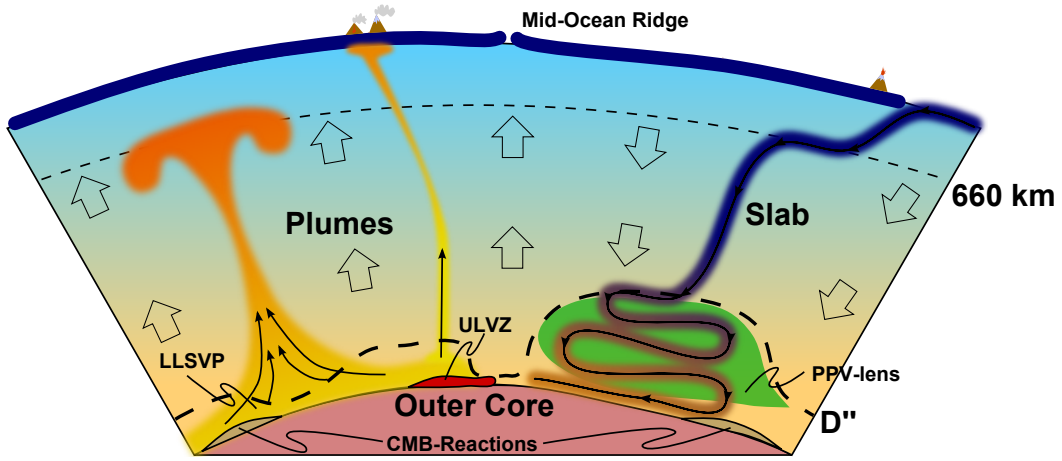

Figure 3: **Sketch of processes in the Earth's lower mantle** modified after[14,15] (not to scale). Plumes are rising from the core-mantle boundary (CMB), one being responsible for hot-spot volcanims, the other being stuck at the bottom of the transition zone. A slab accumulates at the CMB. Its minerals transform into a post-perovskite lens (PPV) in the cooler region. Chemical piles form from CMB-reactions and a ultra-low velocity zone (ULVZ) is present at the edge of the plume-base, a large, low-shear-velocity province (LLSVP)

The other, upper end of the lower mantle, the lower end of the transition zone, is the region of the deepest earthquakes. Here, the viscosity contrast between the slab, transition zone and lower mantle minerals controls whether slabs can penetrate into the lower mantle (and reach the CMB) or become stagnant, i.e. lying on top of the lower mantle. This will directly affect the velocity of the plates attached to the slabs and determine the chemical mixing between the upper and the lower mantle. It is also where plumes can be truncated and branch out.

Surprisingly, the lower mantle is seismically very homogeneous and structureless except in the lowermost 300 km's, the so-called D″. On one hand, the seismic homogeneity can be attributed the absence of rapid changes of physical properties as a result of sharp phase transitions or large chemical heterogeneities. On the other hand, its constituent minerals are strongly elastically anisotropic. The seismic homogeneity, therefore, also indicates the absence of any texture, be it lattice preferred orientation (LPO) or phase separation.

However, the absence of seismic anisotropy does not preclude a phase change. High pressure experiments on iron-bearing periclase revealed that ferrous iron (Fe^{2+}) changes from a high spin state to a low spin state if pressure exceeds 60 GPa (1000 km)[16–18]. While physical properties change across the transition, it has been found that the transition is very smooth (population numbers change gradually) due to temperature effects[19,20] which renders the transition essentially invisible to seismic waves. The geophysical significance of this phase transition thus, so far, remains small.

Successive experiments then found the same transition of the spin state of iron in perovskite[21–23], at pressures expected near D″. However, the exact nature of the transition is controversial as it is not smooth and composition-dependent. Further controversy was added by later experiments reporting the observation of an intermediate spin-state throughout the lower mantle conditions[24,25]. The spin state of iron in perovskite at high pressures thus is still not well understood and again, it's geophysical relevance still needs to be clarified.

In D″, in contrast to the rest of the lower mantle, rapid changes in seismic velocity, anisotropy and complex structures[14,15,26–30] are observed. Some features have been suggested to be chemical piles (e.g. from interaction with the core) or thermal anomalies, others as the bases of plumes or the accumulation of subducted slabs, some as partially molten regions (being responsible for ultra-low (seismic) velocity zones (ULVZ)) and again others as the generation of LPO due to large stresses. However, all these explanations do not explain the full spectrum of complex structures seen in seismic images. In 2004, the discovery of a new phase, $MgSiO_3$ post-perovskite[31–33], allowed us to explain some seismic observations as a simple, sharp phase-transformations. The picture of D″ appeared to be clear and consistent and is explained in figure 3.

Then, in 2009, new experiments[34] revealed that impurities such as iron and alumina cause the phase-transformation from perovskite to post-perovskite to be too wide to be responsible for the seismic observations. A new explanation for D″ is thus

required and some results on post-perovskite in this thesis allow me to conclude that D″ might be rather a rheological instead of a phase transition. I suggest that the D″ reflector is a result of soft post-perovskite suddenly forming an interconnected network, softening the aggregate and generating texture. This reconciles seismic observations with geophysical data.

To conclude, the issue in the seismically homogeneous lower mantle (above D″) is that we know there are phase transitions occurring in this region but, up to now, we do not see them seismically nor can we assign any geophysical phenomenon to them. In D″, we encounter the opposite problem of observing a wide spectrum of seismic structures which are hard to explain consistently with our current mineralphysical and geophysical knowledge. Thus, in one case we know something happens but we don't see it, while in the other, we see that something happens but we do not know what.

The Problem from the Mineralphysicist's View

From the discussion above it should be clear that the investigation of diffusion processes in minerals of the lower mantle is crucial for our understanding of the thermochemical evolution of the Earth. Ideally, the physical properties of these minerals would be studied in experiments at the relevant temperature, pressure and composition. However, current experimental techniques to investigate diffusion are incapable of reaching the extreme physical conditions of the lower mantle. Only recently it has become possible to experimentally probe diffusion at conditions of the shallow lower mantle[11,35–41] (down to 700 km). This is well below the known phase transitions (high- to low-spin and perovskite to post-perovskite) and leaves about 70 % of the Earth's volume inaccessible to experiments (see figure 2). Therefore, diffusion coefficients of the minerals in the lower mantle are unknown, in particular of post-perovskite for which no experimental data exist.

Theoretical methods, in contrast, allow one to investigate the properties of minerals at all pressures and temperatures reached in the lower mantle. The method used in this work is density functional theory (DFT) which enables one to perform atomistic first-principles calculations (*ab initio*; no approximation or simplification of the investigated system) of any mineral (although some approximations have to be made: one for our lack of understanding quantum mechanics, others for computational efficiency). However, the increased availability of computational power allows one today to perform first principles calculations to an accuracy never seen

before.

This thesis strives to extend the present understanding of diffusion in the minerals of the Earth's lower and lowermost mantle at relevant pressures and temperatures by applying first principle methods. Ideally, one would perform molecular dynamics simulations in order to avoid any possible biasing by making certain choices for the investigated system (e.g. diffusion mechanism, vacancy concentrations) because nature often does the unexpected. This is the advantage of experiments over theoretical simulations: experimental results are real and unbiased (except by the experimental set-up). Unfortunately, the slowness of solid-state diffusion — or the lack of computer power — currently make it impossible to simulate diffusion using first principles molecular dynamics. Luckily, the theory of diffusion provides an expression that relates atomistic quantities to the diffusion coefficient. I can calculate all these quantities with DFT, at least in the harmonic approximation.

It will be shown in this thesis that these first principles calculations can be as accurate as the results of experiments by comparison with the latter. Moreover, this comparison will, to some extent, limit the biasing of choosing a certain diffusion mechanism and provide confidence of being close to reality. This will ultimately allow me to predict diffusion rates across the iron-spin transitions and in post-perovskite which will further clarify their geophysical significance.

Part II.
Density Functional Theory

The investigation of atomistic systems requires quantum mechanics. In quantum mechanics, a physical system is described by the solutions of its according Schrödinger equation. These solutions are quantum mechanical states of the system and each state has its specific energy. As long as the system is time independent (in the sense that no energy is added or removed), the system is most likely in its ground state which is the state of lowest energy at all times. As most systems are in the ground state, this is the very state one would like to investigate first. Moreover, the ground state energy allows one to calculate equilibrium structures, elastic, dielectric and vibrational properties of crystals and, most importantly for this project, formation and migration energies of crystal defects.

While it is straight forward to set up Schrödinger's equation and its solution formally for N interacting particles, unfortunately, analytical solutions of Schrödinger's equation only exist for systems of one and two particles. Any system of more than two particles can only be solved by making approximations. The problem lies in the complexity of the N-particle wave-function. Particularly in solid state physics where one easily has systems of the order 10^{23} atoms, good approximations are essential. In solid-state and molecular systems the basic concepts are the inhomogeneous electron-gas and the Born-Oppenheimer approximation (static atomic nuclei).

A very effective and successful method to investigate the quantum mechanical many body problem is density functional theory (DFT). In theory, DFT does not make any approximation - while in practice some approximations have to be made yielding, nevertheless, very accurate results. This section will first review DFT precursors like the ideal Fermi-gas and the Thomas-Fermi theory for molecules. These two sections will provide a conceptual idea of DFT. Afterwards, the DFT formalism is derived basing on the Hohenberg-Kohn theorems. Two approaches will be taken giving the same result. First, the classical approach taken by Kohn and Sham is followed. Second, Lieb's approach will be briefly outlined revealing other aspects of and new insights into DFT. Once the concepts of DFT are explained, I will focus on more technical aspects which allow efficient computations.

This section shall only provide a brief summary of DFT as there is a wide range of literature available providing more thorough reviews and discussions of recent

developments and problems. The reader is therefore referred to references such as[42–44] just as examples.

1. Why Density Functional Theory?

Let me start with a brief digression to discuss why I have used the computationally expensive DFT method and not empirical methods.

The system is described as set of interacting atoms or ions, and it is these interactions that govern its behaviour. The interactions can either be described from first principles (i.e., quantum mechanically) or empirically. The first principles method treats the system as a set of interacting nuclei and electrons, and uses (approximate) solutions to Schrödinger's equations to obtain energies and forces. Currently, almost all work involving first principles methods, such as the one that will be discussed in this thesis, make use of density functional theory (DFT,[45,46]). Other first principles methods such as quantum Monte-Carlo are more accurate but also computationally much more expensive, or simply not accurate enough such as the Hartree-Fock method which ignores electron-correlation.

The empirical approach uses a predefined inter-atomic (or inter-molecular) potential, which is fit to some experimental property or to a first-principles result. There are also the so-called semi-empirical methods, which are based on quantum mechanics but contain many approximations and include experimentally derived parameters. The different methods have their pluses and minuses. The empirical approach allows one to look at far larger systems than the first principles (or *ab initio*) methods. The downside is that the empirically-derived potentials may not work accurately in systems and atomic environments for which they were not originally designed. This is a particular worry for diffusion studies since atoms migrate from their normal configuration through a very different coordination environment than their equilibrium position. Moreover, some empirical potentials have bond-angle dependent parameters and it is not clear what to do with those as atoms migrate. For instance, potential models for Si-O interaction often have a three-body bond angle term in order to maintain the correct coordination with oxygen. For tetrahedrally coordinated silicon, this would be 109.47°. But as the silicon ion moves out of the tetrahedron, it changes coordination, and the bond-angle term may impose inappropriate forces. The *ab initio* techniques do not suffer from this in the same way, although they do have other approximations which add uncertainty to the results.

2. DFT: Hohenberg-Kohn-Sham

2.1. Ideal Fermi-Gas

Sommerfeld's theory[47] of the ideal gas of fermions (i.e. ideal Fermi-gas) is of major importance for solid state physics as it provides readily access to the qualitative behaviour of weakly bound electrons in condensed matter. Moreover, it forms the foundation of the Thomas-Fermi theory discussed in the next section 2.2 and is a key ingredient for the success of DFT (as it is used within the local density approximation). It is also the first attempt to relate the energy of an electronic system to its particle-density.

Sommerfeld's theory idealizes condensed matter as a cubic box of volume L^3 containing a uniform (i.e. non-interacting, also called jellium) electron-gas of density $n = \frac{N}{L^3}$ (N is the number of electrons) exposed to a constant potential $V(\mathbf{x}) = V_0$ (i.e. not periodically varying as it would result from the periodically arranged atomic cores within the crystal). In fact, setting the constant potential equal to 0 would not change the result as it is only an additive constant to the electron energies. Hence, the ideal electron gas is often also called the free electron gas. In order to simulate an ideal (i.e. infinitely large, to avoid surface effects) crystal, periodic boundary conditions are applied. In order to find the ground state energy of the electron-gas within this approximation one needs first to solve Schrödinger's equation for a single electron

$$\left[-\frac{\hbar^2}{2m}\Delta + V_0\right]\psi(\mathbf{x}) = E\psi(\mathbf{x}). \tag{2.1}$$

The solutions of this equation with periodic boundary conditions are the well known wave-functions in the form of plane waves

$$\psi(\mathbf{x}) \propto e^{i\mathbf{k}\cdot\mathbf{x}}$$

with the wavevector

$$\mathbf{k} = \frac{2\pi}{L}\mathbf{n} \tag{2.2}$$

with $\mathbf{n} \in \mathbb{N}^3$. Furthermore, the electron's wave-vector is related to its momentum $\mathbf{p}$ by the de Broglie relation $\mathbf{p} = \hbar\mathbf{k}$ and therewith to its energy $E = \frac{\mathbf{p}^2}{2m}$. These relations completely determine all the available states within the cubic box as each

state is uniquely characterized by its energy. Apparently, the electrons behave like free electrons.

The energy of the highest occupied state in a system of fermions is the Fermi-energy E_F. This state is also associated with the Fermi-wavevector $\mathbf{k_F}$. At zero temperature, i.e. $T = 0°K$, all states with energies lower than the Fermi-energy are occupied while all higher lying states are unoccupied. Thus, being interested in the ground state energy of a uniform electron gas of density $n = \frac{N}{L^3}$, one needs to find the relation between the electron density n and the Fermi-energy E_F.

It can be readily seen from equation (2.2) for the wave-vectors that each state occupies a volume of $\left(\frac{2\pi}{L}\right)^3$. In the reciprocal space, the occupied states lie within a sphere, the so-called Fermi-sphere, with radius of the Fermi-wave-vector k_F. Thus, the total number of states within the Fermi-sphere is given by

$$N = 2 \cdot \frac{4}{3}\pi k_F^3 \cdot \left(\frac{L}{2\pi}\right)^3 = \frac{k_F^3 L^3}{3\pi^2}. \tag{2.3}$$

The factor 2 comes from the fact that each state can be occupied twice if one considers the electron-spin. This equation directly relates the electron density $n = \frac{N}{L^3}$ to the length of the Fermi-vector k_F and therewith to the Fermi-energy E_F:

$$E_F = \frac{\hbar^2 k_F^2}{2m} = \frac{\hbar^2}{2m}\left(3\pi^2 n\right)^{\frac{2}{3}}. \tag{2.4}$$

The ground state energy is then being found by performing a transition from the sum over the energies of the occupied states to an integral over an averaged energy density of all occupied states. The ground state energy is then given by

$$E_0 = 2 \cdot \left(\frac{L}{2\pi}\right)^3 \cdot \int_{k<k_F} d^3k \frac{\hbar^2 \mathbf{k}^2}{2m} = \frac{L^3 \hbar^2}{10\pi^2 m} k_F^5. \tag{2.5}$$

Obviously, the average energy per electron (the kinetic energy) is $\epsilon = \frac{3}{5}E_F$.

2.2. Thomas-Fermi Theory

The Thomas[48]-Fermi[49] theory (TFT) of many-electron systems gives a first simple impression of how the density-functional theory is working and can be regarded as the conceptual origin of DFT. TFT calculates the ground-state energy and ground-state electron distribution of non-uniform electron systems, i.e. it considers the variation of the potential. The difference between Thomas-Fermi and DFT is that

the former does explicit approximations while DFT, at least in theory, is exact. In fact, Thomas-Fermi theory is DFT of a non-interacting electron gas. TFT really maps the properties of an N-particle wave-function (in form of a Slater-determinant) of degree $3N$ onto a function called electron density of degree 3 and assumes a uniform electron distribution in phase space. Furthermore, it assumes that there is neither interaction nor correlation between the single electrons. While TFT allows one to make qualitatively correct predictions for neutral atoms (atom sizes, existence of bound states), it fails to describe molecular bonding.

Assume an electron density $n(\mathbf{x})$ around an atomic core of charge $Z \gg 1$ fixed at the origin $\mathbf{0}$. Charge neutrality then requires that the number of electrons

$$N = \int d^3x n(\mathbf{x}) = Z. \tag{2.6}$$

In theory, it is exactly known what the electron-density looks like:

$$n(\mathbf{x}) = N \sum_{\substack{s_j=\uparrow,\downarrow \\ j=1,...,N}} \int \prod_{i=2}^{N} d^3x_i |\Psi(\mathbf{x}_1, s_1, \mathbf{x}_2, s_2, ...\mathbf{x}_N, s_N)|^2. \tag{2.7}$$

A single electron feels the following, averaged potential

$$V(\mathbf{x}) = e^2 \int d^3y \frac{n(\mathbf{y})}{4\pi|\mathbf{x}-\mathbf{y}|} - \frac{Ze^2}{4\pi|\mathbf{x}|}. \tag{2.8}$$

The first term on the right hand side of equation (2.8) describes the interaction of a single electron with the surrounding electron cloud of all other electrons of the atom, the second term originates from the electron interaction with the core. Unfortunately, it is not possible to find the electron-density $n(\mathbf{x})$ from equation (2.7) for large electron-numbers N.

Thomas and Fermi then made the following approximation which holds if the average energy of the electrons is much larger than the potential energy: The entire space is filled with cubes of size L^3 where the potential inside the cubes is constant $V = constant$. TFT assumes that in each of these cubes an ideal electron gas as discussed in section 2.1 predominates. Using equation (2.4), the electron-density within such a cube can thus be written as

$$n(\mathbf{x}) = \frac{N(\mathbf{x})}{L^3} \approx \frac{k_F(\mathbf{x})^3}{3\pi^2} = \frac{[2m(\epsilon_F - V(\mathbf{x})]^{\frac{3}{2}}}{3\pi^2\hbar^3} \tag{2.9}$$

Using now the relations for the ideal electron gas of section 2.1, one finally finds the Thomas-Fermi energy functional

$$\mathcal{E}(n) = \int d^3x \left[C\frac{\hbar^2}{m} n(\mathbf{x})^{\frac{5}{3}} - Ze^2 \frac{n(\mathbf{x})}{4\pi|\mathbf{x}|} + \frac{e^2}{2} \int d^3x \int d^3y \frac{n(\mathbf{x})n(\mathbf{y})}{4\pi|\mathbf{x}-\mathbf{y}|} \right] \tag{2.10}$$

where the first term of the right hand side is the kinetic energy of the ideal electron gas from equation (2.4) (where $C = \frac{3}{10}(3\pi^2)^{2/3}$), the second term is the Coulomb-attraction between the atomic core and the electron density and the third term describes Coulomb repulsion between the electrons. The ground state of the system is then found at the minimum of the Thomas-Fermi energy functional (2.10). This is a variational problem (analogous to the Euler-Lagrange equation in classical mechanics) with constraint (2.6) of which the solution is found by variation of the Functional

$$\mathcal{F}(n) = \mathcal{E}(n) - \lambda \left(\int d^3x n(\mathbf{x}) - N \right). \tag{2.11}$$

The variation of $\mathcal{F}(n)$ yields the Thomas-Fermi equation

$$\frac{5}{3} C\frac{\hbar^2}{m} n(\mathbf{x})^{\frac{2}{3}} - \frac{Ze^2}{4\pi|\mathbf{x}|} + e^2 \int d^3y \frac{n(\mathbf{y})}{4\pi|\mathbf{x}-\mathbf{y}|} - \lambda = 0 \tag{2.12}$$

with solution

$$n(\mathbf{x}) = \frac{[2m(\epsilon_F - V(\mathbf{x}))]^{\frac{3}{2}}}{3\pi^2\hbar^3} \tag{2.13}$$

and $\lambda = \epsilon_F$. The Thomas-Fermi equation (2.12) can be recast into a differential equation for the potential

$$-\Delta V(\mathbf{x}) = -Ze^2\delta(\mathbf{x}) + e^2 n(\mathbf{x}) \tag{2.14}$$

for which solutions are known. TFT correctly reproduces the leading behaviour of the ground-state energy for large systems (i.e. Z large) but fails to describe negatively charged systems as well as molecular bonding (Teller's theorem[50]). A wide range of literature about Thomas-Fermi theory is readily available and for a more thorough discussion the reader is referred to e.g.[51] and references therein.

2.3. Hohenberg-Kohn Theorems

DFT is founded on two basic theorems first stated by Hohenberg and Kohn in 1964[45]. The result of these theorems is the so-called Hohenberg-Kohn functional for which Kohn and Sham[46] developed a method to solve it. The solution yields, at least in theory, the exact ground state energy of the system. In order to state and prove the Hohenberg-Kohn theorems, some definitions need to be made first.

The Hamiltonian H of a system of interacting electrons in an electrostatic field of nuclei can be written as

$$H = T + U + V = H_0 + V \tag{2.15}$$

where T is the kinetic, U the mutual interaction and V the potential (due to interaction with nuclei) energy. The Hamiltonian of the interacting electron system itself is $H_0 = T + U$ (without external field). The potential energy V for an arbitrary external field is

$$V = \sum_{i=1}^{N} v(\mathbf{r}_i) \tag{2.16}$$

with $\mathbf{r}_i$ the position of electron i. The many-body-wave-function shall be Ψ for any given external potential $v(\mathbf{x})$. The ground state energy E_G is given by

$$E_G = \langle \Psi | H_0 + V | \Psi \rangle \tag{2.17}$$

and the electron density $n(\mathbf{x})$ by

$$n(\mathbf{x}) = \langle \Psi | \hat{n}(\mathbf{x}) | \Psi \rangle \tag{2.18}$$

where the density operator $\hat{n}(\mathbf{x})$ is defined as

$$\hat{n}(\mathbf{x}) = \sum_{i=1}^{N} \delta(\mathbf{x} - \mathbf{x}_i). \tag{2.19}$$

Theorem 1 (Density as Basic Variable: Hohenberg-Kohn[45])**.** *It is impossible that two different external potentials give rise to the same ground-state density distribution* $n(\mathbf{x})$.

Proof. Given two Hamiltonians $H = H_0 + V$ and $H' = H_0 + V'$ with according

ground-state functions Ψ and Ψ'. If the two external potentials $v(\mathbf{x})$ and $v'(\mathbf{x})$ associated with V and V' differ by more than an additive constant, then $\Psi \neq \Psi'$ because they satisfy different Schrödinger equations. It will now be shown that under these conditions the resulting two ground-state densities $n(\mathbf{x})$ and $n'(\mathbf{x})$ have to be different.

The variational principle implies for the ground-state energies E and E'

$$E' = \langle \Psi' | H' | \Psi' \rangle < \langle \Psi | H' | \Psi \rangle = \langle \Psi | H + V + (V' - V) | \Psi \rangle$$

Hence:

$$E' < E + \langle \Psi | V' - V | \Psi \rangle = E + \int d^3x n(\mathbf{x})(v'(\mathbf{x}) - v(\mathbf{x})).$$

Similarly, by interchanging prime and unprimed quantities:

$$E <= E' + \int d^3x n'(\mathbf{x})(v(\mathbf{x}) - v'(\mathbf{x}))$$

Adding both equations yields

$$E' + E < E' + E - \int d^3x \left(n'(\mathbf{x}) - n(\mathbf{x})\right)\left(v'(\mathbf{x}) - v(\mathbf{x})\right)$$

This is a strict inequality and hence $n'(\mathbf{x}) \neq n(\mathbf{x})$. □

Corollary 1. *The electron ground-state density $n(\mathbf{x})$ uniquely specifies the external potential $v(\mathbf{x})$ and hence the many-body wave-function Ψ.*

The first Hohenberg-Kohn theorem (Theorem 1) states that the mapping between the potential $V(\mathbf{x})$ and the electron-density $n(\mathbf{x})$ is invertible, i.e. for each electron density there is a unique potential and vice versa. Thus, the ground-state energy E_G is uniquely determined by the electron density $n(\mathbf{x})$ such that it can be written as a functional

$$E_G[n(\mathbf{x})] = F[n(\mathbf{x})] + \int d^3x v(\mathbf{x}) n(\mathbf{x}) \tag{2.20}$$

where

$$F[n(\mathbf{x})] = \langle \Psi | H_0 | \Psi \rangle \tag{2.21}$$

is the ground-state expectation value of H_0 as defined in equation (2.15) when the

electron density is $n(\mathbf{x})$. $F[n(\mathbf{x})]$ is the so-called Hohenberg-Kohn functional.

Theorem 2 (Variational Principle: Hohenberg-Kohn[45])**.** *The ground-state energy for a given potential $v(\mathbf{x})$ is obtained by minimising $E_G[n(\mathbf{x})]$ with respect to the electron density $n(\mathbf{x})$ for a fixed $v(\mathbf{x})$ under the condition*

$$N = \int d^3x n(\mathbf{x}).$$

The electron density $n(\mathbf{x})$ yielding the minimum is the density ground-state.

Proof. Let $v(\mathbf{x})$ and $v'(\mathbf{x})$ be two different external potentials with ground-state energies E_G and E'_G and ground-state wave-function Ψ and Ψ'. The Rayleigh-Ritz[52,53] variational principle gives:

$$E_G < \langle \Psi' | H_0 + V | \Psi' \rangle = F[n'(\mathbf{x})] + \int d^3x v(\mathbf{x}) n'(\mathbf{x}). \tag{2.22}$$

Assuming a non-degenerate ground-state, this proves the theorem. □

This second Hohenberg-Kohn theorem (Theorem 2) provides a method to exactly calculate the ground-state energy and electron density. This task would be straight forward, if $F[n(\mathbf{x})]$ was a well known and a sufficiently simple functional. This is not the case: the kinetic energy of an interacting electron gas as well as the electron energies from mutual interaction between the electrons are unknown and cannot be calculated exactly. Therefore, it is important to develop simple functionals that are adequate approximations of these energies. This will be done in section 2.5, after a brief digression to Lieb's derivation of the theorems via Legendre-transforms.

2.4. DFT: Legendre-Transform

Lieb[54] was the first to point out the connection between DFT and the Legendre-transforms used in thermodynamics. This approach to DFT is particularly intriguing as it clarifies the situation of mappings. The direct approach taken by Hohenberg and Kohn suggests a mapping of the many body wavefunction of degree 3N onto the electron density n of degree 3 being apparently a magnificent reduction in degrees of freedom making the problem much simpler. However, it shall be shown in this section that the actual mapping occurs from the potential V of degree 3 onto the electron density n of degree 3. As in thermodynamics, the change of variables reduces the complexity of certain problems.

As suggested by S. Baroni during a lecture at UCL in 2007, the problem of solving the Schrödinger equation for the N-body wave-function is, in fact, also mapped onto a new problem of finding the correct Hamiltonian. In the end, the advantage of DFT is that finding a good approximation for the Hamiltonian is apparently much simpler than finding a good approximation to the many-body wave-function.

This section shall only very briefly depict this connection between DFT and Legendre-transformations and has not the intention to be mathematically thorough.

2.4.1. Reminder of Thermodynamics

It is well known that thermodynamical potentials can be obtained from each other by a change of variable by applying Legendre-transformations. The Helmholtz free energy $F(N,T,V)$, e.g., can be obtained from a Legendre-transformation of the grand potential $\Omega(\mu,T,V)$:

$$F(N,T,V) = \min_N \left(\Omega(\mu(N),T,V) + \mu(N)N\right). \tag{2.23}$$

The chemical potential $\mu(N)$ transforms from an independent variable into a function of the particle number N. The new independent variable is now N given by

$$N(\mu,V,T) = -\frac{\partial\Omega}{\partial\mu}. \tag{2.24}$$

The same is also true the other way around, i.e., the derivative of F with respect to N is equal to μ, the free variable of Ω.

2.4.2. Hohenberg-Kohn Theorems from Legendre-Transforms

Legendre-transforms are only well defined if the considered function $F(X)$ is concave or convex as this ensures that the mapping between its independent variables and its partial derivatives are invertible: $X \mapsto \frac{\partial F}{\partial X}$.

Definition (Convex, Concave)**.** A function(al) $F(x)$ is called strictly convex (concave) if

$$F\left(\alpha x_1 + (1-\alpha)x_2\right) > (<)\alpha F(x_1) + (1-\alpha)F(x_2)$$

which is equivalent in stating:

$$\frac{d^2F(x)}{dx^2} > (<)0.$$

Lemma 1 (Lieb[54])**.** *The ground state energy $E_G[V]$ as a functional of the external potential V is concave.*

Proof. It is possible to prove concavity by showing that the second derivative is negative (definite) by using perturbation theory. However, for the sake of brevity, the direct proof is chosen.

Let $V^\alpha = \alpha V(1)+(1-\alpha)V(0)$ and $\hat{H}^\alpha = \alpha\hat{H}(1)+(1-\alpha)\hat{H}(0)$. The corresponding ground-state function shall be Ψ^α. Then, the ground state energy as a function of the external potential is then given by

$$\begin{aligned} E_G[V^\alpha] &= \langle\Psi^\alpha|\hat{H}^\alpha|\Psi^\alpha\rangle \\ &= \alpha\langle\Psi^\alpha|\hat{H}(1)|\Psi^\alpha\rangle + (1-\alpha)\langle\Psi^\alpha|\hat{H}(0)|\Psi^\alpha\rangle \\ &> \alpha E_G[V(1)] + (1-\alpha)E_G[V(0)]. \end{aligned}$$

the inequality comes from the fact that expectation values of the Hamiltonian are calculated with respect to a "wrong" wave-function. □

Consider now the ground state energy (2.21)

$$E_G[\Psi;V] = \int d^3x v(\mathbf{x})n[\Psi](\mathbf{x}) + F[\Psi].$$

The Hellman-Feynman theorem[55] implies that the partial derivative is equal to the total derivative such that

$$\frac{\delta E_G}{\delta v(\mathbf{x})} = n(\mathbf{x}),$$

which is equivalent to equation 2.24.

Apparently, the Legendre-transform of the ground state energy $E_G[V]$ is the Hohenberg-Kohn Functional $F[n]$. This finding gives rise to the first Hohenberg-Kohn theorem (Theorem 1) stating that the mapping $V \mapsto n$ is invertible. The

inverse Legendre-transform of $F[n]$ is the ground state energy $E_G[V]$, i.e.:

$$E_G[V] = \min_n \left(F[n] + \int V(\mathbf{x}) n(\mathbf{x}) d\mathbf{x} \right) \tag{2.25}$$

$$= F[n[V]] + \int V(\mathbf{x}) n[V](\mathbf{x}) d\mathbf{x} \tag{2.26}$$

where $n[V]$ solves the variational problem of the first line of the equations above which is nothing but the second Hohenberg-Kohn theorem (Theorem 2).

2.5. Kohn-Sham: Self-Consistency

The Hohenberg-Kohn theorems discussed in the previous sections 2.3 and 2.4 provide a simple framework to calculate ground-state energies. The stated theorems are not surprising but rather trivial. Unfortunately, they do not allow one to analytically solve any relevant problem as the Hohenberg-Kohn functional $F[n(\mathbf{x})]$ of equation (2.21) is not exactly known. It is the great achievement of Kohn and Sham[46] to provide an adequate approximation for $F[n(\mathbf{x})]$ and constructing a Schrödinger equation for the many-particle problem that can be readily solved and allows efficient implementation in computer codes. Their method which turned the Hohenberg-Kohn theorems into one of the most successful methods in quantum mechanical computations shall be briefly reviewed here.

To this end, one first writes the Hohenberg-Kohn functional (2.21) as

$$F[n] = T_{ni}[n] + G[n] \tag{2.27}$$

where $T_{ni}[n]$ is the kinetic energy of a system of non-interacting electrons with density distribution $n(\mathbf{x})$ and $G[n]$ is still an unknown functional containing the difference in the kinetic energy of interacting electrons as well as all the mutual interactions among the electrons. So far, the theory is still exact, as everything that cannot be calculated is hidden in the functional $G[n]$. Now, apply the second Hohenberg-Kohn theorem (Theorem 2): Applying the variational principle to the ground state energy functional

$$E_G[n(\mathbf{x})] = \int d^3x v(\mathbf{x}) n(\mathbf{x}) + T[n(\mathbf{x})] + G[n(\mathbf{x})]$$

yields

$$0 = \delta E = \int d^3x \left[v(\mathbf{x}) + \frac{\delta T}{\delta n(\mathbf{x})} + \frac{\delta G}{\delta n(\mathbf{x})} \right] \delta n(\mathbf{x})$$

which is subject to the constraint

$$\int d^3x \delta n(\mathbf{x}) = 0.$$

The constraint just states a constant particle number. This problem can now be rewritten by using a Lagrange undetermined multiplier μ (chemical potential) in the form of the Euler-equation:

$$v(\mathbf{x}) + \frac{\delta T}{\delta n(\mathbf{x})} + \frac{\delta G}{\delta n(\mathbf{x})} = \mu. \tag{2.28}$$

The brilliant idea by Kohn and Sham now is to define an effective potential

$$v_{eff}(\mathbf{x}) = v(\mathbf{x}) + \frac{\delta G}{\delta n(\mathbf{x})}. \tag{2.29}$$

As T is the kinetic energy functional of a non-interacting electron system, the new equation for the system of interacting electrons is the same as the equation of a system of non-interacting electrons feeling the effective potential:

$$\frac{\delta T}{\delta n(\mathbf{x})} + v_{eff}(\mathbf{x}) = \mu. \tag{2.30}$$

But this equation is equivalent to the Schrödinger equation

$$-\frac{\hbar^2}{2m}\Delta\Psi_i + v_{eff}(\mathbf{x})\Psi_i = \epsilon_i \Psi_i \tag{2.31}$$

with $n(\mathbf{x})$ given by

$$n(\mathbf{x}) = 2 \sum_{\epsilon_i < \mu} |\Psi_i|^2. \tag{2.32}$$

This is the so-called Kohn-Sham equation 2.31 and the Kohn-Sham orbitals Ψ_i.

The above equations are now used to solve any problem iteratively: Assume that one knows $G[n]$ (or at least an adequate approximation).

1. Make an initial guess of $n(\mathbf{x})$.
2. Calculate $\frac{\delta G}{\delta n(\mathbf{x})}$ and therewith $v_{eff}(\mathbf{x}) = v(\mathbf{x}) + \frac{\delta G}{\delta n(\mathbf{x})}$.
3. Solve the Kohn-Sham equation (2.31) to get the Kohn-Sham orbitals.
4. Calculate the new electron density via equation (2.32).
5. The new density is not equal to the input density hence this procedure is iterated till convergence (reduce residual).

This iterative procedure is called searching for self-consistency. It is important to notice that at this point, no approximations have been made as all mathematical and physical problems are hidden in the functional $G[n]$.

3. DFT Technicalities

In the previous sections it has been shown how DFT provides (theoretically) an exact method to solve the quantum-mechanical many body problem. Unfortunately, in practice, the exact form of the functional $G[n]$ is unknown and approximations have to be made. A particular problem is the approximation of the exchange and correlation energy for many electron systems. Additionally, in order to obtain an efficient computational algorithm, suitable representations of the ionic potentials and the electrons in the system are required. With all these approximations shall be dealt just superficially in this section as a more thorough discussion would be beyond the scope of this work.

3.1. Exchange-Correlation Energy

As stated in the previous section 2.4, the new problem in DFT is that the many body Hamiltonian is unknown. The quality of the results using DFT depends on the ability of the exchange-correlation functional to model the many-body electronic interactions. The most common exchange correlation functionals are the local density (LDA) and the general gradient approximation (GGA)[56–58].

Consider the Hohenberg-Kohn functional (2.21)

$$F[n(\mathbf{x})] = T[n(\mathbf{x})] + U[n(\mathbf{x})]$$

where $T[n(\mathbf{x})]$ is the kinetic energy of the system of interacting electrons of density $n(\mathbf{x})$ and $U[n(\mathbf{x})]$ describes the mutual interaction between all the electrons in the system. A first approximation can be made by using the kinetic energy of non-interacting electrons T_{ni} as it was used to develop the self-consistency loop in section 2.5 (there, the difference in kinetic energy was hidden in the functional $G[n]$). T_{ni} is not the kinetic energy of a system of interacting electrons, but is a first approximation to it. Next, the so-called Hartree energy, which is the electrostatic energy of the electronic charge distribution, is separated out:

$$E_H[n(\mathbf{x})] = \frac{e^2}{2} \int d\mathbf{x} d\mathbf{y} \frac{n(\mathbf{x})n(\mathbf{y})}{|\mathbf{x} - \mathbf{y}|}. \tag{3.1}$$

Such that finally the exchange-correlation energy E_{xc} is defined as

$$E_{tot}[n] = T[n] + V[n] + E_H[n] + E_{xc}[n] \tag{3.2}$$

containing all the electron-electron interaction one cannot compute exactly for an arbitrary system. However, the exchange-correlation energy is only known exactly for the uniform electron gas (see section 2.1). The exchange-correlation energy per electron in the uniform electron gas is denoted with ϵ_{xc}. The local density approximation (LDA) was introduced by Kohn and Sham[46] and is given by the following definition:

Definition (Local Density Approximation, LDA)**.** The exchange-correlation energy per unit volume at position $\mathbf{x}$ is $n(\mathbf{x})\epsilon_{xc}(\mathbf{x})$ such that

$$E_{xc}[n(\mathbf{x})] = \int n(\mathbf{x})\epsilon_{xc}(\mathbf{x}).$$

While the above expression is exact for the uniform electron gas, in reality it is only an approximation as $n(\mathbf{x})$ is non-uniform, in fact, it often changes rapidly. Additionally it is expected to be spin-dependent. Hence, one can introduce the exchange-correlation enhancement factor F_{xc} to account for dependence of the exchange-energy on the density gradient and spin (up: $\uparrow$ and down: $\downarrow$). This yields the generalised gradient approximation (GGA) in which the exchange-correlation energy is described by

$$E_{xc}^{GGA}[n^{\uparrow}(\mathbf{x}), n^{\downarrow}(\mathbf{x})] = \int d\mathbf{x}\epsilon_{xc}^{jellium}(n(\mathbf{x}))F_{xc}(n^{\uparrow}(\mathbf{x}), n^{\downarrow}(\mathbf{x}), |\nabla n^{\uparrow}(\mathbf{x})|, |\nabla n^{\downarrow}(\mathbf{x})|) \tag{3.3}$$

where $\epsilon_{xc}^{jellium}$ is the usual exchange-correlation energy of an electron in a uniform electron gas (jellium). It is then important to develop a suitable form for F_{xc}. More thorough discussions of LDA and GGA can be found elsewhere[56–58].

3.2. Pseudopotentials

Generally, the many-electron wave-function in solids is complex and difficult to represent. The wave-function $\Psi_n(\mathbf{x})$ from the Kohn-Sham equation needs to be represented in the form of a known basis set $\phi_\alpha(\mathbf{x})$, i.e.

$$\Psi_n(\mathbf{x}) = \sum_\alpha c_{n\alpha}\phi_\alpha(\mathbf{x}).$$

This representation is only possible for any arbitrary $\Psi_n(\mathbf{x})$ if the basis set $\phi_\alpha(\mathbf{x})$ is complete. A simple idea would be to use atomic orbitals. Unfortunately, it is in

practice impossible to make these sets complete. Another possibility is to use wave-functions of free electrons as basis set, i.e. plane waves. But, wave-functions near the nucleus are by far not similar to free electrons and hence, their representation would require tremendously many plane-waves.

However, in many materials, valence electrons behave like nearly free electrons suggesting that interaction between valence electrons and atomic cores is often weak. As the band structure of any solid is completely determined by the electron scattering properties of the atoms, it is possible to construct new potentials representing the atoms in such a way, that the scattering is equal to the original potential. More precisely, it is assumed that the core orbitals are the same as in free atoms and only valence orbitals are explicitly calculated. The interaction of valence electrons with atomic cores (and core orbitals) can then be represented by a so-called pseudopotential. Pseudopotentials replace the true potential in such a way that the Kohn-Sham eigenvalues remain unchanged, valence wave-functions are as smooth as possible and states of lowest energy are valence states, not core states.

3.3. Plane-Wave Basis Sets

For computational convenience, DFT codes use periodic boundary conditions such that the simulated cell is infinitely many times repeated in all directions. Therefore, Kohn-Sham eigenfunctions obey Bloch's theorem[59] such that

$$\Psi(\mathbf{x}) = u(\mathbf{x})e^{i(\mathbf{k}\cdot\mathbf{x})}$$

where $u(\mathbf{x}+\mathbf{R}) = u(\mathbf{x})$ is periodic with respect to the lattice vector $\mathbf{R}$. Each eigenfunction is associated with a wavevector $\mathbf{k}$ which need also to be sampled sufficiently. Periodic functions can be represented by Fourier series

$$u(\mathbf{x}) = \sum_{\mathbf{G}} c_{\mathbf{G}} e^{i\mathbf{G}\cdot\mathbf{x}}$$

with $\mathbf{G}$ a reciprocal vector (periodic cells form a Bravais lattice). In practice, one has to truncate the Fourier series at a cut-off energy

$$\frac{\hbar\mathbf{G}^2}{2m} < E_{cut}.$$

3.4. K-Point Mesh

Dealing with Bloch waves (see previous section), one only needs to integrate periodic functions over the first Brillouin-zone (a finite reciprocal space, instead of infinite real space) of the investigated crystal in order to calculate its properties (e.g. charge density, density of states, energy). To get the exact result, one would integrate over the whole Brillouin-zone, i.e. at all k-points. In practice, however, computational efficiency requires that only a special, finite mesh of k-points is used. This mesh needs to be sufficiently dense in order to obtain accurate results. One such mesh was proposed by Monkhorst and Pack[60]. This mesh is uniformly distributed throughout the entire Brillouin-zone, with sampled k-points running along (parallel) the reciprocal lattice vectors. This means, the Brillouin-zone is divided into smaller cells of the same shape with their corners being the k-points of the sampling mesh. These k-points then allow efficient integration by making use of the knowledge of periodicity resulting in only small errors compared with the complete Brillouin-zone integration. Thus, one has to choose the number of k-points used along all three reciprocal lattice directions by testing the convergence (comparing energies between calculations of various dense meshes). While other methods for choosing the k-point mesh exist, I will only use the one described here as it is used in VASP.

3.5. Computational Details of Calculations Performed within this Thesis

This section provides a summary of the computational details of the calculations performed as part of this thesis. The results of these calculations are discussed in part IV, after further technicalities and involved theory has been presented.

I performed density functional theory[45,46] calculations with the *ab initio* total-energy calculation package VASP (Vienna *ab initio* Simulation Package)[61,62]. I have used atomic potentials generated with the projector augmented-wave method[63,64] within the Local Density (LDA) as well as the Generalised Gradient Approximation (GGA)[56–58]. A plane wave basis-set expansion with a cut-off energy of 1000 eV was used for the representation of the valence electrons. Compared with a cut-off energy of 1200 eV, migration enthalpies changed by less than 0.1 %. The characteristics of the super-cells as well as the Monkhorst-Pack k-point mesh[60] used in this study are given in table 1. The comparison with a denser k-point sampling of the reciprocal space ($5\times5\times5$ for periclase, $4\times4\times4$ for perovskite and $5\times5\times5$ for post-perovskite) revealed a difference in the migration enthalpy of less than 0.1 %. Pressure was

imposed by a constant volume approach.

All calculations have been performed in a static, fully relaxed crystal. In order to ensure that there is only one negative frequency at the saddle point (see section 6.1), it is essential to find the saddle-point exactly—i.e., the crystal must be fully relaxed and all atomic forces are relaxed to within a very small tolerance ($< 10^{-6}$ eV/Å).

Table 1: Parameters for the DFT calculations of the lower mantle minerals.

Mineral	Space Group	Supercell	# of atoms	k-point mesh
Periclase	cubic Fm3m	$2 \times 2 \times 2$	64	$3 \times 3 \times 3$
		$3 \times 3 \times 3$	216	$1 \times 1 \times 1$
Perovskite	orthorhombic Pbnm	$2 \times 2 \times 1$	80	$2 \times 2 \times 2$
		$2 \times 2 \times 2$	160	$1 \times 1 \times 1$
Post-Perovskite	orthorhombic Cmcm	$3 \times 1 \times 1$	60	$2 \times 5 \times 5$
		$3 \times 1 \times 2$	120	$2 \times 5 \times 2$

Defect energetics are tightly linked with the cell-volume (as is evident from the strong pressure dependence (see below)). It is, thus, important that experimental and theoretical cell-volumes are equal (or at least similar). I have calculated the imposed pressure on the supercell within GGA. In order to estimate the uncertainty inherent to DFT I have compared GGA with LDA calculations performed at the same cell-volume. In general I find that LDA produces slightly smaller values for the migration enthalpy, by about 5 to 10%. Similarly, I find that the attempt frequency is also about 5% lower when calculated with LDA than with GGA.

Migration enthalpies calculated with larger unit cells agree to within 10 % with those calculated using the smaller cells of table 1. These changes of the energies of the same states in different cell-sizes are not negligible. This suggests that there is some self-interaction of the cell due to the periodic boundary conditions. While dealing with a charged system, the additional energy of monopole-monopole interactions will cancel out as only differences in energies are considered. However, especially for saddle-point configurations and the activated intermediate states of the six jump cycles (see also discussion below), it can be expected that multipoles are induced whose interaction-energies cannot be corrected for as multipoles will vary for each configuration. Thus, the supercells of table 1 are sufficiently large (as the error of the energies in the larger supercell is probably less than 10 %), nevertheless, larger supercells would still be desirable.

The limitation of computational power entailed not only a limitation of the super-

cell size but also limited the number of required parameters to be calculated. More precisely, calculating the $3N$ phonon frequencies for the attempt frequency (see below) requires up to $3N$ electron density optimisations (depending on the symmetry of the structure). I therefore only calculated the attempt frequencies in the small supercells and, in the case of the six jump cycles, assumed that they are equal for the equivalent jumps of different cycles. The effect of an error in the attempt frequency on the absolute diffusion rate, however, is small compared to effect of the error made in the migration enthalpy. I therefore used the migration enthalpies of the larger supercell where possible and the attempt frequency of the smaller supercell. But also the calculation of the exact migration enthalpy/localisation of the exact saddle point is computationally expensive (see below for details).

As a result of the limited computational power, the covered pressure range is only sampled scarcely. I thus made least square fits of a linear or quadratic polynomial (as high as possible while still giving a unique solution) to my data to obtain values of the migration enthalpy, attempt frequency and jump distances at intermediate pressures. By this approach it is possible to obtain smooth diffusion coefficients at any P-T-condition.

Part III.
Simulating Solid State Diffusion

On the macroscopic level, Fick's laws describe how diffusion is driven by a gradient in the chemical potential allowing accurate description of observations ignoring its underlying atomic processes. The entire diffusion process is described by this driving gradient and the so called diffusion coefficient. Random walk theory, on the other hand, provides the atomistic description of this process and links this diffusion coefficient to atomistic quantities that can be calculated with DFT. This section shall review the theory of diffusion on the macro- and microscopic level. Alongside the theory, I describe how diffusion constants can be obtained from first principle calculations. Lengthier discussions of diffusion in solids can by found in e.g.[65–69].

4. Diffusion through a Solid

Solid state diffusion is a complex process allowing atoms to perambulate a crystal. This process and its complexity are depicted in figure 4. Diffusion in a solid makes use of various pathways: diffusion along grain-boundaries can be fast, especially if a fluid is present, cracks and (micro-)nano-pores and -tubes provide diffusion channels inside crystal grains and finally, atoms can migrate through the grains themselves via lattice diffusion. The question then is, which pathway is the most efficient one and which one is rate limiting. Luckily for my concern, experiments[35,38] on minerals at shallow lower mantle conditions found that grain-boundary diffusion is negligible compared with lattice diffusion. This reduces the problem to finding the correct lattice diffusion mechanism and the according vacancy concentrations. Lattice diffusion requires atoms to jump into nearby, unoccupied lattice or interstitial sites or, e.g., two atoms swapping places at the same time (cycles), only to name the simplest variations. Diffusion along dislocations (so-called pipe-diffusion) also provides efficient pathways through the crystal lattice, but will be ignored as it is beyond the scope of this work, and as my results will show, appears not to be relevant.

Let us now consider vacancy diffusion, as it is often the dominating diffusion mechanism and will allow to explain all experiments. In this process, ions migrate through a crystal by jumping into nearby vacancies. Thus, consider a crystal with

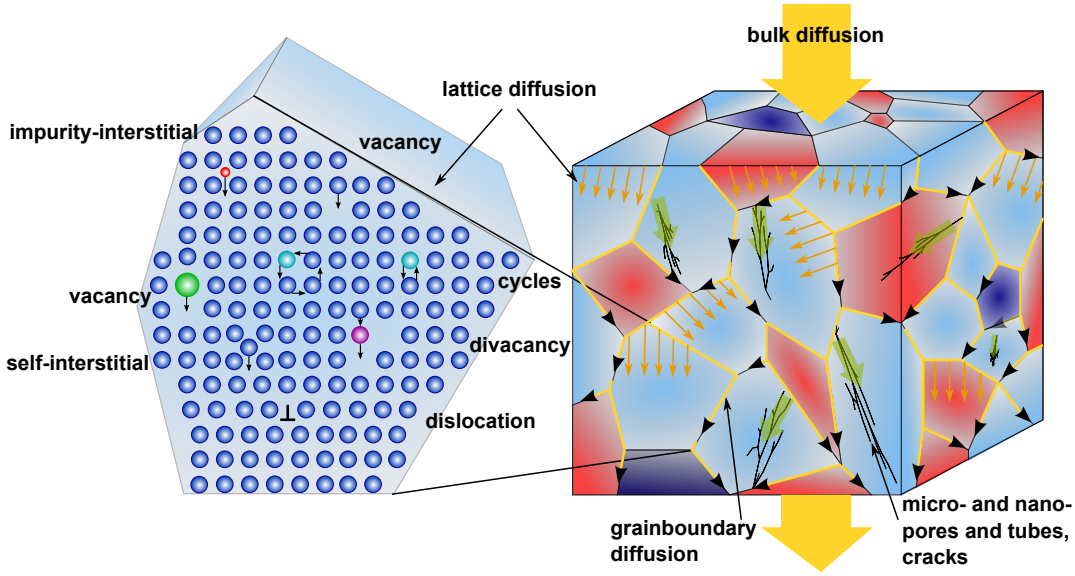

Figure 4: **Bulk diffusion pathways and mechanisms in a mineral aggregate** The aggregate (right) contains various phases (different colours). Diffusion can occur along the grain boundaries, along cracks and (micro-)nano-pores and -tubes and also through the lattice of the crystal grains (may be anisotropic). Within the grain, diffusion takes place via various mechanisms such as vacancy and interstitial, complex cycles, divacancies and along extended defects such as dislocations (pipe-diffusion). Moreover, crystals contain impurities (different colours) that generally control the defect concentrations

a single vacancy. In its equilibrium configuration, the crystal is fully relaxed and its energy is at a minimum. If one waits long enough, thermal excitation will eventually kick a nearby ion towards the vacancy. If the kick was strong enough, the ion migrates towards the vacancy, surpasses the energy-barrier by passing a saddle-point (the maximum energy along the migration path) and relaxes again down into the site of the vacancy (see Figure 7). The migrating ion and the vacancy have swapped their sites and the crystal is again at its equilibrium configuration. The diffusion-rate is, hence, controlled by the number of vacancies and from how far and how often the vacancy jumps.

5. Theory of Diffusion

5.1. Macroscopic View: Fick's Laws of Diffusion

On the macroscopic level, diffusion is described by Fick's laws[70,71] which is a continuum description and purely based on phenomenology. One observes that a substance moves from regions of high concentration to regions of low concentration. Therefore, the driving force of the diffusion process is a gradient of a concentration, more precisely of a chemical potential. While the latter is the correct driving force, the concentration gradient is only a good approximation for the gradient in the chemical potential in many simple systems. Fick's first law describes steady state diffusion and writes

$$J_i = -D_i(T, P)\nabla c_i \tag{5.1}$$

where J_i is the diffusion flux, the amount of substance i that crosses a unit plane per second, $D_i(T, P)$ is the diffusion constant (also diffusivity; may depend on c_j) and c_i the chemical potential of substance i. In the time dependent case, Fick's second law describes mass conservation and writes

$$\frac{\partial \phi}{\partial t} = D\Delta\phi \tag{5.2}$$

where Δ is the Laplace-operator.

It is obvious that the diffusion constant D_i completely characterises diffusion in a given system (a given chemical potential). Thus, the diffusion coefficient needs to be quantified in order to describe a system and to compare it with others. This can either be done by experiments, or, as in this case, from theoretical calculations. To this end, a better understanding of what the diffusion coefficient is and how one can describe it on the atomistic level is needed.

5.2. Atomistic View: The Einstein-Smoluchowski Relation

On the microscopic level, diffusion is nothing but atoms moving around randomly on the crystal lattice by many individual jumps - this is the so-called random-walk theory. This view directly relates the diffusion coefficient to atomistic properties. The atomic movement depends on how far the atoms can jump and at what rate.

It was Einstein[72] and (independently) Smoluchowski[73] who found at the beginning of the last century that the important quantity is the mean square displacement and

derived the now so-called Einstein-Smoluchowski relation

$$D = \frac{\langle R^2 \rangle}{6\tau} \tag{5.3}$$

where $\langle R^2 \rangle$ denotes the mean square displacement and τ the time passed. The pointy brackets denote the average over a large number of particles. On a crystal lattice, there are only a few jump vectors such that we can write (with d being the length projected onto, e.g., the x-axis)

$$\langle R^2 \rangle = \langle n \rangle d^2,$$

where $\langle n \rangle$ is the average number of jumps. Now, the jump rate can be introduced as

$$\Gamma = \frac{\langle n \rangle}{Z\tau}$$

with the coordination number Z. Finally, the diffusion coefficient is related to the jump distance and the rate at which these jumps occur:

$$D = \frac{1}{6} d^2 Z \Gamma. \tag{5.4}$$

This is the so-called vacancy diffusion coefficient. While a vacancy will perform a real random walk, (tracer) atoms will not. Diffusion in a crystal lattice is not completely random, but correlated. This is because after an atom jumped into a nearby vacancy, there is a non-vanishing chance reversing this jump, simply because the vacancy is still there. The atom thus moves slower than expected from a real random walk. While correlation factors for simple structures (such as SC, FCC,BCC, diamond) have been calculated analytically, this is not possible in more complex structures, such as the orthorhombic perovskite and post-perovskite and Monte-Carlo methods have to be used (e.g. kinetic Monte-Carlo, see section 6.3). Moreover, these calculations are further complicated by the fact that I found that silicon in perovskite and magnesium and silicon in post-perovskite diffuse via complex six-jump cycle mechanisms. Thus, such calculations have not been attempted in this work because this correlation effect is generally small and reduces the diffusion coefficient (5.4) by less than a factor of $\frac{1}{2}$ (see table 2). Its effect on the absolute diffusion rate in the orthorhombic structures will, therefore, be ignored in this study as it is small compared with other unknowns of the investigated systems, namely

Table 2: Correlation factors f for vacancy diffusion in cubic lattices (simple cubic (SC) and face-centred cubic (FCC)) relevant for this study as well as in the diamond and body-centred-cubic (BCC) lattice for comparison. Be aware that the investigated $MgSiO_3$-perovskite is orthorhombic such that the values here can only be approximate.

Lattice	f	Example
SC	0.6531	Mg & Si[a] diffusion in perovskite
FCC	0.7815	Vacancy diffusion in periclase
		O diffusion in perovskite
BCC	0.7272	
diamond	0.5	

[a] if it would migrate via direct jumps

vacancy-concentrations, temperature and pressures.

In this work, the main concern is lattice self-diffusion. As most of the time lattice sites will be occupied such that atoms cannot move, the above expression for the vacancy diffusion coefficient, describes how a single vacancy would diffuse within the crystal. The atomic diffusion is thus reduced and controlled by the vacancy concentration N_v and self-diffusion coefficient is defined as:

$$D = \frac{Z}{6} d^2 N_v \Gamma. \tag{5.5}$$

While d is a (known) property of the investigated crystal lattice, there are now two parameters left that still need to be further characterised. This will be done in the next two sections, where first the theory behind the jump rate Γ is discussed and then how vacancies are formed.

6. Calculating the Vacancy Diffusion Coefficient

The first step in calculating the diffusion coefficient is to determine the jump rate of the vacancy/atom. Vineyard-theory[74] provides a simple expression for evaluating frequency factors (rates) in solid state rate processes such as diffusion. It is based upon classical absolute rate theory and its only inherent approximations are the assumption of harmonicity of the saddle point and equilibrium position, negligence of quantum effects and the assumption that the initial and saddle point configuration are well defined states. This section shall just briefly reproduce its essential expressions and show how it is calculated from first principles.

6.1. Vineyard Rate Theory

Ionic jump rates are characterised by the Gibbs free energy of migration ΔG which is required to carry the ion from its initial equilibrium position to the saddle point, and the so-called attempt-frequency, $\tilde{\nu}$, which is associated with the ionic vibration towards the saddle point. The jump rate is then given by the Arrhenius-type expression

$$\Gamma = \tilde{\nu} e^{\frac{-\Delta G}{kT}} \tag{6.1}$$

where ΔG is the Gibbs free energy of migration and $\tilde{\nu}$ the attempt frequency. Even though it is assumed that only one atom jumps at a time, it is a many-body process as the jumping atom interacts with its surrounding atoms. In order to simplify the calculations a couple of approximations need to be made. The first is that the initial (before the jump) and the saddle-point states are well defined. It allows the derivation of an analytical solution for the problem and is required by any transition state theory. The second and third are that quantum effects are neglected throughout and vibrations are assumed to be harmonic (which is why Vineyard theory is also called harmonic transition state theory).

Let me first introduce some terminology in order to simplify the discussion of the derivation of the jump rate. Consider a crystal with N atoms such that there are $3N$ degrees of freedom, $x_1, x_2, ..., x_{3N}$. Each degree is associated with a mass m_j and one introduces new coordinates $y_j = \sqrt{m_j} x_j$. The potential energy of the crystal shall be given by $\Phi(y_1 ... y_{3N})$. In the $3N$-dimensional configuration space of the crystal, Φ has a minimum at a point A which is a vacancy surrounded by atoms in equilibrium positions (see figure 5). I will call this configuration the initial ground state. As one

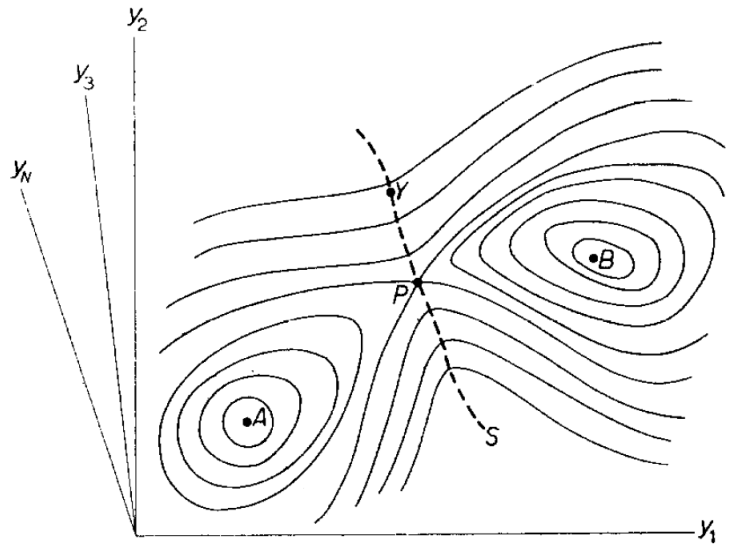

Figure 5: **Schematics of Vineyard-theory** (taken from[74]). Configuration space of 3N dimensions showing, schematically, hyper-surfaces of constant potential energy (solid lines) and imaginary constraining hypersurface (dotted line).

atom swaps the site with the vacancy (makes a diffusing jump), a new minimum in Φ is reached, located at B and I called it final ground state. It is now assumed that these two ground states, A and B, are connected with a single minimum energy pathway (following a valley) that has a single saddle-point P. The region around the ground states can now be separated along a hyper-surface S which passes through the saddle-point P and is perpendicular to the contours of constant Φ. On the 'left' of S, representative points belong to the region of A, to the right to B. It is, thus, assumed that any representative point moving from region A across S will end up in region B. In thermal equilibrium there is now a definite number of representative points Q_A in region A and a definite number I of them is crossing over S per second and reach region B.

Let me now derive the expression for the atomic jump rate Γ. From the above definitions, the atomic jump rate is given by

$$\Gamma = \frac{I}{Q_A} = \frac{1}{\tau} \tag{6.2}$$

where τ is the average lifetime of representative points in region A. Calculating Γ, therefore, requires to calculate the number of representative points in region A as well as how many leave A per second, I. The number of representative points in

region A is given, in thermal equilibrium, by

$$Q_A = \int_A \rho_0 e^{-\frac{\Phi(v)}{kT}} dv \tag{6.3}$$

where ρ_0 is a normalising constant and the integral is over region A. For the number of representative points on I, one needs also to consider the hyper velocity $\mathbf{V} = \{\dot{y_1}...\dot{y_{3N}}\}$. The density of representative points on S at a certain point Y can be written as

$$\rho(Y, \mathbf{V}) = \rho_1 e^{-\frac{\Phi(Y)+\mathbf{V}^2/2}{kT}} \tag{6.4}$$

with the normalising constant

$$\rho_1 = \rho_0 (2\pi kT)^{-\frac{3N}{2}}.$$

Let an element of S at Y be represented by the vector $d\mathbf{S} = \{dS_1...dS_{3N}\}$. The total current of velocity crossing $d\mathbf{S}$ writes

$$d\mathbf{I} = d\mathbf{S} \int \mathbf{V} \rho(Y, \mathbf{V}) d\mathbf{V} \tag{6.5}$$

with $d\mathbf{V} = d\dot{y_1}...d\dot{y_{3N}}$ integrated over all $\mathbf{V}$ with $d\mathbf{S} \cdot \mathbf{V} > 0$. The axes can now be rotated such that, say, y_1 is parallel to $d\mathbf{S}$ at Y such that $dS = |d\mathbf{S}| = dS_1$. After evaluating Gaussian integrals, one finds

$$d\mathbf{I} = \rho_0 \sqrt{kT/2\pi} e^{-\frac{\Phi(Y)}{kT}} dS \tag{6.6}$$

and therewith

$$I = \rho_0 \sqrt{kT/2\pi} \int_S e^{-\frac{\Phi(Y)}{kT}} dS. \tag{6.7}$$

integrating over the hyper-surface S. Now, equations (6.7) and (6.3) are inserted into equation (6.2) yielding

$$\Gamma = \sqrt{\frac{kT}{2\pi}} \frac{\int_S e^{-\frac{\Phi}{kT}} dS}{\int_A e^{-\frac{\Phi}{kT}} dv}. \tag{6.8}$$

The atomic jump rate thus is a ratio of two configurational partition functions. In principle, equation (6.8) accounts for all bodies and all degrees of freedom in the

many-body space. The next step now is to approximate equation (6.8) by applying the theory of small vibrations to the potential energy Φ. Near point A, the potential energy Φ can be expanded in a Taylor series to second order:

$$\Phi \approx \Phi(A) + \sum_{j=1}^{3N} \frac{1}{2}(2\pi f_j)^2 q_j^2 \tag{6.9}$$

where $q_1 ... q_{3N}$ are the normal coordinates and $f_1 ... f_{3N}$ are the normal frequencies for vibrations about point A. The second term in equation (6.9) is a sum over energies of harmonic oscillators with frequencies ν_j. Analogously, around the saddle point P within the constraining surface S:

$$\Phi \approx \Phi(A) + \sum_{j=1}^{3N-1} \frac{1}{2}(2\pi f'_j)^2 q'^2_j \tag{6.10}$$

where $q'_1 ... q'_{3N}$ are the normal coordinates and $f'_1 ... f'_{3N-1}$ are the normal frequencies for vibrations about point P with constraint S. There is exactly one normal frequency and coordinate that is perpendicular to the hyper-surface S such that it does not contribute to the potential energy and, therefore, there are only $3N - 1$ terms in the sum of equation (6.10). This frequency is easy to identify, because the crystal is in an unstable configuration when the ion is at the saddle point. Displacing the atom at the saddle point in the direction perpendicular to S gives rise to one negative frequency in the vibrational spectrum which is the one that is not used. Now, the expression for Φ, equations (6.9) and (6.10), are inserted in equation (6.8) and Gaussian integrals are evaluated (sums in the potential energy Φ become products of exponential functions). This transforms equation (6.8) into

$$\Gamma = \left(\frac{\prod_{j=1}^{3N} f_j}{\prod_{j=1}^{3N-1} f'_j} \right) e^{\frac{-(\Phi(P)-\Phi(A))}{kT}} \tag{6.11}$$

This can be simply rewritten as

$$\Gamma = \left(\frac{\prod_{j=1}^{3N} f_j}{\prod_{j=1}^{3N-1} f'_j} \right) e^{\frac{-\Delta H}{kT}} \tag{6.12}$$

Thermodynamics states that $\Delta G = \Delta H - T\Delta S$ with ΔH and ΔS being the migration enthalpy and migration entropy respectively. Hence, one can rewrite equation (6.1) as

$$\Gamma = \tilde{\nu} e^{\frac{\Delta S}{k}} e^{\frac{-\Delta H}{kT}} \tag{6.13}$$

such that the following identification in equation (6.12) can be made:

$$\left(\frac{\prod_{j=1}^{3N} f_j}{\prod_{j=1}^{3N-1} f'_j} \right) = \tilde{\nu} e^{\frac{\Delta S}{k}}. \tag{6.14}$$

The attempt frequency thus is the product of the $3N$ normal frequencies of the ground state over the product of the $3N-1$ normal frequencies of the saddle-point configuration. If one assumes that all normal frequencies remain unchanged during migration, then the attempt frequency reduces to the normal frequency of the atom vibrating towards the saddle point.

How to calculate the migration enthalpy ΔH will be described in the next section. Thus, it is herewith shown that all quantities of equation (6.12) can be evaluated from the potential energy surface (at zero temperature) and entropic effects are included through the harmonic approximation.

Corrections to Vineyard-Theory Vineyard-theory is not an exact theory. It assumes that the energy surfaces at the saddle-point and at the equilibrium position are perfectly harmonic. This does not have to be strictly true and one has then to correct for the anharmonicity[75]. In figure 6, the solid line shows the anharmonicity an oxygen atom encounters at the saddle point in MgO at 0 GPa in [001]-direction: The solid line is a 4^{th}-order polynomial in z^2 fitted to the calculated energies for different displacements away from the saddle point (diamonds), while the dashed line

is only its harmonic term. Clearly, the negligence of the higher order terms results in a much flatter energy surface and hence the Vineyard-theory will overestimate the attempt frequency. Therefore, the following reduction factor

$$R = \frac{\int_0^{r_0} e^{-\frac{E(\mathbf{r})}{kT}} d\mathbf{r}}{\int_0^{\infty} e^{-\frac{E'(\mathbf{r})}{kT}} d\mathbf{r}} \tag{6.15}$$

should be applied to the product of the frequencies of saddle-point and equilibrium configuration. Here, $E(\mathbf{r})$ is the fitted 4^{th}-order polynomial in z^2 and $E'(\mathbf{r})$ is the harmonic part. The limiting radius r_0 of the integral in the numerator has to be sufficiently large such that a further increase does not significantly increase the integral and has not to be larger than the largest displacement for which calculations have been performed. In many systems, departure from harmonicity is significant only along one direction such that the above integrals become one-dimensional. However, in my DFT calculations we find that anharmonicity is negligible (<1% deviation, see figure 6).

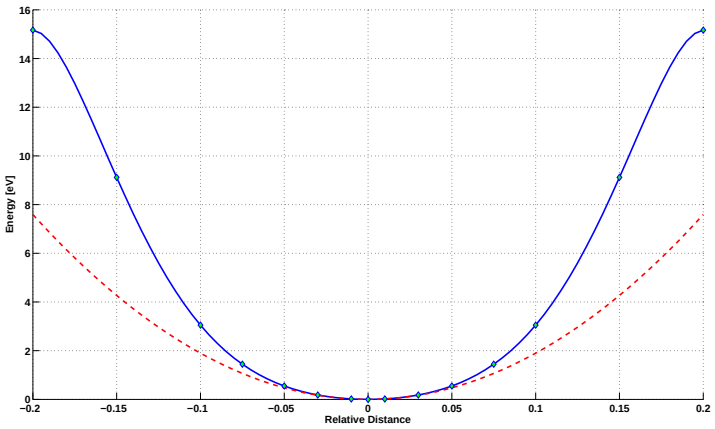

Figure 6: **Anharmonicity an oxygen atom encounters at the saddle point in MgO at 0 GPa in $\langle 001 \rangle$-direction** The solid line is a 4^{th}-order polynomial in z^2 fitted to the calculated energies (in eV) for different displacements (relative to cell-parameter) away from the saddle point (diamonds), while the broken line is its harmonic term

Another idealization is that Vineyard-theory assumes that each jump is successful — i.e., each ion jumping towards a vacancy will reach the vacancy once it has crossed the saddle-point. Again, for real systems this is not the case as the jumping atom can cross the saddle-point only to immediately return back to its initial state. This can

happen because the jump is a complex, dynamical many-body process (dynamical correlation). Luckily, unsuccessful jumps are rare and are unlikely to exceed 10% as has been shown by Flynn and Jacucci[76]. This is because the time after which the system loses its memory of previous jumps (onset of randomization) is generally much shorter than any vibrational period of any particle in the system.

6.1.1. Phonon Calculation

Lattice vibrations of crystals can be described as discrete vibrational modes of well defined energy, frequency and wave-vector. Thus, these vibrations behave like particles (are so-called quasi-particles) and are called phonons. A thorough discussion of phonons and their tremendous importance in solid state physics is beyond the scope of the work but can be found in any standard solid state textbook (e.g.[77,78]).

The vibrational modes of a crystal, the phonons, determine many important properties of the crystal such as specific heat, sound velocity and infrared and Raman absorption. They also provide information on the stability of a certain configuration, e.g., low frequencies indicate a phase transformation or negative frequencies originate in unstable configurations. Additionally, the phonon spectrum provides a good approximation to free energies[79]. It is therefore, apparently, very useful to calculate phonons in condensed matter systems. This section shall describe how phonon spectra can be obtained from first principles.

At low temperatures, where the harmonic approximation is valid, the potential energy of a crystal can be expanded around the equilibrium positions of the nuclei. The linear term in this expansion is negligible and the potential energy writes as the sum of the energy of the crystal when it is at equilibrium plus the quadratic term from the expansion:

$$E_{harm} = E_{eq} + \frac{1}{2} \sum_{ls\alpha, l't\beta} \Phi_{ls\alpha, l't\beta} u_{ls\alpha} u_{l't\beta}. \tag{6.16}$$

Here, $u_{ls\alpha}$ denotes the displacement of atom s in unit cell l along the Cartesian component α and $\Phi_{ls\alpha,l't\beta}$ is the force-constant matrix. The force constant matrix is basically an assemblage of spring constants describing the interaction between all atoms within the crystal: It describes the force $F_{l't}$ the atom $l't$ feels in direction β when the atom ls is displaced by u in direction α. Mathematically, the force-constant

matrix is therefore given by

$$\Phi_{ls\alpha,l't\beta} = -\frac{\partial F_{l't\beta}}{\partial u_{ls\alpha}} = \frac{\partial^2 E_{harm}}{\partial u_{ls\alpha}\partial u_{l't\beta}}. \tag{6.17}$$

The dynamical matrix at wavevector $\mathbf{q}$ is then given by the Fourier-transform of the force-constant matrix:

$$D_{s\alpha,t\beta}(\mathbf{q}) = \frac{1}{\sqrt{M_s M_t}} \sum_l \Phi_{ls\alpha,l't\beta} e^{i\mathbf{q}\cdot(\mathbf{R}_{l'}+\tau_t-\mathbf{R}_l-\tau_s)}. \tag{6.18}$$

$\mathbf{R}_{l'} + \tau_t$ stands for the equilibrium position of atom t in the primitive cell l. In principle, the sum is over the infinite number of primitive cells in the crystal and theoretically, the force-constant elements are non-zero for arbitrarily large separations. In practice, where only supercells and not infinite lattices are used, the cut-off distance beyond which force-constant elements are neglected is the supercell border. Additionally, the displacement of an atom in a supercell with periodic boundary conditions displaces also all images of this atom. This results in the fact, that with the supercell method, the dynamical matrix can only be calculated exactly at discrete wavevectors $\mathbf{q}$ while in between these wavevectors, the values of the dynamical matrix are only interpolations[80]. Ultimately, the phonon frequencies $\omega_{\mathbf{qs}}$ are the eigenvalues of the dynamical matrix.

The force-constant matrix can be constructed by using equation (6.17) by different methods. Either by a method called linear response method which uses density functional perturbation theory (DFPT[81–84]) or the method of small displacements[85,86].

In this work, the small displacement method as implemented in the program PHON[86] was used and I will therefore concentrate on technical details of this method. However, most points are of general concern in any phonon calculation. In the method of small displacements, the force-constant matrix is constructed by displacing one atom at a time and calculating the forces acting on all other atoms due to this displacement. Taking advantage of symmetries, even in defective systems, greatly decreases the number displacements and hence of DFT calculations that have to be performed in order to construct the force-constant matrix of the system. The force-constant matrix is invariant under the point-group symmetries of the crystal.

The elements of a correct force-constant matrix fulfill three relations among each other, the so-called sum rules[79]:

1. Symmetric: $\Phi_{ls\alpha,l't\beta} = \Phi_{l't\beta,ls\alpha}$ (partial differentiation is commutative in equation (6.17))
2. Newton's third law: $\Phi_{ls\alpha,l't\beta} = -\sum_{l\neq l',t\neq s} \Phi_{ls\alpha,l't\beta}$
3. from the previous two: $\sum_{l\neq l',t\neq s} \Phi_{ls\alpha,l't\beta} = \sum_{l\neq l',t\neq s} \Phi_{l't\beta,ls\alpha}$

Errors in constructing the force-constant matrix arise from errors associated with the force evaluation and will result in a violation of these sum-rules. Thus, these rules generally have to be enforced in addition to the ones from the crystal symmetry by a self consistent, iterative procedure.

There are several sources of errors in phonon-calculations: Firstly, there are the errors one makes by using computational methods and the unavoidable obstacle of using physical approximation. Obviously, some errors originate from the problem that one needs to use a finite basis set for the representation of the electron wavefunctions as well as a finite k-point set. Interestingly, errors made due to the choice of the exchange-correlation energy and pseudopotentials do not result in a violation of the sum-rules. In a similar category falls the problem of computational rounding and interpolation errors as the wavefunctions are only represented on a discrete grid.

Secondly, there are errors which are more specific to the system that is analysed. They emerge because of the finite convergence (and size) of the structural parameters and potential anharmonicities in the crystal. Anharmonicities of the crystal can disturb the point-group invariance of the force-constant matrix and the symmetry of the matrix with respect to the point group operations of the crystal has to be enforced[85]. A problem inherent to the method of small displacements is the choice of the amount of displacement. It is a compromise between generating large enough forces throughout the supercell and remaining in the harmonic approximation. Especially if PBCs are used, also the size of the supercell is of concern because self-interaction due to the displacement has to be avoided. I.e., the force-constant matrix elements need to be fallen to a negligible value at the supercell boundary. This can be a problem particularly in ionic materials where the displacement of ions can introduce dipoles resulting in long-range interactions.

The last problem to be aware of also only arises in the small-displacement method. This method ignores the non-analytical part of the dynamical matrix, resulting in an error of the phonon-branches near the centre of the Brillouin-zone: the longitudinal branch of the optical phonons (LO) is described as degenerate with the two transversal optical (TO) phonon branches, i.e. the so-called LO-TO splitting is de-

scribed incorrectly. Nevertheless, as thermodynamical properties of any crystal are described accurately[86] it is a valid method for my purposes.

Quasi-Harmonic Approximation With increasing temperature, the harmonic approximation in the phonon calculation becomes more and more inadequate. Anharmonicity arises because atoms are not located in exactly harmonic minima and because of phonon-phonon interaction. A simple way to partially correct the effects of the former, which basically results in lattice expansion with increasing temperature, is to make the frequencies volume dependent. This is the quasi-harmonic approximation in which anharmonicity is considered as thermal expansion, while phonon calculations are still performed in the harmonic approximation. All that is required is an adequate equation of state $V(P,T)$ relating the volume V to the pressure P and temperature T. While an increase in pressure suppresses anharmonicity, in contrast, an increase of the temperature will deteriorate the quality of the approximation because phonon-phonon interactions will increase. It is known that the quasi-harmonic approximation breaks down above 50-70% of the melting temperature[87,88].

6.2. Migration Enthalpies

The migration enthalpy ΔH is the energy difference between two crystal configurations where in one the crystal is at equilibrium and in the other the migrating ion is at the saddle-point:

$$\Delta H_{migration} = E_{saddlepoint} - E_{equilibrium}. \tag{6.19}$$

Figure 7 depicts the energy-variation of a migrating ion along its migration path and how the maximum energy difference defines the migration enthalpy. This migration enthalpy is also valid for increased temperatures as it has been found in experiments that the migration enthalpy is almost temperature independent[89] (linearity of plots of log(D) to $T^{-}1$), unless there is a change in the migration mechanism.

For systems with high symmetry (i.e., MgO), finding the saddle point is reasonably straightforward since it often lies on a line of symmetry. For lower symmetry materials, such as perovskite, it is not obvious where the saddle point is. It is possible to use trial and error, or a grid searching method to find the saddle point, but this is quite inefficient and inaccurate. The importance of this is exemplified by recent calculations and experiments on $MgSiO_3$ perovskite.

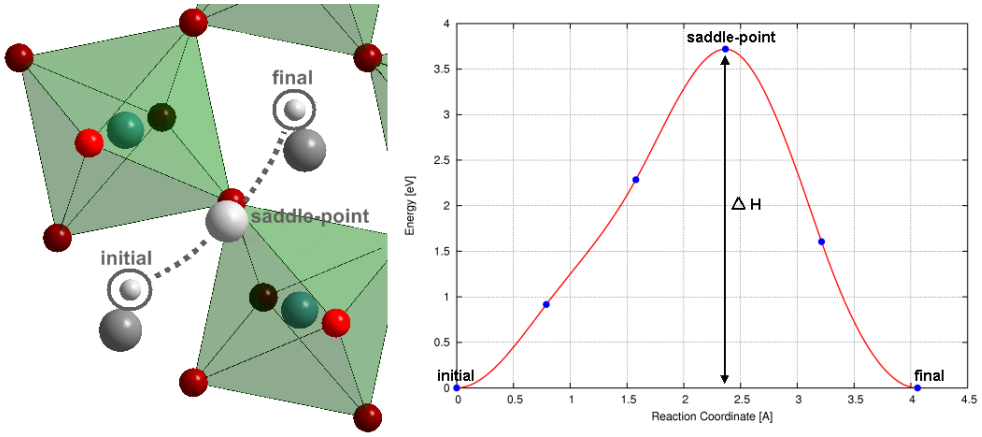

Figure 7: **Definition of the migration enthalpy** Left hand side: a magnesium ion migrates in $MgSiO_3$ perovskite from its initial to its final position by overcoming a saddle-point. Right hand side: The energy barrier encountered by the migrating ion as calculated with CI-NEB (see below). The saddle point is at the maximum of the energy barrier and the energy difference to the initial state defines the migration enthalpy ΔH

Empirical potential calculations[90] on silicon diffusion in $MgSiO_3$ perovskite had estimated the migration enthalpy as being about 9 eV; this was much higher than for oxygen and magnesium, and agreed with the idea that silicon was the slowest diffusing species — and therefore rate limiting the rheology — in mantle perovskites. However, a later experimental study found a significantly lower migration energy of only 3.5 eV[35]. An identical value was also obtained by Dobson et al.[41] but using a different procedure. The calculations were repeated by Karki and Khanduja[91], but in this case using DFT to calculate the necessary energies. Their calculated migration enthalpies for oxygen and magnesium agreed with experimental values, but they also found a very high value for silicon of 8.33 eV (at room pressure). They suggested, therefore, that silicon diffusion must occur via some sort of cooperative mechanism involving oxygen vacancies. However, the reason is more prosaic than that; both theoretical studies chose the wrong migration pathway. Figure 8 is a contour map of computed migration enthalpies in a plane of possible saddle-points for silicon diffusing along the ⟨110⟩ pathway at two different pressures (see[92] for details). The two minimum energy points shown are 3.58 eV and 3.52 eV and are the most likely place through which the migrating atom would pass. The pathway chosen by Wright and Price[90] and Karki and Khanduja[91] are not shown, but are slightly higher on the Z-axis than the 3.52 eV (and 6.59 eV) point. Note that you do not have to be very far from the minimum energy point for the apparent (and

erroneous) migration energy to increase substantially. A better approach is to use a method such as the Nudged-Elastic-Band; this is described next.

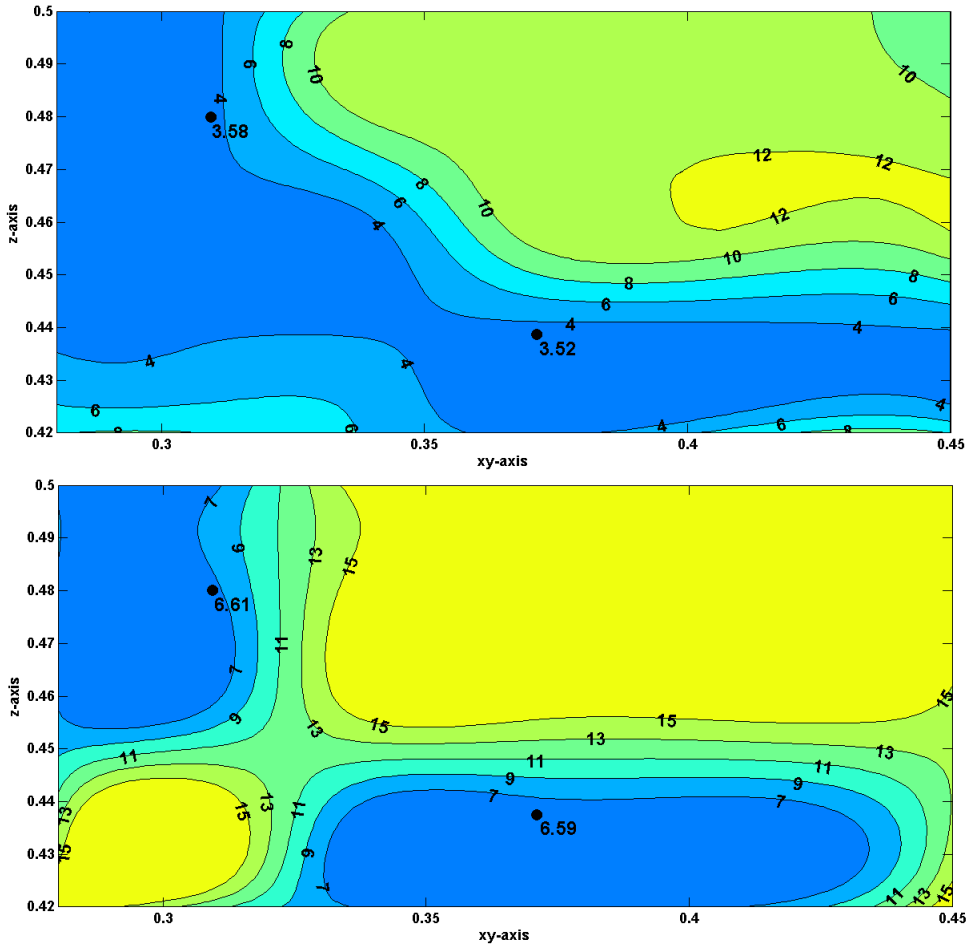

Figure 8: **Contour maps of migration enthalpies for silicon diffusion in $MgSiO_3$ perovskite the direct jump along** $\langle 110 \rangle$. Upper panel at 3.3 GPa and lower panel at 151.7 GPa. The calculated minima are marked with black dots and labelled with their corresponding value. In calculations, a small deviation from the minimum energy migration pathway (black dots) can result in a substantial increase of the migration enthalpy shown

6.2.1. Climbing Image Nudged Elastic Band Method

Finding a saddle point means finding a maximum along a minimum energy path (MEP) that takes the system from one potential energy minimum to another. At any point on a MEP, the atoms are at a minimum of trajectories perpendicular to the path and the force acting on the atoms is only pointing along the path. MEPs

in crystals are migration pathways. Maxima on the MEP are saddle points on the potential energy surface. A first order saddle point is a maximum in one direction and a minimum in all other directions. Therefore, saddle point finding algorithms only need to decide which degree of freedom should be maximized.

There are two possible situations: in the first, the initial and the final states are known and finding a MEP is rather straight forward (to decide whether it is the lowest energy path or not is still difficult) by the application of a nudged elastic band (NEB)[93]. In the second, only the initial state is known and the task basically becomes to navigate in high dimensional space which may be done by using the dimer method[94]. In this work, however, we will only deal with the former case, because the diffusion mechanisms are simply vacancies hopping between nearest neighbour sites (which does not preclude fairly complex diffusion mechanisms as shown below).

The nudged elastic band (NEB) method is an efficient method in finding MEPs if the initial and final state of a transition are known (see[93] and references therein). The MEP is found by constructing a set of images of the system (typically between 4-20). The addition of a spring interaction between adjacent images ensures continuity of the path. These springs mimic an elastic band. Band optimisation involves minimisation of the forces acting on the images bringing the band to the MEP. It is then essential to decompose the true forces and the spring forces into their components perpendicular and along the path. Therewith, true forces will not affect the distribution of the images along the band and spring forces will not interfere with the convergence of the elastic band to the MEP (optimising the atomic positions). A force projection, the so called nudging, will then ensure that only the perpendicular component of the true force and the parallel component of the spring force is included.

Consider an elastic band with $N+1$ images denoted by $[\mathbf{R_0}, \mathbf{R_1}, \mathbf{R_2}, ..., \mathbf{R_N}]$ where the end points $\mathbf{R_0}$ and $\mathbf{R_N}$ are fixed and given by the optimised structures (energy minima) corresponding to the initial and final state. The situation is depicted in figure 9. The $N-1$ intermediate images are adjusted by the algorithm. Generally, a linear interpolation between the initial and final state yields a sufficiently good starting guess for the intermediate images. The NEB force on image i is the sum of the spring force along the local tangent and the true force perpendicular to the local tangent:

$$\mathbf{F}_i^{NEB} = \mathbf{F}_i^{S\parallel} + \mathbf{F}_i^{\perp}. \tag{6.20}$$

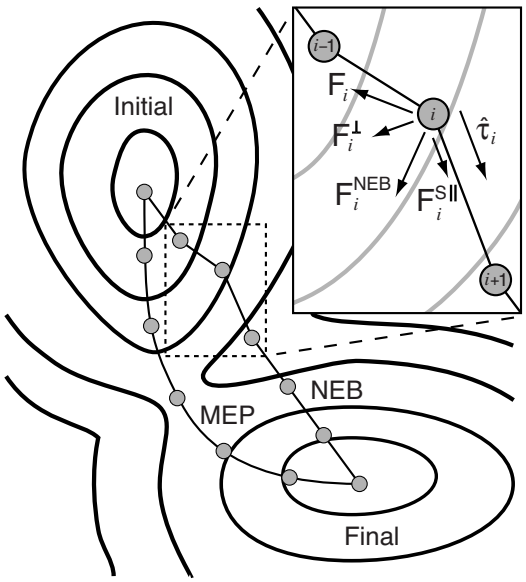

Figure 9: **The nudged elastic band method** The NEB-force $\mathbf{F}_i^{NEB}$ is the sum of the spring force $\mathbf{F}_i^{S\parallel}$, parallel to the local tangent $\hat{\tau}_i$, and the force $\mathbf{F}_i^{\perp}$ from the potential pointing perpendicular to the tangent. For completeness, the unprojected force $\mathbf{F}_i$ is also shown (figure taken from[95])

The true force is then given by

$$\mathbf{F}_i^{\perp} = -\nabla E(\mathbf{R}_i)^{\perp} = -\nabla E(\mathbf{R}_i) + \nabla E(\mathbf{R}_i) \cdot \hat{\tau}_i \hat{\tau}_i \tag{6.21}$$

where E is the energy of the system (a function of all atomic coordinates) and $\hat{\tau}_i$ is the normalised local tangent at image i. The spring force writes

$$\mathbf{F}_i^{S\parallel} = k\left(|\mathbf{R}_{i+1} - \mathbf{R}_i| - |\mathbf{R_i} - \mathbf{R}_{i-1}|\right)\hat{\tau}_i \tag{6.22}$$

where k is the spring constant. As long as all force constants between the images are equal, the spacing between the images is equal as well. Originally, there were often kinks between the images due to the choice of how τ_i has been approximated. However, a better choice of τ_i[96] improves the smoothness of the band and therewith its stability and efficiency (convergence). Finally, a force-based optimisation algorithm is then used to move the images according to equation (6.20). A discussion about the efficiency of several algorithms for NEB calculations is given by[95].

In the method of the climbing image NEB (CI-NEB), the image with the highest energy is pushed towards the saddle point, eventually finding the saddle point exactly. While the forces acting on all other than the highest energy image are given

by equation (6.20), the force acting on the highest energy is determined by

$$\mathbf{F}_{\mathbf{i_{max}}} = -\nabla E(\mathbf{R}_{\mathbf{i_{max}}}) + 2\nabla E(\mathbf{R}_{\mathbf{i_{max}}})|_{\parallel} \tag{6.23}$$

$$= -\nabla E(\mathbf{R}_{\mathbf{i_{max}}}) + 2\nabla E(\mathbf{R}_{\mathbf{i_{max}}}) \cdot \tau_{i_{max}} \tau_{i_{max}}. \tag{6.24}$$

Clearly, this image is not affected by the spring forces, but is moved by the full force due to the potential with the component along the elastic band inverted.

In this work, the VASP implementation of CI-NEB available through the VASP transition state theory tools (VTST) from *http://theory.cm.utexas.edu/vtsttools/* has been used.

6.3. Kinetic Monte-Carlo: Simulating Diffusion

While Vineyard's rate theory allows one to calculate the diffusion rate from single-hop mechanisms (vacancy and interstitial), it is more difficult to obtain it for more complex mechanisms such as cycles. Moreover, in the presence of impurities, vacancies have several options to jump to with each having a different rate. In the former case, the problem lies in finding the exact rate for an atom to diffuse if it has to perform several hops before it is on its new lattice site. In the latter, the problem is that it is not known how the overall system evolves diffusion-wise, if atoms can have varying jump rates. A way to solve these problems is to use kinetic Monte-Carlo (KMC) simulations which I describe by following Voter's review[97].

The advantage of this method is that it removes the time scale problem between lattice/atomic vibrations and the jump rates that one encounters in molecular dynamics simulations. Jump rates are several orders of magnitude slower than atomic vibrations and jumps are thus extremely rare. KMC simulations allow to separate these two movements by only considering the slow jump rates between various states.

The various single jump rates are still calculated within Vineyard-theory. Once all of them are known, the question is how to advance the system in time. First, we decide which jump it is going to make and then how long the (e.g.) vacancy remained on its current site. Assume the vacancy is on lattice site i and the pathways away from this site have rate constants k_{ij}. From the latter an array s of partial sums

$$s(j) = \sum_{q}^{j} k_{ij} \tag{6.25}$$

is created. This procedure is equivalent to assigning each jump rate a certain length

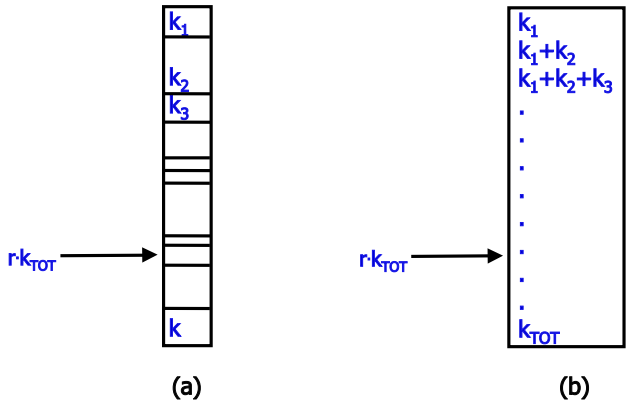

Figure 10: **Schematic illustration of the procedure for picking the reaction pathway to advance the system to the next state in the standard KMC algorithm** (a) Stack containing boxes, each with a length proportional to the rate constant for its pathway. A random number r on (0,1), multiplied by k_{tot}, points to one box with the correct probability. (b) In a computer code, this is achieved by comparing $r \cdot k_{tot}$ to elements in an array of partial sums (figure taken from[97])

in an stack, as depicted in figure 10 (a).

Then a random number $r \in (0, 1)$ is drawn and one goes through the array $s(j)$ stopping at the first j for which the factor $s(j) > rk_{tot}$ ($k_{tot} = \sum_j k_{ij}$, the total escape rate from state i). This is the selected pathway and, as the length of each $s(j)$ varies according to the jump rate, each jump gets selected statistically as often as its rate demands. This procedure is depicted in figure 10. Next, an exponentially distributed random time

$$t_{draw} = -\frac{ln(r)}{k_{tot}}, \tag{6.26}$$

is drawn with a new random $r \in (0, 1)$ and the system clock is advanced by t_{draw}. The system has now progressed into a new state and the algorithm starts again.

As always with Monte-Carlo, it is the long time average of the system that provides the correct answer to the system properties. Especially for diffusion it is thus important to take the average over many random walks and over an extended time period.

7. Vacancy Formation and Concentration

The last unknown required to calculate absolute diffusion rates is the number of vacancies, N_v. Estimating N_v is non-trivial. Vacancy concentrations can vary significantly depending on the experimental conditions (i.e., pressure, temperature, oxygen fugacity, impurity concentration, sample history, etc.). Vacancies in minerals or ionic crystals form out of two reasons: 1) temperature (minimising Gibbs free energy, intrinsic) 2) impurities (maintaining charge neutrality, extrinsic). Estimating vacancy concentrations for minerals in the Earth's mantle, however, is subject to considerable uncertainty. This has to be kept in mind when applying results to the Earth.

7.1. Extrinsic Defect Formation

Extrinsic vacancies form in order to compensate charges from impurity atoms. The extrinsic vacancy concentration is thus determined by the concentration of impurities in the crystal. For instance, Fe^{3+} on a normal 2+ cation site could be charge balanced by cation vacancies. Similarly, oxygen vacancies may be set by the concentration of 1+ ions. For well-characterized experimental samples, these can be estimated reasonably accurately, and allows one to compare my calculated diffusion rates directly with experimental measurements.

7.2. Intrinsic Defect Formation

Intrinsic vacancies are an inherent property of a crystal and an unavoidable product of thermodynamics. It is well known that in thermodynamical equilibrium, the Gibbs free energy $G = H - TS$ has a minimum. Vacancy formation requires energy, i.e., it increases the enthalpy H, but at the same time it also increases the entropy S of the crystal. Therefore, at a finite temperature, vacancies will be generated until the increase in the enthalpy cannot be compensated by the increase in entropy any more. However, for most Earth materials, the formation energies of intrinsic vacancies is large and their concentration is very small, even at very high temperatures (as shown in figure 11).

The excess atoms (that left the vacancy) can either move to the surface of the crystal or onto an interstitial site. In any case, it is important to maintain charge neutrality. Thus, charged point defects have to occur in pairs or groups compensating the charges of each other: for each interstitial there is a corresponding vacancy

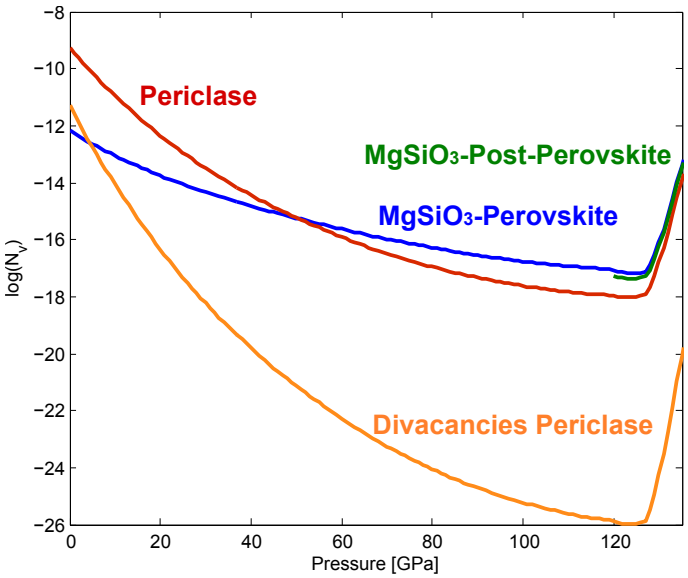

Figure 11: **Intrinsic vacancy concentrations in lower mantle minerals** along a geotherm[98]. The Schottky-formation energies were taken from[91] for perovskite and post-perovskite, and from this study for periclase

(Frenkel defect pair), and for each cation vacancy there is at least one anion vacancy (Schottky defect).

Thermodynamics enables one to calculate the equilibrium vacancy concentration. To form a vacancy in an otherwise perfect crystal, one needs to move an atom from its initial position to the surface of the crystal (Schottky defect) or to an interstitial site (Frenkel defect) in order to maintain the number of atoms and charge neutrality. At the same time, the vacancy and the removed atom should not interact with each other any more. The energy to move this atom to the surface/interstitial site is the Gibbs free energy of formation

$$\Delta G_f = \Delta H_f - \Delta S_f T \tag{7.1}$$

where ΔH_f and ΔS_f are the enthalpy and entropy of formation. It is then well known, that the equilibrium concentration of vacancies N_v is given by

$$N_v = e^{-\frac{\Delta G_f}{kT}} \tag{7.2}$$

$$= e^{\frac{\Delta S_f}{k}} e^{-\frac{\Delta H_f}{kT}} \tag{7.3}$$

The question thus is how to calculate ΔG. Generally, one would like to know the energetics of a single point defect in an otherwise perfect, infinite crystal. The

energetics of more complex defects such as Schottky-defects can then be determined by simple algebraic manipulations of the point defect quantities. As discussed above, the quantity of interest is the Gibbs free energy of formation and its temperature and pressure dependence. The Gibbs free energy of formation per defect can be obtained as follows: for a Schottky defect G_f^S of a material $A_aB_b...Z_z$ it is the sum over all species of the differences in the Gibbs free energies of the perfect crystal $G_{perfect}$ and the crystal with a single vacancy of species i, $G^i_{vacancy}$ plus the binding energy of one unit formula $E_{A_aB_b...Z_z}$,

$$G_f^S = \frac{\sum_i n_i G^i_{defect} - G_{perfect} + E_{A_aB_b...Z_z}}{\sum_i n_i}. \tag{7.4}$$

Here, i runs over the number of species and n_i is the stoichiometric factor of species i, i.e. $n_i = a, b, ...z$. For self-interstitial defects, the Frenkel pair formation energy G_f^F writes

$$G_f^F = \frac{G_{interstitial} + G_{vacancy} - G_{perfect}}{2}. \tag{7.5}$$

Now, intrinsic defect concentrations using equation (7.3) can be calculated from first principles. However, first a couple of caveats and technical details when dealing with defective systems need to be discussed.

7.3. Calculations of Defective Systems

Crystalline defects exert a strong distance dependent perturbation on the crystal. Firstly, defects in crystals are often charged; this results in a Coulomb interaction that decays slowly as $1/r$ (r being the distance). Neutral defects can also have a slowly decaying electrostatic interaction, since they often possess strong dipole and quadrupole moments. Secondly, the crystal lattice is distorted due to relaxation of the ions around the defect (repelled or attracted depending on their charge relative to the defect). It is assumed that this lattice distortion decays as $1/r^3$. When modelling defects, especially highly charged vacancies, care has to be taken to ensure that these long-range interactions are taken into account, and that they do not artificially bias the results.

The classic approach is the Mott-Littleton Method[99]. In this method, the defective crystal is divided into two separately treated spherical regions. The inner region surrounds the defect and is treated accurately by calculating the relaxations

and distortions on the atoms from interatomic forces. The outer region is treated less accurately (as atoms only interact with the distortion and the charge of the defect but not with each other), and is used to shield the charge and distortion caused by the defect (polarization). This approach has only been used with (semi-)empirical interatomic potentials. Codes such as GULP (https://www.ivec.org/gulp/;[100,101]) make this a relatively routine procedure, subject to the accuracy of the interatomic-potentials[102–107].

Using DFT however, the most straightforward implementations make use of super-cells and periodic boundary conditions (PBC). PBC mean that the system is repeated infinitely in space. This is especially useful for crystalline lattices since it is then sufficient to calculate the properties of a single unit cell. Periodic boundary conditions yield the same result as if the unit cell has been repeated infinitely in all directions, forming a perfect, infinitely sized crystal. This approach, however, has its drawbacks when it comes to defect calculations, since the defect is also repeated infinitely along all directions. This leads to a very high concentration of defects, giving rise to spurious elastic interactions between neighbouring cells (mirror images of the simulation). This interaction should scale as $1/L^3$, where L is the cell size. The effect of the elastic interaction can be reduced by using sufficiently large supercells (a large simulation unit built up from several unit cells), such that deformations at the cell-boundaries are negligible. However, the relaxation is almost never completely removed by the edge of the supercell, and the calculations contain a small artificial contribution from this. Nevertheless, this contribution is small and the super-cell method using DFT forces and energies has been used successfully on defect calculations in Earth materials such as olivine[108,109], perovskite[110,111], post-perovskite[91] and periclase[112].

An intermediate approach between using pure DFT with super-cells and Mott-Littleton methods for defect calculations is the so-called embedded cluster method. This again divides up space into regions: a central region, which treats the defect at the quantum mechanical level, a surrounding region that is treated classically via interatomic potentials, and a third outer region which is just a set a of fixed point-charges. This method is implemented in codes such as GUESS[113–115], and has been used to study defects in olivine[116–119].

As mentioned above, PBC in combination with defective systems has its own difficulties. The introduction of charged point defects or defect clusters results in an artificial electrostatic self-interaction between the supercell and all its images. This electrostatic self-interaction can have rather large effects on the calculated defect

energies. It is therefore worthwhile to briefly discuss how one can reduce the error made on the defect energetics when using PBC.

Charged Supercell Correction Leslie and Gillan[120] proposed a simple correction to the self-interaction of charged point defects. A charged defect within a cell with PBC is equivalent to a periodic array of charged defects. However, a periodically repeating array of charged supercells does not have a well-defined energy. This difficulty can be overcome by introducing a uniformly distributed background charge (so-called jellium) compensating the charge of the supercell. The correction term is hence given by the energy of the charged defect array embedded in the compensating jellium. Assuming that the space between the defects is large enough, i.e., the supercell is large enough; a macroscopic approximation can be made: the defect array and the jellium are immersed in a structureless dielectric, whose dielectric constant ϵ is equal to that of the perfect crystal. The energy of such an array, and hence the correction term is given by

$$E_{array} = -\frac{1}{2}\frac{\alpha Q^2}{\epsilon L} \tag{7.6}$$

where α is the appropriate Madelung constant, Q the charge of the defect and L is the lattice parameter of the periodic array. Clearly, large charges result in larger corrections. This correction requires the correct permittivity ϵ; this can now also be calculated reasonably straightforwardly using the same *ab initio* methods as in the defect calculation (e.g.,[87,88]). The charge-interaction correction can then be applied completely self-consistently.

Neutral Supercell Correction: Dipole Correction Neutral or charged defect clusters can also introduce large dipole-moments into the supercell, giving rise to similar (although less strong) interactions as in the case of charged point defects discussed in the previous paragraph. Makov and Payne[121], and more thoroughly Kantorovich and Tupitsyn[122,123], showed that the correcting factor for dipole-dipole interaction is given by

$$E_{dipole} = \frac{2\pi \mathbf{P}^2}{3V_c} \tag{7.7}$$

where $\mathbf{P}$ is the total dipole moment of the supercell and V_c is the supercell volume.

A general point[121] on how to correct for self-interactions in supercells is, that if

one is interested in the system properties at infinite supercell-size, the corresponding limit can be achieved by extrapolation (calculate energies at various cell sizes). This is reflected in the fact that the expressions for the energy corrections vanish at infinite cell size.

With these corrections in hand, defect energies can be readily calculated using the supercell approach. It is important to note that when calculating migration enthalpies, the energy of the two similarly charged systems are subtracted from each other. Since the charge-interaction corrections presented above are the same for each system, they cancel. However, in fact the two systems have very different ionic arrangements (one having two vacancies and a migrating ion at its saddle-point, and the other with a single vacancy) and, therefore, they have different higher order electrostatic moments. A small error in the migration energy is expected from this.

8. Relating Diffusion to other Physical Properties

8.1. Viscosity

It has been established from experiments that, generally, the creep rate $\dot{\epsilon}$ of a material can be written as[124]

$$\dot{\epsilon} = A\frac{DSb}{kT}\left(\frac{b}{G}\right)^{p}\left(\frac{\sigma}{S}\right)^{n} \tag{8.1}$$

where D is the diffusion coefficient, S is the shear-modulus, b is the Burgers vector, k is Boltzmann's constant, T is temperature, G is the grain-size, σ is the shear-stress and n, p and A are dimensionless constants. The viscosity is then given by

$$\eta = \frac{\sigma}{\dot{\epsilon}} \tag{8.2}$$

The most common regimes are dislocation creep (power-law creep), $p = 0$ and $n = 3 - 5$, and diffusion creep, $p = 2$ and $n = 1$ which shall be discussed next.

8.1.1. Diffusion Creep

The absence of seismic anisotropy in the lower mantle, small grain size[125], and low stresses, all argue for diffusion creep being the dominant creep mechanism in the lower mantle[126]. Moreover, viscosity models from glacial rebound indicate linear rheology for most of the mantle, again consistent with diffusion creep.

If a material deforms via diffusion creep, vacancies are formed and moved in such a way that the crystal can yield to the imposed force (shown in figure 12). Consider a crystal onto which a normal stress is applied as shown in figure 12. This results in there being a higher chemical potential at the highly stressed surfaces than at the non-stressed surfaces and a consequent diffusive flux of matter down the chemical potential gradient. This is the mechanism described by the Nabarro-Herring[127] equation for pure shear:

$$\eta = \frac{G^2 kT}{\alpha D_{eff}\Omega} \tag{8.3}$$

where G is the characteristic grain-size, α is a geometrical factor (40/3 or 16/3 with or without grain boundary sliding respectively), Ω is the molecular volume and the

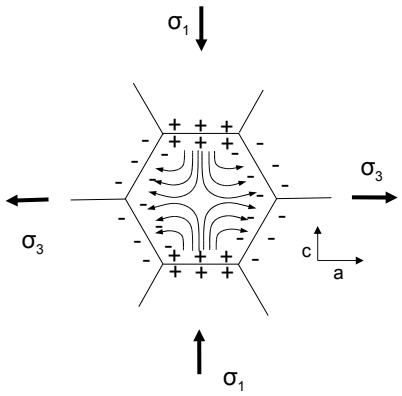

Figure 12: **A segment of polycrystal deforming by lattice diffusion in the pure shear geometry** Surfaces marked with + have higher stress and hence higher chemical potential. Surfaces marked '-' have lower stress and chemical potential. Mass flux occurs along the chemical potential gradients as indicated by the curved arrows

effective diffusion coefficient is given by[128]

$$D_{eff} = \left(\frac{\sum_i \frac{\nu_i}{\tilde{D}_i}}{\sum_i \nu_i} \right)^{-1} . \tag{8.4}$$

Here, ν_i is the stoichiometric factor and $\tilde{D}_i = D_i + \pi\delta D_i^{gb}/G$ is the effective diffusion coefficient of species i. δ is the effective grain-boundary width, D_i^{gb} is the grain-boundary diffusion coefficient and its contribution to $\tilde{D}_i$ can be neglected for grain-sizes > 10 μm in perovskite[35] and > 500 μm in periclase[38]. Grain sizes in the lower mantle have been estimated by Solomatov et al.[125] to be between 0.1 - 1 mm, so we can neglect grain-boundary diffusion for the major chemical species (Mg, Si and O). However, in other systems grain boundary diffusion may be significant, which is then called Coble creep[124].

Herring[127] also derived an equation for the effective viscosity of a material deforming by lattice diffusion in simple shear, which differs from the pure shear equation by a numerical factor of 5/2. In both cases for isotropic, or nearly isotropic, materials the chemical potential gradients, which are perpendicular to the surfaces near the surface result in a diffusive flux which bends through the crystal and the effective viscosity is, therefore a convolution of the diffusivities in different directions and of the grain shape.

8.1.2. Dislocation Creep

Dislocation creep is a power-law function of shear-stress and leads to strong lattice preferred orientation at large strains. In contrast with diffusion creep, this deformation mechanism is grain-size independent. In the high-temperature case relevant in the lower mantle, creep is accommodated by climb-assisted dislocation migration where the rate-limiting step is the transport of matter as unit cells are added to, or removed from, the climbing dislocation half-plane. The dislocation-climb process is shown in figure 13. This is in turn rate-limited by the fastest diffusion direction of the slowest diffusing species. As evident from figure 13, dislocations act as sources and sinks of vacancies.

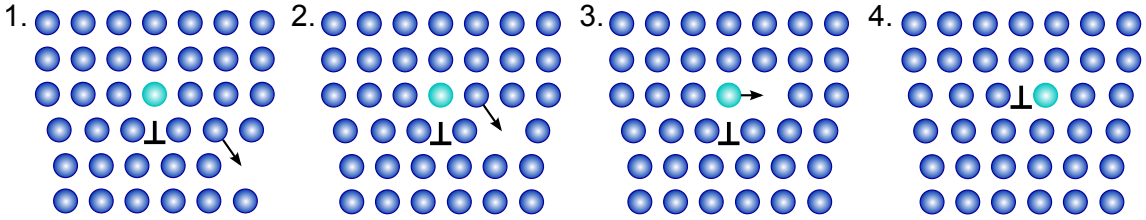

Figure 13: **Dislocation Climb** 1.: Initial configuration with a vacancy approaching the dislocation, marked with ⊥. 2. and 3.: The vacancy further approaches the dislocation. 4.: The dislocation has climbed by one atomic row

It can be seen from equation (8.1) that the parameters controlling the dislocation creep rate are stress, dislocation density (similar to vacancy concentration in diffusion creep) and diffusion rates. Thus, for a certain applied stress it can be simply assumed that dislocation creep viscosity is proportional to diffusion creep viscosity.

8.1.3. Aggregate Viscosity

Flow laws for a mixture of two viscous phases have been developed by, e.g., Handy[129] and Takeda[130]. They investigated two possibilities of how the two phases arrange themselves: either the weaker phase is contained in isolated pockets within the stronger phase (LBF: load-bearing framework), or the weaker phase forms an interconnected layer (IWL: interconnected weak layers). There is experimental evidence for the two-phase system MgO-$MgSiO_3$ perovskite to develop the interconnected layers (of the weaker MgO) under large shear strain deformation and to form isolated pockets in the case of static annealing (see[131] and references there in). The IWL and LBF structure are two end-member situations: IWF gives the lower and LBF

the upper bound for the viscosity of a two-phase mixture. In the LBF structure, viscosity is greatly determined by the viscosity of the harder material. This is in contrast with a system under large shear stress where thin, interconnected films of the weaker phase form and greatly decrease the viscosity of the mixture.

8.2. Ionic Conductivity

An electric current can be carried in ionic crystals by moving the charged vacancies in the crystal along/against the applied electric field (depending on the vacancy charge). This process is called ionic conduction and is related to the mobility of the vacancy / species that uses these vacancies, i.e. its diffusivity. More precisely, the ionic conductivity σ_i of species i is related to its diffusion coefficient D_i via the Nernst-Einstein relation[132]:

$$\sigma_i = \frac{q^2 n}{kT} D_i \tag{8.5}$$

where q is the charge and n the density of the conducting species. The total ionic conductivity is then the sum over all these partial conductivities. However, often only one species dominates the ionic conductivity (as diffusion rates of various species in the same crystal often differ by several orders of magnitudes).

Part IV.
Diffusion in the Lower Mantle

The following results have been published in Physics and Chemistry of Minerals[92], RiMG volume 71[133], Nature[134] and Earth and Planetary Science Letters[135].

9. MgO: Periclase

Ferro-periclase (Fe,Mg)O is thought to be the second most abundant mineral in the lower mantle accounting for about 20% of the volume (e.g.,[136]). The investigation of the diffusional properties of its pure endmember periclase MgO is hence of major importance for Earth Sciences. It crystallizes in the rock-salt structure even under lower mantle conditions[88,137]. Periclase is also an important industrial material with a wide range of applications and often serves as a prototype material for other ionic oxides[138].

MgO is a simple cubic oxide for which high-pressure and high-temperature experimental diffusion measurements exist. Since it crystallises in the rock-salt structure, the location of the saddle point is given trivially by symmetry and is located half-way between the initial and final position. This is, however, only strictly true at high pressures. I find at low pressures, in agreement with Vočadlo et al. (1995)[139], that the magnesium saddle-point bifurcates perpendicular to the jump trajectory. But also these saddle-points can be readily found by offsetting from the half-way position (a second-order saddle-point) and relaxing the migrating ion into the bifurcated first order saddle points (the lowering in energy is though negligible). In contrast with Vočadlo et al. (1995)[139], I have not found any bifurcation along the oxygen jump trajectory. Thus, the CI-NEB method is not required for MgO. The ease of finding the saddle point has meant that absolute diffusion rates in MgO have been calculated within Vineyard-theory a number of times (e.g.,[75,139,140]). The pre-exponential factors from the different studies agree to within about one order of magnitude; some of this scatter can be attributed to different potentials and some to different methods.

Table 3: Migration Enthalpies in MgO at 1 bar from experiments and theory (for single vacancy diffusion). Method abbreviations are explained in appendix VI.

Theory	ΔH_O [eV]	ΔH_{Mg} [eV]	Method (Code)
This Study	2.05	1.93	DFT (VASP) GGA
	1.93	1.82	DFT (VASP) LDA
Ito and Toriumi[141]	2.23	2.09	MD
Gilbert et al.[142]	2.31	2.2	DFT (Plato) LDA
Karki and Khanduja[112]	2.42	2.26	DFT (PWscf) LDA
Kotomin and Popov[138,143]	2.5	2.43	Review (INDO) HF
Ita and Cohen[144]	1.97	1.7	MD
Vočadlo et al.[139]	2.003	1.985	LD (PARAPOCS)
De Vita et al.[145]	2.48	2.28	DFT (CETEP) LDA
Harding et al.[146]	-	2.1	ML (HADES, SHEOL)
Sangster and Stoneham[75]	-	2.26	ML (PLUTO)
Sangster and Rowell[147]	2.11	2.07	ML
Mackrodt and Stewart[148]	2.38	2.16	ML
Experiments			
Yoo et al.[149]	3.24 ±0.13	-	
Shirasaki and Hama[150]	2.42	-	
Shirasaki and Yamamura[151]	2.61	-	
Oishi and Kingery[152]	0.65	-	
Mackwell et al.[153]	-	2.17 ±0.07	Mg-Fe interdiffusion
Holzapfel et al.[39]	-	2.64 ±0.17	Mg-Fe interdiffusion (8-23 GPa)
Yamazaki and Irifune[11]	-	2.34 ±0.33	Mg-Fe interdiffusion (7-35 GPa)
Yang and Flynn[154]	2.66	2.52	Ca-diffusion (2.33 eV this study)
Sempolinsky and Kingery[155]	-	2.28 ±0.21	
Duclot and Departes[156]	-	2.2	
Wuensch et al.[157]	-	2.76 ±0.08	
Lindner and Parfitt[158]	-	3.44 ±0.13	

Even more studies concentrated on the migration enthalpies and all obtained migration enthalpies of about 2 eV for both magnesium and oxygen, which is in agreement with experiments. Some experimental and theoretical values of the migration enthalpies are given in table 3 (which is not exhaustive) and attempt frequencies are given in table 4.

Table 5 summarises calculated migration enthalpies in periclase at high pressures. Ita and Cohen[144,159] as well as Ito and Toriumi[141] performed molecular dynamics simulations using interatomic potentials to calculate the absolute diffusion rates in MgO under lower mantle conditions. While both studies are in agreement with the available experimental data (up to 35 GPa), they disagree with each other at elevated pressures (above 60 GPa). Ita and Cohen[144,159] observe a continuous increase of the migration enthalpy with increasing pressure, while in contrast Ito and Toriumi[141] find that the migration enthalpy decreases after reaching a maximum

Table 4: Attempt Frequencies in periclase for magnesium and oxygen in MgO for the single jumps at 0 GPa.

Author	Species	ν [THz]	$\nu_{corrected}$ [THz]
This study	Mg	12.12	10.92
	O	13.82	11.4
Ita and Cohen[144,159]	Mg	5.2	-
	O	5.2	-
Vocadlo et al.[139]	Mg	18.99	15.95
	O	9.83	8.55
Harding et al.[140]	Mg	31.29	23.15
Sangster and Stoneham[75]	Mg	32.9	23
Experiments			
Sempolinsky and Kingery[155]	Mg	210 ±80	18±7[75]

around 50 GPa. The difference between their results could simply be linked to their different interatomic potentials. My results agree with those of Ita and Cohen[144,159]. Nevertheless, it should be noted that all three studies have an activation volume that is in agreement with the available experimental data[11,38,39] at pressures up to 35 GPa.

Table 5: Migration enthalpies of MgO at pressures P of the lower mantle. ΔH_{MgO} is the migration enthalpy for a divacancy (bound MgO vacancy pair; the higher of the two barriers for magnesium and oxygen hops)

Author	P [GPa	ΔH_{Mg}[eV]	ΔH_O [eV]	ΔH_{MgO} [eV]
This Study	5.3	2.06	2.20	2.81
	30.3	2.61	2.82	2.83
	136.6	3.88	4.27	2.67
Karki and Khanduja[112]	20	3	2.9	-
	50	3.3	3.15	-
	150	4.3	3.95	-
Ito and Toriumi[141]	20	2.59	2.66	-
	50	2.98	3.02	-
	140	2.12	3.31	-
Ita and Cohen[144,159]	20	2.34	2.55	-
	80	3.22	3.64	-
	140	3.99	4.31	-

My results for MgO are shown in figures 14 and 15 and all relevant parameters are collected in table 31. In order to compare my theoretical results with experiments, an estimate of the vacancy concentration in the experiments must be made. The

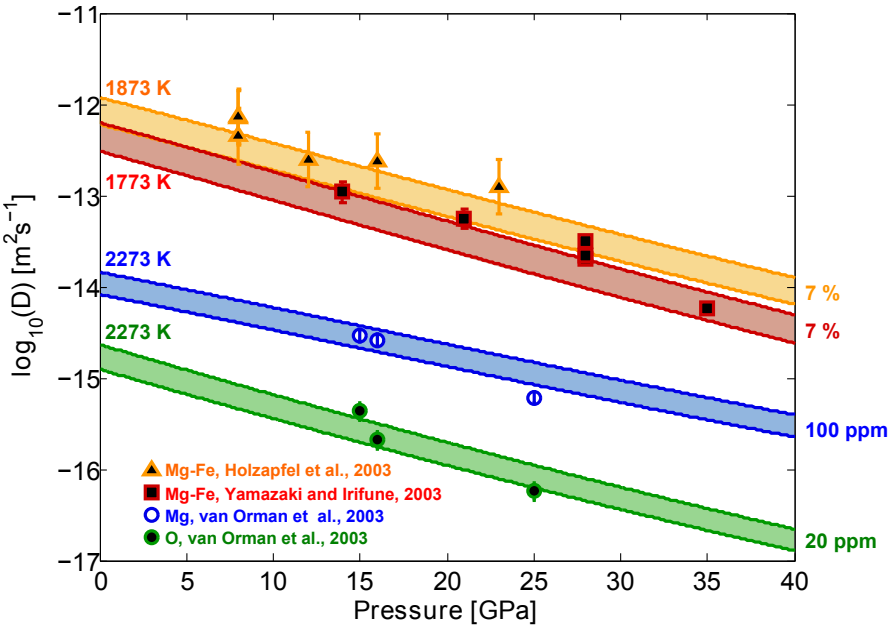

Figure 14: **Comparison of absolute diffusion rates with experiments** My calculated diffusion rates are shown as solid lines (upper limits LDA, lower limits GGA; both at same cell-volume, pressure calculated from GGA), with experiments as symbols. Percentages on the right hand-side indicate the vacancy concentrations estimated from experimental conditions. Diffusion in periclase at different pressures and temperatures[11,38,39]

Schottky-formation energy, ΔH_S, and Frenkel-formation energy, ΔH_F, have been calculated several times over the last 30 years and are given in table 6 (the list is not exhaustive). For the charged defect correction, I adopted the value of the permittivity calculated by Oganov et al. (2003)[88]. Formation energies continuously increase with pressure[111].

My calculations and previous results find formation energies of Schottky and Frenkel-pair defects to be between 6.45-7.7 eV and 10.35-15.2 eV respectively. The equilibrium concentration of intrinsic magnesium vacancies is, therefore, extremely small (see also figure 11). However, the presence of heterovalent impurities will result in the formation of extrinsic vacancies in order to maintain charge neutrality. In fact, only a small concentration of impurities (much less than a few ppm at 2000 K) is sufficient for the number of extrinsic magnesium-vacancies to greatly exceed the number of intrinsic vacancies, and generally, the number of extrinsic magnesium-vacancies is assumed to dominate the number of defects in MgO by several orders of magnitude. It is possible, therefore, to constrain the experimental magnesium-vacancy concentration from their measured impurity concentrations. As shown in

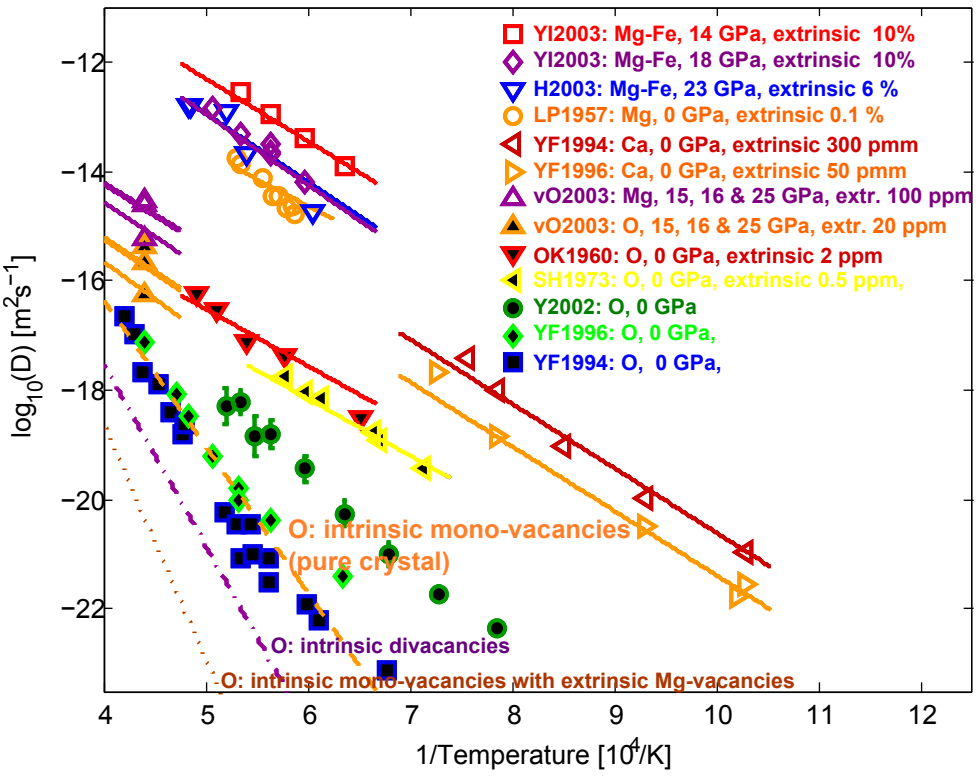

Figure 15: **Comparison of my calculated diffusion rates in periclase with experiments** Lines are the results of my calculations using vacancy concentrations appropriate for the experiments. Empty symbols are magnesium (calcium) diffusion, filled symbols are for oxygen. In all experiments, magnesium diffusion can be readily explained assuming extrinsic vacancy hopping. YI2003: Yamazaki and Irifune (2003)[11]; H2003: Holzapfel et al. (2003)[39]; LP1957: Linder and Parfitt (1957)[158]; YF1996, YF1994: Yang and Flynn (1994, 1996)[154,160]; vO2003: van Orman et al. (2003)[38]; OK1960: Oishi and Kingery (1960)[152]; SH1973: Shirasaki and Hama (1973)[150]; Y2002: Yoo et al. (2002)[149]. The lowest oxygen diffusion data is not explained by theory: free oxygen vacancies are expected to be suppressed by extrinsic magnesium vacancies (for YF1994 &YF1996, they are constrained via Ca-diffusion data) resulting in the dotted line. Intrinsically formed divacancies are at least a magnitude too low (dash-dotted line). Intrinsically formed oxygen (mono-)vacancies could explain the Yang and Flynn data (dashed line) if no impurities (an extrinsic magnesium vacancy below 10^{-8}) are around for suppression (which is not the case)

Table 6: Theoretical Schottky E_S, Frenkel E_F and divacancy E_D (bound MgO vacancy pair) formation energies in MgO at 0 GPa

Author	E_S [eV]	E_F [eV]	E_D [eV]	Method
This Study	6.45	14.21 (O)	3.88	DFT GGA
Gilbert et al.[142]	5.97	10.35 (Mg)	-	DFT LDA
	-	12.17 (O)	-	
Karki and Khanduja[112]	6.83	-	-	DFT LDA
Alfe and Gillen[161]	6.76 ±0.2	-	-	QMC
	7.5 ±0.53	-	-	DMC
	6.99	-	-	DFT LDA
Ita and Cohen[144,159]	6.48	-	4.92	MD
De Vita et al.[145]	6.88	-	-	DFT LDA
Jacobs and Vernon[162]	7.7	12.4 (Mg)	-	
	-	11.6 (O)	-	
Mackrodt[89]	7.66	-	-	ML
Sangster and Rowell[147]	7.72	-	-	MD
Mackrodt and Stewart[148]	7.5	11.9 (Mg)	4.95	ML
	-	15.2 (O)	-	

figure 15, magnesium diffusion in MgO can readily be explained by my results using reasonable vacancy concentrations.

The experiments on oxygen diffusion are more difficult to explain than for magnesium. First of all oxygen diffusion is significantly slower than magnesium, and secondly, the different studies produce different slopes. The slowness is mostly due to the low concentration of oxygen vacancies in the experimental sample. The different slopes suggest that different mechanisms of migration and of intrinsic vacancy formation are at work. Some experiments have been thought to be in the intrinsic regime, where the measured activation energy also contains an activation energy of vacancy formation as well as migration (high slopes), and some are in the extrinsic regime, and so the measured activation energy is the migration energy only (low slopes). However, my results suggest that it cannot be intrinsic diffusion that is responsible for the higher slopes, but another, yet unknown, extrinsic diffusion mechanism.

The experiments of Oishi and Kingery (1960)[152] as well as of Shirasaki and Hama (1973)[150] are easiest to explain. They were performed on relatively impure samples, and the measured diffusion was assumed to be in the extrinsic regime. Plotted on the figure 15 are my absolute diffusion rates, assuming an extrinsic vacancy concentration of about 2 ppm and 0.5 ppm respectively. These fit the experimental

data well.

The experiments of Yang and Flynn (1994, 1996) [154,160] are not as easy to interpret. The dashed line is my prediction for oxygen diffusion assuming the oxygen vacancies are being formed intrinsically. The concentration of oxygen and magnesium vacancies is given by (Schottky-equilibrium)

$$C_{V_O} C_{V_{Mg}} = e^{-\frac{\Delta H_S}{kT}} \tag{9.1}$$

where, for no extrinsic vacancies, $C_{V_O} = N_{V_O}/N$ and $C_{V_{Mg}} = N_{V_{Mg}}/N$ are the oxygen and magnesium vacancy concentrations respectively. Assuming the oxygen and magnesium vacancies are charge balancing each other, then the diffusion coefficient is given as

$$D = N_V \frac{Z}{6} a^2 \nu e^{-\frac{\Delta H_M}{kT}} = N \frac{Z}{6} a^2 \nu e^{-\frac{\Delta H_S/2 + \Delta H_M}{kT}} \tag{9.2}$$

where the defect formation enthalpy, ΔH_S, the migration enthalpy, ΔH_M, and the effective jump frequency, ν, are all calculated from first principles. Although this fits the experimental data well, the good fit is, in fact, fortuitous. Yang and Flynn also measured Ca diffusion in the same MgO samples. These are also shown on figure 15, and are very well described by an extrinsic vacancy diffusion mechanism (i.e. the slope is just the migration enthalpy), with an extrinsic cation vacancy concentration of about 50 to 300 ppm. The problem is that in samples with significant extrinsic concentrations of one of the Schottky pairs, equation 9.2 above shows that the concentration of the other vacancy is proportionally reduced. For $C_{V_{Mg}}$ of a few 10s of ppm, C_{V_O} is reduced to a tiny amount, and there are simply not enough oxygen vacancies to produce the diffusion coefficients shown in figure 15. The oxygen diffusion coefficients for a sample containing 50 ppm magnesium vacancies is shown in figure 15 (dotted line); it is many orders of magnitude too slow.

This problem with rationalising the cation and anion diffusion results simultaneously was realised by Yang and Flynn, and they suggested that their diffusion experiments were actually measuring the diffusion of bound MgO vacancy pairs (so-called divacancies). The concentration of MgO divacancies is given, for the intrinsic case, by

$$C_{V_{MgO}} = e^{-\frac{\Delta H_S + \Delta H_B}{kT}} \tag{9.3}$$

where ΔH_B is the energy of binding the two vacancies together (which is negative

since they are opposite charge and, therefore, attractive). To calculate the mobility of the bound pair, I have calculated the migration enthalpies and frequency factors for the bound vacancies individually, and assumed that the slowest species limits the diffusion of the bound pair (see tables 2, 3 and 4). The binding energy is about -2.6 eV and the effective migration energy for the slowest vacancy is 2.8 eV. My theoretical absolute diffusion rates of the divacancies is shown in figure 4 (dashed-dot lines); they too are much slower than measured in experiments. To date, I am unable to constrain the oxygen diffusion mechanism for the experiments of Yang and Flynn[154,160].

The recent measurement of oxygen diffusion by Yoo et al. (2002)[149], revealed yet another activation energy, and much higher rates than the previous experiments. They suggest tentatively that their measured diffusion rates are actually for interstitial oxygen, although they acknowledge that these are unlikely to be in significant concentrations in MgO. Again, I have tested this by calculating the migration enthalpy for the oxygen interstitial and its formation energy. Interestingly, the migration energy for the interstitial is low: 0.7 eV. However, the formation enthalpy is, as expected, very large (7 eV; half the Frenkel defect formation energy). Therefore, it is concluded that there is not a significant concentration of oxygen interstitials in MgO. What the diffusion mechanism for the experiments of Yoo et al.[149] is, also remains unclear.

Further complicating the assessment of the oxygen vacancy concentration and oxygen diffusion mechanism is the experimental finding that oxygen diffusion along dislocations (pipe-diffusion) has a similar activation energy[163,164] as mono-vacancy diffusion. This has likely been observed by Yang and Flynn (1994, 1996)[154,160] (and maybe also by Yoo et al. 2002[149]) in their low temperature data of oxygen diffusion. At the same time, this might suggest that even the data of Oishi and Kingery (1960)[152] as well as of Shirasaki and Hama (1973)[150] represents pipe-diffusion instead of extrinsic oxygen diffusion as was assumed here.

Although it is not possible to explain all the experimental results for oxygen diffusion in MgO, I am able to model successfully experiments where the migration mechanism is simple and unambiguous. For instance I very accurately model the direct vacancy hopping mechanism for cations when the vacancies are extrinsically controlled. Similarly, I can accurately model oxygen diffusion when it is in the extrinsic regime. In other words, there is good reason to expect that the migration barriers and frequency factors calculated via DFT are accurate to within a few tenths of an eV.

9.1. Geophysical Implications: Viscosity of MgO

It turns out that the periclase remains much softer than perovskite when both deform in diffusion creep (see also next section). This is because the relative diffusivities along a geotherm are almost constant. Thus, if periclase is softer at shallow lower mantle conditions, it will remain softer throughout the lower mantle. The possible implications for the lower mantle of this finding will be discussed in section 12.1 where I address the effect of iron diffusion in periclase. I will thus only very briefly discuss the various deformation regimes of periclase.

It has been found in experiments that in diffusion creep magnesium boundary diffusion will limit creep at grain sizes below 0.5 mm and oxygen boundary diffusion at grain sizes above 3 mm[38,165]. Oxygen volume diffusion would only contribute if grain sizes were much bigger than 1 cm rendering it very unlikely to be important in the lower mantle. Thus they predict a transition from diffusion creep to dislocation creep in the deep lower mantle if shear stress exceeds 1-10 MPa for grain sizes between 0.1-1 mm.

As evident from figure 15, oxygen diffuses much slower than magnesium. Oxygen is, therefore, the rate-limiting species in dislocation creep. The experimental activation energy for dislocation creep is 3.4±0.05 eV[166,167], with a stress exponent of n=4. While dislocation can act as sources and sinks of vacancies, I do not know how they affect the formation energy. Hence, it is not entirely clear how to reconcile this experimental activation energy with my calculated migration enthalpies. For simple vacancy-diffusion, this would mean that the Schottky formation energy is drastically reduced between dislocations to about 1.2 eV. This is also the case for divacancies, for which there would only be 0.6 eV left to form the vacancy-pairs. At the same time, one could argue that the divacancy migration enthalpy is close enough to the activation energy of the experimental dislocation creep, such that extrinsic divacancies near dislocations could be controlling the deformation. If that would be the case, periclase would weaken substantially with depth and increasing temperature, as this mechanism has a negative activation volume. However, ultimately, my results do not allow me to decide on what is the rate-limiting diffusion species/mechanism because I cannot explain all the oxygen diffusion data.

10. $MgSiO_3$ Perovskite

$MgSiO_3$ Perovskite is the dominant phase in the Earth's lower mantle comprising up to 80 % of its volume and it is thus of fundamental importance for understanding the thermochemical evolution of the Earth (e.g.[136]). Computational studies of defect formation energies using the Mott-Littleton method suggest that the dominant defect in perovskite is the MgO partial Schottky defect[90,168]. Frenkel defects (interstitials) are energetically unfavourable. The same result has been found by first principles calculations[91,111] and various defect formation energies calculated in this study are collected in table 17 in the appendix. The high intrinsic formation energies (7.4 eV—MgO partial Schottky; 20.8 eV—full Schottky at 0 GPa; rapidly increasing with increasing pressure) imply that vacancy concentrations in experiments and in the Earth's mantle are controlled extrinsically, i.e., by impurity content (see also figure 11).

10.1. Perovskite Structure

Magnesium silicate perovskite is distorted from the cubic type-structure by tilting of the SiO_6 octahedra as sketched in figure 16. The distortion results in a rotation of the a- and b-axes by 45° from the cubic structure with a consequent increase of the axial lengths of approximately $\sqrt{2}$. The orthorhombic c-axis is doubled from the cubic axis, resulting in four formula units in the unit cell for the orthorhombic structure. Silicon and magnesium nearest neighbours, and hence shortest hopping distances, lie along the axial vectors in the pseudo-cubic setting and along [110] and [001] in the orthorhombic setting (figure 16).

Figure 17 shows the structure of $MgSiO_3$ perovskite. In this study the jumps to nearest neighbours (i.e. along [110]) as well as jumps to next-nearest neighbours in the x-y plane (i.e., along [100] and [010]) were considered. Furthermore, silicon lies on (0.5,0,0.5) such that [110] and [-110] jumps are equivalent. For magnesium, in contrast, they are not equivalent as the positions of the ions near the paths are different due to the tilt of the SiO_6 octahedra (see also figure 17), giving two possible diagonal migration pathways. For oxygen I have considered all of the possible exchanges along the octahedron edges as well as the two inequivalent next-nearest neighbour jumps along [001] (see figures 47 and 48 appendix VI for sketches of the investigated migration paths).

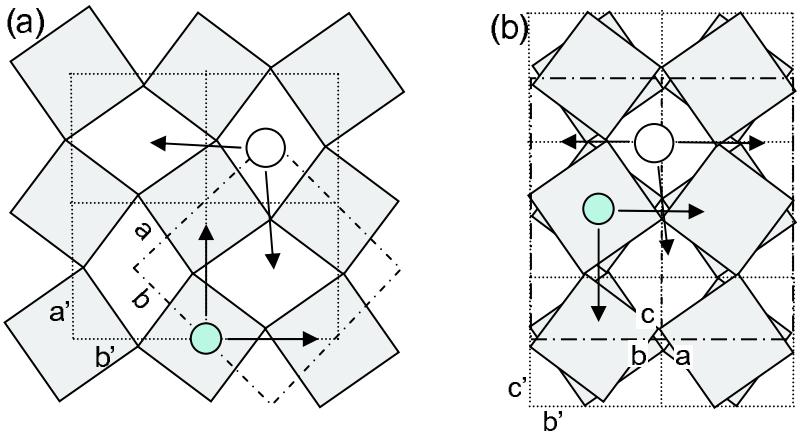

Figure 16: **Sketch of the magnesium silicate structure** (a) view down c-axis; (b) projection onto (110) of the orthorhombic cell. For clarity oxygen atoms have been omitted and the SiO_6 octahedra are indicated in grey. The pseudocubic unit cell is shown using dotted lines and the orthorhombic cell is shown in dot-dashed lines; pseudocubic (orthorhombic) axes are labelled with (without) a tick) One silicon atom (small, green) and one magnesium atom (large, white) are shown along with their nearest-neighbour jumps (arrows)

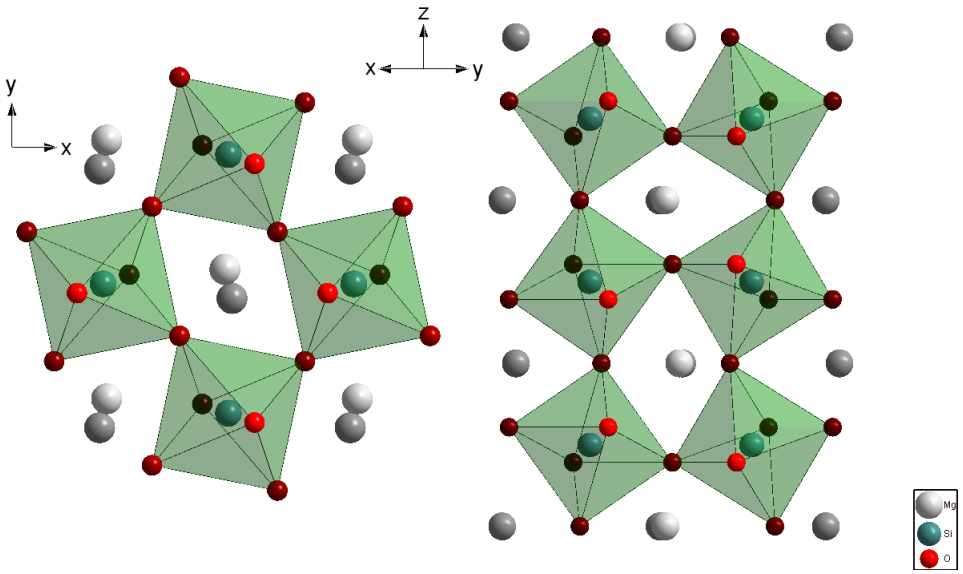

Figure 17: **$MgSiO_3$ Perovskite Structure**

10.2. Oxygen and Magnesium Diffusion

I find that diffusion of both oxygen and magnesium in perovskite occur via simple vacancy hopping. Parameters and sketches of the investigated migration paths can be found in appendix VI. In table 7 values of migration enthalpies are compared with those of previous theoretical studies and experiments.

Table 7: Migration enthalpies of all species in $MgSiO_3$ perovskite from experiments and theory. Values are averages over the migration enthalpies of all different jumps (8 for oxygen, 3 for magnesium). For silicon the value is the maximum energy of the barrier of the six jump cycle

Author	P [GPa]	ΔH_{Mg} [eV]	ΔH_{Si} [eV]	ΔH_{O} [eV]	Method
This study	24	3.81	3.64 LDA	1.06	DFT GGA
	140	6.43	5.98 LDA	2.23	
Karki and Khanduja[91]	30	4.87	9.1	1.41	DFT LDA
	120	7.71	10.48	2.57	
Wright and Price[90]	0	4.57	9.2	0.96	ML
	60	6.13	-	-	
	125	7.43	10.32	-	
Price et al.[168]	0	4.6	-	0.8	ML
Holzapfel et al.[40]	24	4.29±0.64	-	-	Mg-Fe interdiffusion
Dobson et al.[41]	25	-	3.6±0.76	-	
Yamazaki et al.[35]	25	-	3.48±0.38	-	
Dobson[36]	25	-	-	1.35±0.2	Na-doped
Xu and McCammon[37]	25	-	-	1.47	Al-bearing

Figure 18 shows the predicted diffusion rates plotted against those found experimentally. The upper and lower bounds are those found from LDA and GGA respectively. In order to make this comparison, vacancy concentrations in the experiments need to be estimated. For the oxygen diffusion experiments of Dobson[36] this is relatively straightforward since he doped his sample with 0.6% Na in order to extrinsically control oxygen vacancies. Since each oxygen vacancy is charge balancing two Na^+ ions, this results in 0.1% vacancies (per unit cell). At high temperatures, a change in the conduction mechanism has been observed (probably from oxygen ionic to intrinsic electronic) and this contribution was subtracted from the experimental data in order to obtain the pure oxygen ionic conduction. Thereby the predicted diffusion rates for oxygen are only slightly lower than those found by Dobson[36] but with a migration enthalpy almost exactly the same. Earlier studies of the conductivity of perovskite[37,169,170] contained iron and hence the electrical conductivity is dominated by small-polaron electronic conduction. Nevertheless, at the highest temperature the study of Xu et al.[170] showed a contribution from oxygen ionic conduction. Xu and McCammon[37] analysed this oxygen ionic component and found an activation energy in good agreement with my migration enthalpy.

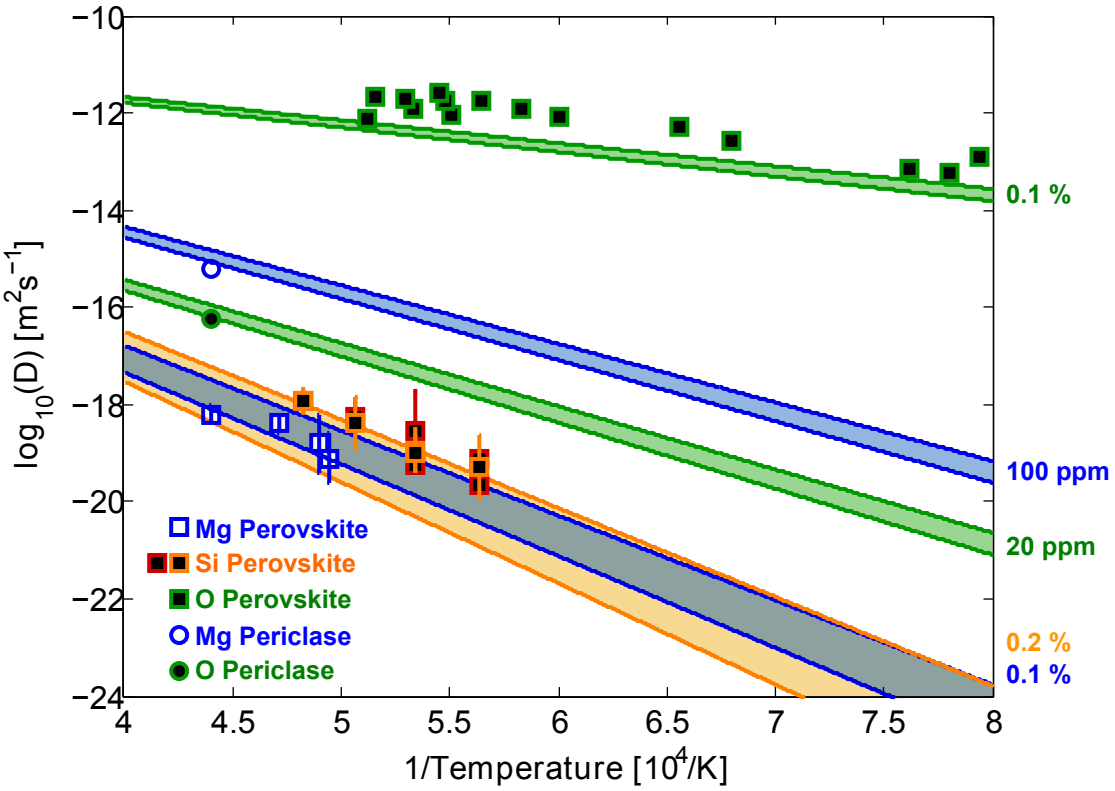

Figure 18: **Comparison of absolute diffusion rates with experiments** My calculated diffusion rates are shown as solid lines (upper limits LDA, lower limits GGA; both at same cell-volume, pressure calculated from GGA), with experiments as symbols. Percentages on the right hand-side indicate the vacancy concentrations estimated from experimental conditions. Diffusion in perovskite and diffusion in pure periclase (same as pure periclase in figure 14) at 25 GPa at varying temperature[35,36,40,41]. Where shown, the error bars represent the experimental error, otherwise, the experimental uncertainties are smaller than the symbol

For the Mg-Fe exchange experiments of Holzapfel et al.[40] the concentration of magnesium vacancies is controlled by the amount of ferric iron. For an Al-free system, the geochemical experiments of Lauterbach et al.[171] and the expected oxygen fugacity in the multi-anvil experiments can be used. Using the expression of Lauterbach et al.[171], the extrinsic concentration of magnesium vacancies is estimated to be about 0.2%. Using this concentration, the predictions for magnesium diffusion are in good agreement with the experiments.

10.3. Silicon Diffusion

Silicon diffusion in $MgSiO_3$ perovskite, however, is complicated by the fact that I find that silicon diffusion does not occur via a simple vacancy method, where silicon jumps from one site directly into an adjacent vacancy, as with magnesium and oxygen. The lowest migration enthalpy for the direct jump is 5.2 eV, substantially higher than the values of 3.6 eV obtained experimentally. Rather, I find that it occurs via a so-called six-jump cycle. This is common in some binary alloys (e.g.,[172–176]). The six jump cycle is shown in figure 19 and the according energy barrier in figure 20. In a normal vacancy hopping mechanism, the migrating ion hops directly to an adjacent vacancy. But in the six-jump cycle, a magnesium ion jumps into the silicon vacancy, making an antisite defect and a magnesium vacancy. The adjacent silicon ion then jumps into the magnesium vacancy, leaving a new silicon vacancy. The situation then repeats itself, with a magnesium jumping into the new silicon vacancy, followed by the first antisite magnesium jumping into the vacated magnesium site. The silicon ion then jumps into the silicon vacancy from the magnesium site, and the cycle finishes with the magnesium on the silicon site jumping into the adjacent magnesium vacancy. The silicon vacancy has jumped to an adjacent site via six different intermediate hops, each with its own activation enthalpy. It should be clear that the six-jump cycle is only the shortest and thus simplest version of a whole class of more complex migration cycles. However, these longer cycles have not been analysed as it is simply not possible to accommodate a single cycle in supercells of the sizes used. In perovskite, due to the tilting of the oxygen octahedra (being in an orthorhombic unit cell), there are twelve inequivalent six-jump cycles for silicon migration along $\langle 110 \rangle$, two along $\langle 111 \rangle$, two along $\langle 100 \rangle$, two along $\langle 010 \rangle$ and eight (plus four 'slow' ones) along $\langle 001 \rangle$. Limited resources only allowed to analyse some of these (shown in figures 49 and 50). Despite being geometrically inequivalent, all (of the analysed) six-jump cycles have, within mutual error, the same activation energy. It was thus assumed, when calculating the final rate, that all six-jump cycles are equivalent to the fastest cycle.

To analyse this complex diffusion process, firstly, it has to be considered what the effective activation energy of the six jumps is, and secondly, how many times the cycle is broken by a vacancy hopping to a site that is not part of the cycle.

An analytical solution to the rate of the six-jump cycle can be obtained using the approach of Arita et al.[177]. This method provides an effective jump-frequency, Γ, for the complete cycle. Also, by calculating the jump-frequency at different tempera-

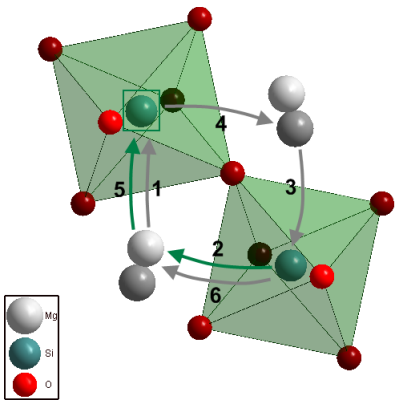

Figure 19: **A six jump cycle in perovskite** Sketch of a six-jump cycle for silicon diffusion along ⟨110⟩ in $MgSiO_3$ perovskite. Darker atoms are farther away from the observer. The initial position of the silicon vacancy is marked with a square

tures, it is possible to obtain an apparent activation (or migration) enthalpy for the cycle. It does, however, require the twelve individual jump-frequencies (obtained from Vineyard theory) and their migration energies. These are shown in figure 20 for the fastest silicon cycle. The effective activation energy lies somewhere between the migration energy of the single largest jump, and the energy difference between the original site and the highest energy saddle point. As shown by Arita et al.[177], the former is appropriate at high temperatures, while the latter is appropriate at low temperatures. The details depend on the particular system. I have used this approach for the cycle shown in figure 20 and find that at all reasonable temperatures, the apparent migration energy, is equal to 3.6 eV. This is the same as the maximum saddle point energy. The apparent migration enthalpy does decrease towards the largest single jump (3.3 eV for the silicon jumping into the magnesium vacancy), but only at very high temperatures. This is as expected since the maximum saddle-point energy (3.6 eV) is very similar to the single largest jump. This migration enthalpy agrees very well with the experimentally derived values of 3.61 eV and 3.5 eV obtained by Dobson et al.[41] and Yamazaki et al.[35] respectively. The entire cycle for one silicon vacancy to migrate can be described as a single Arrhenius process

$$D_v = \nu l^2 e^{-\frac{\Delta H}{kT}} = 3.5 \cdot 10^{12} e^{-\frac{3.6}{kT}}. \tag{10.1}$$

Figure 18 shows the available experimentally obtained diffusion coefficients of sil-

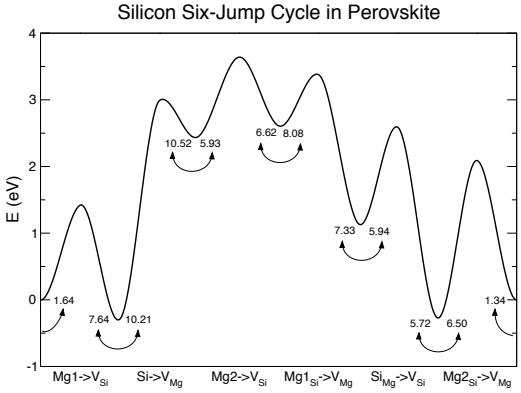

Figure 20: **The energy barrier of the six-jump cycle for silicon diffusion in perovskite** The numbers are the attempt frequencies towards neighbouring states as indicated by the arrows

icon compared to my results. In order to make such a comparison, a silicon vacancy concentration of 0.2% had to be used. This seems unexpectedly high for silicon vacancies, but it seems unavoidable that the experiments do indeed have very high concentrations of silicon vacancies. Using a nearest neighbour jump distance of 2.4 Å, a representative jump frequency of 10 THz, and the experimentally determined migration enthalpy of 3.6 eV, each of the experimental diffusion coefficients of Dobson et al.[41] for the silicon vacancy concentration can be inverted. These range from 0.35% to 0.075%. A similar range is found from the data of Yamazaki et al.[35]. The range is also in rough agreement with the defect calculations of Hirsch and Shankland[178]. So a vacancy concentration of about 0.2% is perfectly consistent with the fast measured diffusion rates.

Although the experimental diffusion rates can be explained by the six-jump cycle, there is an additional complication to be considered. At each step of the cycle there is a possibility that one of the vacancies takes a hop to a site not in the cycle. This, therefore, breaks the cycles until another vacancy comes along. For instance, the first step in the cycle produces a magnesium vacancy. The activation barrier for it to take the next step in the cycle is about 3.3 eV. However, the energy barrier for it to hop to one of the other neighbouring magnesium sites instead of the silicon site, is only between 3.6 and 4.1 eV (large and small supercell respectively); there is, therefore, a non-negligible probability that it will take this jump. These processes of breaking the cycle must be taken into account when calculating silicon diffusion

coefficients.

This can be done using Kinetic Monte Carlo. Given a set of rate constants (diffusion constants in this case), KMC is a way of propagating a dynamic system through a possibly complex set of paths (or phase space). If one images a vacancy at a certain position, it may have a number of possible paths. Normally it will take the one that is most probable (generally the lowest migration barrier), but sometimes it will take another. Once it has moved on, it is faced with another set of possibilities and associated probabilities. KMC provides a way of moving the system through the phase space and determining the overall rate constant (or diffusion constant). I could use this technique as an alternative to the analytic technique for obtaining the effective diffusion coefficient for the full cycle, ignoring possible breaks in the cycle; I do indeed get the same result using both methods. But KMC has to be used when a diffusing species has a choice of paths.

Let me briefly look at the KMC-simulation in more detail. Being interested in how many times the six-jump cycle is broken one not only needs the jump-frequencies for the possible first jumps off the cycle but also the ones of the next jumps in order to ensure that it does not jump back into the cycle. This rapidly becomes an impossibly large number of calculations and the calculation was restricted to the first two jumps off the cycle, after which it was assumed that the vacancy is gone. This scheme is shown in figure 21. The rate of each jump in the KMC is given by $\nu \cdot e^{-E/(kT)}$ where E is the height of the energy barrier for the considered jump and ν is its attempt frequency. States 0-6 are the states of the uninterrupted six-jump cycle (using the forward and backward rates given tables 15 and 23, and the breaking jumps from table t:kmcbreaks). States 7-9 are the states in which the cycling vacancy has been filled with a neighbouring magnesium, breaking the cycle. From these breaking states, it has been assumed that the vacancy has to perform another jump onto state 10 (the same as a free vacancy can do on the magnesium sublattice) to completely abort the cycle or it jumps back and completes the cycle. The KMC simulation was restarted every time the cycle was completed (reached state 6) or was broken (reached state 10). Then, by comparing the number of completed with the total number of run simulations the percentage of cycles that break was obtained.

My results show that the cycle is broken somewhere between about 1% and 20% of the time, depending on the assumed attempt frequency of the breaking jumps (and the used supercell-size). The cycle is mostly broken already at the second step (at the largest single-jump barrier). The reason the cycle breaks can be easily

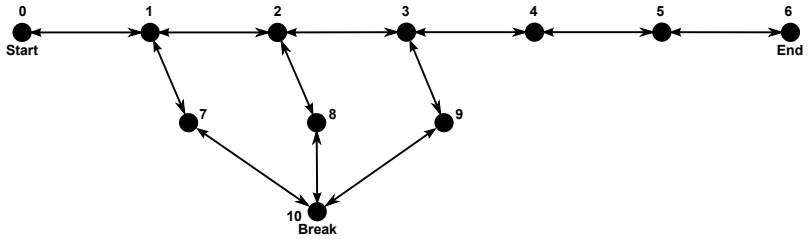

Figure 21: **Schematic diagram of the KMC simulations of the six-jump cycles** (see text for details)

understood: the silicon cycle starts with a silicon vacancy (charge -4), which is then occupied by a magnesium ion forming a magnesium on a silicon site (charge -2) and a magnesium vacancy (charge -2). The antisite and the magnesium vacancy have the same charge sign, and hence repel each other electrostatically. The energy of the reaction

$$Mg_{Mg}^{x} + V_{Si}^{''''} = V_{Mg}^{''} + Mg_{Si}^{''} \tag{10.2}$$

is only -0.3 eV when they are adjacent to each other, however, it decreases to about -2.2 eV (depending on the functional and the permittivity chosen for the charged defect correction) when the magnesium antisite and the magnesium are allowed to be infinitely separated. In other words, regardless of whether or not the cycle breaks, there should only ever be a vanishingly small concentration of silicon vacancies to begin with. This is completely at odds with the large number of vacancies required by fast diffusion coefficients observed experimentally.

One way to overcome the electrostatic repulsion of antisite and magnesium vacancy is to neutralise one of them; the most obvious candidates to do this are protons. This possibility was investigated by calculating several possible configurations of hydrogen incorpration and vacancy formation reactions, however, none was conclusive. The data is collected in table 18. For instance, the energy of the following reaction was calculated:

$$Mg_{Mg}^{x} + 2H_{Si}^{''} = V_{Mg}^{''} + (Mg + 2H)_{Si}^{x} \tag{10.3}$$

where, as with the previous reaction, the two species on the right-hand side are infinitely apart. I find that this reaction is strongly endothermic, with an energy of 2.44 eV. In other words, protons increase the concentration of silicon vacancies, something that has been suggested for other silicates such as forsterite[108,109]. Obvi-

ously the presence of protons may change the jump frequencies, but jumps into sites inhabited with protons become substantially more complicated calculations and I have not attempted these yet.

Also, the formation of vacancy-clusters with oxygen vacancies could stabilise silicon vacancies. It was found indeed that in the presence of two oxygen vacancies, the migration enthalpy can be lowered to about 3.4 eV at 25 GPa while stabilising the silicon vacancy - because of forming a neutral defect cluster. The formation energy is of the order 4.75 eV and thus too high to explain any experimental findings and additionally, temperature and entropy will force this defect cluster to break up and it cannot be expected to be present in perovskite.

At present, it is not possible to explain the high silicon diffusion rates seen experimentally in two independent studies as a six-jump cycle with about 0.2% silicon vacancies stabilised by protons. The activation enthalpy of the direct jump is too high. So far, appreciable amounts of water have not been experimentally verified in perovskite, with some studies showing negligible water solubility[179,180]. Regardless of whether it is water, or some other extrinsic mechanism, the experiments are only consistent with high concentrations of silicon vacancies.

10.3.1. Other investigated silicon diffusion mechanisms

Previous studies[90,91] on silicon migration barriers in perovskite found a decrease in the migration enthalpy in the presence of an oxygen vacancy. However, for my direct pathway[92], the migration energy in the presence of a oxygen vacancy is increased to about 6.2 eV. This finding is not surprising as an oxygen-vacancy has the same charge-sign as the migrating silicon ion.

In many other silicates, silicon diffusion occurs via an interstitial mechanism and migration enthalpy and pre-exponential factor are linearly correlated[181] (compensation law). As observed by Béjina and Jaoul[182], silicon diffusion in perovskite also satisfies this compensation law and they therefore suggested that silicon in perovskite diffuses via an interstitial mechanism. Indeed, a stable split interstitial configuration was found in which two silicon interstitials are located on opposite faces of the oxygen octahedron (slightly elevated above the centre of the triangle faces), around a vacancy at the centre of the octahedron (shown in figure 22). Split interstitials are very common in many materials and for various species (e.g. in forsterite[107,119], quartz[183], various metals[184] and semi-conductors[185]). However, my results indicate that also this split-interstitial mechanism cannot explain the experimental findings

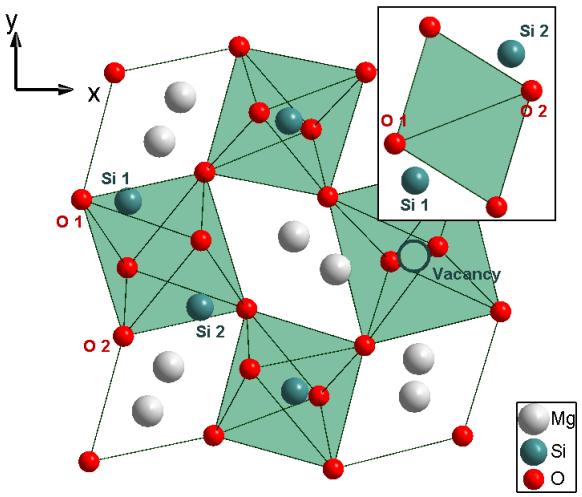

Figure 22: **Silicon split-interstitial configuration in $MgSiO_3$ perovskite**

as the formation energy of this state is about 10 eV at 24 GPa.

Finally, antisite migration was considered. The idea is that the cation sublattice can be partially inverted, i.e., that magnesium ions occupy silicon vacancies and silicon ions occupy magnesium vacancies. The intrinsic generation of such an antisite pair, i.e., magnesium and silicon swap sites at the same time is energetically unlikely (12 eV at 24 GPa). The formation energy of such a bound antisite-pair is, however, only 3.1 eV (at 24 GPa) above the perfect crystal.

Silicon jumping onto magnesium vacancies and magnesium jumping onto silicon vacancies are the energetically most favourable cation jumps (among the ones investigated). There are three mechanisms which make use of these antisites and are energetically feasible: I) the direct jump to second nearest neighbour vacancies in the presence of a magnesium vacancy, II) the antistructure bridge and III) the six-jump cycle.

I In order to migrate silicon efficiently through the crystal by the direct mechanism, magnesium vacancies need to be neighbouring silicon vacancies. Unsurprisingly, this is not the case as they carry the same charge and thus repel each other.

II The antistructure bridge mechanism (also known in binary alloys, e.g.[176]) starts with a silicon-vacancy plus a silicon-antisite atom. The antisite ion jumps into the vacancy effectively changing the type of the vacancy and a nearby silicon ion jumps from its silicon site onto the new magnesium vacancy creating again an antisite plus a silicon vacancy. The analogous process works for magnesium

antisites. While I can expect to have quite some inversion for silicon vacancies (occupied with magnesium ions, formation energy -2.5 eV), there will be only very few silicon atoms occupying magnesium vacancies (formation energy 8 eV). While this mechanism might well contribute to magnesium diffusion, the resulting silicon diffusion rate would be much too slow compared with experiments. One could also envisage a situation in which a magnesium and a silicon swap their sites forming two neighbouring antisites allowing a new mechanism. Such a pair would be electrostatically bound and could be moving via silicon and magnesium vacancy sites in a corporate manner. However, such pairs are rare as the formation energy is about 3.1 eV and the migration barrier is about 4.5 eV.

III The six jump cycle discussed above is the only mechanism I have found which can explain the experiments.

10.4. Implications for the Lower Mantle

10.4.1. Ionic Conduction of Perovskite

Knowledge of the conductivity of the mantle minerals will allow to further constrain the physical and chemical conditions by measuring changes in the global magnetic field and calculating the Earth's response function (e.g. Dobson and Brodholt[186]). Xu and McCammon[37] concluded from their experiments on perovskite that the dominant electric conduction mechanism at high temperatures and high pressures is ionic. They found that ionic conduction dominates over small polaron conduction (electron transfer between Fe^{2+} and Fe^{3+}) at temperatures higher than 1500 K. This has also been found in previous studies[169,187]. However, Dobson[36] observed another change in conduction mechanism at temperatures around 1900 K. He suggests that at low temperatures, extrinsic oxygen ionic conduction dominates, while intrinsic electronic conduction sets in above 1900 K. Additionally, Brodholt[110] found theoretically that extrinsic oxygen defects are destroyed by pressure (at least in aluminous systems). It is therefore very likely, that there is a region in the shallow lower mantle, where the temperature is between 1500-1900 K and oxygen vacancies have not yet been removed by pressure, where oxygen ionic conduction in perovskite is the dominant conduction mechanism.

I tested this assumption by calculating the oxygen ionic conductivity in perovskite and comparing it with Earth's conductivity models derived from geomagnetic trans-

fer function calculations. A comparison with conductivity models derived from calculations of Earth's response function from magnetic field satellite data[188] and from European geomagnetic observatories[189] is shown in figure 23. It shows that an oxygen ionic conduction dominated layer in the shallow lower mantle is indeed in agreement with these results. At the same time, my results demonstrate that mantle conductivity in the lower mantle is not controlled by ionic conduction. Temperatures of at least 5000 K are required to match my oxygen ionic conduction with Olsen's[189] data at the base of the lower mantle. Electromagnetic core–mantle coupling through ionic conduction in perovskite can therefore not explain length of day (ΔLOD) variations on decadal time scales. The ionic conduction of post-perovskite shall here be foreclosed because this observation is to some extent obsolete as recent experiments showed that conductivity in perovskite and post-perovskite is dominated by small polaron conduction[190]. However, the ionic conduction in post-perovskite is at least one order of magnitude slower than in perovskite.

10.4.2. Chemical Equilibrium in the Lower Mantle

The characteristic diffusion length L_D is given by[66] $L_D = \sqrt{4Dt}$ where t is a characteristic time scale. The characteristic diffusion lengths for all species in the dominant mantle minerals are given in table 8.

Table 8: Characteristic diffusion lengths for all species in the dominant mantle minerals for the time scale of the age of the Earth ($4.5{\cdot}10^9$ yr). Values are minima and maxima along a geotherm and used vacancy concentrations are N_v=0.001

Mineral	Species	L_D^{Earth} [m]
Periclase	Mg	20 - 110
	O	10 - 70
Perovskite	Mg	1
	Si	4
	O	250 - 650
Post-Perovskite	Mg	20 - 50
(along $\langle 100 \rangle$)	Si	90 - 270
	O	60 - 130

Again, foreclosing results from post-perovskite, one can conclude that the mantle is significantly heterogeneous in oxygen fugacity and cation composition. The slow diffusivities of the cations in all these minerals imply that chemical heterogeneities of the size of a few meters can persist in the lower mantle for several convection

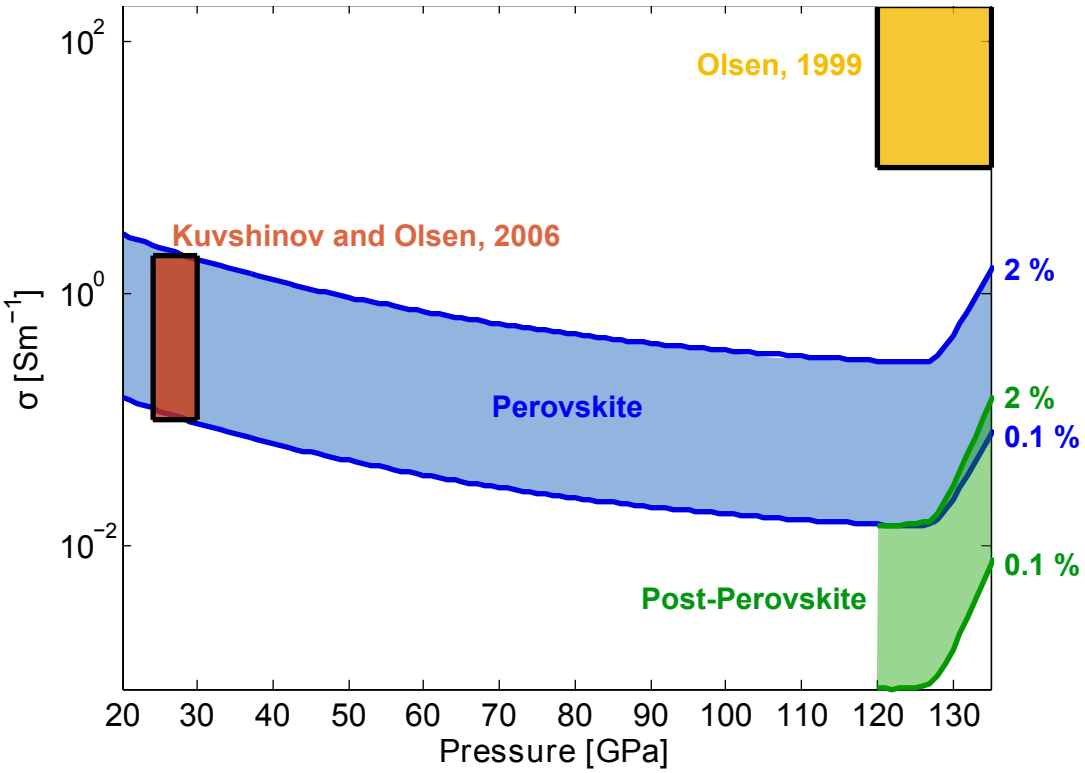

Figure 23: **Conductivity of $MgSiO_3$ perovskite (solid blue) and post-perovskite (solid green) due to oxygen ionic conduction** compared with model conductivities derived from magnetic field satellite data[188] and from European geomagnetic observatories[189]. The used vacancy concentrations are shown on the right hand side of the figure. The red and orange rectangles indicate the spread of the computed conductivities from different models between 24 and 30 GPa and between 120 and 135 GPa. The oxygen vacancy concentration in perovskite has been estimated from the experiments of Lauterbach et al.[171] to be $N_v = 1.5$ %

cycles. Moreover, these slow diffusion rates suggest that there is essentially no chemical interaction between the core and the mantle. The conclusions drawn by Dobson et al.[41] for the chemical equilibrium concerning perovskite remain valid: Slab material will not reach redox equilibrium with the surrounding mantle during subduction through the lower mantle as a maximum of 100 m can be homogenized for oxygen and assimilated into the lower mantle within one cycle (10^8 yr). As oxygen diffusion in post-perovskite is even slower than in perovskite, the width of the reaction layer in D″is actually decreased by the presence of post-perovskite. Chemical exchange with the core would thus need to occur via grain-boundary diffusion[191] and chemical heterogeneities in the mantle could only be removed via mechanical mixing (stretching and thinning) or grain boundary diffusion.

10.4.3. Viscosity of Perovskite

I now consider the effect of my calculated diffusion coefficients on mantle rheology. The absence of seismic anisotropy in the lower mantle, small grain size[125], and low stresses, all argue for diffusion creep being the dominant creep mechanism through the majority of the lower mantle[126]. Moreover, viscosity models from glacial rebound indicate linear rheology for most of the mantle, again consistent with diffusion creep. I can, therefore, estimate the viscosity of the lower-mantle using the Nabarro-Herring expression for diffusion creep (in the case of simple shear, this expression is multiplied by a factor of 2/5)[127]. Grain sizes in the lower mantle have been estimated by Solomatov et al.[125] to be 0.1 - 1 mm, so one can neglect grain-boundary diffusion for the major chemical species (Mg, Si and O)[35,38]. Estimates of lower mantle viscosity from post-glacial rebound, geoid anomalies and convection-related observables of between $10^{21} - 10^{24}$ Pa s[7,192,193] are consistent with my results. My calculated mantle viscosity also bounds the estimates from Mitrovica and Forte[7] (Figure 26), consistent with diffusion creep being the dominant mechanism in the lower mantle. It is important to note that the quality of agreement can be improved as the viscosity is strongly dependent on the geotherm, vacancy concentration and grain size. A taste of the effect of the geotherm on the viscosity profile can be obtained, when one compares the two figures of the perovskite-viscosity profile in figures 24 and 33

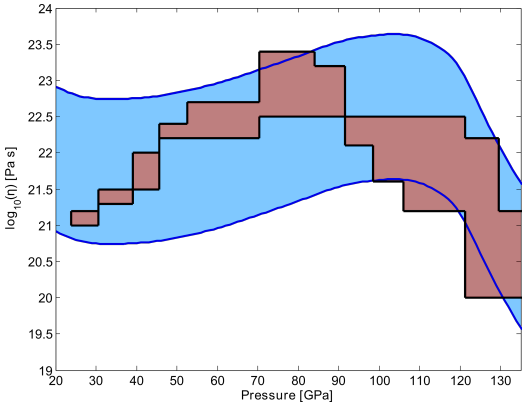

Figure 24: **Calculated viscosity profile of the mantle with a composition of 100 % $MgSiO_3$ perovskite (solid blue) deforming in diffusion creep (geotherm from[194])** Calculated viscosity profile of $MgSiO_3$ perovskite deforming in diffusion creep. Grain size G and vacancy concentration N_v were varied such that $G^2/N_v = 0.01 - 0.1m^2$ for lower and upper bounds respectively. Vacancy concentrations are assumed to be fixed throughout the entire lower mantle. Superimposed are the results from inversion modelling[7].

11. $MgSiO_3$ Post-Perovskite

The phase transition from $MgSiO_3$-perovskite to a $CaIrO_3$-structured phase, so-called post-perovskite, around 120 GPa has been discovered only recently[31–33] and is believed to be responsible for the D″discontinuity observed in seismic waves. Its structure is shown in figure 25. The post-perovskite phase is then stable up to pressures of 1120 GPa where it dissociates into MgO and SiO_2[195]. Post-perovskite is therefore believed to be a large phase in super Earths (7 Earth masses) or in Saturn-like planets and diffusion coefficients have been calculated up to 500 GPa.

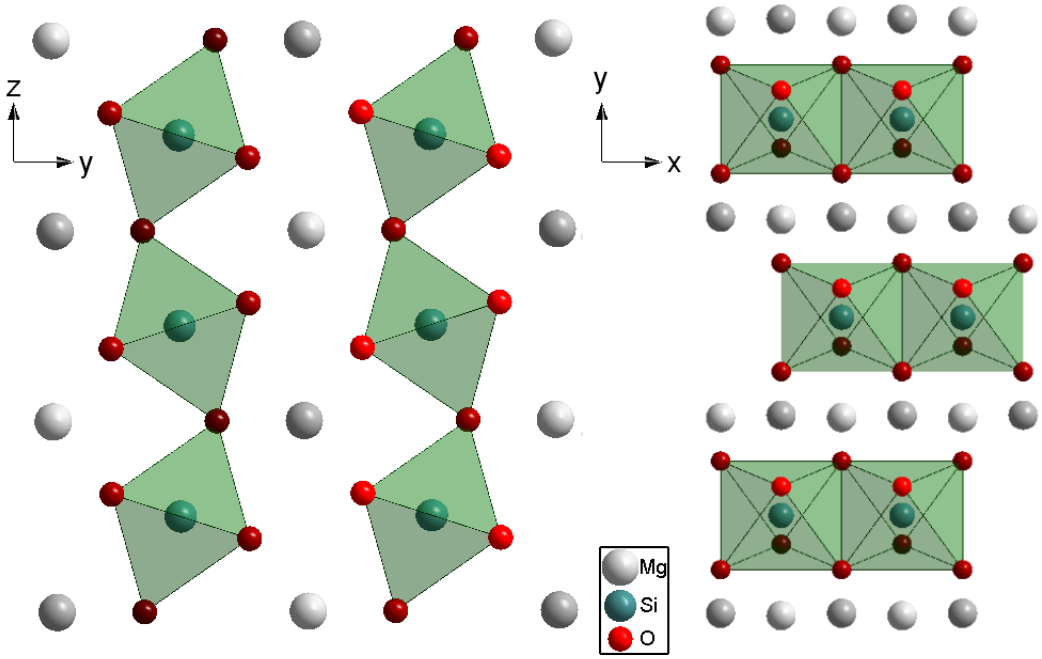

Figure 25: **$MgSiO_3$ Post-Perovskite Structure** Two views of post-perovskite revealing its layered structure

Again, the calculated high formation energy for Schottky defects (46.2 eV at 120 GPa[91]) indicate that vacancy concentrations will be controlled by impurities even at the elevated temperatures at the core-mantle boundary (see also figure 11). As it is not better known, I have assumed that the extrinsic vacancy concentrations are the same in perovskite and post-perovskite when calculating the viscosity.

The agreement of the calculated diffusion rates in perovskite with the experiments for all three ionic species, throughout the pressure and temperature range in which they were measured (see figure 18) is excellent. This provides confidence for the results on post-perovskite for which no data exist and so the current results are the only predictions so far on the diffusion properties of this important mantle phase.

11.1. Single Vacancy Jumps

I first investigated single vacancy jumps to nearest neighbour sites along each direction. I find similar migration enthalpies as Karki and Khanduja[91] for the direct jumps they investigated using DFT within LDA. Parameters and sketches of the investigated migration paths can be found in the appendix VI. I find, indeed, that oxygen diffusion in post-perovskite occurs by single jumps along the octahedral edges (and across the magnesium layers to non-connected octahedra). The rates are similar along all directions resulting in fast, isotropic diffusion. The vacancy diffusivities along a geotherm[98] are shown in figure 26, and are compared to diffusion rates in perovskite and MgO. Note that these are the vacancy diffusion rates and, therefore, are independent of vacancy concentration. The true diffusion rates will depend on the actual vacancy concentrations. As can be seen in figure 26, oxygen vacancy diffusion in perovskite is clearly the fastest diffusing species of all. Oxygen vacancy diffusion in post-perovskite is somewhat slower; oxygen diffusion in periclase is slower again.

As perhaps expected from such a structurally anisotropic material, cation diffusion in post-perovskite is extremely anisotropic, with diffusivities varying by several orders of magnitude between the fastest direction $\langle 100 \rangle$ and slowest direction $\langle 010 \rangle$. My results show that the direct jump along $\langle 010 \rangle$ would lead to diffusion coefficient almost 20 orders of magnitudes below the one of the fast $\langle 100 \rangle$ direction (not shown in figure 26). Thus, diffusion in post-perovskite occurs via simple direct vacancy hopping only along $\langle 100 \rangle$ and $\langle 001 \rangle$, however, the diffusion rates of both silicon and magnesium are much slower in the $\langle 001 \rangle$ direction, and more in line with that found in perovskite. Thus, it is in fact not the slow diffusion across the layers that causes the anisotropy (which is similar to the diffusion rates in perovskite), but the extraordinarily fast diffusion within the layers parallel to $\langle 100 \rangle$. This is the direction of edge-sharing SiO_6-octahedra. Diffusion of silicon, oxygen and magnesium in the $\langle 100 \rangle$ direction in post-perovskite is similar to that of MgO, and several orders of magnitude faster than the isotropic cation diffusion in perovskite.

11.2. Reducing the Anisotropy: Six-Jump Cycles

As discussed above, direct vacancy jumps along $\langle 010 \rangle$, the direction perpendicular to the layers in post-perovskite, are energetically not feasible. Instead, I find that both magnesium and silicon diffuse via a six-jump mechanism, similar to that of silicon in perovskite. The six-jump-cycles result in much faster cation diffusion across the

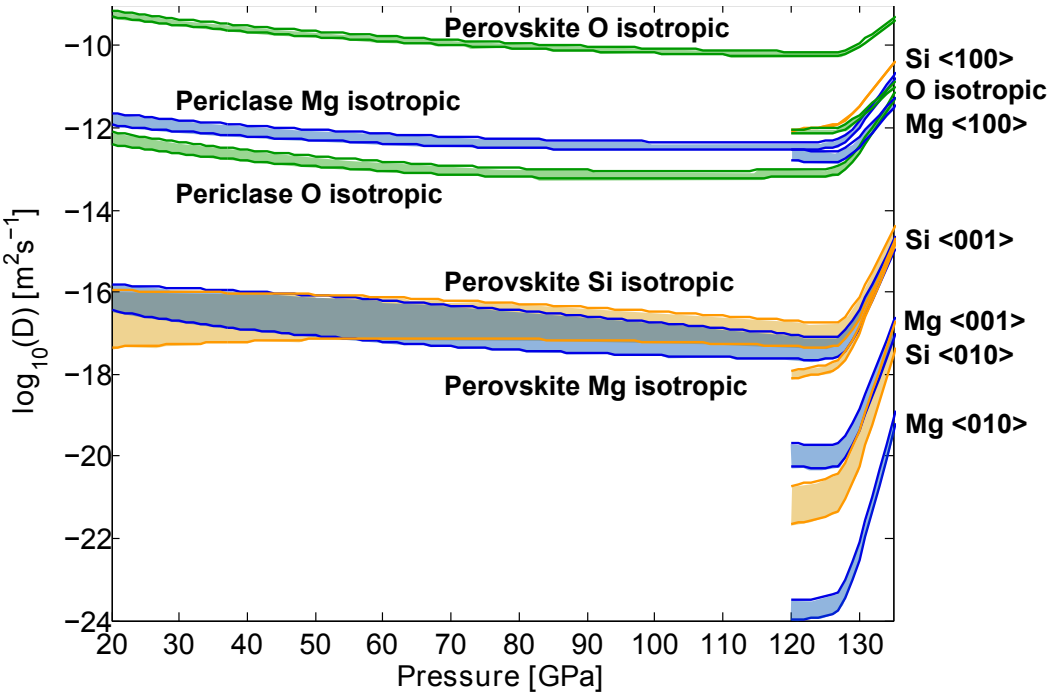

Figure 26: **Vacancy diffusion coefficients** Vacancy-diffusion coefficients of periclase, perovskite and post-perovskite along a geotherm[98]. Upper bounds, LDA calculations;lower bounds, GGA calculations

octahedron-layers, and accelerates the diffusion rates along ⟨010⟩ to similar levels as cation diffusion in perovskite (see figure 26). Although the six-jump-cycle allows faster diffusion in the ⟨010⟩ direction than the direct jump, cation diffusion is still extremely anisotropic in post-perovskite.

However, I find the same problem with maintaining silicon vacancies in post-perovskite as with perovskite. In fact, the barrier of the vacancy jump that breaks the silicon six-jump-cycle in post-perovskite is so low, that all cycles should break up (see also discussion on KMC in section 10). Thus, in post-perovskite and perovskite, silicon vacancies dissociate into a magnesium vacancy plus a magnesium on the silicon site, unless they are stabilised by some neutralising defects. The magnesium six-jump-cycle, in contrast, does not break up: start with a magnesium vacancy (charge -2) which is occupied by a silicon ion forming an antisite (charge +2) and a silicon vacancy (charge -4). Clearly, these defects will attract each other preventing the cycle from breaking up.

At this point, it is interesting to note that the partial inversion of the cationic sublattice (magnesium ions on the silicon sites) in post-perovskite could result in a strong enhancement of the magnesium diffusion across the octahedron layers:

The antisite bridge mechanism starts with a silicon (magnesium)-vacancy plus a silicon (magnesium)-antisite atom. The antisite ion jumps into the vacancy effectively changing the type of vacancy. To close this process, a silicon (magnesium) ion jumps from its silicon (magnesium) site onto the new magnesium (silicon) vacancy creating again an antisite plus the silicon (magnesium) vacancy. Thereby the silicon (magnesium)-vacancy is moved around. While one can expect to have quite some inversion for silicon vacancies (occupied with magnesium ions), there will probably be only very few silicon atoms occupying magnesium vacancies. Using this antisite-bridge mechanism would render the magnesium diffusion in post-perovskite essentially isotropic. Nevertheless, this enhancement would be proportional to the total number of magnesium antisites and thus to the total number of (initial) silicon vacancies which is entirely unknown in post-perovskite.

Since there are no experimental data on diffusion in post-perovskite, the current calculated diffusion rates and the predicted anisotropy await experimental verification. It is possible, for instance, that I have not thought of and investigated all the possible diffusion pathways and mechanisms in post-perovskite. However, it should be noted that these other pathways and mechanisms will only be relevant if they result in faster diffusion rates than the current ones. One such mechanism, the antisite-bridge, has been described above. Slower pathways are irrelevant. The very fast diffusion seen in the [100] direction cannot, therefore, become slower. It is possible, however, that the rates along other directions could be increased; this would have the effect of reducing the anisotropic cation diffusion, but at the same time, it would strongly increase the bulk isotropic diffusion rate, resulting in a very fast creep rate (see below).

11.3. Implications for D" - The Viscosity of Post-Perovskite

11.3.1. Dislocation Creep - A Weak Post-Perovskite

It seems likely that the D″ region is deforming in the dislocation creep regime. The high stresses accumulated at the edges of convecting cells and the observed seismic anisotropy in D″ both argue for deformation by dislocation migration at the base of the mantle. In the high-temperature case relevant to D″, of climb-assisted dislocation migration, the rate-limiting step is the transport of matter as unit cells are added to, or removed from, the climbing dislocation half-plane. This is in turn rate-limited by the fastest diffusion direction of the slowest diffusing species. My results predict that for climb-assisted dislocation creep post-perovskite will be

four orders of magnitude weaker than perovskite. This is supported by recent low-pressure analogue experiments which showed post-perovskite was up to 50 times weaker than perovskite in the $CaIrO_3$ system[196]. I suggest, therefore, that post-perovskite in D″ will be significantly weaker than perovskite.

There are a number of implications of this weakening for the D″ region. Recent experiments[34] have suggested that the transition from perovskite to post-perovskite in natural compositions is not sharp and might, in fact, extend over the whole of the lowermost 200 km of the lower mantle. Such a wide transition is inconsistent with post-perovskite being responsible for the seismic discontinuities observed at the top of D″. If, however, post-perovskite is significantly weaker than perovskite the system will show critical behaviour as the phase fraction of post-perovskite increases sufficiently for it to form an interconnected network. At the critical phase fraction, the rheology of the aggregate will switch from being perovskite dominated to being dominated by post-perovskite. This implies that, while the phase fraction might increase monotonically, once the critical phase fraction is reached there will be a rapid weakening of the two-phase mixture and strain will partition preferentially into the post-perovskite-dominated region. Critical behaviour of this type was observed in rheological studies of $CaIrO_3$ during transformation from perovskite to post-perovskite[196], with the bulk of the weakening occurring at approximately 30 % transformation. In D″, this rapid weakening and strain partitioning will cause the texture of the mixture to change from isotropic to anisotropic over a short distance due to the shear-induced lattice preferred orientation (LPO). Experiments on analogue phases show that strong LPO can be generated in post-perovskite after relatively small strains. Figure 27 shows the effect of rapid generation of LPO in a gradually transforming mixture on the observed seismic velocity for a low angle of incidence ray paths. Assuming that the critical phase fraction for post-perovskite-dominated rheology is 40 % an increase in shear velocity of around 4 % is calculated (after[28]), which is sufficient to explain the observed D″ discontinuity. The rapid development of LPO at the critical phase fraction might therefore be the cause of the D″ seismic discontinuity, even if the transformation from perovskite to post-perovskite occurs over a wide depth range.

The broad region of phase coexistence suggested by[34] is also inconsistent with a lower D″ reflector seen in some regions as being the back-transformation of post-perovskite into perovskite[27–29]. I suggest, however, that the region immediately above the core mantle boundary might be a region where diffusion creep dominates due to: (1) the steep thermal gradients in the thermal boundary layer and (2) the

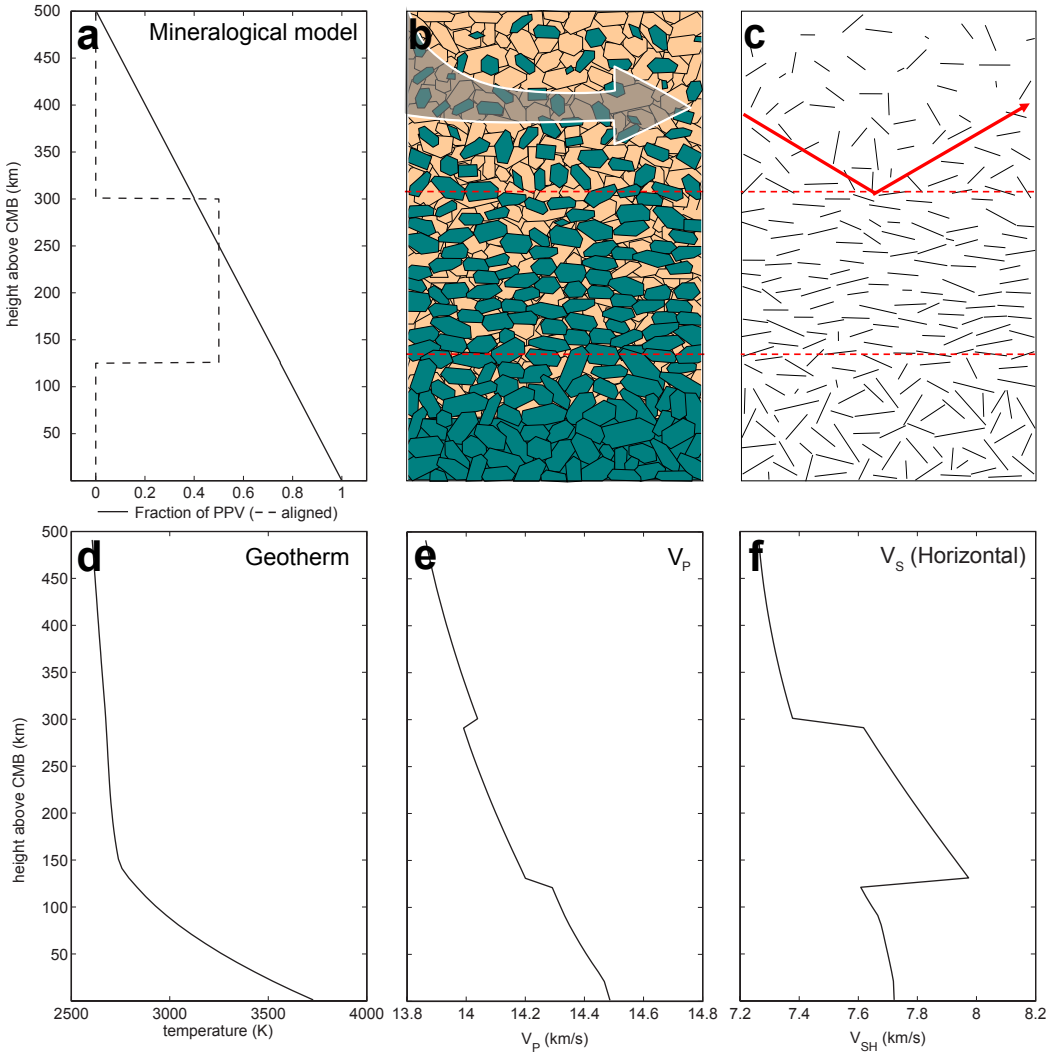

Figure 27: **Seismic velocity as a function of depth for a gradual transformation to post-perovskite, with an abrupt change in deformation** Panel (a); volume fraction of post-perovskite with depth (solid) and degree of alignment (dashed). Panel (b); pictorial representation of the phase fraction (red: perovskite, blue: post-perovskite, arrow represents imposed deformation) and grain orientations. Panel (c); orientation of B-planes and the seismic reflector (arrow) due to flow parallel to the core-mantle boundary. Panel (d); geotherm[98]; For each point on the geotherm an aggregate elastic tensor is constructed comprising perovskite and post-perovskite in the modal proportions given by (a) from *ab initio* calculated elasticities and gradients[197–202])(see below for details of calculation). Panels (e) and (f); P- and S-wave velocities that would be encountered by teleseismic (epicentral distance = 60°) PcP and ScS wave reflections with 45° angle incidence to the texture-boundary; this is similar to the signal which has been measured for the lowermost mantle (e.g[30])

free slip condition imposed by the liquid outer core resulting in a reduction of the shear stress immediately next to the CMB. A transition from dislocation creep to diffusion creep at the very base of D″ would result in a change in the crystallographic texture across this deformation transition, possibly explaining the basal D″ reflector.

In addition to providing an explanation for the observed D″ seismic reflectors, a weak post-perovskite has other implications for D″. First of all it has been shown that a weak D″ strongly increases the heat flux from the core and affects the geotherm[203]. If the viscosity is very low, small scale internal convection may develop within D″, further affecting heat flow from the core. The viscosity would also change laterally as the proportion of perovskite to post-perovskite varies due to lateral temperature gradients. This is supported by recent geoid modelling, which requires colder regions of the deepest lower mantle to be weaker than hotter regions[204].

Seismic Velocity as a Function of Depth for Perovskite - Post-Perovskite Aggregates Determining the effect a localisation of strain in post-perovskite might have on seismic observations of the lowermost mantle requires an estimate of the seismic velocities relevant to the techniques used to image them. The best estimates available for the elastic properties of deep mantle phases come from molecular dynamics calculations (e.g.[200]). These supply single crystal properties for both forms of $MgSiO_3$ at specified points in pressure-temperature space. One can also employ calculated pressure- and temperature-derivatives to extend the space over which the interpolation is possible.

For the $MgSiO_3$ perovskite elasticity the calculated tensors from Oganov et al.[197] were used and extended by using the pressure derivatives calculated by Wentzcovitch et al.[201]. For $MgSiO_3$ post-perovskite the calculations of Stackhouse and Brodholt[198,200] were used. These are extended using the pressure derivatives from Wentzcovitch et al.[202]. Between these points the values are interpolated following the technique of Wookey et al.[28]. In this work, however, the interpolation is extended to also include all elastic constants of perovskite and post-perovskite giving a single crystal elasticity as a function of temperature and pressure for both phases. Isotropic versions of these tensors are computed using the projection method of Browaeys and Chevrot[205].

These are combined in a simple linear fashion with modal proportions according to my mineralogical model (see figure 27 panel b). Perovskite is assumed to always be isotropic. Post-perovskite LPO in the model anisotropy is approximated by using

single crystal properties (with (010) oriented vertically[206]) diluted with the isotropic velocities. So the final aggregate tensor is given by:

$$C_{AGG} = f_{VRH}(C_{PPV-DILUTE}, v_{PPV}, C_{PV-ISO}, (1 - v_{PPV})) \tag{11.1}$$

where

$$C_{PPV-DILUTE} = f_{VRH}(C_{PPV}, v_{aligned}, C_{PPV-ISO}, (1 - v_{aligned})) \tag{11.2}$$

and

$$C_{PV} = C_{PV-ISO}. \tag{11.3}$$

C_{PV} and C_{PPV} are the interpolated elastic tensors for perovskite and post-perovskite respectively. The $_{-ISO}$ and $_{-DILUTE}$ subscripts denote the isotropic and diluted versions. v_{PPV} is the volume fraction of post-perovskite of which $v_{aligned}$ is assumed to be aligned. Finally, f_{VRH} refers to the Voigt-Reuss-Hill average, the method employed for combining tensors (see, e.g., Mainprice (2007)[207], for more details).

Thus, we have an aggregate tensor for the linear mixture of phases as a function of temperature, pressure, and degree of alignment.This is evaluated at 10 km intervals for the bottom 500 km of the mantle using the geotherm proposed by Stacey and Davis[98] to get elasticity as a function of height above the CMB. Since the model is anisotropic over part of its depth range the seismic velocities are a function of wave propagation direction (both in azimuth and inclination). Thus, the velocity profile which might be inferred from a seismic experiment imaging such a model is dependent on the geometry of the sources and receivers relative to the geometry of the aligned post-perovskite. The profiles shown in figure 27 show the velocity profile (calculated using the Kristoffel equation, see, e.g.[199]) to which imaging using teleseismic P- and S-wave reflections at an epicentral distance of 60°, and an azimuth of 45° to the alignment direction of [100] would be sensitive. This shows a small decrease in V_P and a larger increase in V_S as the strain boundary is crossed (and the inverse at the base of the region). This is similar to the signal which has been measured for parts of the lowermost mantle (e.g.[30]). The magnitude and sign of the velocity perturbation associated with the strain boundary is strongly dependent on the azimuth, and more weakly on the epicentral distance. This might be an explanation for the observed variability in the D″ seismic reflectivity signal (e.g.[208]).

11.3.2. Anisotropic Diffusion-Creep Viscosity

The strong diffusion anisotropy in post-perovskite presents problems for predicting its viscosity in lattice-diffusion creep. Let me thus first describe how to deform a single grain in a polycrystal. Because of the large diffusion-anisotropy in post-perovskite, matter will diffuse along the fastest direction for nearly all orientations of the chemical potential gradient (only chemical potential gradients which are very close to perpendicular to the fast diffusion direction will generate significant chemical fluxes away from the fast diffusion direction).

This situation is represented graphically, for simple shear in a polycrystalline material, in figure 28. A shear stress induces increased chemical potential at surfaces marked with '+' and reduced chemical potential at surfaces marked '-'. First, consider the special case where the fast direction is oriented parallel to the shear direction (part (a) of the figure). Here chemical flux along the fast direction will allow full relaxation of the stresses at the grain boundaries even though the chemical potential gradients close to the surfaces are not parallel to the shear direction. Since this is the fastest diffusing direction, the effective viscosity will be lowest when grains are in this direction and the stresses will be relaxed at the grain boundaries without need to rotate grains in this orientation. Grains in this special orientation will therefore tend to remain in this orientation, but might experience passive rotations imposed on them by neighbouring grains.

Consider now the general case where the fast direction is at some high angle to the shear stress. In this case the strain cannot be accommodated by shear without rotation and the grain will rotate. The mismatches at the grain-boundaries between the rotating grain and the surrounding matrix will result in chemical potential gradients which will mainly be relaxed by diffusion along the fast direction. However, in this case the stresses cannot be entirely relaxed by diffusion in the fast direction and further stress relaxation would require either grain-boundary diffusion, or lattice diffusion in directions other than the fast direction. In this case, therefore the effective viscosity will require some convolution of diffusivities the fast direction and at least one other direction. This causes the effective viscosity for the general case to be higher than for the special case described above. A similar process is seen for systems deforming in dislocation creep where there are less than five independent slip systems (e.g. olivine[210]).

The question now is whether textures can be generated in which the special case applies and, if they can be generated and whether they would be preserved in dif-

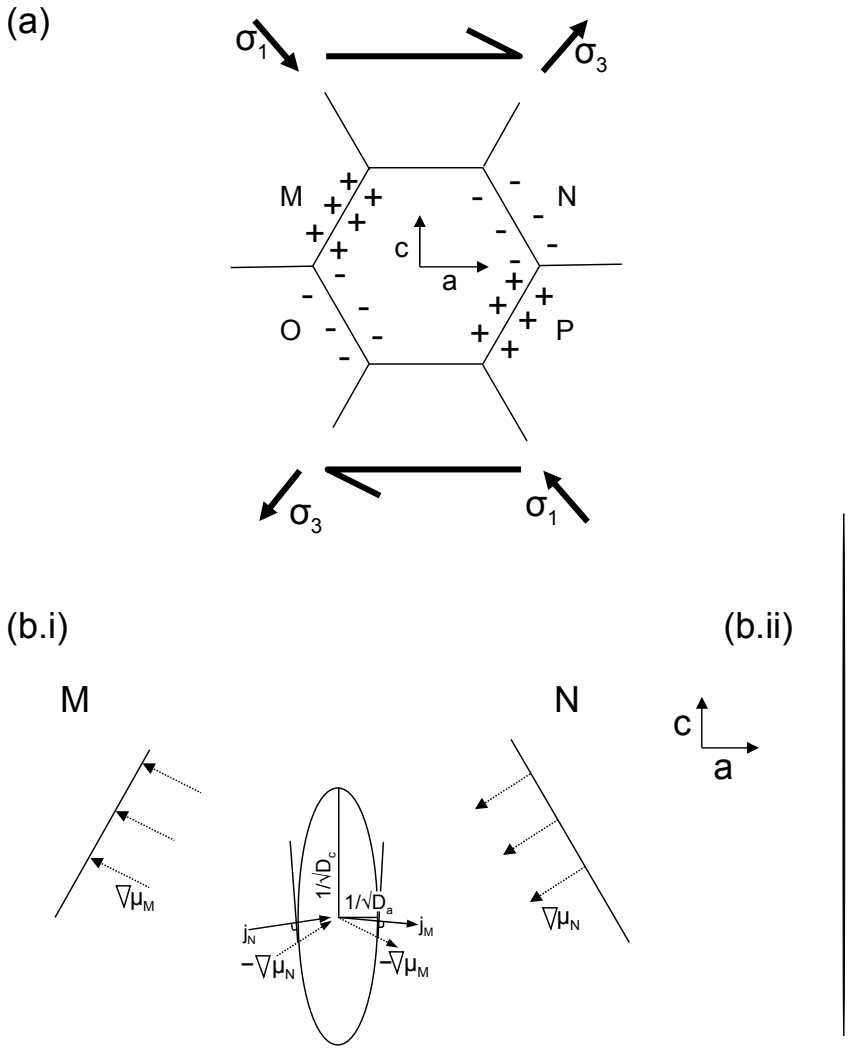

Figure 28: **A segment of a polycrystalline material deforming by lattice diffusion in simple shear with grain boundary sliding**. (a) The shear stress can be resolved into the principal stresses marked as bold arrows. The crystal at the centre of the sketch has its a and c crystallographic axes oriented as marked (a is the fast diffusion direction). The stresses on the grain boundaries result in increased surface energies at M and P and decreased surface energies at N and O. (b.i) The chemical potential gradient at surfaces M and N (dotted arrows), and the a-c section of the representation quadric of the diffusion tensor[209], of the central grain are, for clarity, drawn for the diffusivity along a being ten times the diffusivity along c (In reality D_a is $\approx 10^5$ times faster than D_c for post-perovskite; the a-c section of the quadric is drawn to scale for post-perovskite in figure (b.ii)). The fluxes at M and N (j_M and j_N) are normal to the tangents of the ellipsoid at $-\nabla\mu_M$ and $-\nabla\mu_N$ respectively. In post-perovskite the flux is essentially parallel to the fast diffusion direction for most orientations of the chemical potential gradient

fusion creep. I would argue that, since grains in the special orientation are weaker than grains in the general orientation, shear deformation can be accommodated by grains in the special orientation with less grain rotation than required for the general orientation. This would result in grains tending to rotate into the special orientation. While the exact details of the mechanisms are not clear, there is growing evidence of lattice-preferred orientation being generated by diffusion creep in a range of geological materials[211–213]. Even if a favourable texture could not be generated by diffusion creep it is a fortunate coincidence that the texture generated by dislocation creep in post-perovskite aligns the fast diffusion direction (the crystallographic a-axis) parallel to the shear direction, resulting in generation of the special orientation for weak diffusion creep even by dislocation creep. The preservation of lattice preferred orientation in diffusion creep has recently been demonstrated in experimental and natural samples (e.g.[214]) and in numerical simulations[215]. The exact degree of weakening associated with real lattice preferred orientation textures of anisotropic Nabarro-Herring creep in simple shear is beyond the present study but the diffusivity in the fast (a)-direction will provide the limiting case where all grains are in the special orientation.

The above discussion is limited to simple shear. In pure shear any special orientation is dependent on the shape of a grain as well as the stress-field. Since the deformation necessarily results in grains changing shape special orientations are destroyed by the deformation and the effective viscosity will always be some convolution of the diffusivities in all crystallographic directions.

11.3.3. Effective Viscosity of Aggregates of Post-Perovskite

Let me now describe how to calculate the diffusion-creep viscosity of an aggregate of post-perovskite grains in a simple model. The idea is that the viscosity of the aggregate is controlled by the average viscosity of its constituting grains, while the viscosities of the grains along certain directions will depend on the alignment of the crystal-axis (diffusion-directions) of the constituting grains with the considered direction of deformation and texture.

To this end, in three dimensions, one can write the diffusion coefficient of a single, spherical grain in an arbitrary direction (characterised by azimuth $\phi \in [0, \pi]$ and longitude $\theta \in [-\pi, \pi]$) as

$$D_{eff} = \left(\frac{(cos(\theta)sin(\phi))^2}{D_a} + \frac{(sin(\theta)sin(\phi))^2}{D_b} + \frac{cos(\phi)^2}{D_c} \right)^{-1} \tag{11.4}$$

where D_a, D_b and D_c are the diffusion rates along the corresponding crystallographic axis, where $\phi = 0$ corresponds to [001] and $\phi = 90$; $\theta = 0$ corresponds to [100], as shown in figure 29.

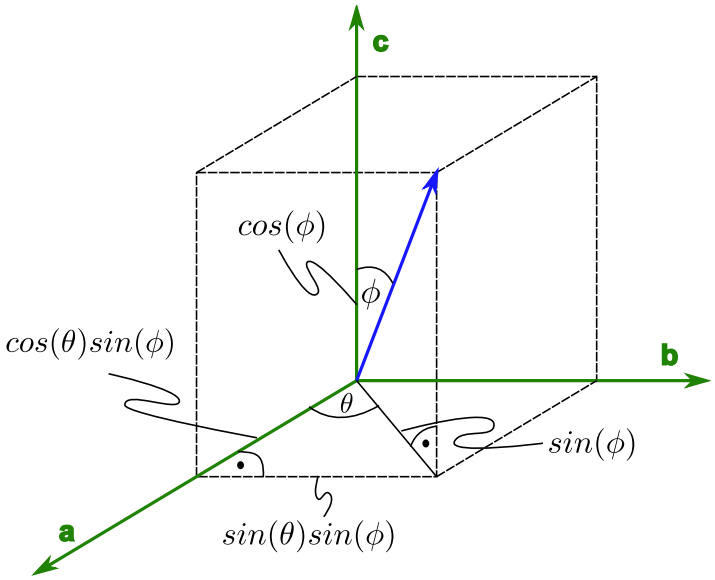

Figure 29: **Calculating diffusion along an arbitrary direction** Calculating the diffusion in an aggregate requires to calculate diffusion in an arbitrary direction of a single grain. The crystallographic axes of the grain are given as a, b and c. The arbitrary direction is shown by the blue arrow, of unity length. Also shown are its lengths along each crystallographic direction

The diffusivity perpendicular to this direction is given by

$$D_{eff}^{\perp} = \left(\frac{P_x^2}{D_a} + \frac{P_y^2}{D_b} + \frac{P_z^2}{D_c} \right)^{-1} \tag{11.5}$$

with $\mathbf{P} = R_z(\theta)R_y(\phi)\mathbf{P'}$, where $\mathbf{P'} = [cos(\delta)\ sin(\delta)\ 0]$ ($\delta \in (0, 2\pi]$ rotates the vector in the perpendicular plane, as shown in figure 30) and $R_z(\theta)$ and $R_y(\phi)$ are the three dimensional rotation matrices around z by θ and around y by ϕ respectively.

The distribution of grain orientations can be modelled using the so-called von Mises-Fisher distribution[216], also known as the normal distribution on a sphere. This distribution describes the angular distribution of orientations about a mean

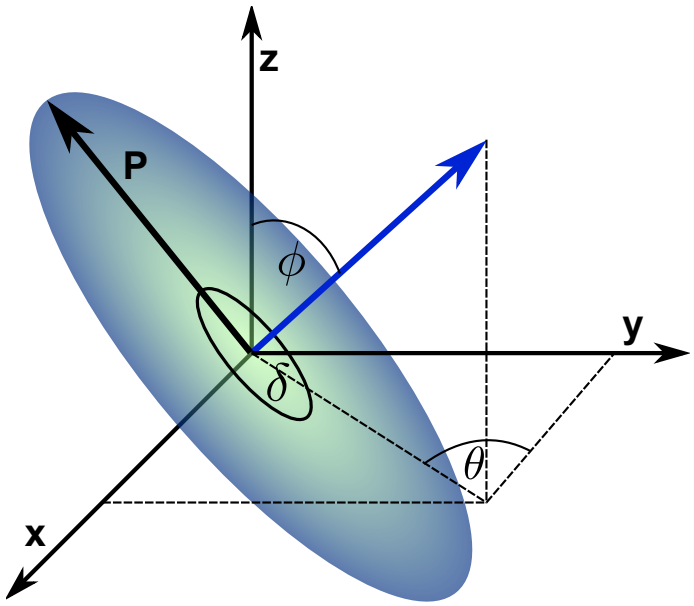

Figure 30: **Schematics to calculate diffusion perpendicular to a texture** The plane perpendicular to the blue arrow (texture direction) is spanned open by rotating the unit-vector **P** around the angle δ. While diffusion along the blue arrow is given as described in figure 29

orientation vector. The probability function of the von Mises-Fisher-distribution is given by

$$f(\phi) = \frac{\kappa e^{\kappa cos(\phi)}}{4sinh(\kappa)} \tag{11.6}$$

where κ is the concentration-factor (Fisher constant, dispersion factor) which describes the tightness of an orientation cluster. The effect of a change in κ on the probability distribution is shown in the right hand side panel in figure 32. The concentration factor is related to the angular standard deviation σ (by analogy with the normal distribution) as[217]

$$\sigma = \frac{81^\circ}{\sqrt{\kappa}}. \tag{11.7}$$

For κ approaching 0, the von Mises-Fisher-distribution becomes the uniform distribution.

I have used the von Mises-Fisher-distribution to model post-perovskite aggregates of completely random grain orientation and in presence of a texture where grains are aligned along the fast diffusion direction with different angular standard deviations.

For these calculations I have used equations 11.4 and 11.5 and aligned the fast diffusion direction with the deforming/diffusing direction, chosen to be [001] (i.e. D_c was swapped with D_a in equation equation 11.4 and 11.5). The number of poles as a function ϕ were distributed according to the von Mises-Fisher-distribution for a certain angular standard deviation. These poles are then randomly rotated such that θ is uniformly distributed. These textures are shown in figure 31 for various angular standard deviations. A small angular standard deviation means that the a-axis of most grains is close to the diffusing/deforming [001]-axis ($\phi = 0$); the larger the standard deviation, the more randomly oriented are all grains with respect to the diffusing/deforming direction.

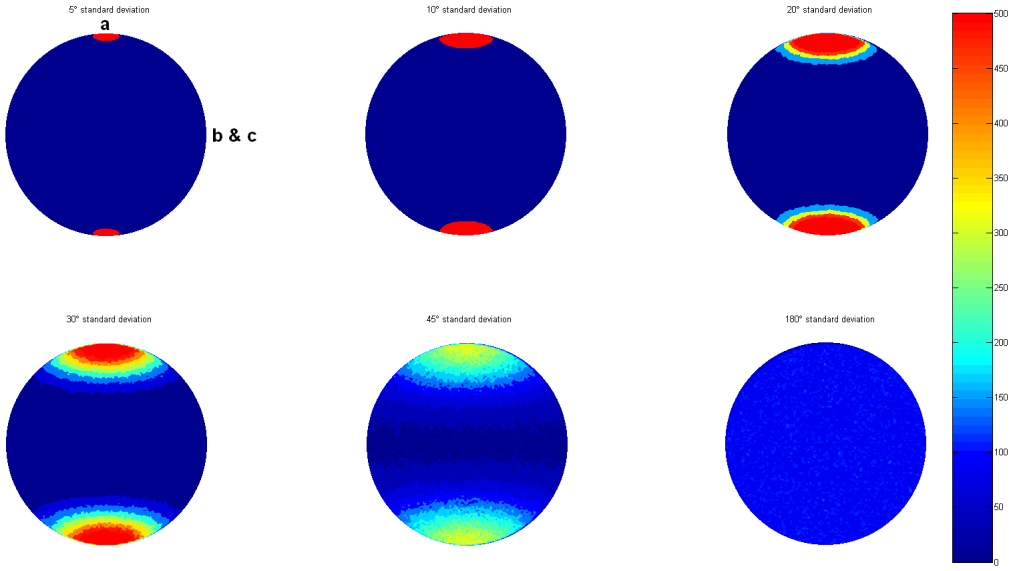

Figure 31: **Polefigures** Lambert projections of the a-axis of post-perovskite textures with different angular standard deviations. Colour code is number of poles per bin, saturating at 500 poles per bin. The resulting average diffusivity and viscosity of these distributions are shown in figure 32

I have calculated the effective diffusivity along [001] for a total number of $N_G = 10^6$ grains of which I then took the average to obtain the mean effective diffusivity along [001] of the post-perovskite aggregate (left hand side panel in Fig 32). I also calculate the effective viscosity of these post-perovskite aggregates if deformed along [001] by taking the Voigt

$$\eta_{eff}^{Voigt} = \frac{1}{N_G} \sum_{i=1}^{N_G} \eta_i \tag{11.8}$$

and Reuss

$$\eta_{eff}^{Reuss} = \frac{1}{N_G} \frac{1}{\sum_{i=1}^{N_G} \frac{1}{\eta_i}} \tag{11.9}$$

averages of the constituting grains of viscosity η_i (centre panel in Fig 32). These calculations show that textureless post-perovskite aggregates are much stiffer than perovskite and their viscosity is close to the one obtained in the cases of the intermediate diffusion (Reuss average) or the slow direction (Voigt average). However, if texture develops, the aggregate weakens by about an order of magnitude while it stiffens in the directions perpendicular to the texture.

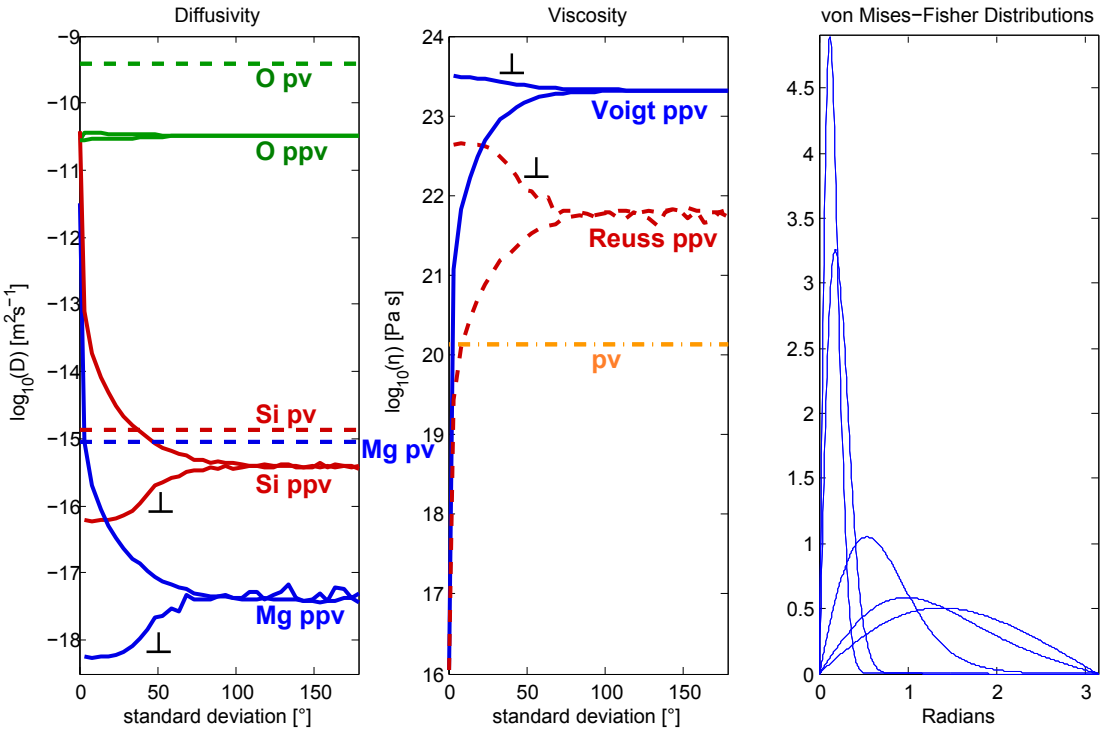

Figure 32: **Diffusivity and viscosity of perovskite and post-perovskite aggregate at 135 GPa**. Left: Change of the effective diffusion rates as a function of angular standard deviations (a smaller standard deviation means stronger a-texture). The lower lines, marked with ⊥, are the diffusivities perpendicular to the texture. Centre: Change of viscosity as a function of angular standard deviations (a-texture, number of vacancies: 10^{-3}, grain size: 1 mm). Post-perovskite aggregate viscosity has been averaged using the Voigt and Reuss averages of the constituting grains. The upper lines, marked with ⊥, are the viscosities perpendicular to the texture. Right: von Mises-Fisher-distributions for different angular standard deviations (values 10°, 15°, 45°, 90° and 180°)

11.3.4. Deformation via Diffusion Creep - Strain Weakening in Post-Perovskite

Let me now discuss the implications of the above calculations for the case of diffusion creep where post-perovskite may exhibit a more complex behaviour than for dislocation creep. Crystals straining via simple shear will deform faster when shear is parallel to the fast diffusing direction (see also below) and slowest when shear is parallel to the slowest direction. These three end-member viscosities are plotted in figure 33 for a similar range of grain sizes and vacancy concentration as in the perovskite field.

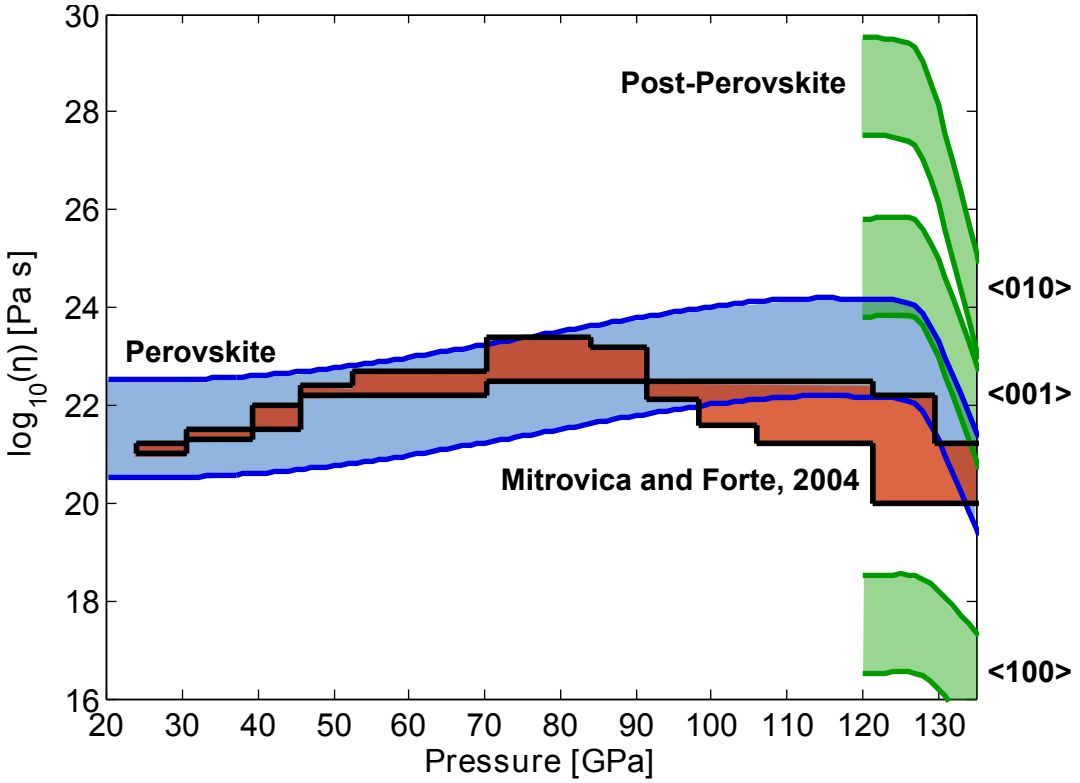

Figure 33: **Calculated viscosity profile, η, of perovskite $MgSiO_3$ deforming by diffusion creep, and end-member viscosities along the crystallographic axes of post-perovskite $MgSiO_3$** Grain size, G, and vacancy concentration, N_v, were varied such that $G^2/N_v = 0.01m^2$ for the lower bounds and 0.1 m^2 for the upper bounds. Vacancy concentrations for both minerals are assumed to be fixed throughout the entire lower mantle. Superimposed are the results from inversion modelling[7]. Except for highly aligned cases, post-perovskite deforming in diffusion creep is stiffer than perovskite as the bulk viscosity falls between the values of the $\langle 010 \rangle$ and $\langle 001 \rangle$ directions

From the previous section it should be clear that these end-member viscosities are never reached in the sense of having a perfectly aligned aggregate, especially not the one of ⟨100⟩. However, the average diffusivity of an aggregate of randomly oriented grains of post-perovskite is close to the intermediate diffusivity along ⟨001⟩ (taking the Reuss average) or even ⟨010⟩ (taking the Voigt average). Thus, invoking only pure lattice diffusion, post-perovskite is between one to three orders of magnitude more viscous than perovskite. This is solely due to the very slow magnesium diffusion along ⟨010⟩ and ⟨001⟩. However, in the presence of texture aligning the fast diffusion direction, post-perovskite can soften by more than an order of magnitude. Assuming that post-perovskite is tracked in the viscosity inversion profile, this finding would strongly suggest that post-perovskite does not deform via diffusion creep as it is too viscous to match the profile. In fact, this stiffness might be the reason why post-perovskite is deforming via dislocation creep since the dislocation creep viscosity would be lower than the diffusion viscosity even for very small stresses. I.e., post-perovskite has a very low transition stress because the activation enthalpy for diffusion creep is the one of the very slow magnesium diffusion along ⟨010⟩, while dislocation creep is activated via the low diffusion enthalpy of the fast diffusion direction ⟨100⟩.

While experiments showed that grain-boundary diffusion is negligible in perovskite, its effect on post-perovskite might be significant. Often, grain-boundary diffusion is about five orders of magnitude faster than lattice diffusion and the grain boundary width is assumed to be about 1 nm e.g.[35]. This makes the grain boundary term in equation 8.4 about four orders of magnitude smaller than the lattice diffusion term. If this is transferable to post-perovskite, and the lattice diffusion is given by the fast diffusion direction, grain-boundary diffusion might play a significant role in the rheology of D″. Lattice diffusion along the fast direction would still be dominant, however, diffusion along the slow directions would occur via grain-boundary diffusion. Grain-boundary diffusion would hence control the viscosity and very likely make post-perovskite weaker than perovskite. Thus, if post-perovskite is also weaker in diffusion creep, it might well be soft enough to avoid the dislocation creep regime completely in D″. Nevertheless, strain weakening would still occur as the fast direction is still faster than the grain boundary diffusion term.

Diffusion creep does, however, not necessarily contradict the observed seismic anisotropy and the assumed underlying cause of LPO. In the hypothetical case of mixed grain-boundary and lattice diffusion creep (Nabarro-Herring-Coble creep, or also pure lattice diffusion creep), I believe that the anisotropic diffusion probably

can still result in the development of a lattice preferred orientation (LPO), either by recrystallisation and grain-boundary reaction[213] or by rotation of grains which are in a high-viscosity orientation to the shear stress (see below). The development of LPO then results in the weak direction aligning with the shear direction and a consequent strain-weakening rheology; in the case of post-perovskite deforming by diffusion creep the strain-weakening is about one order of magnitude. Strain weakening results in shear localisation, implying that the majority of the deforming medium is not affected by the driving stress field, previously developed textures will survive in the non-deforming regions. This means that regions with potentially very different seismic anisotropies could be brought into close proximity. I hypothesise that, given the limited seismic ray coverage of D″, rapid changes in seismic anisotropy associated with shear localisation might be able to generate the rapid changes in seismic wave-speed which are currently interpreted as compositional variations or deformed subducting slab material[29,30].

It is possible that post-perovskite in D″ is deforming entirely within the diffusion creep regime. However, my results show that an isotropic mixture of post-perovskite would be very stiff, something that is inconsistent with geoid modelling and experiments on analogues. It would also be difficult to explain the observed seismic anisotropy with diffusion creep. Diffusion creep may still occur if the grains are rotated such that their fast diffusion directions are parallel to shear. This type of history dependent rheology commonly leads to the development of shear zones, which could also bring regions of different anisotropy into proximity. Regardless, of whether post-perovskite deforms via diffusion creep, or as is more likely, via dislocation creep, the observed sharp D″ reflectors may be interfaces between regions of different anisotropy, and not the phase transition as is commonly assumed.

12. The Iron Spin Transition in Lower Mantle Minerals

Transition metals can undergo a magnetic transition from high-spin to low-spin configurations purely due to an increase of pressure. This change in the electronic structure affects many physical and chemical properties of the ions and its hosting mineral. In fact, the changes can be so strong that the high-spin and low-spin transition metals should be treated as different chemical species. Within the Earth, the only significantly abundant transition metal is iron.

A magnetic transition in a material can either be induced by band widening or by changes in the crystal field[218]. In many transition metal oxide systems, the transition metal suffers a magnetic collapse from high-spin to low-spin because of band broadening with pressure[219], while the crystal field remains largely unchanged. The spin transition is accompanied by an effective reduction of the ionic radius and thereby increases the mineral's density which, in turn, affects its seismic properties.

12.1. Iron Diffusion in MgO: The Effect of the Spin-Transition

Ferro-periclase, (Mg,Fe)O, containing about 15% iron, is the second-most abundant mineral in the Earth's lower mantle (e.g.[220]). A knowledge of its physical properties is thus necessary for a better understanding of the thermochemical evolution of the Earth. It crystallizes in the rock-salt structure even under lower mantle conditions[88,137] and is often regarded as an archetypical oxide.

Complexity was added when a pressure-induced high-to-low-spin transition of iron in ferro-periclase[16] was observed in experiments (around 60 GPa). The subsequent theoretical investigations revealed that the transition is not sharp, but occurs throughout the lower mantle and is not completed at the core-mantle boundary[19,20]. This continuous transition results in a smooth variation of the elastic properties of the material making the change of the spin state difficult to detect with seismic waves. Thus, its geophysical significance remains unclear. The effect of the spin-transition on rheology is currently unknown.

It has been argued, mainly due to the absence of any seismic anisotropy[126], that the lower mantle deforms in diffusion creep, which I consider here. In diffusion creep, the difference between the chemical potentials on the grain surfaces (due to different stresses) leads to the formation and migration of vacancies in the opposite direction of the gradient of the chemical potential (from low to high stresses/potentials). The

deformation, therefore, is controlled by the slowest diffusing species. However, even if deformation occurs via dislocation creep, the deformation controlling step is likely to be dislocation-climb which, again, is rate limited by diffusion.

It has been established from experiments (e.g.[154,155,157,160]) that magnesium diffusion in periclase occurs via simple vacancy diffusion. Oxygen diffusion, on the other hand, is several orders of magnitude slower than magnesium and its diffusion mechanism is not well understood. Anion (oxygen) vacancies are suppressed by extrinsic cation (magnesium) vacancies due to the mass-action law. Thus, it is believed that oxygen diffusion would occur via intrinsic divacancies (bound cation-anion-vacancy pairs). Moreover, oxygen pipe-diffusion appears to have the same activation energy as vacancy diffusion[163,164] adding further complexity to assess the diffusion mechanism of oxygen experimentally. Despite current uncertainty in the diffusion mechanism of oxygen, deformation experiments revealed that the viscosity of periclase deforming in the diffusion creep regime is rate limited by magnesium lattice diffusion and not oxygen diffusion[221,222]. Assuming that this is also the case at elevated pressure, the iron spin transition may have a large effect on the viscosity of ferro-periclase if the diffusion of iron or magnesium on the magnesium sub-lattice changes across the transition. Four points need to be considered:

1. A smaller ionic radius would suggest that the low-spin iron diffuses faster (in a simple elastic strain model)

2. Ions with partially filled 3d-orbitals are affected by the crystal field and experiments suggest that low-spin iron might diffuse much slower than high-spin iron[223]

3. Theoretical models exist for dilute diffusion (less than 1% iron concentration, see below) where correlation effects are controlled by only five different vacancy-jumps inside the crystal (five-frequency model). At the higher iron concentrations expected in the lower mantle (≈15%), correlation effects should be much smaller when nearby iron ions randomise their walks mutually by providing more "special", iron-related jumps to the diffusing vacancy.

4. As well as affecting diffusion rates of iron, the spin-state of iron may also affect the diffusion rates of nearby magnesium ions.

All the above questions need to be clarified in order to understand the effect of the iron spin transition on diffusion and thereby rheology. Diffusion is a poorly understood process in the Earth's lower mantle because its physical conditions are not

(yet) accessible to experimental techniques. Although some diffusion experiments in ferro-periclase have been performed at shallow lower-mantle conditions (below 35 GPa)[11,38,39,153], this is below the spin-transition pressure. I avoid this technical obstacle by using density functional theory (see below for details) that allows me to calculate the diffusion coefficient at lower-mantle conditions from first principles. At the same time I limit this study to the diffusivity of ferrous iron (called only iron hereafter), avoiding the complexity of bound ferric-iron-magnesium-vacancy pairs (or more complex clusters).

Absolute diffusion rates in pure periclase have been calculated previously either by performing molecular dynamics simulations[141,144,159] or by applying harmonic transition state theory[75,139], but none made use of first-principle methods. Nevertheless, all theoretical studies are in good agreement with available experiments. Diffusion of iron in periclase was only considered in one early computational study that used a simple shell model[224] to calculate the migration enthalpy of iron in periclase (NB high-spin), finding it to be lower than of magnesium. Using DFT, I have the caveat that the number of possible jumps that can be investigated is limited due high computational costs, limiting the number of iron concentrations that can be investigated. This caveat can, however, be overcome by using kinetic Monte-Carlo simulations, as described later.

12.1.1. Details of Density Functional Theory Calculations

I have, again, performed density functional theory (DFT) calculations in the general gradient approximation (PAW-GGA[63] with PW91[57] for the exchange correlation functional) with a rotationally invariant Hubbard U (GGA+U) as implemented in the code VASP[61,62]. The iron-potential treats the semi-core p states as valence (14 valence electrons; 3pd7s1), the magnesium-potential has 2 valence electrons (s2p0) the oxygen-potential 6 valence electrons (s2p4). I have used a $3 \times 3 \times 3$ Monkhorst-Pack k-point mesh[60] in the $2 \times 2 \times 2$ supercell (only Γ-point for $3 \times 3 \times 3$ supercells) and a cut-off energy of 1000 eV for the plane-wave basis sets. Compared with denser k-point sampling ($4 \times 4 \times 4$) and higher cut-off energy (1200 eV), my energies are converged to within 0.1%. I relaxed my systems to forces below 10^{-6} eV/Å(for the phonon-calculations).

It is well known that in order to obtain the correct electronic state of iron-bearing systems, one needs to consider the effect of electron-localisation in the d-orbitals of transition metals. One way to do this is to introduce a penalty-energy for the

pairing of electrons (in low-spin), the so-called Hubbard-U, stabilising high-spin states. Although self-consistent methods for choosing U exist ([225]), I have decided to investigate the effect of U on the migration enthalpies and attempt frequencies by varying U systematically. I find that the effect of varying U on migration enthalpies of high-spin iron is no more than a few tenths of an eV (see also figure 37) but can be quite large for low-spin iron (order of eV, see below). The change in migration enthalpy with U also affects the attempt frequency which changes by no more than a (experimentally) negligible factor of two (see tables 29, 28 and 30). The value of U does of course change the spin-transition pressure substantially.

I have investigated a system containing 64 atomic sites ($2 \times 2 \times 2$ cubic supercell; 63 atoms plus one vacancy on a magnesium site) of which one is an iron atom on a magnesium site. The iron concentration in my system thus is $X_{Fe} = 0.03125$. I have also calculated migration enthalpies in a $3 \times 3 \times 3$ supercell (108 atoms, $X_{Fe} = 0.0093$) in order to estimate system-size effects. The migration enthalpy in the larger cell differs by about 10 % from the one in the smaller cell, being smaller at lower pressures and bigger at higher pressures.

12.1.2. Dilute Diffusion: Five-Frequency Model

In the dilute limit, there is a single iron atom embedded in pure periclase. The diffusivity of this single iron atom is described by the well known five-frequency model for FCC crystals, see e.g.[226–228], which involves not only the jump rates of the iron atom but also of neighbouring magnesium ions, as explained in figure 34. Jump rates calculated within harmonic transition state theory[74] are given by

$$W = \tilde{\nu} e^{-\frac{\Delta H}{kT}} \tag{12.1}$$

with the migration enthalpy ΔH, Boltzmann's constant k, temperature T and the attempt frequency $\tilde{\nu}$. The dominant contribution to the jump rate is the migration enthalpy ΔH, which is the height of the energy-barrier (a saddle-point) an ion has to overcome to jump into the nearby vacancy. The attempt frequency $\tilde{\nu}$ is usually of the order of 10 THz and comprises entropy effects (migration entropy) and how often the ion tries to jump over energy barrier.

In the five-frequency model, the following five jump rates (jump frequencies) are required (see figure 34): W_0 is the jump rate in the pure crystal. W_1 is the jump rate where the vacancy remains on an impurity-neighbouring site (non-dissociating). W_2 is the exchange-rate of the vacancy with the impurity. W_3 is the rate away from

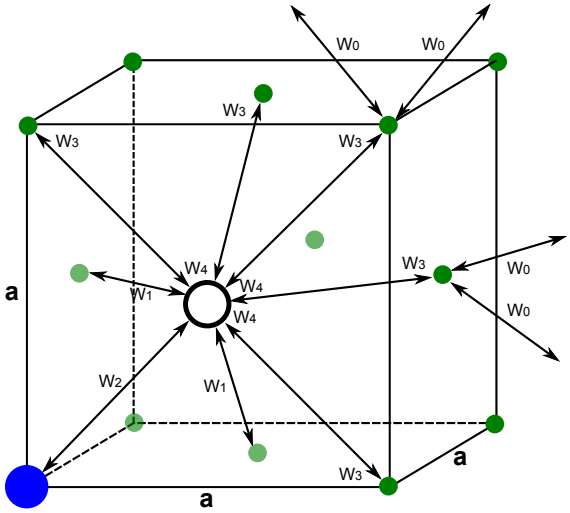

Figure 34: Jump rates W_i of a vacancy (empty circle) neighbouring an impurity (solute atom; large, filled, blue cycle) in an FCC crystal of cell-length a. W_0 is the jump rate in the pure crystal. W_1 is the jump rate where the vacancy remains on an impurity-neighbouring site (non-dissociating). W_2 is the exchange-rate of the vacancy with the impurity. W_3 is the rate away from the impurity (dissociating), W_4 is towards the impurity (associating).

the impurity (dissociating), W_4 is towards the impurity (associating). In the dilute limit, the diffusivity of the impurity is then given as:

$$D_{Fe} = a^2 \cdot f \cdot W_2 \frac{W_4}{W_3} \tag{12.2}$$

where a is the cell length, and f is the correlation factor given by:

$$f = \frac{W_1 + \frac{7}{2}FW_3}{W_2 + W_1 + \frac{7}{2}FW_3} \tag{12.3}$$

and F is the escape probability

$$F = 1 - \frac{1}{7}\frac{10x^4 + 180.5x^3 + 927x^2 + 1341x}{2x^4 + 40.2x^3 + 254x^2 + 597x + 436} \tag{12.4}$$

with $x = \frac{W_4}{W_0}$.

I have calculated all five frequencies within the harmonic transition state theory and their parameters are given in tables 28, 29 and 30. Parameters for magnesium diffusion in pure periclase, W_0, are given in table 31.

12.1.3. The Effect of the Hubbard U

The Hubbard U affects the spin-transition pressure of iron as it stabilises high-spin states by adding a penalty energy to low-spin states. Thus spin-transition pressures increase strongly with an increasing value of U. For diffusion one has to consider four different spin transitions: 1) spin transition of iron far from a vacancy, 2) spin transitions of iron near a vacancy, 3) spin transitions during iron jumps, and 4) spin transitions of iron during magnesium jumps.

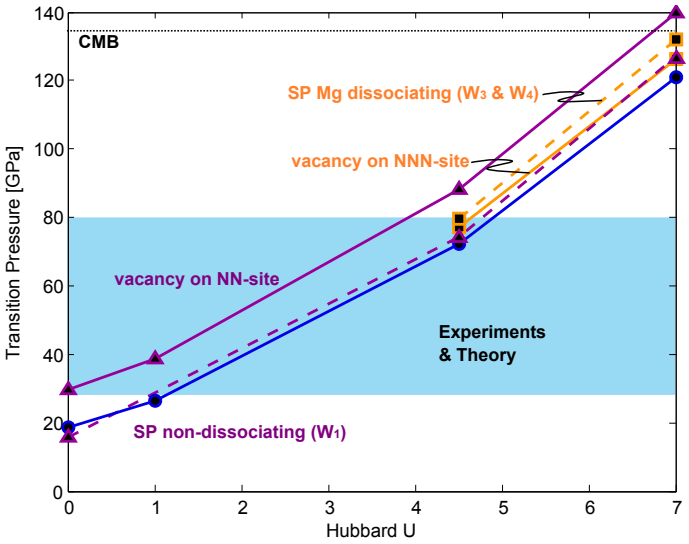

Figure 35: Transition pressures as a function of the Hubbard U. For perfect ferro-periclase (with one iron atom on a magnesium site; solid line, blue circles), defective ferro-periclase (one iron with a vacancy on the nearest neighbour(NN)-site (solid line, violet triangles), and on the next-nearest neighbour(NNN)-site (solid line, orange square)). Transition pressures of the various saddle-points are connected with dashed lines: magnesium jumps between NN-sites of iron (violet squares, dashed lines, W_1) and magnesium migration away/towards the iron (orange squares, dashed lines, W_3 and W_4). Blue shaded area shows the range of the experimental and previous theoretical transition pressures[17–21,24,229–231]. Black dotted line marks the core-mantle boundary (CMB)

Spin-Transitions in Iron far from Vacancies The perfect crystal (periclase containing no vacancies and one iron atom on a magnesium site ($X_{Fe} = 0.03125$); table 26) has the lowest transition-pressure (solid blue line in Figure 2). A value of U of about 3 gives best agreement with the experimental spin-transition pressure (e.g.[16]).

Spin Transitions in Iron with nearby Vacancies Introducing a vacancy on a nearest-neighbour (NN) site to the iron, increases the spin-transition pressure by about 10 GPa (solid violet line; table 27). The vacancy has effectively reduced the local pressure on the iron, thereby allowing the high-spin state to persist to higher pressures than in the vacancy free system. A vacancy on a next-nearest-neighbour (NNN) site to the iron atom increases the transition pressure less (by about 5 GPa - orange solid line; table 27). The effect of the spin transition on diffusion should, therefore, occur at higher pressures than its effect on elasticity (the perfect crystal).

Spin Transitions Occurring during Iron Jumps As the spin-state of iron is not a fixed quantity, its spin can change during a jump. I find that regardless of its initial spin, iron becomes high-spin at the saddle-point (the transition pressure at the saddle-point is around 245 GPa for $U = 0$ and above 400 GPa for $U = 7$). A low-spin iron will, therefore, change to high-spin during the jump, and return to low-spin as the jump completes. Only at extreme pressures, such as could be found in Super-Earths, does low-spin iron at the saddle-point become energetically more favourable than the high-spin, allowing iron to remain low-spin throughout the jump. The fact that high- and low-spin iron go through the same high-spin saddle-point, means that the difference in their migration enthalpy depends only on the energy of their initial state. This leads to the interesting result that low-spin iron in the high-spin regime will have a lower migration enthalpy - and therefore diffuse faster - than the coexisting high-spin iron (see figure 36), and vice versa: high-spin iron in the low-spin regime will diffuse faster than the coexisting low-spin iron. As the pressure approaches the spin-transition pressure of iron in its initial position (i.e. before beginning the jump), the diffusion rates of the two spin states become the same. If one ignores the fact that the spin state at the saddle-point changes, I would erroneously predict that low-spin iron would diffuse very slowly (see figure 37).

Spin transitions during magnesium jumps Another interesting result is that the spin-state of iron can change during nearby magnesium jumps. This, again, can be understood in terms of the local atomic pressure. The pressure depends on the particular jump and on how far away the iron is from the jumping magnesium, see figure 35. As the magnesium jumps between NN-sites (W_1) to the iron, the local pressure is highest when the magnesium is on the saddle-point. The spin-transition pressure of this configuration is, in fact, at a similar pressure as for the vacancy-free

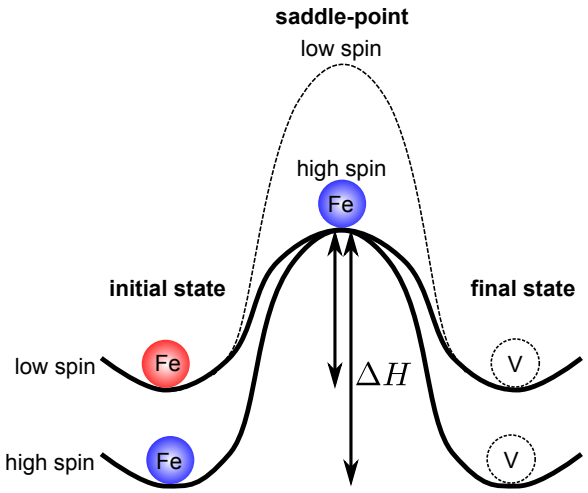

Figure 36: Migration barriers for high- and low-spin iron hops at low pressures (high-spin regime). Iron hops into a nearby vacancy by overcoming an energy barrier of height ΔH. During migration, low-spin iron will swap to high-spin which drastically reduces the height of the energy barrier as its initial state is already at an elevated energy.

system such that above this pressure high-spin iron is forced into low-spin during magnesium jumps between NN-sites. For the dissociating and associating jumps (W_3 and W_4) between the NN- and NNN-sites, the transition pressure is approximately half-way between those of the NN- and the NNN-site. This can be interpreted as a continuous increase of the local atomic pressure when a magnesium jumps into a vacancy on the NN-site from a NNN-site.

In analogy with the iron jumps, magnesium diffusion is accelerated by the presence of minority-spin iron. In other words, at high pressure when iron is mostly in the low-spin state, magnesium jumps in the vicinity of an iron which is in the high-spin state will have a lower migration enthalpy. This is because they start off with a higher energy of the initial state than magnesium near a low-spin iron. Similarly, magnesium jumps nearby low-spin iron in the high-spin regime (below the transition-pressure of the concerning jumps and states) will also encounter a lower migration enthalpy (see figure 37).

It is interesting to note that magnesium jumps during which the spin-state of the neighbouring iron remains constant are similar to those in pure periclase (see figure 37). However, high-spin jumps are slightly slower (higher migration enthalpy) than magnesium jumps in pure periclase, while low-spin jumps are slightly faster (lower migration enthalpies). Thus, magnesium is slowed down in the high-spin regime and accelerated in the low-spin regime. This change in diffusivity from the jump-rates

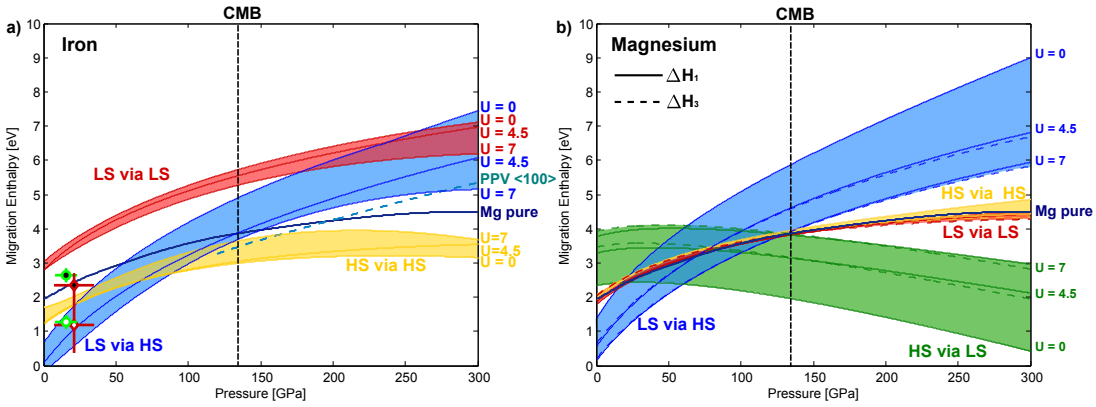

Figure 37: Comparison of migration enthalpies and the effect of a varying Hubbard U. As a reference in both panels I also show the migration enthalpy of magnesium in pure periclase. The vertical dashed line marks the core-mantle boundary (CMB). During migration, the spin-state of the iron can change (from high to low (HS via LS) or from low to high (LS via HS)) or remain the same (HS via HS and LS via LS). a) migration enthalpies of high- and low-spin iron (HS and LS respectively). Both iron species will preferably be in the high-spin state during migration. The dashed line is the migration enthalpy of magnesium in $MgSiO_3$-post-perovskite along the fast diffusion direction ($\langle 100 \rangle$). Also shown are the experimental values from[11] (red diamonds; filled: magnesium, empty: iron) and[39] (green circles; filled: magnesium, empty: iron). b) Magnesium migration enthalpies in the vicinity of a high- or low-spin iron (migration enthalpies of W_4 is not shown for clarity, but would be very similar to W_3)

in the vicinity of an iron is, however, no more than a factor of two.

All the above adds considerable complexity to the diffusion process. For instance, not only can the spin-state on a nearby iron change temporarily while a magnesium hops, it can also change the spin state 'permanently' if the magnesium jump results in it being nearer or farther away from the iron. All these possibilities have to be included in the bulk diffusion computation.

12.1.4. Diffusion at Elevated Iron Concentrations: Kinetic Monte Carlo

While the diffusion rate from single-hop mechanisms (vacancy and interstitial) may be calculated using Vineyard-theory, it is more difficult to obtain in the presence of impurities when vacancies have several jump options, each having a different rate. The problem is to determine how the overall system evolves diffusion-wise when different atoms have different jump rates while competing for the same vacancy. A way to solve these problems is to use kinetic Monte-Carlo simulations (see, e.g.,[97]'s

review).

The advantage of this method is that it removes the time-scale problem between lattice/atomic vibrations and the jump rates that one encounters in molecular dynamics simulations. Jump rates are several orders of magnitude slower than atomic vibrations and are thus extremely rare. Kinetic Monte-Carlo simulations allow the separation of these two movements by only considering the slow jump rates between various states.

I used a $3 \times 3 \times 3$ supercell containing 108 magnesium lattice sites with periodic boundary conditions. One site is occupied with a vacancy which is the jumping particle in the simulation. The remaining 107 lattice sites are either occupied by a magnesium or an iron on randomly chosen sites (depending on the iron concentration). The diffusivity of the vacancy, magnesium and iron is then calculated using the Einstein-Smoluchowski relation

$$D = \frac{\langle R^2 \rangle}{6\tau} \tag{12.5}$$

where $\langle R^2 \rangle$ denotes the mean-square displacement and τ the time passed. The pointy brackets denote the average over a large number of particles. In my case, I performed 10^4 simulations each running for 10^4 jumps. This setting yields precise (small standard deviations) diffusivities for magnesium and iron diffusion (increasing precision with increasing iron-concentration), but results in fairly large standard deviations on the vacancy diffusivity (see below).

I use again the jump rates from the five-frequency model. These five jump-frequencies can be used to create a simple model of diffusion in ferro-periclase at any iron concentration. In doing so, I assume that jump rates are unaffected by the number of iron atoms in the vicinity. For simplicity, I also assume that the jump rate is equal to W_1 if there is at least one iron on a nearest neighbour site to the vacancy before and after the jump. The probabilities of how many iron atoms are surrounding a vacancy after each jump are shown in figure 38: After around 35 % iron a vacany will have at least one iron atom as a nearest neighbour and all magnesium jump-rates become W_1. Finally, in my KMC simluations all iron is either high- or low-spin, there is no thermally induced mixed-spin regime.

There are a couple of known solutions of the diffusion-problem in my model that can be used to benchmark my KMC simulation. At low iron concentrations (dilute), magnesium will diffuse at the pure periclase diffusivity (D_{MgO}) and iron diffusivity is described by the five-frequency model (D_{Fe}^{dilute}). At high iron concentrations, I

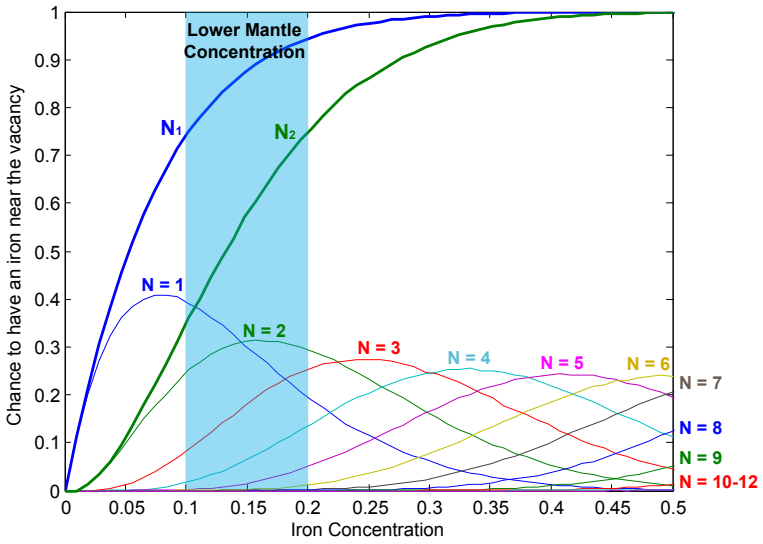

Figure 38: The chance of a vacancy to be next to at least one iron after a diffusing jump as a function of the iron concentration (bold line, N_1; at least two iron N_2). Also shown are the chances of the vacancy to be surrounded by a certain number (N) of iron atoms.

will end up with dilute magnesium diffusion (D_{Mg}^{dilute}) and iron diffuses with the iron jump-rate W_2 (D_{FeO}). For the vacancy diffusion, one expects

$$D_V(X_{Fe}) = \frac{1}{f}(X_{Fe}D_{Fe}(X_{Fe}) + (1 - X_{Fe})D_{Mg}(X_{Fe})) \tag{12.6}$$

where $f = 0.7815$ is the correlation factor of the FCC-lattice and D_{Fe} and D_{Mg} are the diffusivities of iron and magnesium respectively (see below). In all cases, my KMC simulations reproduce the analytical solutions for magnesium, vacancy and iron diffusion. Moreover, as is shown below, my results are in good agreement with the available experimental data that contain up to 20% iron.

The Effect of the Iron Concentration I have investigated the effect of iron concentration by performing KMC-simulations at three different pressure and temperature conditions along the geotherm, corresponding to different spin states of iron. The results are shown in figure 39. Generally, one sees that the more iron there is, the more it will affect the vacancy diffusion by creating an iron-network that either allows fast vacancy-hopping (high-spin) or reduces the number of possible (fast) jumps (low-spin; see figure 39).

The effect of iron on magnesium diffusion is strongest at low iron concentrations, where many magnesium atoms are affected by the presence of each additional iron

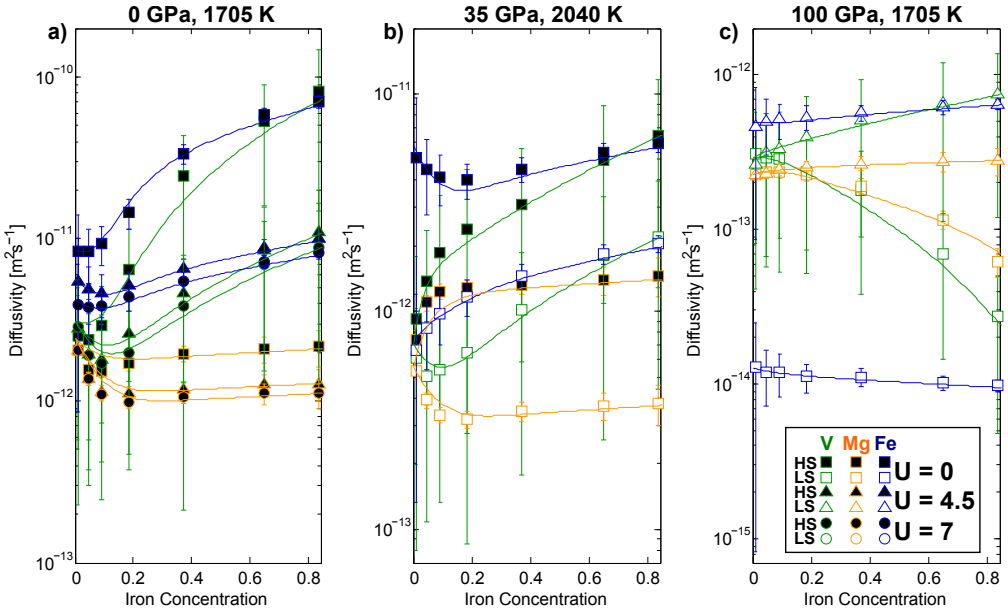

Figure 39: Iron-concentration dependence of the diffusivities ($N_v = 1$) in ferropericlase as calculated from KMC (vacancy: V, magnesium: Mg, iron: Fe, high- and low-spin: HS, LS). Thin lines mark the empirical fit (see supplementary data). a) High-spin iron diffusivity increases with increasing iron concentration (at 0 GPa on the geotherm). b) diffusion of high-spin iron $\approx$ 6 GPa above the spin-transition (at 35 GPa) increases initially because of the change in rates of magnesium jumps (see text for details; all iron atoms are assumed to be high-spin). For low-spin iron at the same conditions, overall diffusivity is lower and the picture is similar to the one in a). c) Low-spin iron diffusivity decreases with increasing iron concentration for U = 0. Magnesium diffusion is increasingly hindered by the slow iron when iron concentration is increased (at 100 GPa on the geotherm). For U = 4.5, the picture is again similar to the one in a).

atom. Any effect of iron on the magnesium diffusion will therefore be dominated by the probability of how often the vacancy neighbours at least one iron atom after each jump (N_1 in figure 38). This effect is seen in the initial dip in the magnesium diffusivity in the 0 GPa case and the strong increase in the 35 GPa high-spin case shown in figure 39. This change is because the average magnesium jump rates will quickly approach W_1 with increasing iron concentrations up to the threshold, 35% iron, after which all magnesium hops will be W_1. I have developed a model which approximates the KMC values using the five-frequency diffusivities (see section 12.1.4 below) and use this to interpolate between the KMC points.

Let us now have a closer look at the specific KMC simulations. In the high-spin case (figure 39 a)), where iron has a higher diffusion rate, an increase of the

iron concentration results in an increase of its diffusivity. Having a slightly higher jump-rate than magnesium, its chance of jumping back to its initial position (after having swapped sites with a vacancy) is increased compared with a magnesium, i.e. correlation effects prevent it from being faster at low iron concentrations. At elevated iron concentrations, the vacancy can migrate via the fast iron-network resulting in a fast iron and vacancy diffusion. At the same time, the magnesium diffusivity decreases initially, because the jump rates in the vicinity of a high-spin iron are slightly lower than in pure periclase.

At pressures just above the spin-transition, magnesium jump rates around the minority species are increased (as discussed above). At elevated iron concentrations, this increase accelerates magnesium diffusion (see figure 39, b)). Such an increased diffusion rate of magnesium could weaken the material by a factor of two to three. However, in reality, less than 50% of all iron atoms can be high-spin after the spin-transition which will inevitably reduce this acceleration. More precisely, at the upper end of the lower-mantle iron concentration estimates (20% iron), even if only a quarter of the iron remains in high-spin, they could still largely affect the magnesium diffusion in the entire crystal as every second jump could be accelerated (see figure 38). At the lower end (10%), however, if one quarter would still be high-spin, there would be almost no effect on the overall magnesium diffusion, as only about every tenth jump could be accelerated

In the low-spin case (once its jump rate is smaller than that of magnesium) (see figure 39, c)), magnesium will jump into the nearby vacancy most of the time because it is faster. At the same time, if a low-spin iron jumped into the vacancy, the chances of jumping back are reduced as the vacancy is most likely carried away from the iron via magnesium jumps (reducing correlation). Thus, in the dilute limit, the reduced correlation makes iron slightly faster than when it were diffusing in FeO (at a jump rate W_2). At iron concentrations as expected in the lower mantle ($\approx$ 15 %) the slow low-spin iron diffusion has a negligible effect on the vacancy and magnesium diffusion.

However, I note that increasing the iron-concentration up to 20 % (the maximum expected in the lower mantle) will change the diffusivities by no more than a factor of two compared with the dilute limit - for any spin-state of iron.

The dependence of the vacancy concentration on the iron content[153] has not been included in these models resulting in a potential further increase in diffusivity not accounted for here. However, the suppression of iron-related vacancies with increasing pressure[232] means that this is unlikely to be significant in the lower mantle..

Empirical Fit to the Iron Concentration Dependence of Diffusion in Ferro-Periclase I here discuss briefly my empirical model with which I fit the iron-concentration dependence of diffusion in my KMC simulations. This will provide a simple mathematical model allowing one to calculate the diffusivity at any iron concentration based on the jump rates used in the five-frequency model.

First, as discussed above, there are a couple of known solutions of the diffusion-problem in my model that can be used to benchmark my KMC simulation and which are end-member diffusivities my model will have to satisfy. At low iron concentrations ($X_{Fe} \approx 0$; dilute), magnesium will diffuse at the pure periclase diffusivity (D_{MgO}) and iron diffusivity is described by the five-frequency model (D_{Fe}^{dilute}). At high iron concentrations ($X_{Fe} \approx 1$), one will end up with dilute magnesium diffusion (D_{Mg}^{dilute}) and iron diffuses with the iron jump-rate W_2 (D_{FeO}). For the vacancy diffusion, one expects

$$D_V(X_{Fe}) = \frac{1}{f}(X_{Fe}D_{Fe}(X_{Fe}) + (1 - X_{Fe})D_{Mg}(X_{Fe})) \tag{12.7}$$

where $f = 0.7815$ is the correlation factor of the FCC-lattice, where X_{Fe} is the iron concentration and D_{Fe} and D_{Mg} are the diffusivities of iron and magnesium respectively (see below).

Second, I introduce an intermediate regime which accounts for the fact that magnesium jumps rapidly saturate at W_1 with increasing iron concentration. As one iron near a vacancy is enough to affect the magnesium jump rates and once the vacancy is neighbouring an iron after each jump, all magnesium jumps will be W_1. This will affect the magnesium and iron diffusion. The iron concentration dependence at low iron concentrations thus follows N_1 with a threshold around 35% iron (see figure 38). This contribution is seen in the initial dip in the magnesium diffusivity in the 0 GPa case and the strong increase in the 35 GPa high-spin case shown in figure 39. With increasing iron concentration, the iron jump rate W_2 becomes more important for the entire system. Iron diffusion, will always have one iron on a nearest neighbour site to the vacancy (!) and one requires at least two iron atoms around the vacancy to diffuse the vacancy on the forming iron-network. Its iron-concentration dependence will thus follow N_2 and the iron-concentration X_{Fe} itself.

Third, with the above diffusivities and the chances of a vacancy to be neighbouring one or two iron after each jump, N_1 and N_2 of figure 38, I can now construct my model. The iron-concentration dependence of magnesium diffusion in my system

can now be approximated by using the following equation:

$$D_{Mg}(X_{Fe}) \approx (1 - N_1(X_{Fe}))D_{MgO} + (N_1(X_{Fe}) - X_{Fe} \cdot N_2(X_{Fe}))D_{MgO}^{W_1} + X_{Fe} \cdot N_2(X_{Fe})D_{Mg}^{dilute} \quad (12.8)$$

where X_{Fe} is the iron concentration and $D_{MgO}^{W_1}$ is the magnesium diffusivity with magnesium jump rates in pure periclase given by W_1.

In analogy, the iron-concentration dependence of iron diffusion can be described by:

$$D_{Fe}(X_{Fe}) \approx (1 - N_1(X_{Fe}))D_{Fe}^{dilute} + (N_1(X_{Fe}) - X_{Fe} \cdot N_2(X))D_{Fe}^{diluteW1} + X_{Fe} \cdot N_2(X_{Fe})D_{FeO} \quad (12.9)$$

where X_{Fe} is the iron concentration and $D_{Fe}^{diluteW1}$ is the dilute diffusivity of iron with all magnesium jump rates being W_1 which accounts for the fact that initially magnesium jumps rapidly approach W_1 with increasing iron concentration.

Thus, using six different diffusivities that can be extracted from the five-frequency model I can model the iron concentration dependence of diffusion (as it results from my KMC simulations) using equations (12.7), (12.8) and (12.9). As shown in figure 39, my empirical model (thin lines) nicely reproduces the KMC simulations at any iron concentration.

Comparison with Experiments I compare my calculated diffusion rates with experiments[11,39,153] in figure 40. All experiments measured iron-magnesium inter-diffusion, which is given by (Nernst-Planck):

$$\tilde{D} = \frac{D_{Mg}D_{Fe}}{(1 - X_{Fe})D_{Mg} + X_{Fe}D_{Fe}} \quad (12.10)$$

Here, D_{Fe} is given by my KMC model (at the appropriate experimental iron concentration) and D_{Mg} is the magnesium diffusivity in pure periclase. Clearly, all these experiments have been performed at 'low' pressure (below 35 GPa) in the high-spin regime. The slow diffusivity in the highest pressure experiment (see figure 40 b)) might be due to the reduction in the vacancy concentration with pressure[232]. While my migration enthalpies and activation volumes are in excellent agreement with the experiments, I require slightly high extrinsic vacancy concentrations to match the data. The experimentally observed dependence of diffusion on iron-concentration

at 0GPa from[153] agrees well with my simulation after correcting for the vacancy-concentration dependence ($N_v \propto X^0.73$). The good agreement with experiments, as well as the one in my previous results for pure periclase (section 9), provides confidence for my results of the absolute diffusion rate in the low-spin iron case, for which no experimental diffusion data exist.

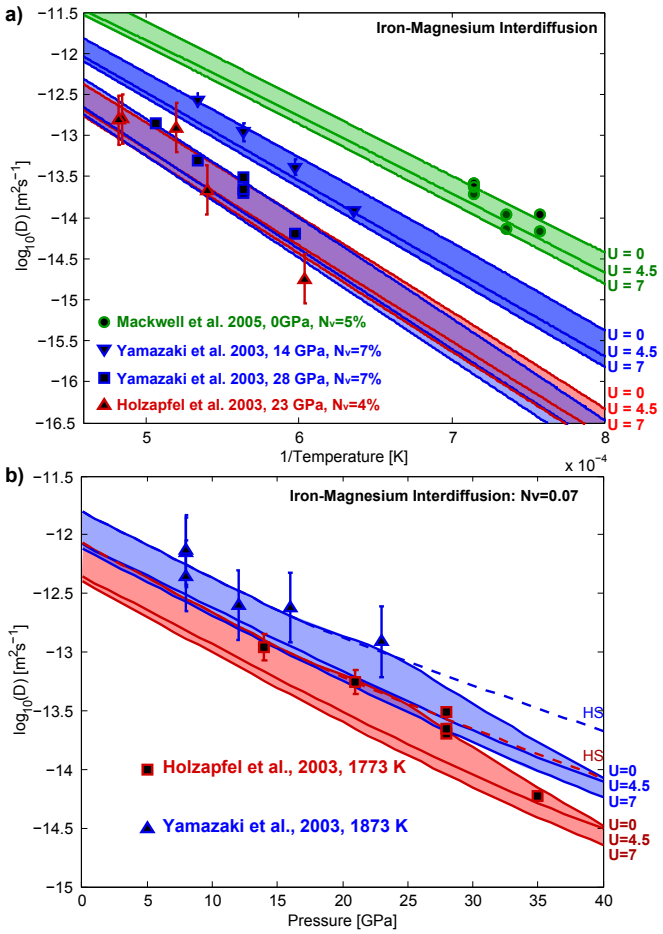

Figure 40: Comparison of my calculated diffusion rates with Fe-Mg-interdiffusion experiments at various pressures and temperatures (see text for details). a) Temperature dependence of inter-diffusion rates. Vacancies are assumed to be extrinsic with concentrations N_v between 4% and 7% and were chosen to match the experimental data with iron concentrations of $X_{Fe} = 0.2$[11,39] and $X_{Fe} = 0.05$[153]. The vacancy concentration in[39]'s experiments (at 23 GPa) appears to be reduced compared with the experiments of[11](at 28 GPa). b) Pressure dependence of the interdiffusion rates. The reduction of the diffusion-rate for U = 0 is due to the spin-transition. The dashed lines mark the diffusion rate if iron remained in high-spin (HS)

12.1.5. Diffusion in the Lower Mantle and the Spin-Transition

Figure 41 shows the calculated diffusion rates in the dilute limit (five-frequency model; lower bounds of curves) as well as according to my KMC model (with iron concentration of 20%; upper bound of curves) in the Earth's lower mantle along a geotherm[98], including magnesium in pure periclase. Clearly, the iron-concentration has a negligible effect on the diffusion rate of iron. Throughout the lower mantle, high-spin iron is faster than magnesium, independent of the value of U.

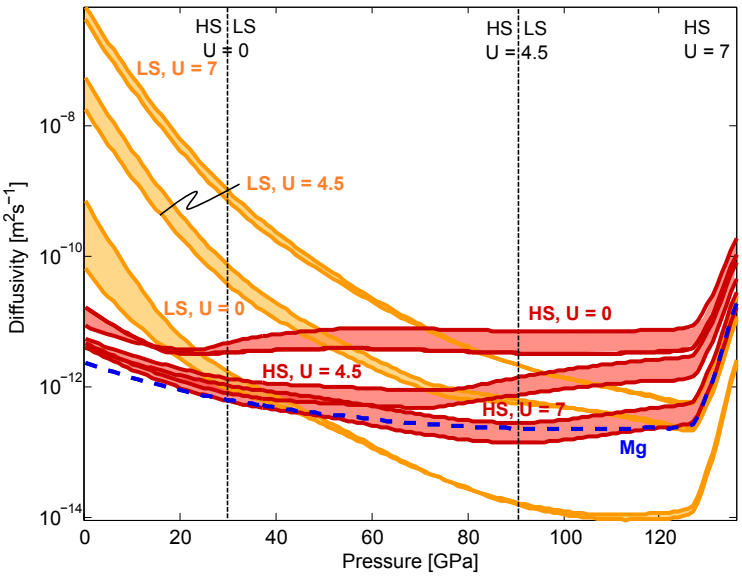

Figure 41: Diffusivities ($N_v = 1$) along a geotherm[98] of high- and low-spin (HS, LS) iron in the dilute limit (lower bound) and according to my empirical fit model (at 20 % iron concentration, upper bound) for various U (solid) and magnesium in pure periclase (dashed). Also shown are the transition pressures (with a vacancy neighbouring an iron atom) for the relevant values of U. The high diffusivities of low-spin iron before the transition will only have a diminishing contribution to the total iron diffusion, as the number of low-spin iron is very small.

Low-spin iron diffusion, in contrast, depends strongly on the chosen value of the Hubbard U. This is because its migration enthalpy has an increased activation volume from the increase of the energy difference between the high- and low-spin ground state, which is strongly dependent on U (figures 35 and 37. In the lower mantle, one will only see an effect of the spin transition for low values of U (i.e., 0), because only in these cases the migration enthalpy becomes bigger than the one of magnesium. However, for a value of U that matches approximately the experimental transition pressure (U = 4.5), even low-spin iron would be faster than magnesium up to the

core-mantle boundary. In Super-Earth's, however, the increase of the migration enthalpy will eventually slow down iron diffusion and make it the slowest species independent of the value of Hubbard U.

12.1.6. Implications for the Rheology of the Lower Mantle

The rheological significance of ferro-periclase will depend on whether it forms an interconnected network or of it remains in isolated grains, leaving the $MgSiO_3$-perovskite (only perovskite hereafter) grains load-bearing. The two resulting end-member (after[130]) diffusion-creep viscosities of the ferro-periclase-perovskite aggregate are shown in figure 42. The absolute value of the viscosity is strongly subject to the total number of magnesium vacancies which is unknown. An order of magnitude more magnesium vacancies in ferro-periclase will result in a viscosity an order of magnitude lower. My chosen magnesium vacancy concentration is consistent with experimental diffusion rates resulting in ferro-periclase being three orders of magnitudes weaker than perovskite in the shallow lower mantle[131,233] (vacancy concentration in perovskite has been chosen to match the inverted viscosity profiles (e.g.[4,7]). The magnesium vacancy concentration in ferro-periclase is then kept constant throughout the lower mantle. It is interesting to note that the relative viscosity of ferro-periclase and perovskite is almost constant throughout the lower mantle (as they have a similar activation volume). At this point it is also important to note, that, while the presence of ferric iron (Fe^{3+}) would increase the number of extrinsic vacancies, it will also reduce the availability of magnesium-vacancies to the other species as it binds the magnesium vacancies (as is the case for aluminium[234]).

My results apply to deformation of ferro-periclase at high temperatures where deformation will be controlled by diffusion, be it deforming in diffusion-creep or dislocation-climb. As discussed above, there are three reasons why the spin-transition leads to a weakening by an increased magnesium diffusion. First, the transition pressure of iron is lower during magnesium jumps which initiates the weakening: magnesium near a high-spin iron will force it into low-spin during migration. Secondly, after the spin transition, viscosity is controlled by magnesium hops that do not affect the spin-state during the jumps which are slightly faster around low-spin than around high-spin iron. This will be the final viscosity once the spin transition is completed. Thirdly, at pressures just above the spin transition of the ground state, there will be still some high-spin iron around in the lower mantle. Around these high-spin iron atoms, the magnesium diffusion is increased as discussed previously

(see figure 37 right, HS via LS; and figure 39, b)). This might enhance a weakening of ferro-periclase in a small region after the spin-transition (depending on the width of the spin-transition; on the other side of the ground-state spin-transition, this would only happen if the spin-transition would be very broad because the spin-transition of the saddle-point lies well below that of the ground-state). However, this weakening is no more than a factor of two and decreases with decreasing iron concentration. Tentatively, one could then interpret the derived reduction in the radial profile of the Q-factor[1] around 50 GPa as a result of the weakening of ferro-periclase due to the spin-transition (assuming the weaker phase is responsible for seismic attenuation).

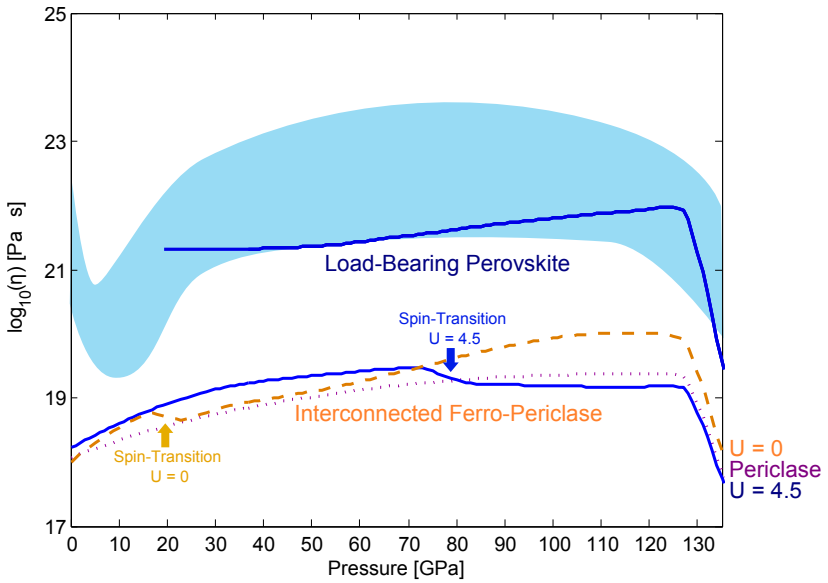

Figure 42: Comparison of diffusion creep viscosities along a geotherm ([98]) with the results from inversion modelling (light blue area; e.g.[2,4,7,8,235,236]). Parameters for ferro-periclase are either a grain size of $G = 1\ mm$ and a vacancy concentration of $N_v = 10^{-3}$ or a grain size of $G = 0.1\ mm$ and a vacancy concentration of $N_v = 10^{-5}$ (see text for details). The viscosity profile of perovskite is the same as in section 10. Vacancy concentrations for both minerals were assumed to be fixed throughout the entire lower mantle. Dashed (U = 0) and solid (U = 4.5) lines are the lower bounds where ferro-periclase forms an interconnected network, for the upper bound perovskite is the load-bearing phase of the two phase system[130] (20% ferro-periclase, containing 20% or 0% (dotted line) iron, 80% perovskite). The small kinks, just after 20 GPa (U = 0) and around 75 GPa (U=4.5) are a viscosity reduction due to the spin-transitions as indicated with arrows (initial kink: transition at th the W_1 saddle-point, final kink transition of the ground-state with vacancy on nearest neighbour site to iron).

Overall, I find that the effect of the spin transition of iron on the lower-mantle rheology is negligible for both end-member viscosities (connected or isolated). The slight increase of the magnesium diffusion near low-spin iron could lead to a weakening of ferro-periclase. As evident from figure 42, it is unlikely for ferro-periclase to form an interconnected network throughout the lower mantle, as the resulting viscosity would be too low compared with the inversion-model. The spin-transition, however, could have an effect on the viscosity of ferro-periclase in Super-Earths, where pressures readily exceed that expected at the core-mantle boundary. There, low-spin iron will eventually become the rate-limiting species leading to a stiffening of ferro-periclase.

At this point, one can only speculate on the role of soft ferro-periclase in the Earth's mantle. Recent experiments and theoretical results showed that ferro-periclase forms isolated grains in a perovskite matrix in a pyrolitic bulk composition under static or low-strain rate conditions[125,131,233]. However, the lower-mantle ferro-periclase-perovskite aggregate is close to the percolation threshold and could become interconnected when strained. This would lead to a history-dependent rheology and the generation of shear-zones. Strongly strained regions could readily decouple from non-strained regions and the localisation of strain would result in narrow, anisotropic bands that are hard to detect seismically, perhaps explaining the seismic homogeneity of the lower mantle despite the presence of slabs and plumes. In regions with high strain such as around slabs and plumes, interconnected ferro-periclase could control the local viscosity and lead to a weakening of plumes and slabs. In a downwelling slab, this might lead to the formation of texture by phase-separation, which might explain the observation of anisotropy near subducted slabs in the shallow lower mantle[237], despite deforming in diffusion creep[126]. In plumes, on the other hand, weakening by the interconnected ferro-periclase network could localise flow to narrow plume conduits which might explain why they are hard to detect seismically in the mid-lower mantle (e.g.[238]).

Comparing the relative viscosities of $MgSiO_3$-post-perovskite and ferro-periclase is not straight forward, as I do not know enough about the physical and chemical conditions in D″. My calculations reveal that the migration enthalpy of low-spin ferrous iron in ferro-periclase is always larger than the one of the rate limiting species, magnesium, in post-perovskite along the fast diffusion direction ⟨100⟩ (see figure 37), even in Super-Earths. At the same time, their activation volumes are similar. Given the same vacancy concentration low-spin iron and magnesium diffusion in ferro-periclase is slightly faster than magnesium diffusion along the fast direction

in post-perovskite at temperature higher than 2100 K (for U = 4.5 at 125 GPa). However, for U = 0, magnesium diffusion in post-perovskite is considerably faster than low-spin iron diffusion in ferro-periclase up to temperatures of 6000 K at 125 GPa. This opens up the interesting possibility that ferro-periclase might not be the weakest phase in D″ or deep in Super-Earths (see figure 43).

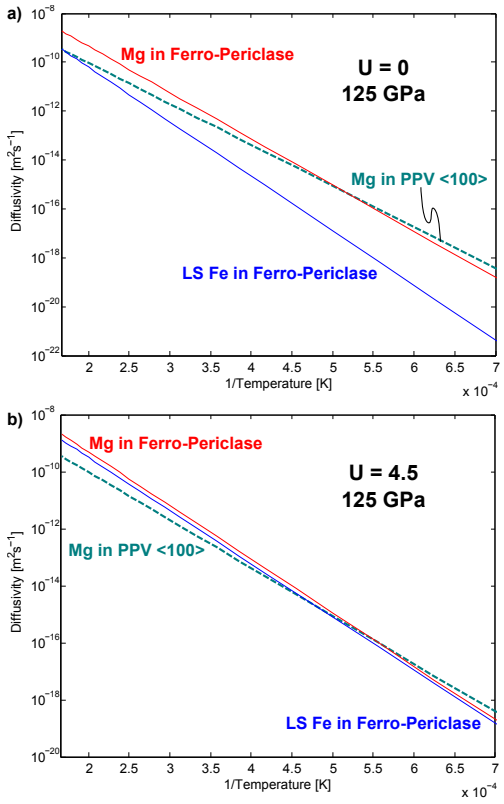

Figure 43: Comparison of diffusivities of magnesium (solid red) and low-spin iron (solid blue) in ferro-periclase with magnesium diffusion along the fast direction ($\langle 100 \rangle$) in $MgSiO_3$ post-perovskite (dashed) at 125 GPa. a) U = 0: Low-spin iron is rate limiting in ferro-periclase and is much slower than magnesium diffusion in post-perovskite along $\langle 100 \rangle$ up to temperatures of 6000 K. b) U = 4.5: All diffusivities are similar at all temperatures and magnesium diffusion in post-perovskite along $\langle 100 \rangle$ becomes fastest above temperatures of 2100 K

The iron diffusivity in ferro-periclase is iron-concentration dependent (figure 39). While it is well known that, because of the spin-transition, the iron partitioning between ferro-periclase, perovskite and post-perovskite varies within Earth's lower mantle (e.g.[239–241]), the current results are (unfortunately) not accurate enough to establish a firm relation between viscosity and iron concentration (as could be used in an inverse-problem).

12.2. Spin Transition in Iron-Bearing Perovskite

Also in perovskite, iron undergoes a spin-transition form a high- to a low-spin state, however at somewhat higher pressures than in ferro-periclase.

First, Badro et al.[21] found a two-stage collapse (70 GPa and 120 GPa) suggesting that the transition might be site specific. Subsequent experiments[22] showed that the presence of aluminium stabilises the highspin state of iron and the transition is gradual and not completed by the base of the lower mantle. A synchrotron Mössbauer study[23] found that Fe^{3+} on the B-site (octahedral) would gradually demagnetise until pressures reach 70 GPa. More recently, two studies suggested that ferrous iron in perovskite undergoes a spin transition around 30 GPa into a intermediate spin state[24,25] which persist throughout the whole lower mantle. This is however not supported by computational studies. The latest experimental study prepared samples with Fe^{3+} on both sites (coupled substitution) and found that the A-site (dodecahedral) is always high-spin for all pressures of the lower mantle, while the B-site changes to low-spin around 60 GPa[242].

An early theoretical study by Cohen et al.[219] predicted the transition pressure of ferrous iron to be around 1000 GPa on the A-site. This was also found by subsequent studies[243,244]: Fe^{2+} is always high-spin, while Fe^{3+} on the B-site is low-spin. In contrast with wüstite, it appears that the iron concentration in perovskite lowers the spin-transition pressure[245,246]. Umemoto et al.[246] showed that ferrous iron can undergo the spin transition inside the lower mantle, but only for special configurations (depending on the used exchange correlation functional: LDA or GGA, somewhere between 60 and 160 GPa).

Thus, theory and experimental results do not yet deliver a complete picture of the spin-transition in perovskite and its relevance in the Earth's lower mantle. On one hand, this is due to the fact that ferric and ferrous iron behave differently depending on which site they are on. Additionally, there is evidence that perovskite is ferric iron rich. On the other hand, the spin-state depends on the mechanism of iron incorporation into perovskite, be it coupled with aluminium or with ferric iron on A and B-site or simply ferrous iron on the A-site.

I will here present results of a preliminary study, where I calculated the diffusivity of ferrous iron. The effect of ferric iron will have to be considered in a future project. The calculated parameters are given in the appendix, table 32. The found migration enthalpies of high- and low-spin iron are very similar to the one of magnesium in pure perovskite (see table 11) and the effect on neighbouring magnesium jumps is

also minor. The attempt frequency, in contrast, is about an order of magnitude larger for iron than for magnesium. Ferrous iron is thus expected to diffuse faster than magnesium, simply due to an increased attempt frequency. However, as the results on iron diffusion in periclase demonstrated, a faster jump rate of iron will not significantly affect the diffusivity of magnesium nor the viscosity. Thus, if magnesium is rate-limiting in perovskite (as found in experiments[40]), the spin-transition would have no effect on the viscosity of perovskite. However,if silicon diffusion is rate limiting the deformation of perovskite, the current study would need to be extended to the six-jump cycles responsible for silicon diffusion. This is, unfortunately, not yet done and will await examination in a future study.

Part V.
Concluding Remarks

13. Synopsis

It has been shown that absolute diffusion rates calculated from first-principles, assuming a vacancy-diffusion mechanism and an extrinsic vacancy concentration, can reproduce all experimental data at shallow lower mantle conditions. This in turn gives us confidence in the calculated rates at lower-mantle conditions that are currently inaccessible to experiments.

An immediate result is, as already discussed in section 10.4.2, that diffusion rates in any mineral throughout the lower mantle are too small to remove any chemical heterogeneities even over time-scales of the age of the Earth. Chemical exchange with the core would thus need to occur via grain-boundary diffusion [191] and chemical heterogeneities in the mantle could only be removed via turbulent mixing (stretching and thinning) or grain boundary diffusion.

More importantly, however, are the implications for the rheology. The viscosity profile of the lower mantle inferred from inversion modelling of post-glacial rebound and geodynamic observables, can be reproduced by assuming diffusion-creep of perovskite. Ferro-periclase remains about three orders of magnitude weaker than perovskite, when relative viscosities are fixed at shallow mantle conditions where experiments are available. The spin-transition of iron in ferro-periclase or iron-bearing perovskite has no effect on the viscosity of the host mineral. Thus, ferro-periclase cannot form an interconnected framework in the lower mantle as the resulting viscosity would be much lower than expected from inversion modelling.

The most important result is that the diffusivity of post-perovskite has been calculated (and constrained) for the first time. The results suggest that post-perovskite is either stiffer than perovskite, if both are deforming in diffusion creep, or in the more likely case of deforming via dislocation creep, that post-perovskite is about four orders of magnitude weaker than perovskite. This finding allows us to reconcile seismic observations of with mineral physical experiments. The sharp reflector seen seismically (D″) represents a rheological transition (not a phase-transition) where the weak post-perovskite becomes interconnected and strain is mainly partitioned into this weak phase resulting in a strong texture.

14. A Word of Caution

Despite the achieved agreement between experimental and calculated diffusion rates, and, especially, the agreement of the calculated and the inverted viscosity profiles one needs to be aware that there are several unknowns and trade-offs between unknowns. Moreover, the accuracy of certain calculated quantities is more important than others. When comparing with experiments, any error made on the vacancy-diffusivity will have to compensated by the assumed vacancy concentration. When extrapolating to the lower mantle, the chosen geotherm will have a stark effect on the absolute diffusion rate.

My calculations showed that it is very likely that the lower mantle is deforming in diffusion creep and that perovskite is the load bearing phase with ferro-periclase residing in isolated grains. Nevertheless, there are too many unconstrained parameters in the profile shown in figure 44.

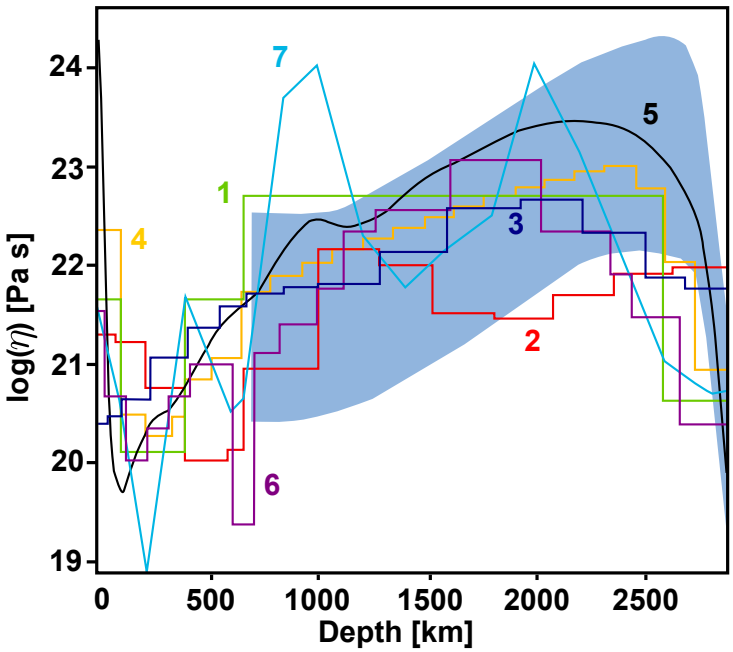

Figure 44: **Radial Mantle Viscosity Models** modified after[1]. (1)[2] (2)[3] (3)[4] (4)[5] (5)[6] (6)[7] (7)[8]. Imposed is the calculated diffusion-creep viscosity profile of perovskite

If we want to better understand and constrain the viscosity of the minerals of the Earth's interior, we will need to know all the parameters that control them. Considering diffusion creep (equation 8.3), the parameters namely are diffusivity, temperature and grain-size. Diffusivity itself depends on the vacancy concentration

and the vacancy-diffusivity which themselves depend on temperature and pressure.

The most important parameter is the absolute diffusion rate which limits the rate at which the minerals can deform. As shown in this thesis, it is possible to calculate diffusivities within a fairly high accuracy, similar to experiments. However, the various parameters that control diffusion differ in their overall importance. Let me, thus, quickly rewrite the expression for the absolute diffusivity:

$$D = D_0 e^{\frac{-\Delta H}{kT}} \tag{14.1}$$

with the prefactor

$$D_0 = \frac{Z}{6} d^2 N_v \tilde{\nu} \tag{14.2}$$

The diffusivity D is dominated by the exponential temperature dependence and the migration enthalpy ΔH which can be readily calculated at the desired pressure. They are again collected in figure 45 and compared with the available experimental data and earlier computational studies. Several things are important to note. Firstly, theoretical studies are generally very close to the experimental values and agree with each other as long as the same pathways and migration mechanisms are considered. Of course, there is an exception to the rule - namely the molecular dynamics study of periclase[141] that found a decrease in the migration enthalpy at high pressures (the difference comes probably from their choice of interatomic potentials). Secondly, pressure-dependencies of the migration enthalpies, the so-called activation volume, are very similar for all atomic species, all phases and among all theoretical studies. Importantly, the activation volumes decrease with pressure suggesting the 'low'-pressure experimental values are not valid at high pressures. Also, the agreement of the theoretical studies provides some confidence for the high pressure values of the migration enthalpies. Lastly, it can be readily seen how the use of the six-jump cycle drastically lowers the migration enthalpy for silicon diffusion in perovskite, reconciling experiments with theory, and along $\langle 010 \rangle$ in post-perovskite compared with the direct jumps.

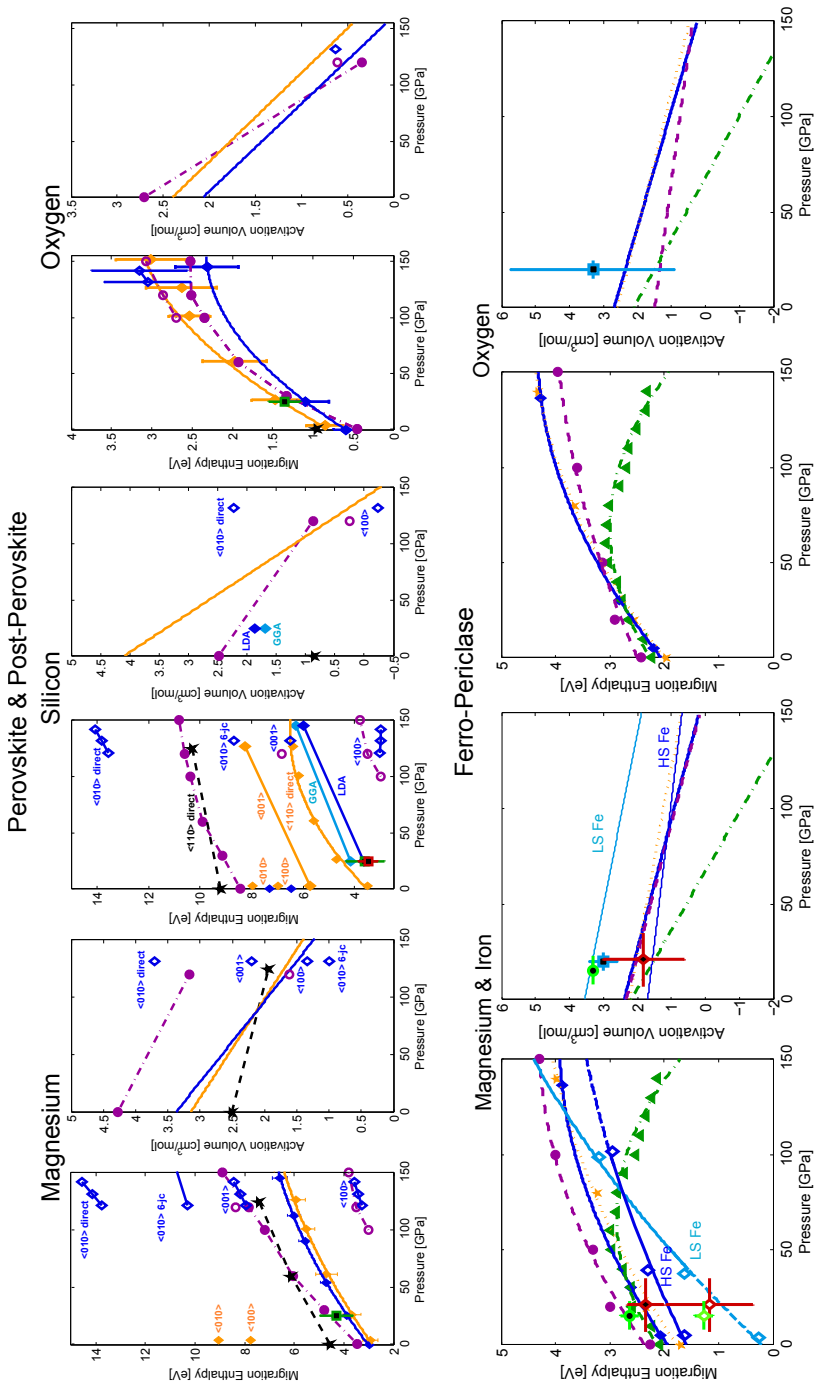

Figure 45: **Migration enthalpies and activation volumes of lower mantle minerals** Results of earlier calculations are marked with black stars[90], violet circles[91,112], orange stars[144,159] and green triangles[141]. Empty (white) markers represent values of post-perovskite or iron in periclase (U = 4.5). Experimental values are marked with squares: Magnesium[40], silicon[35,41] and oxygen[36] in perovskite, oxygen and magnesium in pure periclase[38] (light blue) and magnesium and iron in inter-diffusion experiments in ferro-periclase[11,39] (red and green respectively). Diamonds are my calculations using a geometrically determined saddle points (orange[92]) and using NEB (blue[134])

The absolute diffusion rate and thereby the viscosity is hence strongly dependent on the assumed geotherm. The prefactor is a linear contribution, and the coordination number Z and the jump-distance d are known for each mineral. The attempt frequency and migration entropy, collected in $\tilde{\nu}$, can be calculated within the harmonic transition state theory. However, the computational effort is hardly rewarded as it is (as shown in this thesis) usually of the order of 10^{13} THz, for any mineral. It varies by no more than a factor of five over the pressure range of the lower mantle. Moreover, any error of $\tilde{\nu}$ will need to be compensated by the vacancy concentration to match any experimental data. Interestingly, as shown in figure 46, prefactors D_0 are almost constant throughout the lower mantle as the increase with pressure in the attempt frequency is partly balanced by the reduction of the jump-distances. Also, the prefactors of the diffusivities of the various species are very similar within the same phase, except for the anisotropic post-perovskite (where jump-distances vary significantly between the different directions).

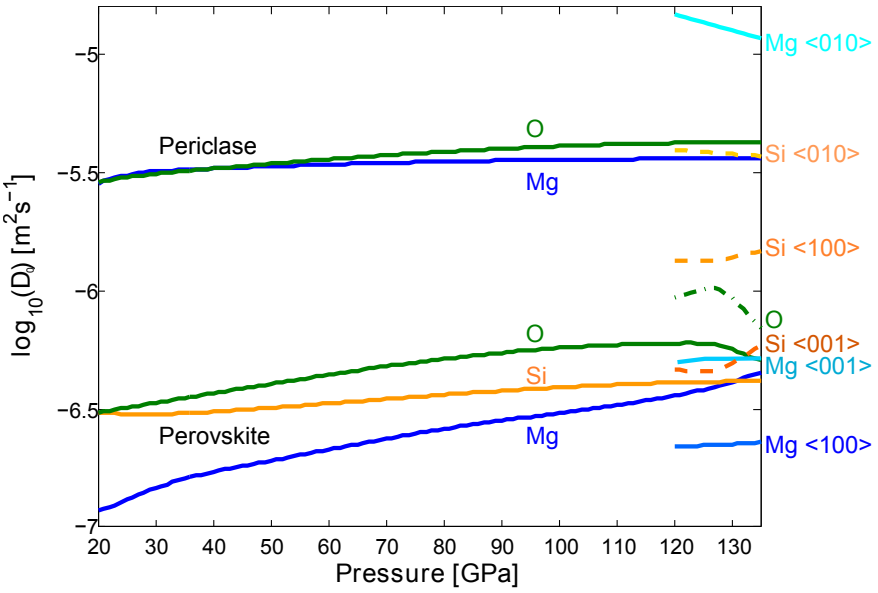

Figure 46: **Prefactors of vacancy-diffusion in periclase, perovskite and post-perovskite** Prefactors are almost constant throughout the lower mantle are similar for all species within a phase, except for post-perovskite

Thus, the only real unknown of the absolute diffusion rate, in fact, is the vacancy concentration, which might vary over several orders of magnitude. Concerning the viscosity, it is important to note that there is a trade-off between the vacancy concentration and the grain-size. My results can thus be used to constrain either pa-

rameter: The minimum absolute diffusivity is obtained with the intrinsic vacancy concentrations which can be calculated from first-principles. The resulting intrinsic vacancy concentrations (using the calculated Schottky formation energies of[91] for perovskite and post-perovskite, and from this study for periclase; shown in figure 11) would be far too small (even for very hot geotherms) and result in a much too stiff lower mantle, unless the grainsize would be of the order of nm. On the other hand, the maximum diffusivity is reached for a vacancy concentration of 1, which would allow a grainsize of the order of 10 cm.

From the values for intrinsic vacancy concentrations shown in figure 11 and their resulting grainsize it is evident that vacancies in the lower mantle have to be extrinsic. However, the extrinsic vacancy concentration and formation is not well constrained and understood in the lower mantle. They form in a crystal in order to charge-balance any excess charges from impurities. On one hand, the impurity concentrations are unknown (poorly constrained; order of 1000 ppm[234,247,248] in periclase). On the other hand, impurity incorporation in perovskite and post-perovskite is often coupled (e.g. Fe^{3+} on a magnesium and a Al^{3+} neighbouring silicon-site[249]), leading to neutral defects. Also, as shown in this study, silicon vacancies are energetically less favourable than a magnesium on a silicon site plus a magnesium vacancy, removing silicon vacancies from the system. It is hence not clear how silicon vacancies are formed, but they might need to be stabilised with hydrogen, as in forsterite[109].

As shown in my study of ferrous iron diffusion in periclase the diffusivity of the majority ions (magnesium) are almost unaffected by the diffusion of the impurity ions (iron) even at elevated concentrations. The viscosity is therefore not affected by neutral impurities at low concentrations. However, this is not necessarily true for charged impurities, such as aluminium and ferric-iron, which will bind vacancies in their vicinity reducing their availability for other cations diffusing via a vacancy mechanism (e.g.[234]). The loss of available vacancies will have a strong effect on the absolute diffusion rate and therewith on the viscosity. This is especially true for perovskite, for which only the diffusivity of ferrous iron was calculated. It is very likely that large proportions of iron in perovskite are in fact ferric and should hence change their spin-state from high to low with increasing pressure at lower pressures than ferrous iron. Also, I did not have the time to investigate the effect of the spin-transition on the silicon six-jump cycles which might have an effect on the viscosity of perovskite.

Thus, to better constrain our diffusion creep profile (figure 44), vacancy concen-

trations (impurity concentrations and formation mechanisms) and grain-sizes need to be better understood and constrained. It is, nevertheless, very encouraging that with the current, reasonable estimates (used in this study), the viscosity profile from inversion modelling can be reproduced. Also, if D″ is deforming in dislocation creep, we need means to estimate the dislocation densities and the occurring stresses in order to estimate the absolute viscosity of post-perovskite, especially if we want to compare it with the one of perovskite and periclase, which might still be deforming in diffusion creep.

Finally, I would like to point out that it is not well understood how to translate the massive diffusion-anisotropy in post-perovskite into diffusion-creep viscosity. The ideas of how a post-perovskite aggregate deforms in diffusion-creep as outlined in section 11.3 are only a starting point and more sophisticated simulations should be carried out (e.g.[215]), especially if deformation is a collaborative process of many grains. This would also reveal if anisotropic diffusion can produce a texture even when deforming in diffusion-creep, leading to strain-weakening of post-perovskite.

15. Outlook

Having demonstrated that diffusivities can be calculated from first-principles for the considered mineral phases, future research should focus on other phases that are currently out of reach for diffusion experiments. I shall here only give a short list of possibilities.

As the lower mantle has largely been covered in this study, the most important future project should focus on iron-self diffusion in the Earth's core. The viscosity of the Earth's core is only very poorly constrained (e.g.[250]) and no activation energies for diffusion are available. This might even give a hint on the crystal structure of iron, if diffusivities vary strongly between the different iron phases HCP, FCC[251] and BCC[252].

Other phases in which diffusion is difficult to measure experimentally are, e.g., iron-oxides, SiO_2 stishovite and $CaSiO_3$ perovskite under the lower mantle conditions. But also diffusion in the transition zone minerals needs to be better understood in order to better understand and quantify the viscosity contrast between the upper and the lower mantle as well as its effect on deep earthquakes.

Lastly it needs to be mentioned that oxygen diffusion in periclase, often called the simplest oxide, is not yet completely understood (see figure 15) and requires further investigations.

Part VI.
Appendices

Formal Acknowledgements

This work was funded by the European Commission through the Marie Curie Research Training Network "c2c" (Crust to Core) Contract No. MRTN-CT-2006-035957. The authors acknowledge the use of UCL Research Computing facilities of Legion and of HECToR, the UK's national high-performance computing service, which is provided by UoE HPCx Ltd at the University of Edinburgh, Cray Inc and NAG Ltd, and funded by the Office of Science and Technology through EPSRC's High End Computing Programme.

Personal Acknowledgements

At this point I would like to express my gratitude to my two superb supervisors, John Brodholt and David Dobson, for their invaluable advice, great enthusiasm and knowledge that they shared with me. This has been a fantastic project that deepened my love for science and ignited a new fascination for our Earth.

My thanks also go out to all my fellow students at the office with whom I had many drinks, be it coffee or beer, that made dull days still great. Moreover, it is a pleasure to thank all the people of the c2c-network for absolutely awesome meetings, conferences and field-trips.

I would like to thank my family for their support and enthusiasm for everything I have done in my life. And, last but not least, I thank Corinne for her endless support, enthusiasm and love ever since I know her.

Alphabetical List of Abbreviations

Abbreviation	**Denotation**
CI-NEB	Climbing Image Nudged Elastic Band
DFPT	Density Functional Perturbation Theory
DFT	Density Functional Theory
DMC	Diffusion Monte Carlo
GGA	Generalised Gradient Approximation
HF	Hartree-Fock
IWL	Interconnected Weak Layers
KMC	Kinetic Monte Carlo
LBF	Load-Bearing Framework
LD	Lattice Dynamics
LDA	Local Density Approximation
LPO	Lattice Preferred Orientation
MD	Molecular Dynamics
MEP	Minimum Energy Path
MFPT	Mean Free Passage Theory
ML	Mott-Littleton
NEB	Nudged Elastic Band
PBC	Periodic Boundary Conditions
QMC	Quantum Monte Carlo
TDDFT	Time-Dependent Density Functional Theory
TFT	Thomas-Fermi Theory
TST	Transition State Theory
VASP	Vienna *ab initio* Simulation Package

References

1. J. F. Lawrence and M. E. Wysession. QLM9: A new radial quality factor (Q_μ) model for the lower mantle. *Earth and Planetary Science Letters*, 241:962–971, 2006.

2. B. H. Hager and M. A. Richards. Long-wavelength variations in Earth's geoid: physical models and dynamical implications. *Philos. Trans. R. Soc. Lond. A*, 328:309–327, 1989.

3. A. M. Forte and J. X. Mitrovica. New inferences of mantle viscosity from joint inversion of long-wavelength mantle convection and post-glacial rebound data. *Geophys. Res. Lett.*, 34:1147–1150, 1996.

4. Y. Ricard and B. Wuming. Inferring the viscosity and the 3-D density structure of the mantle from geoid, topography and plate velocities. *Geophys. J. Int.*, 105:561–571, 1991.

5. B. M. Steinberger and A. R. Calderwood. Mineral physics constraints on viscous flow models of mantle flow. *J. Conf. Abstr.*, 6:–, 2001.

6. A. K. McNamara, P. E. van Keken, and S.-I. Karato. Development of finite strain in the convecting lower mantle and its implications for seismic anisotropy. *J. Geophys. Res.*, 108:doi:10.1029/2002JB001970, 2003.

7. J. X. Mitrovica and A. M. Forte. A new inference of mantle viscosity based upon joint inversion of convection and glacial isostatic adjustment data. *Earth Planet. Sc. Lett.*, 225:177–189, 2004.

8. A. M. Forte and J. X. Mitrovica. Deep-mantle high-viscosity flow and thermochenical structure inferred from seismic and geodynamic data. *Nature*, 410:1049–1056, 2001.

9. T. Irifune. Phase transformations in the Earth's mantle and subducting slabs: Implications for their compositions, seismic velocity and density structures and dynamics. *The Island Arc*, 2:55–71, 1993.

10. J. M. Brown and T. J. Shankland. Thermodynamic parameters in the Earth as determined from seismic profiles. *Geophys. J.R. Astron. Soc.*, 66:579–596, 1981.

11. D. Yamazaki and T. Irifune. Fe-Mg interdiffusion in magnesiowüstite up to 35 GPa. *Earth Planet. Sc. Lett.*, 216:301–311, 2003.

12. A. E. Ringwood. The chemical composition and origin of the Earth. *Advances in Earth Sciences, Hurley, P. M. (Ed)*, 1966.

13. A. E. Ringwood. *Composition and Petrology of the Earth's Mantle*. McGraw-Hill, 1975.

14. T. Lay, Q. Williams, and E. J. Garnero. The core-mantle boundary layer and the deep Earth dynamics. *Nature*, 392:461–468, 1998.

15. E. J. Garnero and A. K. McNamara. Structure and dynamics of Earth's lower mantle. *Science*, 320:626–628, 2008.

16. J. Badro, G. Fiquet, F. Guyot, J.-P. Rueff, V. V. Struzhkin, G. Vankó, and G. Monaco. Iron partitioning in Earth's mantle: towards a deep lower mantle discontinuity. *Science*, 300:789–791, 2003.

17. S. Speziale, A. Milner, V. E. Lee, S. M. Clark, M. P. Pasternak, and R. Jenaloz. Iron spin transition in Earth's mantle. *P. Natl. Acad. Sci. USA*, 102:17918–17922, 2005.

18. J.-F. Lin, V. V. Struzhkin, S. D. Jacobsen, M. Y. Hu, P. Chow, J. Kung, H. Liu, H. Mao, and J. H. Russell. Spin transition of iron in magnesiowüstite in the Earth's lower mantle. *Nature*, 436:377–380, 2005.

19. T. Tsuchiya, R. M. Wentzcovitch, C. R. S. da Silva, and S. de Gironcoli. Spin transition in magnesiowüstite in Earth's lower mantle. *Phys. Rev. Lett.*, 96:198501:1–4, 2006.

20. R. M. Wentzcovitch, J. F. Justo, Z. Wu, C. R. S. da Silva, D. A. Yuen, and D. Kohlstedt. Anomalous compressibility of ferropericlase throughout the iron spin cross-over. *P. Natl. Acad. Sci. USA*, 106:8447–8452, 2009.

21. J. Badro, J.-P. Rueff, G. Vankó, G. Monaco, G. Fiquet, and F. Guyot. Electronic transistions in perovskite: possible nonconvecting layers in the lower mantle. *Science*, 305:383–386, 2004.

22. Li, J. and Struzhkin, V. V. and Mao, H. and Shu, J. and Hemley, R. J. and Fei, Y. and Mysen, B. and Dera, P. and Prakapenka, V. and Shen, G. Electronic spin state of iron in lower mantle perovskite. *P. Natl. Acad. Sci. USA*, 101:14027–14030, 2004.

23. J. M. Jackson, W. Sturhahn, G. Shen, J. Zhao, M. Y. Hu, D. Errandonea, J. D. Bass, and Y. Fei. A synchrotron Mössbauer spectroscopy study of (Mg,Fe)SiO_3 perovskite up to 120 GPa. *American Mineralogist*, 90:199 – 205, 2005.

24. J.-F. Lin, H. Watson, G. Vankó, E. Alp, V. B. Prakapenka, P. Dera, V. V. Struzhkin, A. Kubo, J. Zhao, C. McCammon, and W. J. Evans. Intermediate-spin ferrous iron in lowermost mantle post-perovskite and perovskite. *Nature Geoscience*, 1:688–691, 2008.

25. C. McCammon, I. Kantor, O. Narygina, J. Rouquette, U. Ponkraz, I. Sergueev, M. Mezouar, V. Prakapenka, and L. Dubrovinsky. Stable intermediate-spin ferrous iron in lower mantle perovskite. *Nature Geoscience*, 1:684–687, 2008.

26. E. J. Garnero. Heterogeneity of the lowermost mantle. *Annu. Rev. Earth Planet. Sci.*, 28:509–537, 2000.

27. J. W. Hernlund, C. Thomas, and P. J. Tackley. A doubling of the post-perovskite phase boundary and structure of the Earth's lowermost mantle. *Nature*, 434:882–886, 2005.

28. J. Wookey, S. Stackhouse, J.-M. Kendall, J. Brodholt, and G. D. Price. Efficacy of the post-perovskite phase as an explanation for lowermost-mantle seismic properties. *Nature*, 438:1004–1007, 2005.

29. T. Lay, J. Hernlund, E. J. Garnero, and M. S. Thorne. A post-perovskite lens and D″ heat flux beneath the central pacific. *Science*, 314:1272–1276, 2006.

30. A. R. Hutko, T. Lay, J. Revenaugh, and E. J. Garnero. Anticorrelated seismic velocity anomalies from post-perovskite in the lowermost mantle. *Science*, 320:1070–1074, 2008.

31. M. Murakami, K. Hirose, K. Kawamura, N. Sata, and Y. Ohishi. Post-perovskite phase transition in $MgSiO_3$. *Science*, 204:855–858, 2004.

32. A. R. Oganov and S. Ono. Theoretical and experimental evidence for a post-perovskite phase of $MgSiO_3$ in Earth's D″ layer. *Nature*, 430:445–448, 2004.

33. T. Tsuchiya, J. Tsuchiya, K. Umemoto, and R. M. Wentzcovitch. Phase transition in $MgSiO_3$ perovskite in the Earth's lower mantle. *Earth Planet. Sc. Lett.*, 224:241–248, 2004.

34. K. Catalli, S.-H. Shim, and V. Prakapenka. Thickness and Clapeyron slope of the post-perovskite boundary. *Nature*, 462:782–786, 2009.

35. D. Yamazaki, T. Kato, H. Yurimoto, E. Ohtani, and M. Toriumi. Silicon self-diffusion in $MgSiO_3$ perovskite at 25 GPa. *Phys. Earth Planet. In.*, 119:299–309, 2000.

36. D. P. Dobson. Oxygen ionic conduction in $MgSiO_3$ perovskite. *Phys. Earth Planet. In.*, 139:55–64, 2003.

37. Y. Xu and C. McCammon. Evidence for ionic conductivity in lower mantle $(Mg,Fe)(Si,Al)O_3$ perovskite. *J. Geophys. Res.*, 107:doi:10.1029/2001JB000677, 2002.

38. J. A. Van Orman, Y. Fei, E. H. Hauri, and J. Wang. Diffusion in MgO at high pressures: constraints on deformation mechanisms and chemical transport at the core-mantle-boundary. *Geophys. Res. Lett.*, 30:28:1–4, 2003.

39. C. Holzapfel, D. C. Rubie, S. Mackwell, and D. J. Frost. Effect of pressure on Fe-Mg interdiffusion in $(Fe_xMg_{1-x})O$, ferropericlase. *Phys. Earth Planet. In.*, 139:21–34, 2003.

40. C. Holzapfel, D. C. Rubie, D. J. Frost, and F. Langenhorst. Fe-Mg interdiffusion in (Mg,Fe)SiO_3 perovskite and lower mantle reequilibration. *Science*, 309:1707–1710, 2005.

41. D. P. Dobson, R. Dohmen, and M. Wiedenbeck. Self-diffusion of oxygen and silicon in $MgSiO_3$ perovskite. *Earth Planet. Sc. Lett.*, 270:125–129, 2008.

42. K. Capelle. A bird's-eye view of density-functional theory. *http://arxiv.org/abs/cond-mat/0211443v5*, 2006.

43. N. Argaman and G. Makov. Density functional theory: An introduction. *Am. J. Phys.*, 68:69–79, 2000.

44. E. V. Ludena. Is the Hohenberg-Kohn-Sham version of DFT a semi-empirical theory? *Journal of Molecular Structure (Theochem)*, 709:25–29, 2004.

45. P. Hohenberg and W. Kohn. Inhomogenous electron gas. *Phys. Rev.*, 136:B864–B871, 1964.

46. W. Kohn and L. J. Sham. Self-consistent equations including exchange and correlation effects. *Phys. Rev.*, 140:A1133–A1138, 1965.

47. A. Sommerfeld. Pressure and Kinetic Energy of the Electron Gas. *Z. Phys.*, 47:1–60, 1928.

48. L. H. Thomas. The calculation of atomic fields. *Phys. Rev. Lett.*, 84:1942–1945, 2000.

49. E. Fermi. Un metodo statistico per la determinazione di alcune prioprieta dell'atome. *Rend. Accad. Naz. Lincei*, 6:602–607, 1927.

50. E. Teller. On the stability of molecules in Thomas-Fermi theory. *Rev. Mod. Phys.*, 34:627–631, 1962.

51. E. H. Lieb. Thomas-Fermi theory. *Kluwer Encyclopedia of Mathematics, Supplement Vol. II*, pages 455–457, 2000.

52. J. W. Rayleigh. In finding the correction for the open rnd of an organ-pipe. *Phil. Trans*, 161:77, 1870.

53. W. Ritz. Über eine neue Methode zur Lösung gewisser Variationsprobleme der mathematischen Physik. *J. reine angew. Math.*, 135:1–61, 1908.

54. E. H. Lieb. Density functionals for Coulombic systems. *Int. J. Quantum Chem.*, 24:243–277, 1983.

55. R. P. Feynman. Forces in molecules. *Phys. Rev.*, 56:340–343, 1939.

56. J. P. Perdew and A. Zunger. Self-interaction correction to density-functional approximations for many-electron systems. *Phys. Rev. B*, 23:5048–5079, 1981.

57. J. P. Perdew and Y. Wang. Accurate and Simple Analytic Representation of the Electron-Gas Correlation Energy. *Phys. Rev. B*, 45:13244–13249, 1992.

58. J. P. Perdew and Burke K. Comparison shopping for a gradient-corrected density functional. *Int J of Quantum Chem*, 57:309–319, 1996.

59. F. Bloch. Über die Quantenmechanik der Elektronen in Kristallgittern. *Zeitschrift für Physik*, 52:555–600, 1928.

60. H. J. Monkhorst and J.D. Pack. Special points for Brillouin-zone integrations. *Phys. Rev. B*, 23:5048–5192, 1976.

61. G. Kresse and J. Hafner. Ab initio molecular dynamics for liquid metals. *Phys. Rev. B*, 47:558–561, 1993.

62. G. Kresse and J. Furthmüller. Efficiency of ab-initio total energy calculations for metals and semiconductors using a plane-wave basis Set. *Comput. Mat. Sci.*, 6:15–50, 1996.

63. P. E. Blöchl. Projector augmented-wave method. *Phys. Rev. B*, 50:17953–17979, 1994.

64. G. Kresse and J. Joubert. From ultrasoft pseudopotentials to the projector augmented wave method. *Phys. Rev. B*, 59:1758–1775, 1999.

65. R. E. Howard and A. B. Lidiard. Matter Transport in Solids. *Rep. Prog. Phys.*, 27:161–240, 1964.

66. J. Crank. *Mathematics of Diffusion*. Oxford University Press, 1975.

67. A. R. Allnatt and A. B. Lidiard. Statistical theories of atomic transport in crystalline solids. *Rep. Prog. Phys.*, 50:373–472, 1987.

68. E. B. Watson and E. F. Baxter. Diffusion in Solid-Earth Systems. *Earth Planet. Sc. Lett.*, 253:307–327, 2007.

69. H. Mehrer. *Diffusion in Solids*. Springer, 2007.

70. A. Fick. Über diffusion. *Annalen der Physik*, 94:59–86, 1855.

71. A. Fick. On liquid diffusion. *Philos Mag*, 10:30–39, 1855.

72. A. Einstein. Über die von der molekularkinetischen Theorie der Wärme geforderte Bewegung von in ruhenden Flüssigkeiten suspendierten Teilchen. *Annalen der Physik*, 17:549–560, 1905.

73. M. van Smoluchowski. Zur kinetischen Theorie der Brownschen Molekularbewegung und der Suspensionen. *Annalen der Physik*, 21:756–780, 1906.

74. G. H. Vineyard. Frequency factors and isotope effects in solid state rate processes. *J. Phys. Chem. Solids*, 3:121–127, 1957.

75. M. J. L. Sangster and A. M. Stoneham. Calculation of absolute diffusion rates in oxides. *J. Phys. C: Solid State Phys.*, 17:6093–6104, 1984.

76. C. P. Flynn and G. Jacucci. Dynamical corrections to rate theory. *Phys. Rev. B*, 25:6225–6234, 1982.

77. N. W. Ashcroft and N. D. Mermin. *Solid State Physics*. Brooks Cole, 1976.

78. H. Ibach and H. Lüth. *Festkörperphysik - Einführung in the Grundlagen*. Springer, 2002.

79. G. J. Ackland, M. C. Warren, and S. J. Clark. Practical Methods in ab initio Lattice Dynamcis. *J. Phys.: Condens. Matter*, 9:7861–7872, 1997.

80. D. Alfè. PHON - A Program to Calculate Phonons Using the Small Displacement Method. *http://chianti.geol.ucl.ac.uk/ dario/*, 2005.

81. S. Baroni, P. Giannozzi, and A. Testa. Green's-function approach to linear response in solids. *Phys. Rev. Lett.*, 58:1861–1864, 1987.

82. P. Giannozzi, S. de Gironcoli, P. Pavone, and S. Baroni. Ab initio calculation of phonon dispersion in semiconductors. *Phys. Rev. B*, 43:7231–7242, 1991.

83. K. Parlinski, Z. Q. Li, and Y. Kawazoe. First-principles determination of the soft mode in cubic zro_2. *Phys. Rev. Lett.*, 78(21):4063–4066, 1997.

84. S. Baroni, S. de Gironcoli, A. Dal Corso, and P. Giannozzi. Phonons and related crystal properties from density-functional perturbation theory. *Rev. Mod. Phys.*, 73:515–562, 2001.

85. G. Kresse, J. Furthmüller, and J. Hafner. Ab initio force constant approach to phonon dispersion relations of diamond and graphite. *Europhys. Lett.*, 32:729–734, 1995.

86. D. Alfè. PHON: A program to calculate phonons using the small displacement method. *Comput. Phys. Commun.*, 180:2622–2633, 2009.

87. B. B. Karki, R. M. Wentzcovitch, S. de Gironcoli, and S. Baroni. High-pressure lattice dynamics and thermoelasticity of MgO. *Phys. Rev. B*, 61:8793–8800, 2000.

88. A. R. Oganov, M. J. Gillan, and G. D. Price. Ab initio lattice dynamics and structural stability of MgO. *J. Chem. Phys.*, 118:10174–10182, 2003.

89. W. C. Mackrodt. Temperature dependence of lattice and defect properties of MgO and Li_2O. *Journal of Molecular Liquids*, 39:121–136, 1988.

90. K. Wright and G. D. Price. Computer simulation of defects and diffusion in perovskite. *J. Geophys. Res.*, 98:22.245–22.253, 1993.

91. B. B. Karki and G. Khanduja. A Computational study of ionic vacancies and diffusion in $MgSiO_3$ perovskite and post-perovskite. *Earth Planet. Sc. Lett.*, 260:201–211, 2007.

92. M. W. Ammann, J. P. Brodholt, and D. P. Dobson. DFT study of migration enthalpies in $MgSiO_3$ perovskite. *Phys. Chem. Miner.*, 36:151–158, 2009.

93. G. Henkelman, B. P. Uberuaga, and H. Jónsson. A climbing image nudged elastic band method for finding saddle points and minimum energy paths. *J. Chem. Phys.*, 113:9901–9904, 2000.

94. G. Henkelman and H. Jónsson. A dimer method for finding saddle points on high dimensional potential surfaces using only first derivatives. *J. Chem. Phys.*, 111:7010–7022, 1999.

95. D. Sheppard, R. Terrell, and G. Henkelman. Optimization methods for finding minimum energy paths. *J. Chem. Phys.*, 128:134106:1–10, 2008.

96. G. Henkelman and H. Jónsson. Improved tangent estimate in the nudged elastic band method for finding minimum energy paths and saddle points. *J. Chem. Phys.*, 113:9978–9985, 2000.

97. A. F. Voter. *Introduction to the Kinetic Monte Carlo Method*. Springer, NATO Publishing Unit, 2005.

98. F. D. Stacey and P. M. Davis. High pressure equations of state with applications to the lower mantle and core. *Phys. Earth Planet. In.*, 142:137–184, 2004.

99. N. F. Mott and M. J. Littleton. Conduction in polar crystals. I. Electrolyte conduction in solid salts. *Trans. Faraday Soc.*, 34:485–499, 1938.

100. J. D. Gale. GULP: A computer program for the symmetry-adapted simulation of solids. *JCS Trans. Faraday*, 93:629–637, 1997.

101. J. D. Gale and A. L. Rohl. The General Utility Lattice Program (gulp). *Mol. simul.*, 29:291–341, 2003.

102. M. Cherry, M. S. Islam, and C. R. A. Catlow. Oxygen ion migration in perovskite-type oxides. *Journal of Solid State Chemistry*, 118(1):125 – 132, 1995.

103. M. Cherry, M. S. Islam, J. D. Gale, and C. R. A. Catlow. Computational studies of protons in perovskite-structured oxides. *The Journal of Physical Chemistry*, 99(40):14614–14618, 1995.

104. M. Blanchard, K. Wright, and J. D. Gale. Atomistic simulation of Mg_2SiO_4 and Mg_2GeO_4 spinels: a new model. *Phys. Chem. Miner.*, 32:332–338, 2005.

105. S. Lowitzer, D. J. Wilson, B. Winkler, V. Milman, and J. D. Gale. Defect properties of albite. *Phys. Chem. Min.*, 35:129–135, 2008.

106. J. A. Ball, S. T. Murphy, R. W. Grimes, D. Bacorisen, R. Smith, B. P. Uberuaga, and K. E. Sickafus. Defect processes in $MgAl_2O_4$ spinel. *Solid State Sciences*, 10:717–724, 2008.

107. F. Béjina, M. Blanchard, K. Wright, and G. D. Price. A computer simulation study of the effect of pressure on mg diffusion in forsterite. *Phys. Earth Planet. In.*, 172(1-2):13 – 19, 2009.

108. J. Brodholt. Ab initio calculations on point defects in forsterite (Mg_2SiO_4) and implications for diffusion creep. *American Mineralogist*, 82:1049–1053, 1997.

109. J. Brodholt and K. Refson. An ab initio study of hydrogen in forsterite and a possible mechanism for hydrolytic weakening. *J. Geophys. Res.*, 105:18,977–18,982, 2000.

110. J. Brodholt. Pressure-induced changes in the compression mechanism of aluminous perovskite in the Earth's mantle. *Nature*, 407:620–622, 2000.

111. B. B. Karki and G. Khanduja. Computer simulation and visualization of vacancy defects in $MgSiO_3$ perovskite. *Phys. Rev. B*, 61:8793–8800, 2006.

112. B. B. Karki and G. Khanduja. Vacancy defects in MgO at high pressure. *American Mineralogist*, 91:511–516, 2006.

113. P. V. Sushko, A. L. Shluger, C. R. A. Catlow, and R. C. Baetzold. Embedded cluster approach: application to complex defects. *Radiation Effects and Defects in Solids*, 151:215–221, 1999.

114. P. V. Sushko, A. L. Shluger, R. C. Baetzold, and C. R. A. Catlow. Embedded cluster calculations of metal complex impurrity defects: properties of the iron cyanide in NaCl. *J. Phys.: Condens. Matter*, 12:8257–8266, 2000.

115. Peter V. Sushko, Alexander L. Shluger, and C. Richard A. Catlow. Relative energies of surface and defect states: ab initio calculations for the mgo (001) surface. *Surface Science*, 450(3):153 – 170, 2000.

116. J. S. Braithwaite, P. V. Sushko, K. Wright, and R. C. A. Catlow. Hydrogen defects in forsterite: A test case for the embedded cluster method. *The Journal of Chemical Physics*, 116(6):2628–2635, 2002.

117. J. S. Braithwaite, K. Wright, and R. C. A. Catlow. A theoretical study of the energetics and ir frequencies of hydroxyl defects in forsterite. *J. Geophys. Res.*, 108:2284, 2003.

118. A. M. Walker, S. Demouchy, and K. Wright. Computer modelling of the energies and vibrational properties of hydroxyl groups in α- and β-Mg_2SiO_4. *Eur. J. Mineral.*, 18:529–543, 2006.

119. A. M. Walker, S. M. Woodley, B. Slater, and K. Wright. A computational study of magnesium point defects and diffusion in forsterite. *Phys. Earth Planet. In.*, 172(1-2):20 – 27, 2009.

120. M. Leslie and M. J. Gillan. The energy and elastic dipole tensor of defects in ionic crystal calculated by the supercell method. *J. Phys. C: Solid State Phys.*, 18:973–982, 1985.

121. G. Makov and M. C. Payne. Periodic boundary conditions in ab initio calculations. *Phys. Rev. B*, 51:4014–4022, 1995.

122. L. N. Kantorovich. Elimination of the long-range interaction in calculations with periodic boundary conditions. *Phys. Rev. B*, 60:15475–15479, 1999.

123. L. N. Kantorovich and I. I. Tupitsyn. Coulomb potential inside a large finite crystal. *J. Phys.: Condens. Matter*, 11:6159–6168, 1999.

124. J. P. Poirier. *Creep of Crystals*. Cambridge University Press, 1985.

125. V. S. Solomatov, R. El-Khozondar, and V. Tikare. Grain size in the lower mantle: constraints from numerical modeling of grain growth in two-phase systems. *Phys. Earth Planet. In.*, 129:265–282, 2002.

126. S. Karato, S. Zhang, and H. R. Wenk. Superplasticity in Earth's lower mantle: evidence from seismic anisotropy and rock physics. *Science*, 270:458–461, 1995.

127. C. Herring. Diffusional viscosity of a polycrysralline solid. *J. Appl. Phys.*, 21:437–445, 1950.

128. R. L. Stocker and M. F. Ashby. On the rheology of the upper mantle. *Rev. Geophys. Space Ge.*, 11:391–426, 1973.

129. M. Handy. Flow laws for rocks containing two non-linear viscous phases: A phenomenological approach. *J. Struct. Geol.*, 16:287–301, 1994.

130. Y.-T. Takeda. Flow in rocks modelled as a multiphase continua: Application to polymineral rocks. *J. Struct. Geol.*, 20:1569–1578, 1998.

131. D. Yamazaki and S.-I. Karato. Some mineral physics constraints on the rheology and geothermal structure of Earth's lower mantle. *Am. Mineral.*, 86:185–391, 2001.

132. J. P. Poirier. *Introduction to the Physics of the Earth's Interior*. Cambridge University Press, 1991.

133. M. W. Ammann, J. P. Brodholt, and D. P. Dobson. Simulating Diffusion. *Reviews in Mineralogy and Geochemistry: Theoretical and Computational Methods in Mineral Physics: Applications to Geophysics*, 71:201–224, 2010.

134. M. W. Ammann, J. P. Brodholt, J. Wookey, and D. P. Dobson. First-principles constraints on diffusion in lower-mantle minerals and a weak D″ layer. *Nature*, 466:462–465, 2010.

135. M. W. Ammann, J. P. Brodholt, and D. P. Dobson. Ferrous iron diffusion in ferro-periclase across the spin transition. *Earth Plant. Sc. Lett.*, -:doi:10.1016/j.epsl.2010.12.031, 2010.

136. I. Jackson. Elasticity, composition and temperature of the Earth's lower mantle: a reappraisal. *Geophysical Journal International*, 134:291–311, 1998.

137. J.-F. Lin, D. L. Heinz, H.-K. Mao, R. J. Hemley, J. M. Devine, and G. Shen. Stability of magnesiowüstite in Earth's lower mantle. *P. Natl. Acad. Sci. USA*, 100:4405–4408, 2002.

138. E. A. Kotomin, M. M. Kuklja, R. I. Eglitis, and A. I. Popov. Quantum chemical simulations of the optical properties and diffusion of electron centres in MgO. *Materials Science and Engineering B*, 37:212–214, 1996.

139. L. Vočadlo, A. Wall, S. C. Parker, and G. D. Price. Absolute ionic diffusion in MgO - computer calculations via lattice dynamics. *Phys. Earth Planet. In.*, 88:193–210, 1995.

140. J. H. Harding. Defects and clusters in UO_2 and (U,Pu)O_2. *J. Chem. Soc., Faraday Trans 2*, 83:1177–1187, 1987.

141. Y. Ito and M. Toriumi. Pressure effect of self-diffusion in periclase (MgO) by molecular dynamics. *J. Geophys. Res.*, 112:B04206: 1–7, 2007.

142. C. A. Gilbert, S. D. Kenny, R. Smith, and E. Sanville. Ab initio Study of Point Defects in Magnesium Oxide. *Phys. Rev. B*, 76:184103:1–10, 2007.

143. E. A. Kotomin and A. I. Popov. Radiation-induced point-defects in simple oxides. *Nuclear Instruments and Methods in Physics Research B*, 141:1–15, 1998.

144. J. Ita and R. E. Cohen. Effects of pressure on diffusion and vacancy formation in MgO from nonempirical free-energy integrations. *Phys. Rev. Lett.*, 79:3198–3201, 1997.

145. A. De Vita, M. J. Gillan, J. S. Lin, M. C. Payne, I. Stich, and L. J. Clarke. Defect energetics in MgO treated by first-principles methods. *Phys. Rev. B*, 46:12964–3322, 1992.

146. J. H. Harding, M. J. L. Sangster, and A. M. Stoneham. Cation diffusion in alkaline-Earth oxides. *J. Phys. C: Solid State Phys*, 20:5281–5292, 1987.

147. M. J. L. Sangster and D. K. Rowell. Calculation of defect energies and volumes in some oxides. *Phil. Mag. A*, 44:613–624, 1981.

148. W. C. Mackrodt and R. F. Stewart. Defect properties of ionic solids. III. The calculation of the point-defect structure of the alkaline-Earth oxides and CdO. *J. Phys. C: Solid State Phys.*, 12:5015–5036, 1979.

149. H.-I. Yoo, B. J. Wuensch, and W. T. Petuskey. Oxygen self-diffusion in single-crystal MgO: Secondary-ion mass spectrometric analysis with comparison of results from gas-solid and solid-solid exchange. *Solid State Ionics*, 150:207–221, 2002.

150. S. Shirasaki and M. Hama. Oxygen-diffusion characteristics of loosely sintered polycrystalline MgO. *Chem. Phys. Lett.*, 20:361–365, 1973.

151. S. Shirasaki and H. Yamamura. -. *Japanese Journal of applied Physics*, 12:1634, 1970.

152. Y. Oishi and W. D. Kingery. Oxygen diffusion in periclase crystals. *J. Chem. Phys.*, 33:905–906, 1960.

153. S. Mackwell, Bystricky M., and C. Sproni. Fe-Mg interdiffusion in (Mg,Fe)O. *Phys. Chem. Miner.*, 32:418–425, 2005.

154. M. H. Yang and C. P. Flynn. Intrinsic diffusion properties of an oxide: MgO. *Phys. Rev. Lett.*, 13:1809–1812, 1994.

155. D. R. Sempolinsky and W. D. Kingery. Ionic conductivity and magnesium vacancy mobility in magnesium oxide. *Journal of America Ceramics Society*, 63:664–669, 1980.

156. M. Duclot and C. Departes. Effect of impurities on cationic conductivity of magnesium-oxide single-crystals. *J. Solid State Chem.*, 31:337–385, 1980.

157. B. J. Wuensch, W. C. Steele, and T. Vasilos. Cation self-diffusion in single-crystal MgO. *J. Chem. Phys.*, 58:5258–5266, 1973.

158. R. Lindner and G. D. Parfitt. Diffusion of radioactive magnesium in magnesium oxide crystals. *J. Chem. Phys.*, 26:182–185, 1957.

159. J. Ita and R. E. Cohen. Diffusion in MgO at high pressure: implications for lower mantle rheology. *Geophys. Res. Lett.*, 25:1–4, 1998.

160. M. H. Yang and C. P. Flynn. Ca^{2+} and $^{18}O^{2-}$ diffusion in ultrapure MgO. *J Phys: Condens Matter*, 8:L279–L283, 1996.

161. D. Alfè and M. J. Gillan. The Shottky defect formation energy in MgO calculated by diffusion Monte Carlo. *Phys. Rev. B*, 71:220101: 1–3, 2005.

162. P. W. M. Jacobs. The entropy of a point defect in an ionic crystal. *J. Chem. Soc. Faraday Trans.*, 86:1197–1201, 1990.

163. J. Narayan and J. Washburn. Self-diffusion in magnesium oxide. *Acta Metallurgica*, 21:533–538, 1973.

164. I. Sakaguchi, H. Yurimoto, and S. Sueno. Self-diffusion along dislocations in single-crystal MgO. *Solid State Communications*, 84:889–893, 1992.

165. J. D. Hodge and R. S. Gordon. Grain growth and creep in polycrystalline magnesium oxide fabricated with and without a Lif additive. *Ceramurgia international*, 4:17–20, 1978.

166. J. Wolfenstine and D. L. Kohlstedt. Creep of (Mg,Fe)O single crystals. *Journal of Materials Science*, 23:3550–3557, 1988.

167. I. Stretton, F. Heidelbach, S. Mackwell, and F. Langenhorst. Dislocation creep of magnesiowüstite ($Mg_{0.8}Fe_{0.2}O$). *Earth Planet. Sc. Lett.*, 194:229–240, 2001.

168. G. D. Price, A. Wall, and S. C. Parker. The properties and behaviour of mantle ninerals: a computer-simulation approach. *Philosophical Transactions of the Royal Society of London. Series A, Mathematical and Physical Sciences*, 328:391–407, 1989.

169. K. Sato T. Katsura and E. Ito. Electrical conductivity of silicate perovskite at lower-mantle conditions. *Nature*, 395:493–495, 1998.

170. Y. Xu, C. McCammon, and B. T. Poe. The effect of alumina on the electrical conductivity of silicate perovskite. *Science*, 282(5390):922–924, 1998.

171. S. Lauterbach, C. A. McCammon, P. van Aken, F. Langenhorst, and F. Seifert. Mössbauer and ELNES spectroscopy of (Mg,Fe)(Si,Al)O_3 perovskite: A highly oxidised component of the lower mantle. *Contrib. Mineral. Petrol.*, 138:17–26, 2000.

172. E. W. Elcock and C. W. McCombie. Vacancy diffusion in binary ordered alloys. *Phys. Rev.*, 109:605–606, 1957.

173. H. B. Huntington, N.C. Miller, and V. Nerses. Self-diffusion in 50-50 gold-cadmium. *Acta metall.*, 9:749–754, 1961.

174. S. B. Debiaggi, P. M. Decorte, and A. M. Monti. Diffusion by vacancy mechanism in Ni, Al, and Ni_3Al: calculation based on many-body potentials. *Phys. Stat. Sol.*, 195:37–54, 1996.

175. S. Divinski and C. Herzig. On the six-jump cycle mechanism of self-diffusion in NiAl. *Intermetallics*, 8:1357–1368, 2000.

176. J. Duan. Atomistic simulations of diffusion mechanisms in stoichiometric Ni_3Al. *J. Phys.: Condens. Matter*, 18:1381–1394, 2006.

177. M. Arita, M. Koiwa, and S. Ishioka. Diffusion mechanisms in ordered alloys - a detailed analysis of six-jump vacancy cycle in the B2 type lattice. *Acta metall.*, 37:1363–1374, 1989.

178. L. M. Hirsch and T. J. Shankland. Point defects in (Mg,Fe)SiO_3 perovskite. *Geophys. Res. Lett.*, 18:1305–1308, 1991.

179. K. Litasov, E. Ohtani, F. Langenhorst, H. Yurimoto, T. Kubo, and T. Kondo. Water solubility in mg-perovskites and water storage capacity in the lower mantle. *Earth Planet. Sc. Lett.*, 211:189–203(15), 2003.

180. N. Bolfan-Casanova. Water in the earth's mantle. *Mineral Mag.*, 69:229–257, 2005.

181. F. Béjina and O. Jaoul. Silicon diffusion in minerals. *Earth Planet. Sc. Lett.*, 153:229–238, 1997.

182. F. Béjina, O. Jaoul, and R. C. Liebermann. Diffusion in minerals at high Pressure: a review. *Phys. Earth Planet. In.*, 139:3–20, 2003.

183. G. Roma, Y. Limoge, and S. Baroni. Oxygen Self-Diffusion in α-Quartz. *Phys. Rev. Lett.*, 86:4564–4567, 2001.

184. W. Schilling. Self-interstitial atoms in metals. *J. Nuc. Mat.*, 69 and 70:465–489, 1978.

185. S.-G. Lee W.-C. Lee and K. J. Chang. First-Principles Study of the Self-Interstitial Diffusion Mechanism in Silicon. *J. Phys. Condens. Matter*, 10:995–1002, 1998.

186. D. P. Dobson and J.P. Brodholt. The electrical conductivity and thermal profile of the Earth's mid-mantle. *Geophys. Res. Lett.*, 27:2325–2328, 2000.

187. T. J. Shankland, J. Peyronneau, and J.-P. Poirier. Electrical conductivity of the Earth's lower mantle. *Nature*, 366:453–455, 1993.

188. A. Kuvshinov and N. Olsen. A Global Model of Mantle Conductivity Derived from 5 Years of CHAMP, Orsted and SAC-C Magnetic data. *Geophys. Res. Lett.*, 33:L18301:1–5, 2006.

189. N. Olsen. Long-period (30 days - 1 year) electromagnetic sounding and the electrical conductivity of the lower mantle beneath Europe. *Geophys. J. Int.*, 138:179–187, 1999.

190. K. Ohta, S. Onoda, K. Hirose, R. Sinmyo, K. Shimizu, N. Sata, Y. Ohishi, and A. Yasuhara. The electrical conductivity of post-perovskite in Earth's D″ layer. *Science*, 320:89–91, 2008.

191. L. A. Hayden and E. B. Watson. A Diffusion Mechanism for Core-Mantle Interaction. *Nature*, 450:709–712, 2007.

192. G. Ranalli. Mantle rheology: radial and lateral viscosity variations inferred from microphysical creep laws. *J. Geodyn.*, 32:425–444, 2001.

193. A. Paulson, S. Zhong, and J. Wahr. Inference of mantle viscosity from GRACE and relative sea level data. *Geophys. J. Int.*, 171:497–508, 2007.

194. F. D. Stacey. *Physics of the Earth*. Brooksfield Press, 1992.

195. K. Umemoto, R. M. Wentzcovitch, and P. B. Allen. Dissociation of $MgSiO_3$ in the cores of gas giants and terrestrial exoplanets. *Science*, 311:983–986, 2006.

196. S. A. Hunt, D. J. Weidner, L. Li, L. Wang, N. P. Walte, J. P. Brodholt, and D. P. Dobson. Weakening of calcium iridate during its transformation from perovskite to post-perovskite. *Nature Geoscience*, 2:794–797, 2009.

197. A. R. Oganov, J. P. Brodholt, and G. D. Price. The elastic constants of $MgSiO_3$ perovskite at pressures and temperatures of the Earth's mantle. *Nature*, 411:934–937, 2001.

198. S. Stackhouse, J. P. Brodholt, J. Wookey, J.-M. Kendall, and G. D. Price. The effect of temperature on the seismic anisotropy of the perovskite and post-perovskite polymorphs of $MgSiO_3$. *Earth Planet. Sc. Lett.*, 230:1–10, 2005.

199. J. Wookey, J.-M. Kendall, and G. Rümpker. Lowermost mantle anisotropy beneath the north Pacific from differential S-ScS splitting. *Geophys. J. Int.*, 161:829–838, 2005.

200. S. Stackhouse and J. P. Brodholt. The high temperature elasticity of $MgSiO_3$ post-perovskite. *Geophysical Monograph: Post-perovskite - The last mantle phase transition*, 174:99–113, 2007.

201. R. M. Wentzcovitch, B. B. Karki, M. Cococcioni, and S. de Gironcoli. Thermoelastic properties of of $MgSiO_3$ perovskite: insights on the nature of the Earth's lower mantle. *Phys. Rev. Lett.*, 92:018501, 2004.

202. R. M. Wentzcovitch, T. Tsuchiya, and J. Tsuchiya. $MgSiO_3$ postperovskite at D″ conditions. *P. Natl. Acad. Sc. USA*, 103:543–546, 2006.

203. H. Čížková, O. Čadek, C. Matyska, and D. A. Yuen. Implications of post-perovskite transport properties for core-mantle dynamics. *Phys. Earth Planet. In.*, In Press, Corrected Proof:–, 2009.

204. O. Čadek and L. Fleitout. Effect of lateral viscosity variations in the core-mantle boundary region on predictions of the long-wavelength geoid. *Stud. Geophys. Geod.*, 50:217–232, 2005.

205. J. T. Browaeys and S. Chevrot. Decomposition of the elastic tensor and geophysical applications. *Geophys. J. Int.*, 159:667–678, 2004.

206. D. Yamazaki, T. Yoshino, H. Ohfuji, J.-I. Ando, and A. Yoneda. Origin of seismic anisotropy in the D″ layer inferred from shear deformation experiments on post-perovskite phase. *Earth Planet. Sc. Lett.*, 252:372–378, 2006.

207. D. Mainprice. Seismic anisotropy of the deep Earth from a mineral and rock physics perspective. *Treatise on Geophysics*, 2:437–492, 2007.

208. T. Lay and E. J. Garnero. Reconciling the post-perovskite phase with seismological observations of lowermost mantle structure. *Geophysical Monograph: Post-perovskite - The last mantle phase transition*, 174:129–153, 2007.

209. J. F. Nye. *Physical Properties of Crystals: Their Representation by Tensors and Matrices*. Oxford University Press, 1985.

210. D. M. Parks and S. Ahzi. Polycrystalline plastic deformation and texture evolution for crystals lacking five independent slip systems. *J. Mech. Phys. Solids.*, 38:701–724, 1990.

211. P. D. Bons and B. den Brok. Crystallographic preferred orientation development by dissolution-precipitation creep. *J. Struct. Geol.*, 22:1713–1722, 2000.

212. J. G. Barreiro, I. Lonardelli, H. R. Wenk, G. Dresen, E. Rybacki, Y. Ren, and C. N. Tome. Preferred orientation of anorthite deformed experimentally in Newtonian creep. *Earth Planet. Sc. Lett.*, 264:188–207, 2007.

213. M. Sundberg and R. F. Cooper. Crystallographic preferred orientation produced by diffusional creep of harzburgite: effects of chemical interactions among phases during plastic flow. *J. Geophys. Res.*, 113:B12208:1–16, 2008.

214. T. Lapworth, J. Wheeler, and D. J. Prior. The deformation of plagioclase investigated using electron backscatter diffraction crystallographic preferred orientation data. *J. Struct. Geol.*, 24:387–399, 2002.

215. J. Wheeler. The preservation of seismic anisotropy in the Earth's mantle during diffusion creep. *Geophys. J. Int.*, 178:1723–1732, 2009.

216. R. Fisher. Dispersion on a sphere. *P. Roy. Soc. Lond. A Mat.*, 217:295–305, 1953.

217. R. F. Butler. *Paleomagnetism: magnetic domains to geologic terranes (Chapter 6)*. Blackwell Science, 1992.

218. S. Ohnishi. A theory of the pressure-induced high-spin–low-spin transition of transition-metal oxides. *Physics of The Earth and Planetary Interiors*, 17:130 – 139, 1978.

219. R. E. Cohen, I. I. Mazin, and D. G. Isaak. Magnetic collapse in transition metal oxides at high perssure: implications for the Earth. *Science*, 275:654–657, 1997.

220. E. Mattern, J. Matas, Y. Ricard, and J. Bass. Lower mantle composition and temperature from mineral physisc and thermodynamic modelling. *Geophys. J. Int.*, 160:973–990, 2005.

221. R. S. Gordon. Mass transport in the diffusional creep of ionic solids. *Journal of the American Ceramic Society*, 56:147–152, 1973.

222. R. S. Gordon. *Diffusional creep phenomena in polycrystalline oxides: in Schock, R. N. (Ed), Point defects in minerals, Geophysical Monograph 31.* AGU, 1985.

223. K. L. Crispin and J. A. van Orman. Influence of the crystal field effect on chemical transport in Earth's mantle: Cr^{3+} and Ga^{3+} diffusion in periclase. *Physics of the Earth and Planetary Interiors*, 180:159–171, 2010.

224. W. H. Gourdin and W. D. Kingery. The defect structure of mgo containing trivalent cation solutes: shell model calculations. *Journal of Materials Science*, 14:2053–2073, 1979.

225. M. Cococcioni and S. de Gironcoli. Linear response approach to the calculation of the effective interaction paramters in the LDA+U method. *Pysical Review B*, 71:035105:1–16, 2005.

226. A. B. Lidiard. Impurity diffusion in crystals (mainly ionic crystals with the sodium chloride structure). *Philos. Mag.*, 46:1218–1237, 1955.

227. A. B. Lidiard. The influence of solutes on self-diffusion in metals. *Philos. Mag.*, 5:1171–1180, 1960.

228. J. Manning. Correlation factors for impurity diffusion. bcc diamond, and fcc. *Phys. Rev.*, 136:A1758–A1766, 1964.

229. J.-F. Lin, G. Vankó, S. D. Jacobsen, V. Iota, V. V. Struzhkin, V. B. Prakapenka, A. Kuznetsov, and C.-S. Yoo. Spin transition zone in Earth's lower mantle. *Science*, 317:1740–1743, 2007.

230. J. C. Crowhurst, J. M. Brown, A. F. Goncharov, and S. D. Jacobsen. Elasticity of (Mg,Fe)O through the spin transition of iron in the lower mantle. *Science*, 319:451–453, 2008.

231. H. Marquardt, S. Speziale, H. J. Reichmann, D. J. Frost, F. R. Schilling, and E. J. Garnero. Elastic shear anisotropy of ferropericlase in Earth's lower mantle. *Science*, 324:224–226, 2009.

232. C. McCammon. Effect of pressure on the composition of the lower mantle end member Fe_xO. *Science*, 259:66–68, 1993.

233. D. Yamazaki, T. Yoshino, T. Matsuzaki, T. Katsura, and A. Yoneda. Texture of (Mg,Fe)SiO_3 perovskite and ferro-periclase aggregate: implications for rheology of the lower mantle. *Phys. Earth Planet. In.*, 274:138–144, 2009.

234. J. A. Van Orman, C. Li, and K. L. Crispin. Aluminum diffusion and Al-vacancy association in periclase. *Phys. Earth Planet. In.*, 172:34–42, 2009.

235. B. M. Steinberger and A. R. Calderwood. Models of large-scale viscous flow in the Earth's mantle with constraints from mineral physics and surface observations. *Geophys. J. Int.*, 167:1461–1481, 2006.

236. W. R. Peltier and R. Drummond. Rheological stratification of the lithosphere: a direct inference based upon the geodetically observed pattern of the glacial isostatic adjustment of the North American continent. *Geophys. Res. Lett.*, 35:L16314:1–5, 2008.

237. J. Wookey, J.-M. Kendall, and G. Barruol. Mid-mantle deformation inferred from seismic anisotropy. *Nature*, 415:777–780, 2002.

238. H.-C. Nataf and J. VanDecar. Seismological detection of a mantle plume? *Nature*, 364:115–120, 1993.

239. A.-L. Auzende, J. Badro, F. J. Ryerson, P. K. Weber, S. J. Fallon, A. Addad, J. Siebert, and G. Fiquet. Elemt partitioning between magnesium silicate perovskite and ferro-periclase: new insights into bulk lower-mantle geochemistry. *Earth Planet. Sc. Lett.*, 269:164–174, 2008.

240. T. Sakai, E. Ohtani, H. Terasaki, M. Miyahara, M. Nishijima, N. Hirao, Y. Ohishi, and N. Sata. Fe-Mg partitioning between post-perovskite and ferropericlase in the lowermost mantle. *Phys. Chem. Minerals*, 37:487–496, 2010.

241. T. Irifune, T. Shinmei, C. A. McCammon, N. Miyajima, D. C. Rubie, and D. J. Frost. Iron partitioning and density changes of pyrolite in Earth's loewr mantle. *Science*, 327:193–195, 2010.

242. K. Catalli, S.-H. Shim, V. B. Prakapenka, J. Zhao, W. Sturhahn, P. Chow, Y. Xiao, H. Liu, H. Cynn, and W. J. Evans. Spin state of ferric iron in $MgSiO_3$ perovskite abd its effect on elastic properties. *Earth Planet. Sc. Lett.*, 289:68–75, 2010.

243. F. Zhang and A. R. Oganov. Valence state and spin transitions of iron in Earth's mantle silicates. *Earth Planet. Sc. Lett.*, 249:436–443, 2006.

244. S. Stackhouse, J. P. Brodholt, and G. D. Price. Electronic spin transitions in iron-bearing $MgSiO_3$ perovskite. *Earth Planet. Sc. Lett.*, 253:282–290, 2007.

245. A. Bengtson, K. Persson, and D. Morgan. Ab initio study of the composition dependece of the pressure induced spin crossover in perovskite $(Mg_{1-x},Fe_x)SiO_3$. *Earth Planet. Sc. Lett.*, 265:535–545, 2008.

246. K. Umemoto, R. M. Wentzcovitch, Y. G. Yu, and R. Requist. Spin transition in $(Mg,Fe)SiO_3$ perovskite under pressure. *Earth Planet. Sc. Lett.*, 276:198–206, 2009.

247. T. Stachel, J. W. Harris, G. A. Brey, and W. Joswig. Kankan diamonds (Guinea) II: lower mantle inclusion parageneses. *Contrib. Mine. Petrol.*, 140:16–27, 2000.

248. B. J. Wood. Phase transformations and partitioning relations in peridotite under lower mantle conditions. *Earth Planet. Sci. Lett.*, 174:341–354, 2000.

249. N. C. Richmond and J. P. Brodholt. Calculated role of aluminium in the incorporation of ferric iron into magnesium silicate perovskite. *American Mineralogist*, 82:947–951, 1998.

250. J. A. Van Orman. On the viscosity and creep mechanism of Earth's inner core. *Geophys. Res. Lett.*, 31:L20606:1–4, 2004.

251. A. S. Côté, L. Vočadlo, D. P. Dobson, D. Alfè, and J. P. Brodholt. Ab initio lattice dynamics calculations on the combined effect of temperature and silicon on the stability of different iron phases in the Earth's inner core. *Physics of the Earth and Planetary Interiors*, 178:2–7, 2010.

252. L. Vočadlo and Alfè, D. and Gillan, M.J. and Wood, I. G. and Brodholt, J. P. and Price, G. D. Possible thermal and chemical stabilization of bedy-centred-cubic iron in the Earth's core. *Nature*, 424:536–539, 2003.

Parameters for the Diffusion Rate in Lower Mantle Minerals

Periclase

Table 10: Calculated values of the quantities required for the absolute diffusion rate in MgO periclase. Values in brackets are calculated in a $3\times3\times3$ supercell. Values marked with * are calculated within LDA, not marked values were obtained within GGA

Pressure [GPa]	ΔH_{Mg} [eV]	$\tilde{\nu}_{Mg}$ [THz]	ΔH_O [eV]	$\tilde{\nu}_O$ [THz]	l [Å]
4.96 (5.25)	2.21 (2.06, 1.95*)	12.12	2.36 (2.20, 2.08*)	13.82[a]	2.9645
10.95	2.37	-	-	-	2.9345
18.68	2.55	-	-	-	2.8991
27.67	2.74	-	-	-	2.8638
30.15 (30.32)	2.79 (2.61, 2.50*)	22.69	3.02 (2.82, 2.71*)	19.18	2.8537
136.06 (136.64)	3.95 (3.88, 3.79*)	28.40	4.34 (4.27, 4.17*)	30.77	2.6294
293.70	4.5	28.56	4.86	36.26	2.4749

[a] 27.64 considering the bifurcation

Perovskite

Magnesium and Oxygen

The investigated migration pathways for oxygen and magnesium diffusion in perovskite are explained in Figures 47 and 48[92]. In perovskite the jump-distances become vectors such that diffusion along different principal crystal axes differ from each other. The jump vectors and their pressure dependence are given in table 14. The migration enthalpies and jump frequencies are given in tables 12, 13 and 11.

Table 11: Calculated values (in a $2\times2\times1$ supercell) of the quantities required for the absolute diffusion rate of magnesium in $MgSiO_3$ perovskite. Values in brackets are calculated in a $2\times2\times2$ supercell. Values marked with * are calculated within LDA, not marked values were obtained within GGA

Pressure	ΔH^a_{Mg}	$\tilde{\nu}^a_{Mg}$	ΔH^b_{Mg}	$\tilde{\nu}^b_{Mg}$	ΔH^z_{Mg}	$\tilde{\nu}^z_{Mg}$
0.34	3.12 (3.02)	1.84	2.84	3.87	2.96	3.54
23.86	4.07 (3.95, 3.69*)	-	3.72 (3.64, 3.40*)	5.39	3.8 (3.84, 3.59*)	-
52.66	4.95	-	4.52	-	-	-
87.5	5.82	-	5.31	-	-	-
108.84	6.28	-	5.74	-	-	-
139.82	6.88 (6.48, 6.24*)	8.48	6.29 (6.32, 6.09*)	20.82	6.33 (6.49, 6.22*)	22.86

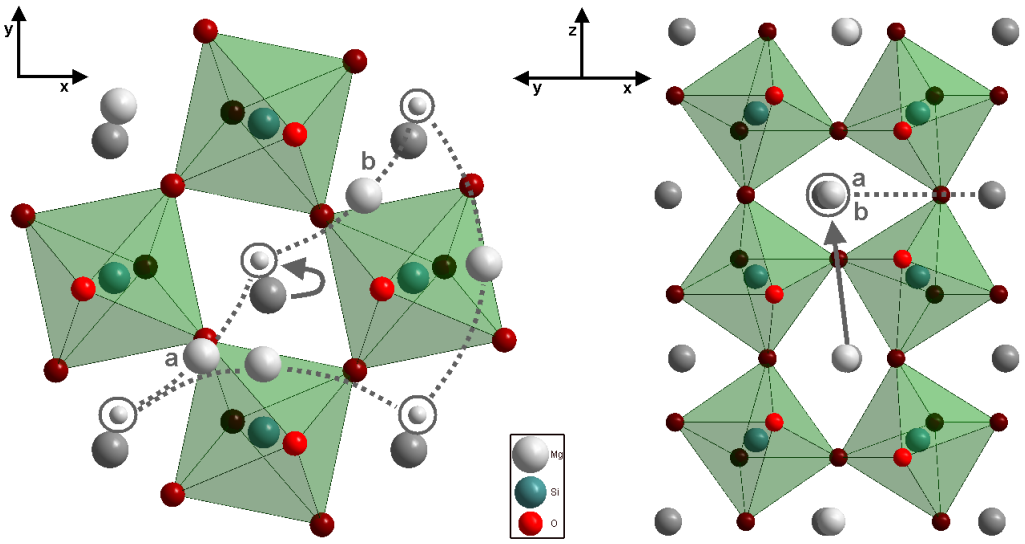

Figure 47: **Sketch of magnesium migration pathways in orthorhombic $MgSiO_3$ perovskite** left: view in z-direction, right: projection onto (110). Straight line pathways are indicated as solid arrows. Darker atoms are farther away from the observer. On the curved pathways, the migrating magnesium is positioned at the saddle-point location (only in the left figure). Vacancy locations are indicated with circles.

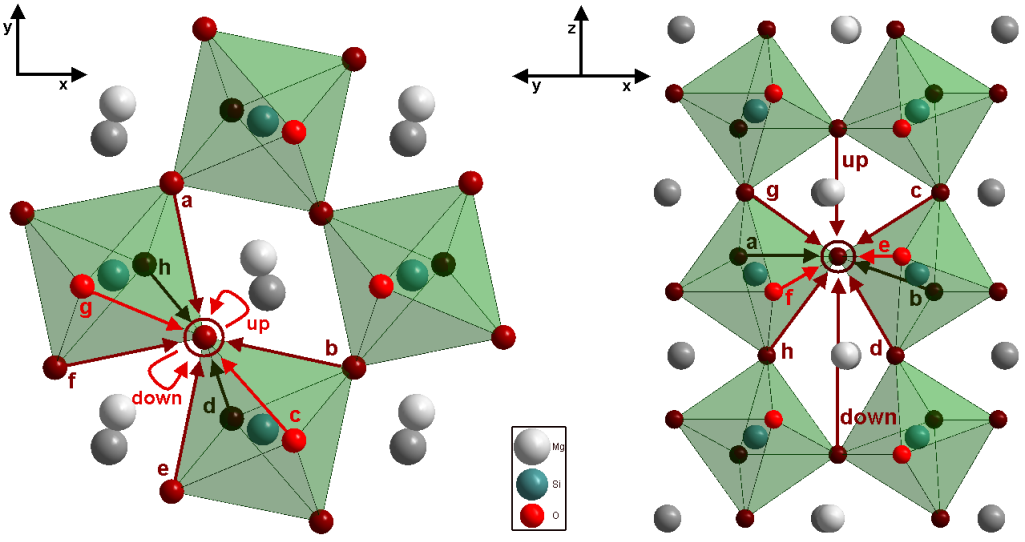

Figure 48: **Sketch of oxygen migration pathways in orthorhombic $MgSiO_3$ perovskite** left: view in z-direction, right: projection onto (110). Straight line pathways are indicated as solid arrows. Darker atoms are farther away from the observer. The vacancy location is indicated with a circle.

Table 12: Calculated migration enthalpies for different pathways of oxygen in $MgSiO_3$ perovskite using a $2 \times 2 \times 1$ supercell. Values in brackets are calculated in a $2 \times 2 \times 2$ supercell. Values marked with * are calculated within LDA, not marked values were obtained within GGA

Pressure	a=e	b=f	c	d	g	h
0.34	0.42 (0.48)	0.64	0.71	-	- (0.54)	- (0.96)
23.86	0.88 (0.95, 0.90*)	1.06 (1.03, 0.99*)	1.04 (0.96)	1.05	0.98	1.76 (1.49)
139.82	2.12 (2.18)	2.26	1.89	2.21	2.18	3.16 (2.69)

Table 13: Calculated attempt frequencies for different pathways of oxygen in $MgSiO_3$ Perovskite using a $2 \times 2 \times 1$ supercell (within GGA)

Pressure	a=e	b=f	c
0.34	1.53	-	-
23.86	2.22	4.16	8.68
139.82	8.21	-	19.86

Table 14: Jump distances of magnesium, silicon and oxygen in $MgSiO_3$ perovskite and corresponding number of equivalent jumps. The pressure dependence of the jump-distances is obtained by fitting the scaling factor S=[1, 0.9716, 0.9475, 0.9252, 0.914, 0.9] to the corresponding pressure P=[0.337, 23.861, 52.657, 87.5, 108.842, 139.82]. The jump distance at P then equals $l \cdot S$.

Jump	l_x [Å]	l_y [Å]	l_z [Å]	Z
Mg_a	2.264	2.487	0	2
Mg_b	2.556	2.487	0	2
Mg_z	0.146	0.560	3.485	2
$Si_{\langle 100\rangle}$	4.820	0	0	2
$Si_{\langle 010\rangle}$	0	4.974	0	2
$Si_{\langle 001\rangle}$	0	0	3.485	2
$Si_{\langle 110\rangle}$	2.410	2.487	0	4
$Si_{\langle 111\rangle}$	2.410	2.487	3.485	8
O_a	0.509	2.487	0	2
O_b	2.410	0.480	0.755	2
O_c	1.455	1.660	1.365	1
O_d	0.446	1.307	2.120	1
O_g	1.964	0.827	1.365	1
O_h	0.955	1.180	2.120	1

Silicon: Six-Jump Cycles

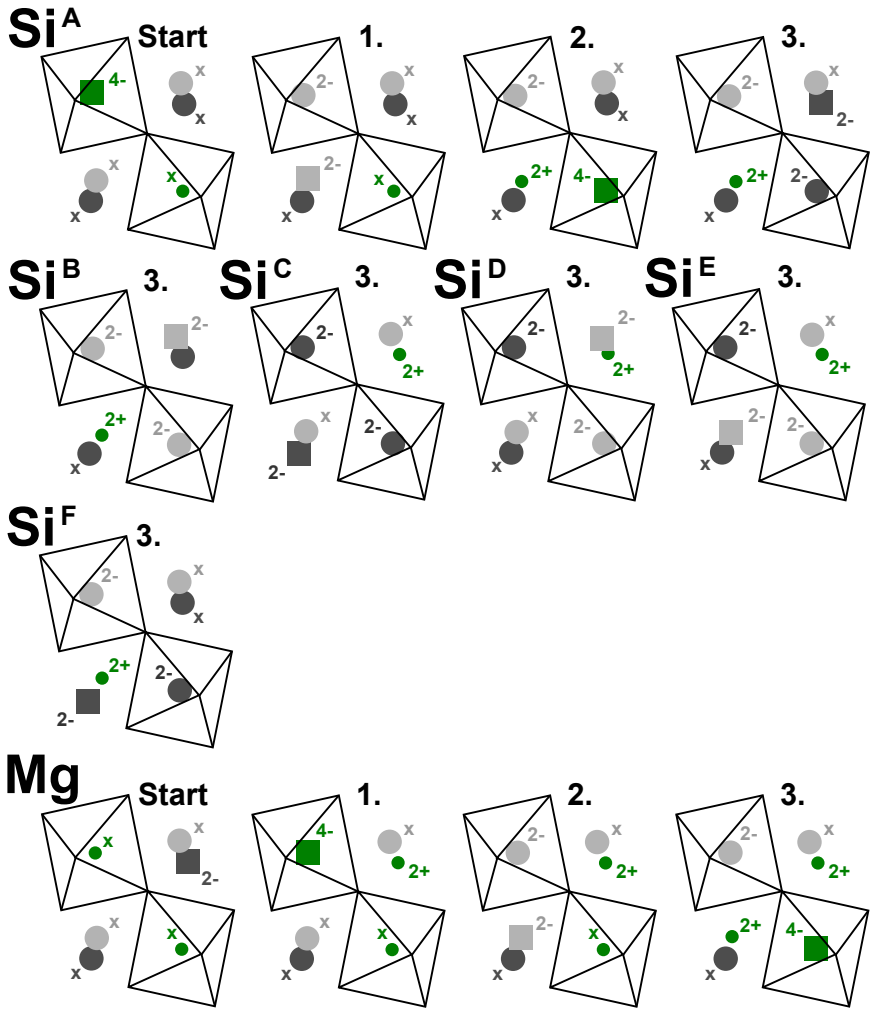

Figure 49: **Sketches of the considered six jump cycles for silicon and magnesium diffusion along $\langle 110 \rangle$ in perovskite** For cycle A of silicon and the magnesium cycle, the initial state plus the first three intermediate, activated states are shown. For the remaining silicon cycles (that have been investigated), only the most activated state is shown (which uniquely determines the cycle). All sketches also show the nominal charges carried by the atomic sites. Squares represent vacancies, green stands for silicon, grey for magnesium (dark is lower than light grey).

Table 15: Calculated energies of intermediate states and saddle-points (SP) for different six-jump cycles of silicon along ⟨110⟩ in $MgSiO_3$ perovskite using a $2 \times 2 \times 1$ supercell. Values in brackets are calculated in a $2 \times 2 \times 2$ supercell. Attempt-frequencies have only been calculated in a $2 \times 2 \times 1$ supercell and the values on the same level as energies of states are for the forward jumps (towards the next state) while backward jumps are on the level of the saddle-point energies. Values marked with * are calculated within LDA, unmarked values were obtained within GGA

Pressure	E^A [eV] 23.86 GPa	ν^A [THz] 23.86 GPa	E^A [eV] 139.82 GPa	ν^A [THz] 139.82 GPa	E^B [eV] 23.86 GPa	E^C [eV] 23.86 GPa	E^D [eV] 23.86 GPa	E^E [eV] 23.86 GPa	E^F [eV] 23.86 GPa
Initial State	0	1.64	0	5.05	0	(0)	0	(0)	(0)
1^{st} SP	1.47 (1.42)	7.64	2.88 (2.65, 2.47*)	39.27	1.47	-	-	(1.65)	-
State 1	-0.22 (-0.19, -0.29*)	10.21	0.57 (0.44, 0.23*)	32.92	-0.31 (-0.27)	(-0.32)	1.17	(-0.32)	-
2^{nd} SP	3.14 (3.51, 2.99*)	10.52	5.60 (6.06, 5.84*)	4.75	2.98	(2.56)	-	(2.56)	-
State 2	2.14 (2.61, 2.46*)	5.77, 5.93*	3.38 (3.85, 3.40*)	6.17	1.55 (2.03)	(1.10)	2.23	(1.10)	(2.74)
3^{rd} SP	4.23 (4.15, 3.64*)	7.52, 6.62*	6.59 (6.29, 5.98*)	13.57	4.09	(3.36)	4.18 (4.70)	(4.38)	(4.62)
State 3	2.99 (2.88, 2.61*)	11.8, 8.08*	5.25 (5.03, 4.67*)	18.62	2.81 (3.38)	(2.28)	1.95 (2.23)	(2.78)	(4.17)
4^{th} SP	4.65 (3.93, 3.38*)	9.53, 7.33*	7.54 (6.10, 5.77*)	9.85	4.53 (4.95)	(5.11)	(4.40)	(3.97)	(1.25)
State 4	1.29 (1.24, 1.15*)	5.94	2.44 (2.39, 2.25*)	4.51	1.82 (2.38)	(1.93)	(1.93)	(1.93)	-
5^{th} SP	2.55 (2.59)	5.72	4.17 (4.09, 3.91*)	26.94	2.92	(2.97)	-	-	-
State 5	-0.32 (-0.27)	6.50	0.25 (0.21. 0.02*)	17.96	-0.59	(-0.18)	-	-	-
6^{th} SP	1.86 (2.09)	1.34	3.47 (3.71, 3.49*)	2.30	1.85	-	-	-	-

Table 16: Calculated energies (in eV) of intermediate states and saddle-points (SP) for the six-jump cycles of silicon along $\langle 001 \rangle$ and to second nearest neighbours (i.e. $\langle 100 \rangle$, $\langle 010 \rangle$ and $\langle 111 \rangle$; see figure 50 for explanation of cycle names) in a $2 \times 2 \times 2$ supercell and magnesium (a $2 \times 2 \times 1$ supercell) in $MgSiO_3$ perovskite. Values marked with * are calculated within LDA, unmarked values were obtained within GGA

	E^{Si_x}	E^{Si_y}	$E_a^{Si_z}$	$E_a^{Si_z}$	$E_b^{Si_z}$	$E_a^{\langle 111 \rangle}$	$E_b^{\langle 111 \rangle}$	E^{Mg}
Pressure	23.86 GPa	23.86 GPa	23.86 GPa	139.82 GPa	23.86 GPa	23.86 GPa	23.86 GPa	23.86 GPa
Initial State	0	0	0	0	0	0	0	0
1^{st} SP	-	-	1.65, 1.51*	2.83, 2.64*	-	1.42	-	-
State 1	-	-	-0.32, -0.41*	-0.02, -0.19*	-	-0.19	-0.27	2.82
2^{nd} SP	-	-	2.88, 2.74*	5.26, 5.05*	-	2.93	-	5.19
State 2	2.94	3.01	2.76, 1.98*	4.28, 4.35*	-	2.04, 1.94*	2.99	3.87
3^{rd} SP	5.11	4.38	5.25, 4.98*	8.17, 7.86*	-	-	4.66	6.50
State 3	2.56	2.32	3.78, 3.57*	5.87, 5.56*	3.51	2.60, 2.38*	2.82	4.86
4^{th} SP	4.71	4.51	5.25, 4.98*	8.17, 7.86*	4.61	4.44, 4.15*	4.1	6.41
State 4	2.26	1.06	2.76, 1.98*	4.38, 4.35*	2.13	1.39, 1.31*	2.43	3.53
5^{th} SP	-	-	2.88, 2.74*	5.26, 5.05*	-	2.74	-	5.17
State 5	-	-	-0.32, -0.41*	-0.02, -0.19*	-	-0.27	-0.53	2.26
6^{th} SP	-	-	1.65, 1.51*	2.83, 2.64*	-	2.05	-	3.37

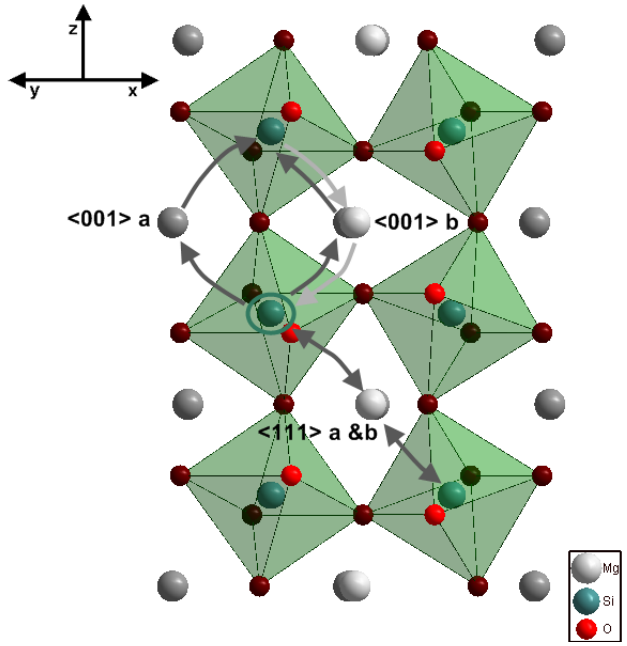

Figure 50: **Sketches of the investigated six jump cycles for silicon diffusion along $\langle 111 \rangle$ and $\langle 001 \rangle$ in perovskite (projection onto (110))**. Darker atoms are farther away from the observer. The location of the silicon vacancy is indicated with a circle.

Defect Formation and Protons

(See next two pages)

Table 17: Calculated (GGA) formation energies (in eV) of various defects in perovskite (in a $2 \times 2 \times 2$ supercell, with $2 \times 2 \times 2$ k-points grid) at 23.86 GPa. Also shown are formation energies E_F (in eV) of various reactions. The correction term[120] for charged systems is given by $\frac{1.82q^2}{\epsilon}$ where q is the charge (-2, -4,+2 for the magnesium, silicon and oxygen vacancies respectively) and ϵ the dielectric constant of the system (in the table I have used ϵ=8). PFU = per formula unit, PV = per vacancy (always using corrected values)

	#atoms (Mg,Si,O,q)	Energy	Corrected	E_F	Reaction
$MgSiO_3$	(32,32,96,0)	-1120.21	-	-35.01 PFU	$Mg + Si + 3O \rightarrow MgSiO_3$
V_{Mg}	(31,32,96,-2)	-1095.91	-1095.00	-	-
V_{Si}	(32,31,96,-4)	-1070.53	-1066.89	-	-
V_O	(32,32,95,+2)	-1129.60	-1128.69	-	-
Mg_{Si}	(33,31,96,-2)	-1095.38	-1094.47	-2.37	$MgSiO_3 + V_{Si} \rightarrow V_{Mg} + Mg_{Si}$
Si_{Mg}	(31,33,96,+2)	-1140.90	-1139.99	8.33	$MgSiO_3 + V_{Mg} \rightarrow V_{Si} + Si_{Mg}$
Bound antisites($SiMgO_3$)	(32,32,96,0)	-1117.08	-	3.13	$MgSiO_3 \rightarrow SiMgO_3$
Unbound antisites	-	-	-	5.97	$2 \cdot MgSiO_3 \rightarrow Mg_{Si} + Si_{Mg}$
$(Mg_{Mg}Mg_{Si}O_2V_O)$ A	(33,31,95,0)	-1105.30	-	20.10 PFU	$(Mg_{Mg}Mg_{Si}O_2V_O)_A - 31 \cdot MgSiO_3^{PFU}$
$(Mg_{Mg}Mg_{Si}O_2V_O)$ B	(33,31,95,0)	-1105.46	-	20.26 PFU	$(Mg_{Mg}Mg_{Si}O_2V_O)_B - 31 \cdot MgSiO_3^{PFU}$
SiO_2 Stishovite	(2,0,4,0)	-46.47	-	-23.23 PFU	$Si + 2O \rightarrow SiO_2$
MgO	(32,0,32,0)	-382.9	-	-11.97 PFU	$Mg + O \rightarrow MgO$
Full Schottky	-	-10.82	-18.10	3.62 PV	$5 \cdot MgSiO3_3 \rightarrow V_{Mg}V_{Si}3V_O + MgSiO_3$
Partial SiO_2 Schottky	-	-7.67	-13.14	4.38 PV	$3 \cdot MgSiO3_3 \rightarrow MgV_{Si}2V_OO + SiO_2$
Partial MgO Schottky	-	-3.03	-4.85	2.43 PV	$2 \cdot MgSiO3_3 \rightarrow V_{Mg}SiO_2V_O + SiO_2$
Forming Mg_{Si}	-	-	-	3.48	$MgSiO_3 + MgO \rightarrow (Mg_{Mg}Mg_{Si}O_2V_O) + SiO_2$
Forming Mg_{Si}	-	-	-	3.45	$2 \cdot MgSiO_3 \rightarrow (Mg_{Mg}Mg_{Si}O_2V_O) + 2 \cdot SiO_2$
Forming Mg_{Si}	-	-	-	6.16	$MgSiO_3 + MgO + SiO_2 \rightarrow Mg_{Si} + Si_{Mg}$

Table 18: Calculated (GGA) energies (in eV) of various protonation possibilities (introducing protons $H^\bullet$ into vacancies or interstitial sites in the perfect lattice) in perovskite (in a $2 \times 2 \times 2$ supercell, with $2 \times 2 \times 2$ k-points grid) at 23.86 GPa. Also shown are formation energies E_F (in eV) of various reactions. The correction term[120] for charged systems is given by $\frac{1.82q^2}{\epsilon}$ where q is the charge (-2, -4,+2 for the magnesium, silicon and oxygen vacancies respectively) and ϵ the dielectric constant of the system (in the table I have used ϵ=8). PFU = per formula unit (always using corrected values). Brackets mean that it is obtained from a single calculation/supercell.

	#atoms (Mg,Si,O,$H^\bullet$,q)	Energy	Corrected	E_F	Reaction
$(MgSiO_3 + H_i^\bullet)$ A	(32,32,96,1,+1)	-1131.83	-1131.61	-	on the level (along $\langle 001 \rangle$) of magnesium
$(MgSiO_3 + H_i^\bullet)$ B	(32,32,96,1,+1)	-1131.19	-1130.96	-	on the level (along $\langle 001 \rangle$) of silicon
H_2	(0,0,0,2,0)	-6.80	-	-	-
H_2O	(0,0,1,2,0)	-14.14	-	-	-
$H^\bullet_{V_{Si}}$	(32,31,96,1,-3)	-1084.24	-1082.19	-3.91	$(MgSiO_3 + H_i^\bullet) + V_{Si} \rightarrow MgSiO_3 + H^\bullet_{V_{Si}}$
$2H^\bullet_{V_{Si}}$	(32,31,96,2,-2)	-1097.99	-1097.08	-7.40	$2 \cdot (MgSiO_3 + H_i^\bullet) + V_{Si} \rightarrow 2 \cdot MgSiO_3 + 2H^\bullet_{V_{Si}}$
$3H^\bullet_{V_{Si}}$	(32,31,96,3,-1)	-1110.93	-1110.71	-9.63	$3 \cdot (MgSiO_3 + H_i^\bullet) + V_{Si} \rightarrow 3 \cdot MgSiO_3 + 3H^\bullet_{V_{Si}}$
$4H^\bullet_{V_{Si}}$	(32,31,96,4,0)	-1123.91	-	-11.44	$4 \cdot (MgSiO_3 + H_i^\bullet) + V_{Si} \rightarrow 4 \cdot MgSiO_3 + 4H^\bullet_{V_{Si}}$
$H^\bullet_{V_{Mg}}$	(31,32,96,1,-1)	-1109.26	-1109.03	-2.18	$(MgSiO_3 + H_i^\bullet) + V_{Mg} \rightarrow MgSiO_3 + H^\bullet_{V_{Mg}}$
$2H^\bullet_{V_{Mg}}$	(31,32,96,2,0)	-1122.17	-	-3.93	$2 \cdot (MgSiO_3 + H_i^\bullet) + V_{Si} \rightarrow 2 \cdot MgSiO_3 + 2H^\bullet_{V_{Si}}$
$(Mg_{Si} + H^\bullet)$	(33,31,96,1,-1)	-1107.40	-1107.17	-1.32	$(MgSiO_3 + H_i^\bullet) + Mg_{Si} \rightarrow MgSiO_3 + (Mg_{Si} + H^\bullet)$
$(Mg_{Si} + 2H^\bullet)$	(33,31,96,2,0)	-1119.40	-	-2.14	$2 \cdot (MgSiO_3 + H_i^\bullet) + Mg_{Si} \rightarrow 2 \cdot MgSiO_3 + (Mg_{Si} + 2H^\bullet)$
$(Mg_{Si} + H^\bullet_{V_{Mg}})$	(32,31,96,1,-3)	-1084.41	-1082.36	-4.21	$(MgSiO_3 + H_i^\bullet) + Mg_{Si} \rightarrow MgSiO_3 + (H^\bullet_{V_{Mg}+Mg_{Si}})$
$(Mg_{Si} + 2H^\bullet_{V_{Mg}})$	(32,31,96,2,-2)	-1097.68	-1096.77	-7.22	$2 \cdot (MgSiO_3 + H_i^\bullet) + Mg_{Si} \rightarrow 2 \cdot MgSiO_3 + 2 \cdot (Mg_{Si} + H^\bullet_{V_{Mg}})$
Forming Mg_{Si}	-	-	-	3.68	$MgSiO_3 + MgO + H_2O \rightarrow Mg_{Mg}Mg_{Si}O_3 2H + SiO_2$
Forming Mg_{Si}	-	-	-	-1.10	$MgSiO3_3 + H^\bullet_{V_{Si}} \rightarrow Mg_{Si} + H^\bullet_{V_{Mg}}$
Forming Mg_{Si}	-	-	-	0.65	$MgSiO3_3 + 2H^\bullet_{V_{Si}} \rightarrow Mg_{Si} + 2H^\bullet_{V_{Mg}}$
Forming Mg_{Si}	-	-	-	-0.23	$MgSiO3_3 + H^\bullet_{V_{Si}} \rightarrow (Mg_{Si} + H^\bullet) + V_{Mg}$
Forming Mg_{Si}	-	-	-	2.44	$MgSiO3_3 + 2H^\bullet_{V_{Si}} \rightarrow (Mg_{Si} + 2H^\bullet) + V_{Mg}$
Forming Mg_{Si}	-	-	-	1.08	$MgSiO3_3 + 2H^\bullet_{V_{Si}} \rightarrow (Mg_{Si} + H^\bullet) + H^\bullet_{V_{Mg}}$
Forming Si_{Mg}	-	-	-	7.07	$MgSiO3_3 + H^\bullet_{V_{Mg}} \rightarrow Si_{Mg} + H^\bullet_{V_{Si}}$
Forming Si_{Mg}	-	-	-	5.32	$MgSiO3_3 + 2H^\bullet_{V_{Mg}} \rightarrow Si_{Mg} + 2H^\bullet_{V_{Si}}$
Forming MgO	-	-	-	0.21	$MgSiO_3 + H_2O \rightarrow 2H^\bullet_{V_{Mg}} + MgO$
Forming SiO_2	-	-	-	1.35	$MgSiO_3 + 2H_2O \rightarrow 4H^\bullet_{V_{Si}} + SiO_2$
Forming MgO	-	-	-	5.53	$2 \cdot MgSiO_3 + H_2O \rightarrow 2H^\bullet_{V_{Si}} + Si_{Mg} + MgO$

Kinetic Monte Carlo: Cycle Breaking Jumps

Table 19: Energies (above initial state of the six-jump cycle) of the states and barriers of the six-jump cycle breaking jumps in perovskite (PV, at 23.86 GPa, in the $2 \times 2 \times 1$ supercell; in the $2 \times 2 \times 2$ supercell in brackets) and post-perovskite (PPV, at 131.61 GPa, in the $3 \times 1 \times 1$ supercell)

	Si^{PV}	Si^{PPV}	Mg^{PPV}
Barrier 7	4.15 (3.56)	2.91	8.74
State 7	-1.06 (-1.27)	-0.88	6.89
Barrier 8	4.65	6.82	9.79
State 8	2.67	3.59	5.70
Barrier 9	6.55	8.30	11.83
State 9	2.12	4.08	10.42

Post-Perovskite

The considered pathways for post-perovskite are shown in figure 51. The quantities required to calculate the absolute diffusion rate in post-perovskite are given in tables 20, 21,22 and 23. The jump vectors and their pressure dependence are given in table 24.

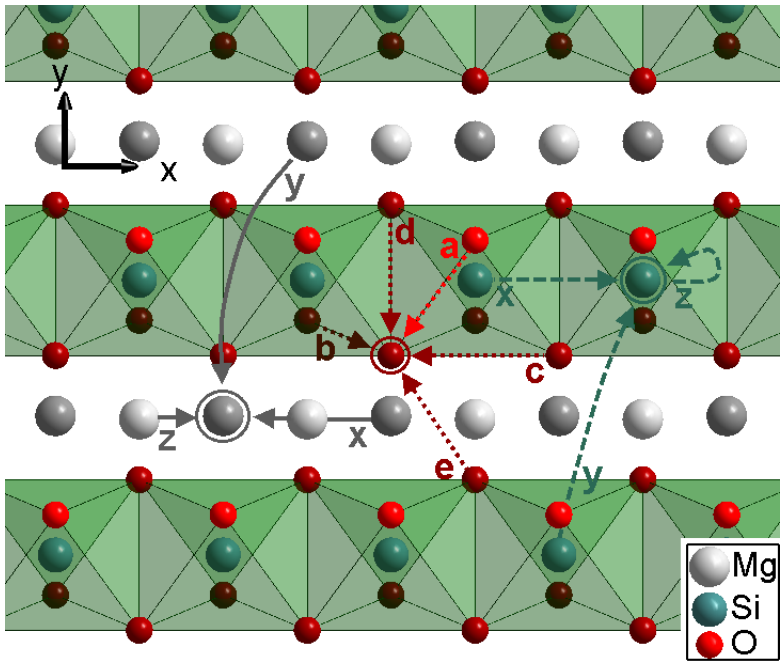

Figure 51: **Sketch of the considered migration-pathways (direct jumps only) in $MgSiO_3$ post-perovskite** Darker atoms are farther away from the observer. The ionic vacancies are marked with a circle. Solid, dashed and dotted arrows indicate migration pathways of magnesium, silicon and oxygen respectively.

Table 20: Calculated values (in a $3\times1\times1$ supercell) of the quantities required for the absolute diffusion rate of magnesium in $MgSiO_3$ post-perovskite. Values in brackets are calculated in a $3\times1\times2$ supercell. Values marked with * are calculated within LDA, unmarked values were obtained within GGA

Pressure	ΔH^x_{Mg}	$\tilde{\nu}^x_{Mg}$	ΔH^y_{Mg}	$\tilde{\nu}^y_{Mg}$	ΔH^z_{Mg}	$\tilde{\nu}^z_{Mg}$
121.50	3.29	-	13.76	-	7.95	-
131.61	3.43 (3.43, 3.28*)	11.22	14.16	-	8.19 (7.68, 7.37*)	8.31
142.28	3.58	-	14.56	-	8.43	-
505.42	6.93 (7.10)	33.34	23.13	-	13.82	22.61
1016.05	9.26 (9.60)	-	-	-	-	-

Table 21: Calculated values (in a $3 \times 1 \times 1$ supercell) of the quantities required for the absolute diffusion rate of silicon in $MgSiO_3$ post-perovskite. Values in brackets are calculated in a $3 \times 1 \times 2$ supercell. Values marked with * are calculated within LDA, unmarked values were obtained within GGA

Pressure	ΔH^x_{Si}	$\tilde{\nu}^x_{Si}$	ΔH^y_{Si}	$\tilde{\nu}^y_{Si}$	ΔH^z_{Si}	$\tilde{\nu}^z_{Si}$
121.50	3.04	-	13.57	-	-	-
131.61	3.01 (3.26, 3.27*)	65.84, 66.27[a]	13.81 (13.52)	51.44	(6.61, 6.51*)	-
142.28	2.99	-	14.05	-	-	-
505.42	2.52	78.56	18.82	-	-	-

[a]increased cut-off energy of 1500 eV

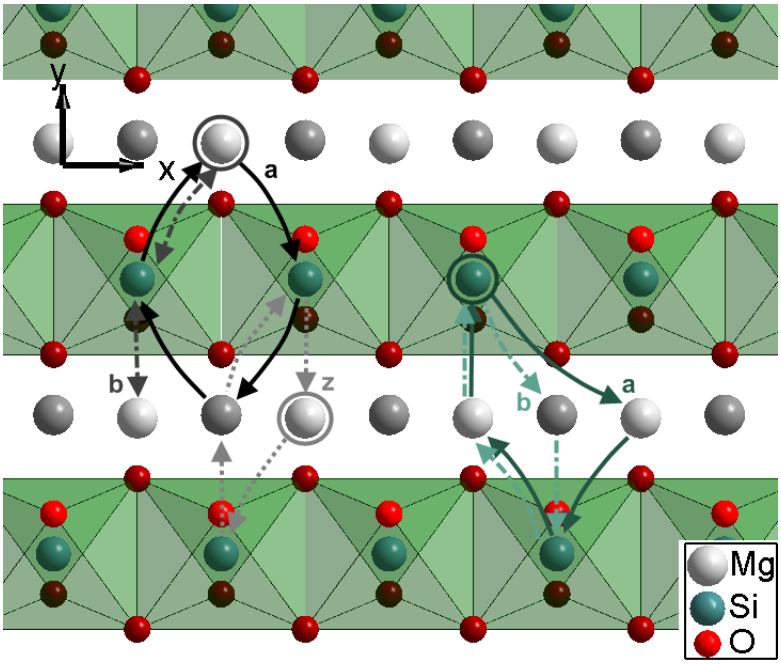

Figure 52: **Sketches of the investigated six jump cycles for silicon and magnesium diffusion along $\langle 010 \rangle$ and $\langle 001 \rangle$ in post-perovskite (view in z direction)** Darker atoms are farther away from the observer. The initial positions of the vacancies are indicated with a circles.

Table 22: Calculated values (in a $3 \times 1 \times 1$ supercell) of the quantities required for the absolute diffusion rate of oxygen in $MgSiO_3$ post-perovskite. Values in brackets are calculated in a $3 \times 1 \times 2$ supercell. Values marked with * are calculated within LDA, unmarked values were obtained within GGA

Pressure	ΔH_O^a	$\tilde{\nu}_O^a$	ΔH_O^b	$\tilde{\nu}_O^b$	ΔH_O^c	$\tilde{\nu}_O^c$	ΔH_O^d	$\tilde{\nu}_O^d$	ΔH_O^e	$\tilde{\nu}_O^e$
131.61	2.61 (2.48, 2.48*)	19.54	3.07	-	4.30 (4.31, 4.17*)	10.13	3.80 (3.72, 3.57*)	9.88	2.73	29.47
142.28	2.67	-	3.17	-	4.47	-	3.99	-	2.77	-
505.42	3.44	-	5.37	-	8.56	-	8.64	35.74	3.44	34.21

Table 23: Calculated energies of intermediate states and saddle-points (SP) for different six-jump cycles of silicon and magnesium along ⟨010⟩ and ⟨001⟩ in $MgSiO_3$ post-perovskite using a $3 \times 1 \times 1$ supercell at 131.61 GPa(labels are explained in figure 52). Values in brackets are calculated in a $3 \times 1 \times 2$ supercell. Attempt-frequencies have only been calculated in a $3 \times 1 \times 1$ supercell and the values on the same level as energies of states are for the forward jumps (towards the next state) while backward jumps are on the level of the saddle-point energies. Values marked with * are calculated within LDA, unmarked values were obtained within GGA

	E^{Si_a} [eV]	ν^{Si_a} [THz]	E^{Si_b} [eV]	E^{Si_z} [eV]	E^{Mg_a} [eV]	E^{Mg_b} [eV]	E^{Mg_z} [eV]
Initial State	0	6.46	0	0	0	0	(0)
1^{st} SP	4.05 (3.85, 3.61*)	34.76	4.05 (3.85, 3.61*)	- (2.07)	6.62 (6.50, 6.41*)	6.62 (6.50, 6.41*)	(6.54)
State 1	-0.16 (-0.35, -0.51*)	71.26	-0.16 (-0.35, -0.51*)	0.14 (0.02)	5.34 (5.26, 5.24*)	5.34 (5.26, 5.24*)	(5.26)
2^{nd} SP	3.96 (4.10, 3.93*)	3.68	3.96 (4.10, 3.93*)	-	9.55 (9.48)	7.69 (7.72, 7.55*)	(8.00)
State 2	3.13 (3.17, 3.03*)	17.14	3.13 (3.17, 3.03*)	3.86 (2.19)	5.93 (6.06, 5.87*)	6.38 (6.25, 6.06*)	(6.16)
3^{rd} SP	9.06 (9.40, 8.95*)	98.33	15.07 (14.92)	9.57 (8.26)	10.87 (10.31, 10.06*)	10.08 (9.79, 9.61*)	(12.68)
State 3	4.70 (4.61, 4.24*)	27.70	3.47 (3.31)	7.08 (5.78)	10.24 (9.90, 9.69*)	9.85 (8.39, 8.24*)	(8.93)
4^{th} SP	6.62 (6.65, 6.28*)	10.44	8.17	9.57 (8.26)	10.87 (10.31, 10.06*)	12.20	-
State 4	3.61 (3.52, 3.34*)	4.66	3.62 (3.66)	3.86 (2.19)	5.93 (6.06)	6.27	(5.99)
5^{th} SP	5.73 (5.48, 5.21*)	45.57	-	-	9.55 (9.48, 5.87*)	-	-
State 5	0.14 (0.02, -0.16*)	26.28	-	0.14 (0.02)	5.34 (5.26, 5.24*)	-	-
6^{th} SP	2.08 (2.07, 1.90*)	4.48	-	- (2.07)	6.62 (6.50, 6.41*)	-	-

Table 24: Jump distances of magnesium, silicon and oxygen in $MgSiO_3$ post-perovskite and corresponding number of equivalent jumps. The corresponding path-names are shown in figure 51 and 52. The pressure dependence of the jump-distances is obtained by fitting the scaling factor S=[1.005, 1, 0.995, 0.9] to the corresponding pressure P=[121.501, 131.606, 142.281 ,505.42]. The jump distance at P then equals $l \cdot S$.

Jump	l_x [Å]	l_y [Å]	l_z [Å]	Z
Mg_x	2.462	0	0	2
Mg_y^a	0	3.978	3.054	4
Mg_y^b	1.231	4.027	0	4
Mg_z	1.231	0	3.054	4
Si_x	2.462	0	0	2
Si_y	1.231	4.027	0	4
Si_z	0	0	3.054	2
O_a	1.231	1.691	1.167	2
O_b	1.231	0.515	1.887	2
O_c	2.462	0	0	2
O_d	0	2.207	0.721	1
O_e	1.231	1.820	0.721	2

Table 25: Calculated (GGA) formation energies (in eV) of various defects in post-perovskite (in a $3 \times 1 \times 2$ supercell, with $2 \times 5 \times 2$ k-points grid) at 131.61 GPa. The correction term[120] for charged systems is given by $\frac{1.39q^2}{\epsilon}$ where q is the charge (-2, -4,+2 for the magnesium, silicon and oxygen vacancies respectively) and ϵ the dielectric constant of the system (in the table we have used ϵ=8). PFU = per formula unit, PV = per vacancy (always using corrected values)

	#atoms (Mg,Si,O,q)	energy [eV]	Corrected [eV]	Formation [eV]	Reaction
$MgSiO_3$	(24,24,72,0)	-754.70, -872.23*	-	-31.45 PFU	$Mg + Si + 3O \rightarrow MgSiO_3$
V_{Mg}	(23,24,72,-2)	-725.95, -842.11*	-724.90, -841.07*	-	-
V_{Si}	(24,23,72,-4)	-690.94, -806.71*	-686.76, -802.53*	-	-
V_O	(24,24,71,+2)	-770.94, -887.03*	-769.90, -885.98*	-	-
Mg_{Si}	(25,23,71,-2)	-720.43	-719.39	-	-
Schottky	-	-	-	-20.68, -23.25	$MgSiO_3 \rightarrow V_{Mg} + V_{Si} + V_O + MgSiO3$

Iron Spin-Transition

Ferro-Periclase

Table 26: Cell-parameter (L [Å]), energies (E [eV]) and pressures (P [GPa]) of the perfect $2 \times 2 \times 2$ cubic unit cell of periclase containing one iron atom ($X_{Fe} = 0.03125$) in the low-spin and high-spin state. The values are given for different values of the Hubbard U.

low-spin	U = 0		U = 1		U = 4.5		U = 7	
L	E	P	E	P	E	P	E	P
4.2	-389.22	3.53	-388.66	3.58	-386.97	3.79	-386.00	3.95
4.1	-386.57	17.81	-	-	-	-	-	-
4.0	-379.94	37.21	-379.35	37.28	-377.53	37.56	-376.48	37.77
3.9	-368.35	63.38	-367.74	63.46	-365.86	63.77	-364.75	64.01
3.8	-350.59	98.54	-349.96	98.63	-348.00	98.96	-346.84	99.22
3.5	-243.25	292.89	-242.57	292.96	-240.42	293.24	-239.10	293.46
high-spin								
4.2	-389.59	4.84	-389.20	4.87	-388.24	4.95	-387.73	4.99
4.1	-386.57	19.41	-	-	-	-	-	-
4.0	-	-	-379.10	39.19	-378.09	39.28	-377.57	39.3
3.9	-367.42	65.74	-367.00	65.78	-	-	-	-
3.8	-349.08	101.37	-348.65	101.44	-347.60	101.51	-347.08	101.49
3.5	-	-	-	-	-237.94	297.85	-237.50	297.49

Table 27: Cell-parameter (L [Å]) and energies (E [eV]) of a $2 \times 2 \times 2$ cubic unit cell of periclase containing one iron atom ($X_{Fe} = 0.03125$) and a vacancy on a nearest-neighbour (NN) or next-nearest-neighbour (NNN) site to the iron atom. The values are given for different values of the Hubbard U.

low-spin	U = 0		U = 1		U = 4.5		U = 7	
L	E NN	E NNN	E NN	E NNN	E NN	E NNN	E NN	E NNN
4.2	-370.14	-370.20	-369.58	-	-367.89	-367.94	-366.93	-366.96
4.0	-358.19	-358.23	-357.6	-	-355.79	-355.82	-354.73	-354.76
3.9	-345.30	-	-	-	-342.80	-	-341.70	-
3.8	-326.28	-326.27	-325.65	-	-323.69	-323.68	-322.53	-322.52
3.5	-215.95	-215.74	-215.27	-	-213.09	-212.92	-211.76	-211.61
high-spin								
4.2	-370.62	-370.52	-370.23	-	-369.25	-369.18	-368.74	-368.67
4.1	-366.27	-366.15	-	-	-	-	-	-
4.0	-357.90	-358.23	-357.5	-	-356.47	-356.35	-355.94	-355.83
3.9	-344.52	-344.34	-344.12	-	-	-	-342.52	-
3.8	-324.93	-	-324.53	-	-323.45	-323.27	-322.91	-322.75
3.5	-	-	-	-	-210.79	-210.46	-210.32	-210.03

Table 28: Cell-parameter (L [Å]), migration enthalpies (Δ H [eV]) and attempt frequencies ($\tilde{\nu}$ [THz]), for the five-frequency model, U = 0 (a $2 \times 2 \times 2$ cubic unit cell with $X_{Fe} = 0.03125$). Values in brackets are in a $3 \times 3 \times 3$ cubic unit cell with $X_{Fe} = 0.00926$. Low-spin iron is jumping via the high-spin saddle-point, magnesium jumps are fixed spin.

high-spin	W2		W1		W3		W4	
L	ΔH_2	$\tilde{\nu}_2$	ΔH_1	$\tilde{\nu}_1$	ΔH_3	$\tilde{\nu}_3$	ΔH_4	$\tilde{\nu}_4$
4.2	1.34 (1.19)	2.51	2.07	6.2	2.21	-	2.11	-
4.0	2.09	4.96	2.93	-	-	-	-	-
3.9	2.45	-	3.32	-	3.32	-	3.15	-
3.8	2.79 (2.74)	6.43	3.70	-	-	-	-	-
low-spin								
4.2	0.86 (0.64)	4.14	1.90	4.44	2.13	-	2.19	-
4.0	2.38 (2.17)	8.62	2.73	-	2.87	21.95	2.91	22.26
3.8	4.14 (4.04)	13.36	3.54	21.73	3.58	-	3.56	-
3.5	-	-	4.47	-	4.25	24.24	4.04	22.36

Table 29: Cell-parameter (L [Å]), migration enthalpies (Δ H [eV]) and attempt frequencies ($\tilde{\nu}$ [THz]), for the five-frequency model, U = 4.5 (a $2\times2\times2$ cubic unit cell with $X_{Fe} = 0.03125$). Values in brackets are in a $3 \times 3 \times 3$ cubic unit cell with $X_{Fe} = 0.00926$. Low-spin iron is jumping via the high-spin saddle-point, magnesium jumps are fixed spin.

high-spin	W2		W1		W3		W4	
L	ΔH_2	$\tilde{\nu}_2$	ΔH_1	$\tilde{\nu}_1$	ΔH_3	$\tilde{\nu}_3$	ΔH_4	$\tilde{\nu}_4$
4.2	1.62 (1.48)	-	2.12	-	2.23	-	2.14	-
4.0	2.31 (2.16)	-	2.91	-	2.94	-	3.82	-
3.8	2.96 (3.29)	-	3.66	-	3.65	-	3.47	-
3.5	3.71 (4.22)	-	4.44	-	4.32	-	3.99	-
low-spin								
4.2	0.26 (0.04)	-	1.97	-	2.15	-	2.19	-
4.0	1.63 (1.41)	-	2.77	-	2.89	-	2.92	-
3.8	3.20 (3.49)	-	3.54	-	3.60	-	3.59	-
3.5	6.01	-	4.44	-	4.27	-	4.10	-

Table 30: Cell-parameter (L [Å]), migration enthalpies (Δ H [eV]) and attempt frequencies (ν [THz]), for the five-frequency model, U = 7 (a $2 \times 2 \times 2$ cubic unit cell with $X_{Fe} = 0.03125$). Values in brackets are in a $3 \times 3 \times 3$ cubic unit cell with $X_{Fe} = 0.00926$. Low-spin iron is jumping via the high-spin saddle-point, magnesium jumps are fixed spin.

high-spin	W2		W1		W3		W4	
L	ΔH_2	ν_2	ΔH_1	ν_1	ΔH_3	ν_3	ΔH_4	ν_4
4.2	1.74 (1.60)	4.29	2.14	-	2.20	-	2.14	-
4.0	2.42 (2.26)	-	2.92	-	2.94	-	2.83	-
3.9	2.75 (2.60)	-	-	-	-	-	-	-
3.8	3.37 (2.87)	-	3.66	-	3.66	-	3.49	-
3.5	3.71 (4.18)	8.68	4.44	-	4.34	-	4.04	-
low-spin								
4.2	-0.07 (-0.28)	-	2.01	-	2.16	-	2.19	-
4.0	1.22 (1.00)	-	2.79	-	2.90	-	2.92	-
3.8	2.98 (3.30)	-	3.55	-	3.61	-	3.60	-
3.5	5.14 (5.57)	-	4.42	-	4.28	-	4.13	-

Table 31: Calculated values of the migration enthalpy (H), attempt frequency $\tilde{\nu}$ and jump distance l in MgO periclase (W_0). Values in brackets are calculated in a $3 \times 3 \times 3$ supercell.

Pressure [GPa]	ΔH_{Mg} [eV]	$\tilde{\nu}_{Mg}$ [THz]	ΔH_O [eV]	$\tilde{\nu}_O$ [THz]	l [Å]
4.96 (5.25)	2.21 (2.06)	12.12	2.36 (2.20)	13.82	2.9645
10.95	2.37	-	-	-	2.9345
18.68	2.55	-	-	-	2.8991
27.67	2.74	-	-	-	2.8638
30.15 (30.32)	2.79 (2.61)	22.69	3.02 (2.82)	19.18	2.8537
136.06 (136.64)	3.95 (3.88)	28.40	4.34 (4.27)	30.77	2.6294
293.70	4.5	28.56	4.86	36.26	2.4749

Ferrous Iron in Perovskite

(See next two pages)

Table 32: Cell-scale-parameter (L), migration enthalpies (Δ H) and attempt frequencies ($\tilde{\nu}$) of an iron (migrating on the magnesium sublattice) or a magnesium or an oxygen jumping into a vacancy near a low or high spin iron (migration on nearest neighbour sites) in perovskite (a $2 \times 2 \times 1$ unit cell with $X_{Fe} = 0.0625$). Entries marked with an asteriks (*) are intermediate spin at the saddle-point.

low spin		U = 0		U = 2		U =7	
Species	L [Å]	Δ H	$\tilde{\nu}$	Δ H	$\tilde{\nu}$	Δ H	$\tilde{\nu}$
Fe a	0.97	3.68	-	-	-	-	-
	0.90	6.54	-	-	-	-	-
Fe b	0.97	3.54	53.7	-	-	-	-
	0.90	6.25	221.6	-	-	-	-
Fe z	0.97	3.45	-	-	-	-	-
	0.90	6.83	-	-	-	-	-
Mg a	0.97	4.23	-	-	-	-	-
	0.90	6.81	-	-	-	-	-
O a	0.97	1.66	-	-	-	-	-
	0.90	-	-	-	-	-	-
high spin							
Fe a	0.97	3.65*	-	-	-	-	-
	0.90	5.70*	-	-	-	-	-
Fe b	0.97	3.57*	-	3.85	-	4.00	-
	0.90	5.47*	-	6.16	54.2	6.27	-
Fe z	0.97	-	-	-	-	-	-
	0.90	5.50*	-	-	-	-	-
Mg a	0.97	4.15	-	-	-	-	-
	0.90	6.69	-	-	-	-	-
O a	0.97	-	-	-	-	-	-
	0.90	-	-	-	-	-	-

Table 33: Calculated energies (in eV) of intermediate states and saddle-points (jump) for the six-jump cycles of silicon along ⟨110⟩ in the presence of a low spin iron (for various U) in a $2 \times 2 \times 1$ supercell of $MgSiO_3$ perovskite at 24 GPa (Cell-scale parameter 0.97). The iron jumps from state 2 to 3 and from 5 to 6.

low spin	U = 0		U = 2		U =7	
	Δ H ls	Δ H hs	Δ H ls	Δ H hs	Δ H ls	Δ H hs
start	-511.92	-512.61	-510.83	-511.93	-508.68	-510.74
jump 1	1.53	1.59	-	-	-	-
state 1	-0.19	-0.08	-	-	-	-
jump 2	3.03	3.34	-	-	-	-
state 2	1.83	2.48	1.83	2.25	1.86	2.22
jump 3	5.43	4.13	-	4.20	5.56	4.43
state 3	2.23	3.62	2.32	3.65	2.56	3.71
jump 4	3.69	-	-	-	-	-
state 4	0.29	1.04	-	-	-	-
jump 5	-	-	-	-	-	-
state 5	-1.05	-0.36	-	-	-	-
jump 6		-	-	-	-	-
state 6	0.44	0.21	-	-	-	-
high spin						

Publications

Phys Chem Minerals (2009) 36:151–158
DOI 10.1007/s00269-008-0265-z

ORIGINAL PAPER

DFT study of migration enthalpies in $MgSiO_3$ perovskite

M. W. Ammann · J. P. Brodholt · D. P. Dobson

Received: 28 March 2008 / Accepted: 7 September 2008 / Published online: 23 September 2008

Abstract The effect of pressure on ionic diffusion in orthorhombic $MgSiO_3$ perovskite has been investigated using density functional theory. An intensive investigation of possible silicon pathways revealed new positions of the saddle-points and an enthalpy of migration at 26.2 GPa of 4.7 eV that is in fair agreement with the experimental values of about 3.5 eV at 25 GPa. This is much lower than found in previous studies ($\sim$9 eV) and removes the need to explain silicon diffusion by a complicated process involving coupled oxygen vacancies, as has been previously proposed. Our migration enthalpies for oxygen and magnesium are in excellent agreement with experiments. We find that oxygen diffusion occurs via a chain of several inequivalent jumps along the octahedron edges, and that magnesium occurs via two inequivalent [110] jumps and one [001] jump. We also present activation volumes for all three species at 25 and 135 GPa.

Keywords Migration enthalpies · $MgSiO_3$ perovskite · High pressure · Rheology of lower mantle

Introduction

An accurate knowledge of the transport properties of Earth's mantle is necessary for modelling its thermo-chemical evolution and understanding its present state (Dobson and Brodholt 2000). The rheology, reaction rates and (ionic) electrical conductivity of mantle minerals are all ultimately controlled by the chemical diffusivities of their constituent chemical species. Magnesium silicate, $MgSiO_3$, perovskite is the volumetrically dominant mineral in the mantle, comprising some 70–80% of the lower mantle and the change in viscosity at 670 km depth is thought to exert a fundamental control on mantle convection (Hager 1984). Despite its importance, however, chemical diffusivity in silicate perovskite is poorly understood. There are very few experimental studies of diffusion in perovskite and only at the pressures of the uppermost few kilometers of the lower mantle. Furthermore, previous numerical simulation studies (Karki and Khanduja 2007; Wright and Price 1993) could not reproduce the experimental values for silicon migration enthalpy and disagree in the migration direction of magnesium. Here we present an ab initio simulation study of the migration enthalpies of magnesium, silicon and oxygen in $MgSiO_3$ perovskite at various pressures throughout the Earth's mantle. The migration enthalpies determined here agree well with experimentally determined values for all three species.

M. W. Ammann (✉) · J. P. Brodholt · D. P. Dobson
Department of Earth Sciences, University College London, Gower Street, London WC1E 6BT, UK
e-mail: m.ammann@ucl.ac.uk

Methodology

Calculations were performed using the ab initio total-energy calculation package VASP (Vienna ab initio Simulation Package) (Kresse and Hafner 1993; Kresse and Furthmüller 1996) which uses density functional theory (Hohenberg and Kohn 1964; Kohn and Sham 1965). The Generalised Gradient Approximation (Perdew and Wang 1992) and the projector augmented-wave method (Blöchl 1994; Kresse and Joubert 1999) were used. Pressure was imposed by a constant volume approach as suggested by Karki and Khanduja (2006). All calculations have been performed in a static, fully relaxed crystal. A $2 \times 2 \times 2$-supercell of orthorhombic $MgSiO_3$ perovskite

in the Pbnm space group was used containing 160 atoms. Migrations enthalpies calculated with the 2 × 2 × 2 cell agree to within 0.05 eV with those calculated using a smaller 2 × 2 × 1 cell; the 2 × 2 × 2 cell is, therefore, sufficiently large. All calculations have been performed using a single k-point (Γ-point) sampling. The comparison with a 4 × 4 × 4-k-point sampling revealed a difference in the migration enthalpy of less than 0.2%. A plane wave basis-set expansion with a cut-off energy of 1000 eV was used for the representation of the valence electrons. Compared with a cut-off energy of 1200 eV, migration enthalpies changed by less than 0.1%.

Migration enthalpies

Atomic migration is considered as a hopping process: an ion moves from one site into a nearby vacancy. In this work we are only considering the ionic defects and remove either an Mg^{2+}, Si^{4+} or O^{2-} in each calculation. The net charges of the magnesium, silicon and oxygen vacancies are, therefore, −2, −4 and +2, respectively, which are considered the dominant defect in silicates (Karki and Khanduja 2007; Wright and Price 1993). Generally, the computation of the energies of charged systems using periodic boundary conditions requires a correction for the self-interaction with the system's images (Brodholt 1997). However, as only energy differences were considered in this study, no such correction needed to be applied as the corrections cancel each other. During migration of a single ion, it needs to overcome the potential energy barrier which it crosses at a saddle-point where it has the highest energy. In the activated state, the diffusing ion sits at the top of the saddle-point, in an interstitial site, with two near-neighbour vacancies, one on the site which the ion has vacated and one on the site which the ion is migrating to. The migration enthalpy of an ion is then defined as the energy difference between the equilibrium defective system and the defective system with an ion at the saddle-point:

$$E_{\text{migration}} = E_{\text{saddlepoint}} - E_{\text{equilibrium}}$$

Although the saddle-point lies approximately halfway between the occupied and vacant site, as stated by Wright and Price (1993), finding the exact location is not always straightforward. We have, therefore, spent considerable effort in locating the saddle-point, as described below. This is particularly important for silicon migration.

Perovskite structure

Magnesium silicate perovskite is distorted from the cubic type-structure by tilting of the SiO_6 octahedra as sketched in Fig. 1. The distortion results in a rotation of the *a*- and *b*-axes by 45° from the cubic structure with a consequent increase of the axial lengths of approximately $\sqrt{2}$. The orthorhombic *c*-axis is doubled from the cubic axis, resulting in four formula units in the unit cell for the orthorhombic structure. Silicon and magnesium nearest neighbours, and hence shortest hopping distances, lie along the axial vectors in the pseudo-cubic setting and along [110] and [001] in the orthorhombic setting (Fig. 1). In the present study we consider the jumps to nearest neighbours (i.e. along [110]) as well as jumps to next-nearest neighbours in the x-y plane (i.e. along [100] and [010]). Furthermore, silicon lies on (1/2, 0, 1/2) such that [110] and [−110] jumps are equivalent. For magnesium, in contrast,

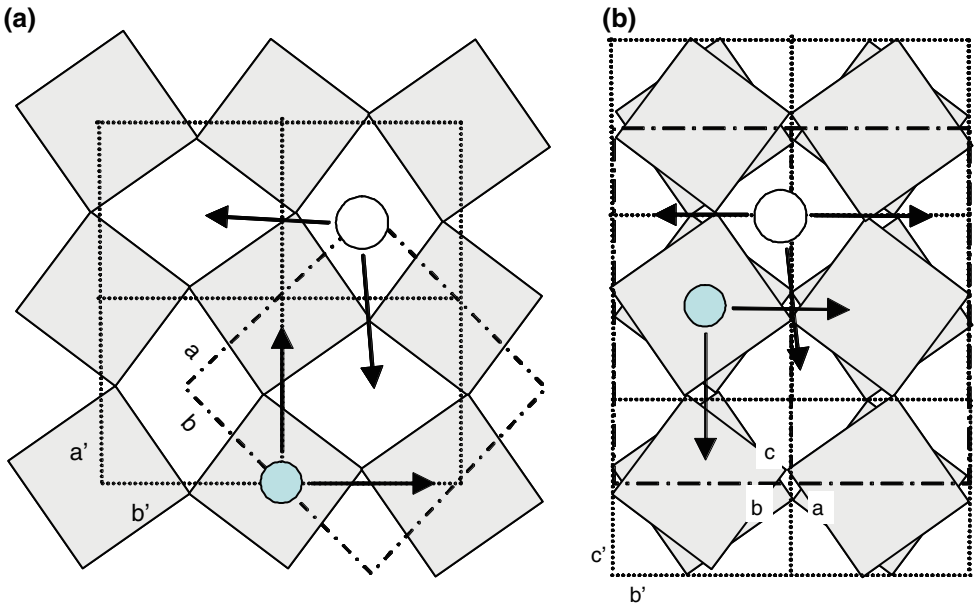

Fig. 1 Sketch of the magnesium silicate structure. **a** View down *c*-axis; **b** projection onto (110) of the orthorhombic cell. For clarity oxygen atoms have been omitted and the SiO_6 octahedra are indicated in *grey*. The pseudocubic unit cell is shown using *dotted lines* and the orthorhombic cell is shown in *dot-dashed lines*; pseudocubic (orthorhombic) axes are labelled with (without) a *tick*. One silicon atom (small *green*) and one magnesium atom (large *white*) are shown along with their nearest neighbour jumps (*arrows*)

they are not equivalent as the positions of the ions near the paths are different due to the tilt of the SiO_6 octahedra (see also Fig. 4), giving two possible diagonal migration pathways. For oxygen we have considered all of the possible exchanges along the octahedron edges as well as the two inequivalent next-nearest neighbour jumps along [001] (see below).

Silicon migration

The silicon migration pathways are complex and a geometrical analysis yields only a vague indication of the saddle-point's position: in order to avoid the obstructing oxygens, the migrating silicon ion passes approximately half-way between all the oxygen and magnesium ions. The situation is shown in Fig. 2. Assuming that the saddle-point lies halfway between the vacant and the jumping ion's site, one needs to search in a plane of possible saddle-points half-way between the two sites. For the [110]-pathway, the initial and final sites are respectively (1/2, 1/4, 1/2) and (1/4, 1/2, 1/2) in relative coordinates within the $2 \times 2 \times 2$-supercell. The condition $x = y$ defines the saddle-point plane, and we searched within that plane for the minimum energy. For the [001]-pathway, the initial and final sites are respectively (1/2, 1/4, 1/4,) and (1/2, 1/4, 1/2), where the condition $z = 3/8$ defines the saddle-point plane within which we search. For the second nearest neighbour jumps, i.e. along [100] and [010], we again assume that the saddle-point plane is exactly half-way between the two sites. However, we find that these jumps are always energetically very unfavourable compared with the nearest neighbour jumps (see Table 1) and so we have not searched the entire saddle-point plane.

By sampling the plane at many different points, the minimum energy location in the plane of possible saddle-points was found to be $z = 0.44$ and $x = y = 0.37$ with respect to the supercell for the [110]-pathway and $x = 0.6$, $y = 0.33$ and $z = 0.375$ for the [001]-pathway. Figure 3 shows contour maps of saddle-point energies (migration enthalpies) created by cubic interpolation between the sampling points in the plane of possible saddle-points on the [110]-pathway at 3.3 and 151.7 GPa. The minimum for the pathway along the [001]-direction is not particularly strong and therefore no map is shown. A comparison of the two contour maps at 3.3 and 151.7 GPa shown in Fig. 3 reveals a small change in the topology of the energy surface in the plane of possible saddle-points with pressure: with increasing pressure, the high energy plateaus surrounding the oxygen (upper right corner) and the magnesium (lower left corner) are pushed closer together resulting in two possible pathways for the migrating silicon. One passes underneath the oxygen, the other one avoids it by going around it on its left side. Both pathways are marked with their corresponding migration enthalpy in Fig. 3. The location of the minimum migration enthalpy for both pathways does not change between the 3.3 GPa and 151.7 GPa simulations and we thus assumed that the location of the saddle-point remains at the same relative position at all pressures. The maps also clearly demonstrate how choosing the saddle-point position in different regions can result in much too high migration enthalpies explaining findings of previous studies. Furthermore, the calculated migration enthalpies

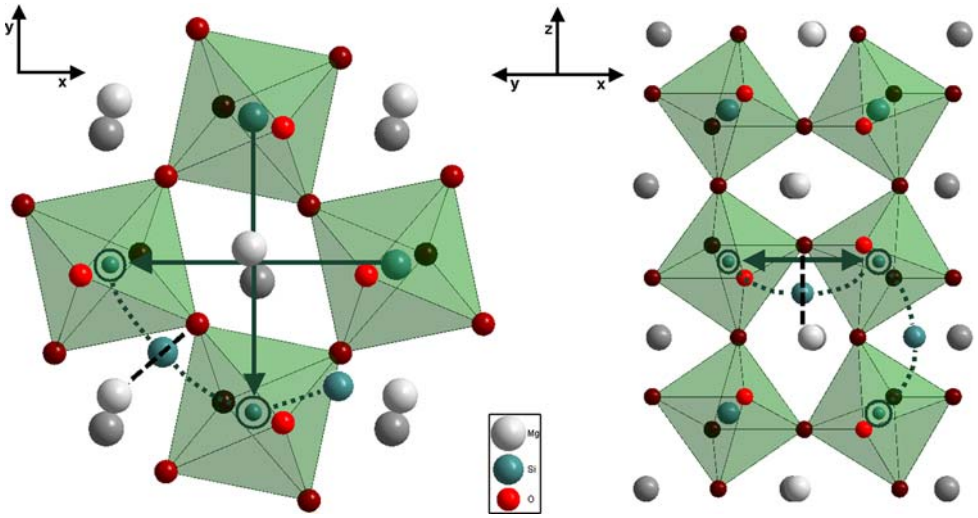

Fig. 2 Sketch of silicon migration pathways in orthorhombic $MgSiO_3$ perovskite [*left* view in *z*-direction, *right* projection onto (110)]. *Straight-line* pathways are indicated as *solid arrows* and are much higher energy than the curved pathways (see Table 1). In the right hand side figure, the *straight-line* pathways have a component out of the paper. *Darker* atoms are farther away from the observer. On the curved pathways, the migrating silicon is positioned at the saddle-point location. Vacancy sites are indicated with *circles* and the plane of possible saddle-points is shown by *dashed lines*

Table 1 Migration enthalpies (in eV) of silicon in orthorhombic $MgSiO_3$ perovskite for different migration pathways at different pressures (in GPa)

	Pathway	3.3 GPa	26.2 GPa	61.0 GPa	101.1 GPa	126.6 GPa	151.7 GPa
This Study	[110]	3.52	4.7	5.6	6.17	6.41	6.59
	[100]	6.98	–	–	–	–	–
	[010]	7.95	–	–	–	–	–
	[001]	5.72	–	–	–	8.25	–
Karki and Khanduja (2007)	[110]	8.33[a]	9.1[b]	~9.7	~10.2	10.48[c]	~10.8
	[001]	19.56[a]	–	–	–	–	–
Wright and Price (1993)	[110]	9.2[a]	–	–	–	10.32[d]	–
Dobson et al. (2008)	Exp.	–	3.6 ± 0.76[e]	–	–	–	–
Yamazaki et al. (2000)	Exp.	–	3.48 ± 0.38[e]	–	–	–	–

The "~" symbol indicates that the numbers were read out of figures

[a] At 0 GPa

[b] At 30 GPa

[c] At 120 GPa

[d] At 125 GPa

[e] At 25 GPa

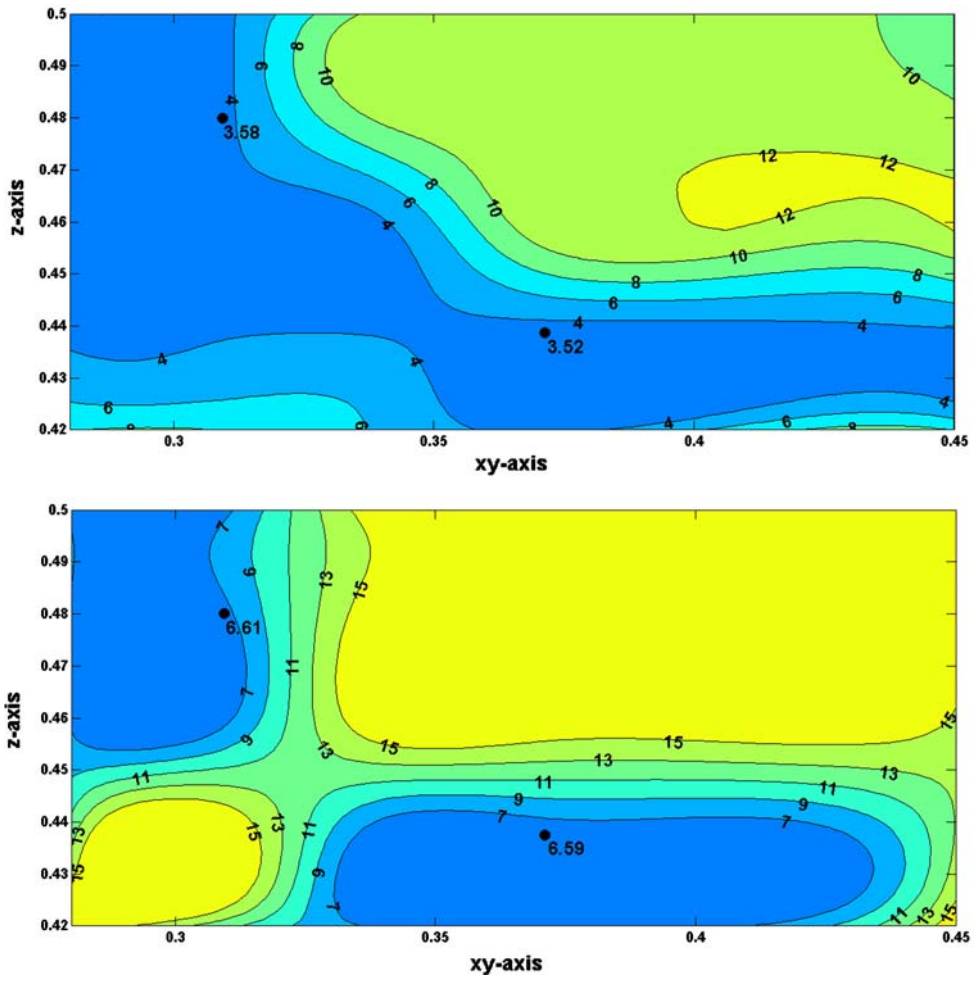

Fig. 3 Contour maps of the computed migration enthalpies (in eV) in the sampled plane of possible saddle-points for silicon migration along the [110]-pathway in orthorhombic $MgSiO_3$ perovskite at 3.3 GPa (*upper*) and at 151.7 GPa (*lower*). The locations of the minimum of migration enthalpy for two possible silicon pathways are marked with a *black dot* and labelled with their corresponding value

can depend on the initial crystal structure since the energy surface of the activated state contains many local minima. Thus, if the system is allowed to relax from an initial configuration of an interstitial silicon placed in the perfect structure (with vacancies placed on the starting and final silicon-sites of the migration pathway) it finds a minimum energy which is ~5 eV higher than if the initial configuration uses a structure which has been relaxed around a vacancy on the target site. This suggests that only a local minimum is found when one starts the structural optimisation from the perfect structure, and highlights the difficulty in finding global minima. The agreement between our results and experiments, shown below, suggests that we must be close to the global minimum. Finally we tested whether the saddle-point is in a local minimum of the migration path by moving the ion a small distance off the plane towards a vacancy and confirming the energy decreased.

The silicon migration enthalpies for different directions at a range of pressures are shown in Table 1. Each jump between nearest neighbours in any direction in the *x*–*y*-plane is equivalent and only two jumps are required to cross a unit cell. The [100] and [010] migration pathways which constitute direct jumps across one unit cell to the second nearest neighbours (solid lines in Fig. 1) are energetically unfavourable. The high migration enthalpy in the [001]-direction (Table 1) is in agreement with anisotropic silicon-diffusion seen in experimental data (Dobson et al. 2008). A comparison between the silicon migration enthalpy at 26.2 GPa of 4.7 eV and its experimental values of 3.6 ± 0.76 eV (Dobson et al. 2008) and 3.48 ± 0.38 eV (Yamazaki et al. 2000) at 25 GPa shows the best agreement found so far in any theoretical study.

The migration enthalpies increase with pressure as expected from the decreased inter-atomic distances in the compressed structures. The activation volume decreases from 3.5 cm^3/mol at 25 GPa to 0.7 cm^3/mol at 135 GPa.

Magnesium migration

There are three distinct pathways to nearest neighbour sites for magnesium as shown in Fig. 4. Pathways to second nearest neighbours around the octahedra (between oxygen and magnesium) along [100] and [010] are energetically unfavourable (as shown in Table 2). The two [110]-pathways (*a* and *b*) pass between two octahedra and are strongly affected by nearby oxygens, and so one cannot assume a straight-line path. For path *b* a migration enthalpy of 2.52 eV is found for a magnesium ion passing halfway between the initial and final ion site and halfway between the nearest oxygen neighbours (as shown in Fig. 4), whereas a straight-line between the two magnesium yields a much higher migration enthalpy of 13.5 eV. Shifting the ion off the straight-line path is less important for pathway *a* with the migration enthalpy changing from 3.3 to 3.1 eV by shifting off the straight-line path. Similarly, the straight-line path in the [001]-direction passes halfway between pairs of oxygens and yields a saddle-point halfway between the initial and final sites. The positions of the saddle-points have been re-calculated for each pressure as the local ionic structure changes slightly with increasing pressure. As in the case of silicon migration, it is unlikely that the saddle-point has been found exactly and as such all migration enthalpies are, within errors, approximately equal to each other and to the experimental value. Moreover, the results show that diffusion of magnesium is isotropic.

The computed magnesium migration enthalpies for different directions and pressures are shown in Table 2. The average magnesium migration enthalpy at 26.2 GPa of 3.69 ± 0.37 eV is somewhat smaller than the experimental value for Fe–Mg-interdiffusion of 4.29 ± 0.64 eV at 24 GPa (Holzapfel et al. 2005). However, as the locations of the chosen saddle-points do not correspond exactly with the real saddle-points, it is possible that they lie close to the

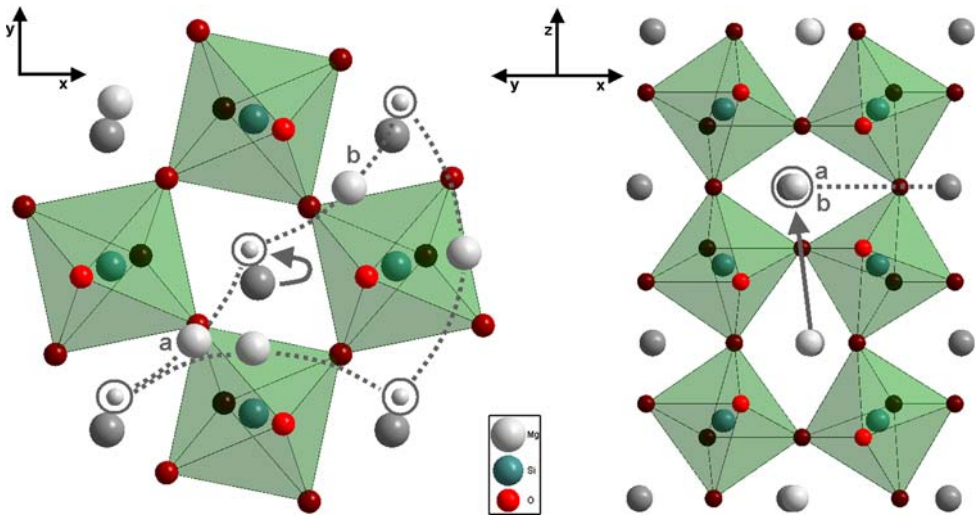

Fig. 4 Sketch of magnesium migration pathways in orthorhombic $MgSiO_3$ perovskite [*left* view in *z*-direction, *right* projection onto (110)]. *Straight-line* pathways are indicated as *solid arrows*. *Darker* atoms are farther away from the observer. On the curved pathways, the migrating magnesium is positioned at the saddle-point location (only in the left figure). Vacancy locations are indicated with *circles*

Table 2 Migration enthalpies (in eV) of magnesium in orthorhombic $MgSiO_3$ perovskite for different migration pathways at different pressures (in GPa)

	Pathway		3.3 GPa	26.2 GPa	61.0 GPa	101.1 GPa	126.6 GPa	151.7 GPa
This Study	[110]	a	3.1	3.96	5.21	5.7	6.2	6.71
	[110]	b	2.52	3.27	4.35	5.12	5.55	6.15
	[001]		2.87	3.84	4.82	5.74	6.21	6.73
	Average		2.83 ± 0.29	3.69 ± 0.37	4.79 ± 0.43	5.52 ± 0.34	5.98 ± 0.38	6.53 ± 0.33
	[100]		7.74	–	–	–	–	–
	[010]		9.07	–	–	–	–	–
Karki and Khanduja (2007)	[110]		3.47[a]	4.78[b]	~6.1	~7	7.71[c]	~8.7
	[001]		13.54[a]	–	–	–	–	–
Wright and Price (1993)	[110]		4.57[a]	–	6.13[d]	–	7.43[e]	–
Holzapfel et al. (2005)	Exp.		–	4.29 ± 0.64[f]	–	–	–	–

The "~" symbol indicates that the numbers were read out of figures

[a] At 0 GPa

[b] At 30 GPa

[c] At 120 GPa

[d] At 60 GPa

[e] At 125 GPa

[f] Fe-Mg inter-diffusion at 24 GPa

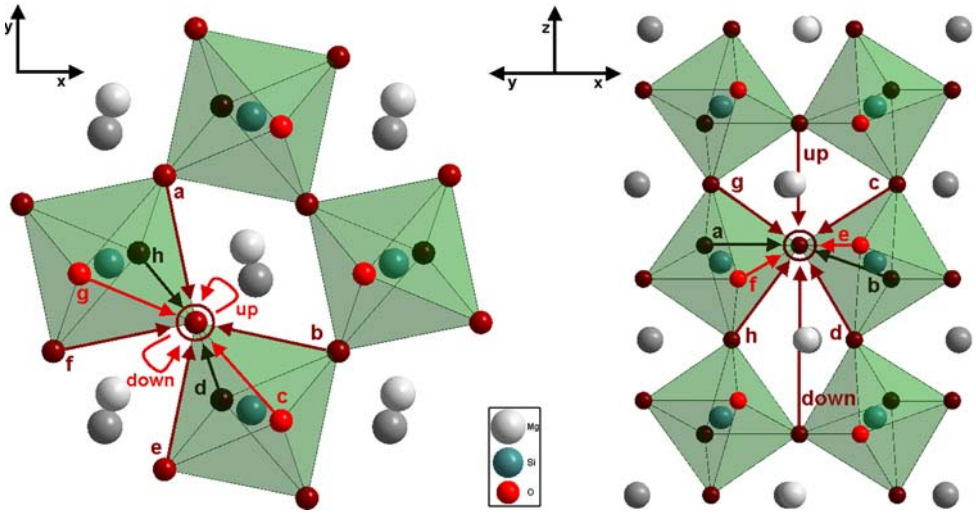

Fig. 5 Sketch of oxygen migration pathways in orthorhombic $MgSiO_3$ perovskite [*left* view in *z*-direction, *right* projection onto (110)]. *Straight-line* pathways are indicated as *solid arrows*. *Darker* atoms are farther away from the observer. The vacancy location is indicated with a *circle*

correct path resulting in lower migration enthalpies. Additionally, one can expect a lower enthalpy for pure magnesium migration, as observed here, since iron is larger than magnesium resulting in a stronger lattice distortion at the saddle-point and increased migration enthalpies. Thus, the present values are consistent with experiment. The activation volumes calculated from the average values at 25 GPa is 3.37 cm^3/mol and at 135 GPa 2.05 cm^3/mol.

Oxygen migration

Oxygen migration can take place along many distinct pathways as shown in Fig. 5. Although there are only two inequivalent oxygen positions within the unit cell, there are eight different (non-equivalent) jumps that an oxygen can perform along octahedra edges.

The migration enthalpies were calculated by setting an oxygen exactly halfway between the initial and end sites. Again, the saddle-point may not lie exactly halfway between two oxygen sites, but as all migration enthalpies are equal to the experimental value within error, the mid-way position must be close to the true saddle-point. These are shown in Table 3. Note that the eight different jumps along the edges of the octahedra have similar migration enthalpies; this is to be expected since the octahedral distortions are small. The average oxygen migration enthalpy

Table 3 Migration enthalpies (in eV) of oxygen in orthorhombic $MgSiO_3$ perovskite for different migration pathways at different pressures (in GPa)

	Pathway		3.3 GPa	26.2 GPa	61.0 GPa	101.1 GPa	126.6 GPa	151.7 GPa
This Study	[001]	Up	2.9	2.99	–	–	–	3.29
	[001]	Down	10.71	–	–	–	–	–
		a	0.72	1.5	2.11	2.75	2.89	2.87
		b	0.8	1.78	2.24	2.88	2.91	3.05
		c	1.29	1.16	1.94	2.38	1.58	2.08
		d	0.92	0.97	1.24	2.26	2.65	2.96
		e	0.55	1.5	1.79	2.38	2.73	3.31
		f	0.86	1.63	2.56	2.78	2.76	3.51
		g	0.66	1.42	1.74	2.2	2.61	3.22
		h	0.97	1.8	2.17	2.52	2.9	3.07
	Average		0.85 ± 0.23	1.47 ± 0.29	1.97 ± 0.4	2.53 ± 0.26	2.63 ± 0.44	3.01 ± 0.43
Karki and Khanduja (2007)	[100]		0.57[a]	1.41[b]	~2	~2.5	2.57[c]	~2.5
	[110]		2.78[a]	–	–	–	–	–
Wright and Price (1993)	[100]		0.96[a]	–	–	–	–	–
Dobson (2003)	Exp.		–	1.35 ± 0.2[d]	–	–	–	–
Xu and McCammon (2002)	Exp.		–	1.47[d]	–	–	–	–

The definition of the pathways and their labels are given in Fig. 5. The average values are given with their standard deviations. The "~" symbol indicates that the numbers were read out of figures

[a] At 0 GPa

[b] At 30 GPa

[c] At 120 GPa

[d] At 25 GPa

at 26.2 GPa of 1.47 eV is in excellent agreement with the experimental value of 1.35 eV (Dobson 2003) or 1.47 eV (Xu and McCammon 2002) at 25 GPa. The activation volume calculated from the average values at 25 GPa is 1.95 cm^3/mol, and decreases to 1.49 cm^3/mol at 135 GPa. The high migration enthalpies for the pathways up and down clearly demonstrate that migration takes place along the octahedra edges. The similar migration enthalpies along octahedra edges means that oxygen diffusion in perovskite is essentially isotropic.

Discussion

First-principles simulations of orthorhombic $MgSiO_3$ perovskite have been performed in order to compute the migration enthalpies of magnesium, silicon and oxygen under different pressures up to lower mantle conditions. All migration enthalpies increase monotonically with increasing pressure. Our results agree well with experimental results. A new silicon migration pathway has been proposed yielding a migration enthalpy much closer to the experimental value than in previous studies (Karki and Khanduja 2007; Wright and Price 1993). We suggest, therefore, that silicon diffuses via a simple hopping mechanism and does not require a complicated process involving adjacent oxygen vacancies, as suggested by the previous studies.

The rate of deformation in high-temperature dislocation-migration regimes is limited by the slowest diffusing species. Our calculated migration enthalpies for silicon diffusion are about 20% higher than magnesium at all pressures, and substantially higher than oxygen. This suggests that silicon will be the rate-limiting species throughout the Earth's mantle, as is the case with most silicates (Dobson et al. 2008). Recent experiments (Holzapfel et al. 2005; Dobson et al. 2008) suggest that silicon and magnesium have very similar diffusivities such that silicon is not necessarily the rate-limiting species. However, the experiments of (Holzapfel et al. 2005) are Fe–Mg inter-diffusion and so the migration enthalpy they measure may well be higher than that for magnesium self-diffusion. Furthermore, the formation energy of silicon vacancies is generally significantly higher than for magnesium or oxygen vacancies (e.g. Brodholt 1997).

Holzapfel et al. (2005) extrapolate their Fe-Mg inter-diffusion values to deep lower mantle conditions using a constant activation volume of 2.1 cm^3/mol from Wright and Price (1993). This activation volume is equal (within error) to those found in this study and we do not find a

strong pressure dependence of activation volume for magnesium migration. The conclusions of Holzapfel et al. (2005) are therefore not affected by the present study. In contrast, the extrapolation by Xu and McCammon (2002) will underestimate oxygen mobility at the base of the lower mantle since they use an activation volume of about 2.1 cm^3/mol, which is somewhat larger than the value found here at high pressure. This makes it even more likely that oxygen ionic conduction in $MgSiO_3$ occurs towards the base of the lower mantle.

Acknowledgments This work was funded by the European Commission through the Marie Curie Research Training Network "c2c" Contract No. MRTN-CT-2006-035957. This work made use of the facilities of HECToR, the UK's national high-performance computing service, which is provided by UoE HPCx Ltd at the University of Edinburgh, Cray Inc and NAG Ltd, and funded by the Office of Science and Technology through EPSRC's High End Computing Programme.

References

Blöchl PE (1994) Projector augmented-wave method. Phys Rev B 50:17953–17979. doi:10.1103/PhysRevB.50.17953

Brodholt JP (1997) Ab initio calculations on point defects in forsterite (Mg_2SiO_4) and implications for diffusion creep. Am Mineral 82:1049–1053

Dobson DP (2003) Oxygen ionic conduction in $MgSiO_3$ perovskite. Phys Earth Planet Inter 139:55–64. doi:10.1016/S0031-9201(03)00144-4

Dobson DP, Brodholt JP (2000) The electrical conductivity and thermal profile of the earth's mid-mantle. Geophys Res Lett 27:2325–2328. doi:10.1029/1999GL008409

Dobson DP, Dohmen R, Wiedenbeck M (2008) Self-diffusion of oxygen and silicon in $MgSiO_3$ perovskite. Earth Planet Sci Lett 270:125–129. doi:10.1016/j.epsl.2008.03.029

Hager BH (1984) Subducted slabs and the geoid: constraints on mantle rheology and flow. J Geophys Res 89:6003–6015. doi:10.1029/JB089iB07p06003

Hohenberg P, Kohn W (1964) Inhomogenous electron gas. Phys Rev 136:B864–B871. doi:10.1103/PhysRev.136.B864

Holzapfel C, Rubie DC, Frost DJ, Langenhorst F (2005) Fe–Mg interdiffusion in (Mg; Fe)SiO_3 perovskite and lower mantle reequilibration. Science 309:1707–1710. doi:10.1126/science.1111895

Karki BB, Khanduja G (2006) Vacancy defects in MgO at high pressure. Am Mineral 91:511–516. doi:10.2138/am.2006.1998

Karki BB, Khanduja G (2007) a computational study of ionic vacancies and diffusion in $MgSiO_3$ perovskite and post-perovskite. Earth Planet Sci Lett 260:201–211. doi:10.1016/j.epsl.2007.05.031

Kohn W, Sham LJ (1965) Self-consistent equations including exchange and correlation effects. Phys Rev 140:A1133–A1138. doi:10.1103/PhysRev.140.A1133

Kresse G, Hafner J (1993) Ab initio molecular dynamics for liquid metals. Phys Rev B 47:558–561. doi:10.1103/PhysRevB.47.558

Kresse G, Furthmüller J (1996) Efficiency of ab-initio total energy calculations for metals and semiconductors using a plane-wave basis set. Comput Mat Sci 6:15–50. doi:10.1016/0927-0256(96)00008-0

Kresse G, Joubert J (1999) From ultrasoft pseudopotentials to the projector augmented wave method. Phys Rev B 59:1758–1775. doi:10.1103/PhysRevB.59.1758

Perdew JP, Wang Y (1992) Accurate and simple analytic representation of the electron-gas correlation energy. Phys Rev B 45:13244–13249. doi:10.1103/PhysRevB.45.13244

Wright K, Price GD (1993) Computer simulation of defects and diffusion in perovskite. J Geophys Res 98:22.245–22.253

Yamazaki D, Kato T, Yurimoto H, Ohtani E, Toriumi M (2000) Silicon self-diffusion in $MgSiO_3$ perovskite at 25 GPa. Phys Earth Planet Inter 119:299–309. doi:10.1016/S0031-9201(00)00135-7

Xu Y, McCammon C (2002) Evidence for ionic conductivity in lower mantle (Mg,Fe)(Si,Al)O_3 perovskite. J Geophys Res 107. doi:10.1029/2001JB000677

Reviews in Mineralogy & Geochemistry
Vol. 71 pp. 201-224, 2010

Simulating Diffusion

Michael W. Ammann, John P. Brodholt, and David P. Dobson

Department of Earth Sciences
University College London
London, WC1E 6BT, United Kingdom

m.ammann@ucl.ac.uk

INTRODUCTION

Ionic or atomic diffusion controls chemical exchange between and within different crystalline, melt and fluid phases. It can control the kinetics of phase transitions, the rate at which minerals grow, the degree of compositional zoning in minerals, and other important geochemical processes. Diffusion also plays a central role in the rheological properties of minerals and melts. In diffusion creep stress is accommodated through ions migrating from regions of high stress to regions of low stress. This is achieved either through bulk diffusion or grain boundary diffusion. In dislocation creep the rate-limiting step is often dislocation climb—the process where a dislocation has to migrate out of the dislocation plane to avoid an obstacle—and this requires ionic diffusion.

There are two main reasons for studying diffusion theoretically. The first is to determine the atomistic mechanism of diffusion. This can provide understanding of the underlying mechanisms, and allow one to extrapolate results to other systems. When different sets of experimental results disagree, theory can often help to decide which is correct or explain the differences. But the most valuable reason for using theory is to predict diffusion properties for systems or conditions where no data exist. As will be shown, theoretical calculations can be used to predict absolute diffusion rates very accurately—perhaps as accurately as is obtainable in high-pressure and high-temperature experiments. However, let it be understood that we are not advocating abandoning experimentation for theory.

In this paper we will use our recent *ab initio* calculations on the absolute diffusion rates of periclase and perovskite as an example of what can be done and how to do it.

BASIC METHODS

Ab initio vs. empirical potentials

The basis for the techniques described here are atomistic; the system is described as set of interacting atoms or ions, and it is these interactions that govern its behavior. The interactions can either be described from first principles (i.e., quantum mechanically) or empirically. The first principles method treats the system as a set of interacting nuclei and electrons, and uses (approximate) solutions to Schrödinger's equations to obtain energies and forces. Currently, almost all work involving first principles methods, such as the one that will be discussed in this chapter, make use of density functional theory (DFT, Hohenberg and Kohn 1964; Kohn and Sham 1965). The empirical approach uses a predefined inter-atomic (or inter-molecular) potential, which is fit to some experimental property or to a first-principles result. There are also the so-called semi-empirical methods, which are based on quantum mechanics but contain many approximations and include experimentally derived parameters. The different methods

1529-6466/10/0071-0010$05.00 DOI: 10.2138/rmg.2010.71.10

have their pluses and minuses. The empirical approach allows us to look at far larger systems than the first principles (or *ab initio*) methods. The downside is that the empirically-derived potentials may not work accurately in systems and atomic environments for which they were not originally designed. This is a particular worry for diffusion studies since atoms migrate from their normal configuration through a very different coordination environment than their equilibrium position. Moreover, some empirical potentials have bond-angle dependent parameters and it is not clear what to do with those as atoms migrate. For instance, potential models for Si-O interaction often have a three-body bond angle term in order to maintain the correct coordination with oxygen. For tetrahedrally coordinated silicon, this would be 109.47°. But as the silicon ion moves out of the tetrahedron, it changes coordination, and the bond-angle term may impose inappropriate forces. The *ab initio* techniques do not suffer from this in the same way, although they do have other approximations which add uncertainty to the results.

Predicting diffusion coefficients in fluids and melts

Although this paper will concentrate on modeling diffusion in crystalline phases, it is worth mentioning how diffusion is modeled in fluids and melts. Using atomistic level simulations to predict the diffusion properties of fluids and melts is, in principle, simpler than in solids. Molecular dynamics simulations, for instance, allows one to follow the path of all the atoms as they move as function of time. By keeping track of the mean-squared-displacement of each of atom in the simulation, one obtains a direct measurement of the diffusion coefficient for each atomic species. The only complication for viscous silicate melts is that the simulation must be run for sufficient time to allow adequate sampling of space by the atoms (e.g., Wan et al. 2005; Mookherjee et al. 2008; Nevins et al. 2009). Less viscous fluids, such as aqueous solution, need far less time. This molecular dynamic approach has also been attempted for solids, but diffusion coefficients in solids are many orders of magnitude slower than even viscous melts and jumps are very rare. This means that the simulation times are generally prohibitively long, and can only be used with empirical potentials and for simple jumps. Nevertheless, this technique has been used for MgO (see below) and for diffusion of relatively small impurity ions such as H and He (e.g., Reich et al. 2007).

Predicting diffusion coefficients in crystalline phases

As mentioned in the previous section, the situation for mineral phases is not so simple; diffusion time scales are orders of magnitude slower than in melts and fluids such that atomic jumps in a direct MD simulation are very rare events. With slower diffusing systems or when using *ab initio* methods, the normal approach for calculating diffusion coefficients is to break the diffusion process into parts and calculate the different parts individually. The process is given pictorially in Figure 1.

Basically the process is one of calculating the number of times a vacancy jumps between two sites per unit time. This is known as the jump frequency, Γ. For an individual defect the jump frequency is given by (e.g., Poirier 1985)

$$\Gamma = \nu e^{\frac{\Delta G}{kT}} = \nu e^{\frac{\Delta S}{k}} e^{\frac{-\Delta H}{kT}} \quad (1)$$

where ΔG, ΔS and ΔH are the migration free energy, the entropy and enthalpy respectively. ν is a characteristic attempt frequency of the atom trying to jump over the barrier. T and k have their usual meanings of temperature and the Boltzmann constant respectively. The diffusion coefficient for a species is then given as

$$D = N_V \frac{Z}{6} l^2 \Gamma \quad (2)$$

where N_V is the vacancy concentration in the crystal at the particular temperature and pressure, l is the jump distance, and Z is a geometric factor incorporating the number of possible jumps.

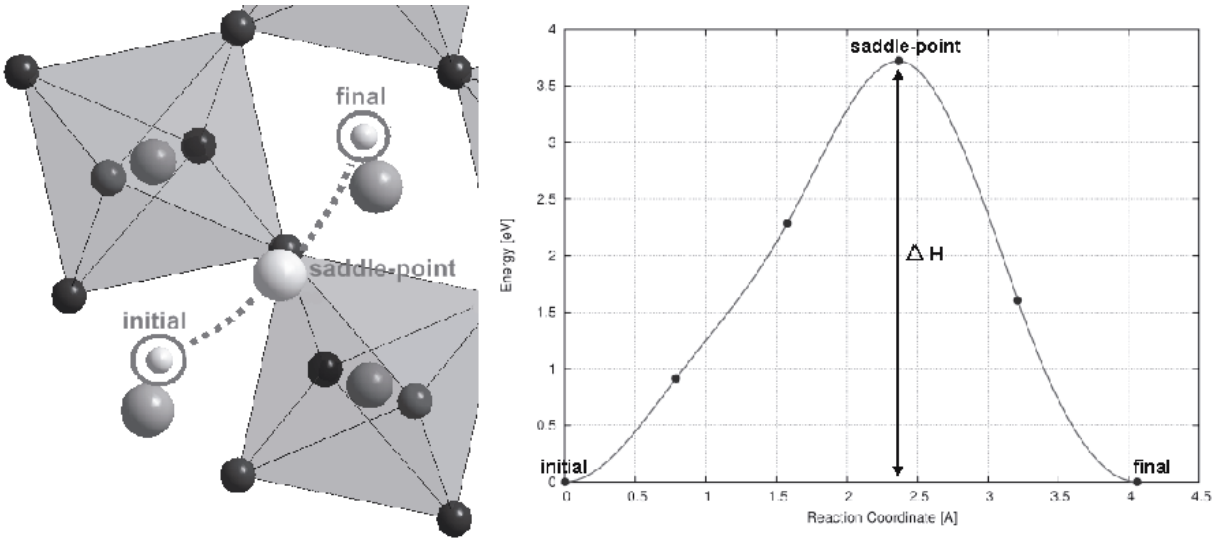

Figure 1. Left hand side: a magnesium ion migrates in $MgSiO_3$ perovskite from its initial to its final position by overcoming a saddle-point. Right hand side: The energy barrier encountered by the migrating ion as calculated with CI-NEB. The saddle point is at the maximum of the energy barrier and the energy difference from the initial state defines the migration enthalpy ΔH.

The enthalpy of migration, ΔH, is obtained from the difference between the energy of the system at the saddle point and its ground state energy before attempting a jump:

$$\Delta H = E_{saddle} - E_{groundstate} \tag{3}$$

where the simulation is performed at constant volume. The issue of how to compare thermodynamic quantities measured in experiments (at constant pressure) with the ones obtained from theoretical calculations (at constant volume) is discussed at length by, e.g., Catlow et al. (1981) or Harding (1989).

For systems with high symmetry (i.e., MgO), finding the saddle point is reasonably straightforward since it often lies on a line of symmetry. For lower symmetry materials, such as perovskite, it is not obvious where the saddle point is. It is possible to use trial and error, or a grid searching method to find the saddle point, but this is quite inefficient. A better approach is to use a method such as the Nudged-Elastic-Band; this is described later.

The attempt frequency and the migration entropy are obtained together using harmonic transition-state theory. This is also called Vineyard Theory (Vineyard 1957). In this theory, many-body effects are incorporated by calculating the full 3N vibrational frequencies at the equilibrium point and the $3N-1$ non-negative vibrational frequencies at the saddle point. It can be shown that ν and ΔS are simultaneously obtained from

$$v^* = ve^{\Delta S/k} = \frac{\prod_{j=1}^{3N} f_j}{\prod_{j=1}^{3N-1} f_j'} \tag{4}$$

where N is the number of atoms in the simulation cell, f_j are the vibrational frequencies at the equilibrium site, and f_j' are the frequencies at the saddle point. The phonon spectrum at the saddle point contains one negative frequency; this is due to the unstable atom sitting exactly on the saddle point. The product of frequencies at the saddle point only contains, therefore, $N-1$ positive frequencies. The phonon spectra can be calculated using a standard lattice dynamics approach, either using *ab initio* forces or empirical potentials.

Vineyard-theory is not an exact theory. It assumes that the energy surfaces at the saddle-point and at the equilibrium position are perfectly harmonic. This does not have to be strictly true and one has then to correct for the anharmonicity (Sangster and Stoneham 1984). However, in our DFT calculations we find that anharmonicity is negligible (<1% deviation). Another idealization is that Vineyard-theory assumes that each jump is successful—i.e., each ion jumping towards a vacancy will reach the vacancy once it has crossed the saddle-point. Again, for real systems this is not the case as the jumping atom can cross the saddle-point only to immediately return back to its initial state. This can happen because the jump is a complex, dynamical many-body process (dynamical correlation). Luckily, unsuccessful jumps are rare and are unlikely to exceed 10% as has been shown by Flynn and Jacucci (1982). This is because the time after which the system loses its memory of previous jumps (onset of randomization) is generally much shorter than any vibrational period of any particle in the system.

In order to ensure that there is only one negative frequency at the saddle point, it is essential to find the saddle-point exactly—i.e., the crystal must be fully relaxed and all atomic forces are relaxed to within a very small tolerance (typically $<10^{-6}$ eV/Å). This is another reason to use a method such as the nudged-elastic band, rather than trial and error or random searching.

The last unknown required to calculate absolute diffusion rates is the number of vacancies, N_V. Estimating N_V is non-trivial. Vacancy concentrations can vary significantly depending on the experimental conditions (i.e., pressure, temperature, oxygen fugacity, impurity concentration, sample history, etc.). It is possible to estimate the intrinsic vacancy concentration directly and self-consistently by calculating the vacancy energies. For instance, the number of Schottky vacancies n (where an atom is taken from the bulk of the crystal and added to the surface) is given as

$$n = Ne^{-\frac{\Delta G_V}{kT}} \tag{5}$$

where N is the number of atoms in the crystal and ΔG_V is the Gibbs free energy of vacancy formation. The energy can, if necessary, be calculated directly from first principles. However, for most Earth materials, the intrinsic concentration is very small, even at very high temperatures. The vacancy concentration of the crystal is more likely to be set by the number of impurities (i.e., the extrinsic concentration). For instance, Fe^{3+} on a normal 2+ cation site could be charge balanced by cation vacancies. Similarly, oxygen vacancies may be set by the concentration of 1+ ions. For well-characterized experimental samples, these can be estimated reasonably accurately, and allow us to compare our calculated diffusion rates directly with experimental measurements. Estimating vacancy concentrations for minerals in the Earth's mantle, however, is subject to considerable uncertainty. This has to be kept in mind when applying results to the Earth.

Defect calculations: Mott-Littleton, super-cells and embedded clusters

Crystalline defects exert a strong distance dependent perturbation on the crystal. Firstly, defects in crystals are often charged; this results in a Coulomb interaction that decays slowly as $1/r$ (r being the distance). Neutral defects can also have a slowly decaying electrostatic interaction, since they often possess strong dipole and quadrupole moments. Secondly, the crystal lattice is distorted due to relaxation of the ions around the defect (repelled or attracted depending on their charge relative to the defect). It is assumed that this lattice distortion decays as $1/r^3$. When modeling defects, especially highly charged vacancies, care has to be taken to ensure that these long-range interactions are taken into account, and that they do not artificially bias the results.

The classic approach is the Mott-Littleton Method (Mott and Littleton 1938). In this method, the defective crystal is divided into two separately treated spherical regions. The inner region surrounds the defect and is treated accurately by calculating the relaxations and distortions on the atoms from interatomic forces. The outer region is treated less accurately

(as atoms only interact with the distortion and the charge of the defect but not with each other), and is used to shield the charge and distortion caused by the defect (polarization). This approach has only been used with (semi-)empirical interatomic potentials. Codes such as GULP (*https://www.ivec.org/gulp/*; Gale 1997; Gale and Rohl 2003) make this a relatively routine procedure, subject to the accuracy of the interatomic-potentials (Cherry et al. 1995a,b; Blanchard et al. 2005; Lowitzer et al. 2008; Ball et al. 2008; Béjina et al. 2009).

If we wish to use *ab initio* methods, in particular DFT, the most straightforward implementations make use of super-cells and periodic boundary conditions (PBC). PBC mean that the system is repeated infinitely in space. This is especially useful for crystalline lattices since it is then sufficient to calculate the properties of a single unit cell. Periodic boundary conditions yield the same result as if the unit cell has been repeated infinitely in all directions, forming a perfect, infinitely sized crystal. This approach, however, has its drawbacks when it comes to defect calculations, since the defect is also repeated infinitely along all directions. This leads to a very high concentration of defects, giving rise to spurious elastic interactions between neighboring cells (mirror images of the simulation). This interaction should scale as $1/L^3$, where L is the cell size. The effect of the elastic interaction can be reduced by using sufficiently large supercells (a large simulation unit built up from several unit cells), such that deformations at the cell-boundaries are negligible. However, the relaxation is almost never completely removed by the edge of the supercell, and the calculations contain a small artificial contribution from this. Nevertheless, this contribution is small and the super-cell method using DFT forces and energies has been used successfully on defect calculations in Earth materials such as olivine (Brodholt 1997; Brodholt and Refson 2000), perovskite (Brodholt 2000; Karki and Khanduja 2006a), post-perovskite (Karki and Khanduja 2007) and periclase (Karki and Khanduja 2006b).

An intermediate approach between using pure DFT with super-cells and Mott-Littleton methods for defect calculations is the so-called embedded cluster method. This again divides up space into regions: a central region, which treats the defect at the quantum mechanical level, a surrounding region that is treated classically via interatomic potentials, and a third outer region which is just a set a of fixed point-charges. This method is implemented in codes such as GUESS (Sushko et al. 1999, 2000a,b) and has been used to study defects in olivine (Braithwaite et al. 2002, 2003; Walker et al. 2006, 2009).

In our diffusion calculations which we discuss in this chapter, we used the supercell approach. First of all we wish to avoid the use of empirical pair-potentials and use *ab initio* energies and forces. We can use the tried and tested pseudopotentials (and closely related PAW parameters (Blöchl 1994; Kresse and Joubert 1999) in codes like VASP (Kresse and Hafner 1993; Kresse and Furthmüller 1996a,b). Secondly, super-cells of up to a few hundred atoms can now be routinely calculated. And thirdly, routines are readily available for the lattice dynamics calculations (Parlinski 2008; Baroni et al. 2001; Alfè 2009) required for the jump frequencies, and nudged-elastic-bands (Henkelman et al. 2000) for finding saddle points of the migrating atoms—something that is very important in complicated migrating pathways.

As mentioned above, PBC in combination with defective systems has its own difficulties. The introduction of charged point defects or defect clusters results in an artificial electrostatic self-interaction between the supercell and all its images. This electrostatic self-interaction can have rather large effects on the calculated defect energies. It is therefore worthwhile to briefly discuss how one can reduce the error made on the defect energetics when using PBC.

Firstly, Leslie and Gillan (1985) proposed a simple correction to the self-interaction of charged point defects. A charged defect within a cell with PBC is equivalent to a periodic array of charged defects. However, a periodically repeating array of charged supercells does not have a well-defined energy. This difficulty can be overcome by introducing a uniformly distributed background charge (so-called jellium) compensating the charge of the supercell. The correction term is hence given by the energy of the charged defect array embedded in the

compensating jellium. Assuming that the space between the defects is large enough, i.e., the supercell is large enough; a macroscopic approximation can be made: the defect array and the jellium are immersed in a structureless dielectric, whose dielectric constant ε is equal to that of the perfect crystal. The energy of such an array, and hence the correction term is given by $E_{array} = -\alpha Q^2/(2\varepsilon L)$ where α is the appropriate Madelung constant, Q the charge of the defect and L is the lattice parameter of the periodic array. Clearly, large charges result in larger corrections. This correction requires the correct permittivity ε; this can now also be calculated reasonably straightforwardly using the same *ab initio* methods as in the defect calculation (e.g., Karki et al. 2000; Oganov et al. 2003). The charge-interaction correction can then be applied completely self-consistently.

Secondly, neutral or charged defect clusters can also introduce large dipole-moments into the supercell, giving rise to similar (although less strong) interactions as in the case of charged point defects discussed in the previous paragraph. Makov and Payne (1995), and more thoroughly Kantorovich (1999) and Kantorovich and Tupitsyn (1999), showed that the correcting factor for dipole-dipole interaction is given by $E_{dipole} = 2\pi P^2/(3V_c)$ where P is the total dipole moment of the supercell and V_c is the supercell volume.

With these corrections in hand, defect energies can be readily calculated using the supercell approach. It is important to note that when calculating migration enthalpies, the energy of the two similarly charged systems are subtracted from each other. Since the charge-interaction corrections presented above are the same for each system, they cancel. However, in fact the two systems have very different ionic arrangements (one having two vacancies and a migrating ion at its saddle-point, and the other with a single vacancy) and, therefore, they have different higher order electrostatic moments. A small error in the migration energy is expected from this.

The climbing image nudged elastic band method

As discussed previously, a key aspect to obtaining diffusion rates is finding the saddle point. This is necessary for the migration enthalpy and for ensuring that there is only one negative vibrational frequency for the Vineyard theory. The importance of this is exemplified by recent calculations and experiments on $MgSiO_3$ perovskite.

Empirical potential calculations on silicon diffusion in $MgSiO_3$ perovskite had estimated the migration enthalpy as being about 9 eV (Wright and Price 1993); this was much higher than for oxygen and magnesium, and agreed with the idea that silicon was the slowest diffusing species—and therefore rate limiting the rheology—in mantle perovskites. However, a later experimental study found a significantly lower migration energy of only 3.5 eV (Yamazaki et al. 2000). An identical value was also obtained by Dobson et al. (2008) but using a different procedure. The calculations were repeated by Karki and Khanduja (2007), but in this case using DFT to calculate the necessary energies. Their calculated migration enthalpies for oxygen and magnesium agreed with experimental values, but they also found a very high value for silicon of 8.33 eV (at room pressure). They suggested, therefore, that silicon diffusion must occur via some sort of cooperative mechanism involving oxygen vacancies. However, the reason is more prosaic than that; both theoretical studies chose the wrong migration pathway. Figure 2 is a contour map of computed migration enthalpies in a plane of possible saddle-points for silicon diffusing along the [110] pathway at two different pressures (see Ammann et al. 2009 for details). The two minimum energy points shown are 3.58 eV and 3.52 eV and are the most likely place through which the migrating atom would pass. The pathway chosen by Wright and Price (1993) and Karki and Khanduja (2007) are not shown, but are slightly higher on the Z-axis than the 3.52 eV (and 6.59 eV) point. Note that you do not have to be very far from the minimum energy point for the apparent (and erroneous) migration energy to increase substantially.

The climbing image nudged elastic band (CI-NEB) method (Henkelman et al. 2000) has transformed the search for saddle points. The method is shown graphically in Figure 3. Each

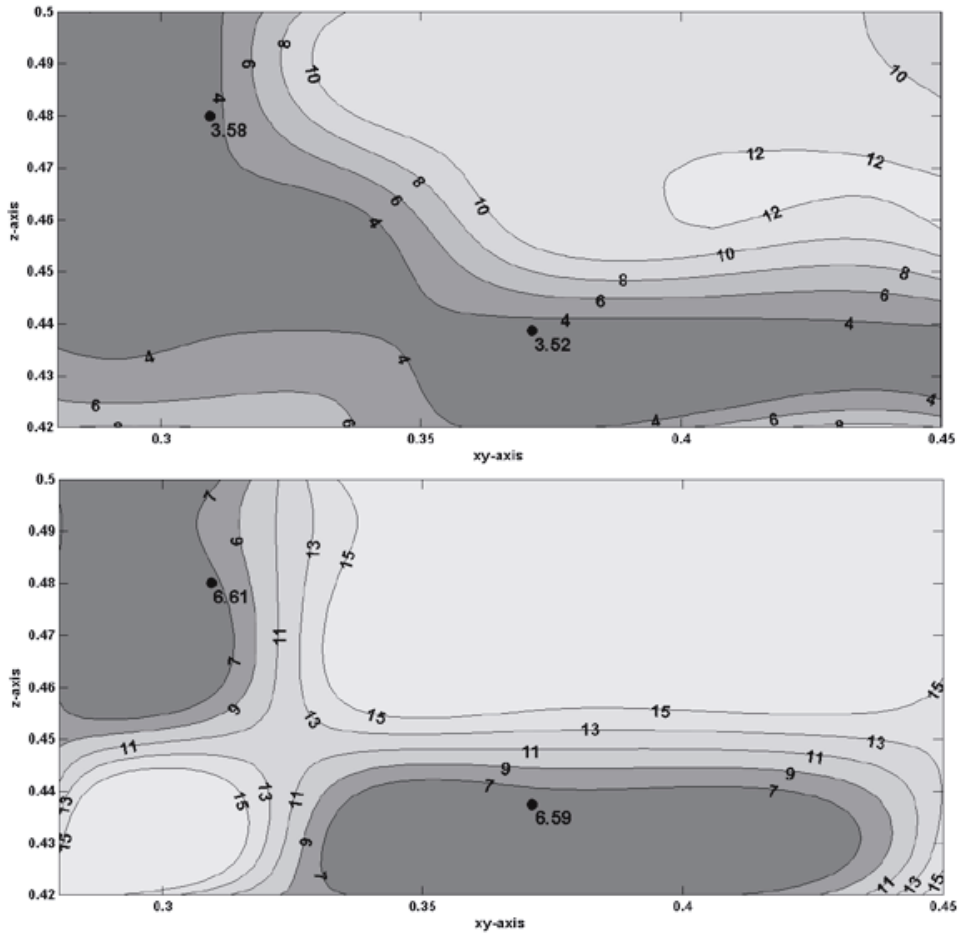

Figure 2. Contour maps of migration enthalpies for silicon diffusion in $MgSiO_3$ perovskite for the direct jump along <110> at 3.3 GPa (upper) and 151.7 GPa (lower). The calculated minima are marked with black dots and labeled with their corresponding value. In calculations, a small deviation from the minimum energy migration pathway (black dots) can result in a substantial increase of the migration enthalpy shown [With kind permission from Springer Science+Business Media: *Physics and Chemistry of Minerals*, "DFT study of migration enthalpies in $MgSiO_3$ perovskite." Vol. 36, 2009, p 151-158, Ammann et al., Figure 3.]

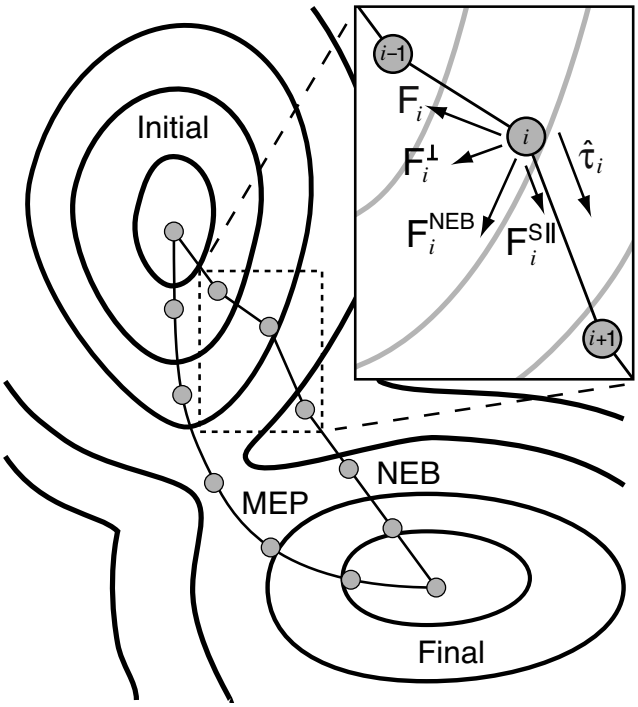

Figure 3. In order to find the minimum energy pathway (MEP) one can use the nudged elastic band (NEB) method. The nudged elastic band force $\mathbf{F}^{NEB}$ is the sum of the spring force $\mathbf{F}^{S||}$ along the tangent τ plus the perpendicular force from the potential $\mathbf{F}^{\perp}$. The unprojected force due to the potential $\mathbf{F}$ is also shown [Reprinted with permission from Sheppard et al. (2008) *Journal of Chemical Physics*, Vol. 128, Issue 13, 134106. Copyright 2008, American Institute of Physics.]

of the points corresponds to a set of atoms for which the forces and energies are calculated. The two end points are the initial and final equilibrium positions. The points in-between are possible configurations of atoms which the system might take as an atom hops from one side of the barrier to the other. Initially atomic positions may be just linearly interpolated between their positions in the initial and final systems. The idea is to evolve the different systems such that they all lie on the MEP (minimum energy pathway) by minimizing the NEB-force $\mathbf{F}^{\mathrm{NEB}}$. The image (set of atomic coordinates) with the highest energy is pushed upwards along the NEB until it reaches exactly the saddle point. The CI-NEB method provides a recipe for doing this. Moreover, there is a toolkit for use with the DFT code VASP available from *http://theory.cm.utexas.edu/vtsttools/*. Since we are only interested in the saddle point and not the whole minimum energy pathway, we use only four images. Nevertheless, for a low-symmetry pathway like silicon in perovskite, this requires on the order of 200 individual electronic minimizations of the super-cell to find the saddle point.

LDA vs. GGA

The quality of the results using DFT depends on the ability of the exchange-correlation functional to model the many-body electronic interactions. The most common exchange correlation functionals are the local density (LDA) and the general gradient approximation (GGA) (Perdew and Zunger 1981; Perdew and Y. Wang 1992; Perdew and Burke 1996). On the other hand, defect energetics are tightly linked with the cell-volume (as is evident from the strong pressure dependence(see below)). It is, thus, important that experimental and theoretical cell-volumes are equal (or at least similar). We have calculated the imposed pressure on the supercell within GGA. In order to estimate the uncertainty inherent to DFT we have compared GGA with LDA calculations performed at the same cell-volume. In general we find that LDA produces slightly smaller values for the migration enthalpy, by about 5 to 10%. Similarly, we find that ν^0 is also about 5% lower when calculated with LDA than with GGA.

RESULTS ON MANTLE PHASES

Results on MgO

Magnesiowüstite (Fe, Mg)O is thought to be the second most abundant mineral in the lower mantle accounting for about 20% of the volume (e.g., Jackson 1998). The investigation of the diffusional properties of its pure endmember periclase MgO is hence of major importance for Earth Sciences. It crystallizes in the rock-salt structure even under lower mantle conditions (Lin 2002; Oganov et al. 2003). Periclase is also an important industrial material with a wide range of applications and often serves as a prototype material for other ionic oxides (Kotomin et al. 1996).

MgO is a simple cubic oxide for which high-pressure and high-temperature experimental diffusion measurements exist. Since it crystallizes in the rock-salt structure, the location of the saddle point is given trivially by symmetry and is located half-way between the initial and final position. This is, however, only strictly true at high pressures. We find at low pressures, in agreement with Vočadlo et al. (1995), that the magnesium saddle-point bifurcates perpendicular to the jump trajectory. But also these saddle-points can be readily found by offsetting from the half-way position (a second-order saddle-point) and relaxing the migrating ion into the bifurcated first order saddle points (the lowering in energy is though negligible). In contrast with Vočadlo et al. (1995), we have not found any bifurcation along the oxygen jump trajectory. Thus, the CI-NEB method is not required for MgO. The ease of finding the saddle point has meant that absolute diffusion rates in MgO have been calculated within Vineyard-theory a number of times (e.g., Sangster and Stoneham 1984; Harding et al. 1987; Vočadlo et al. 1995). The pre-exponential factors from the different studies agree to within about 1 order of magnitude; some of this scatter can be attributed to different potentials and some to different methods.

Even more studies concentrated on the migration enthalpies and all obtained migration enthalpies of about 2 eV for both magnesium and O, which is in agreement with experiments. Some experimental and theoretical values of the migration enthalpies are given in Table 1 (which is not exhaustive) and attempt frequencies are given in Table 2.

Table 3 summarizes calculated migration enthalpies in periclase at high pressures. Ita and Cohen (1997, 1998) as well as Ito and Toriumi (2007) performed molecular dynamics simulations using interatomic potentials to calculate the absolute diffusion rates in MgO under lower mantle conditions. While both studies are in agreement with the available experimental data (up to 35 GPa), they disagree with each other at elevated pressures (above 60 GPa). Ita and Cohen (1997, 1998) observe a continuous increase of the migration enthalpy with increasing pressure, while in contrast Ito and Toriumi (2007) find that the migration enthalpy decreases after reaching a maximum around 50 GPa. The difference between their results could simply be linked to their different interatomic potentials. Our results agree with those of Ita and Cohen (1997, 1998). Nevertheless, it should be noted that all three studies have an activation volume that is in agreement with the available experimental data (Yamazaki and Irifune 2003; Holzapfel et al. 2003; Van Orman et al. 2003) at pressures up to 35 GPa.

Table 1. Migration enthalpies in MgO at 1 bar from experiments and theory (for single vacancy diffusion). DFT: density functional theory, LDA: local density approximation, GGA: general gradient approximation, MD: molecular dynamics, HF: Hartree-Fock, LD: lattice dynamics, ML: Mott-Littleton.

Theory	ΔH_{Mg} **[eV]**	ΔH_{O} **[eV]**	**Method**
This study	1.93	2.05	DFT GGA
	1.82	1.93	DFT LDA
Ito and Toriumi (2007)	2.09	2.23	MD
Gilbert et al. (2007)	2.20	2.31	DFT LDA
Karki and Khanduja (2007)	2.26	2.42	DFT LDA
Kotomin and Popov (1998)	2.43	2.50	HF
Ita and Cohen (1997, 1998)	1.70	1.97	MD
Vočadlo et al. (1995)	1.99	2.00	LD
De Vita et al. (1992)	2.39	2.48	DFT LDA
Harding et al. (1987)	—	2.1	ML
Sangster and Stoneham (1984)	—	2.26	ML
Sangster and Rowell (1981)	2.07	2.11	ML
Mackrodt and Stewart (1979)	2.16	2.38	ML
Experiments			
Yoo et al. (2002)	—	3.24±0.13	
Shirasaki and Hama (1973)	—	2.43±0.21	
Oishi and Kingery (1960)	—	2.71±0.26	
Mackwell et al. (2005)	2.17±0.07	—	Mg-Fe interdiffusion
Holzapfel et al. (2003)	2.64±0.17	—	Mg-Fe interdiffusion (8-23 GPa)
Yamazaki and Irifune (2003)	2.34±0.33	—	Mg-Fe interdiffusion (7-35 GPA)
Yang and Flynn (1994,1996)	2.52	6.91	Ca-diffusion (2.33 this study)
Sempolinsky and Kingery (1980)	2.28±0.21	—	
Duclot and Departes (1980)	2.20	—	
Wuensch et al. (1973)	2.76±0.08	—	
Lindner and Parfitt (1957)	3.44±0.13	—	

Table 2. Attempt frequencies for magnesium (ν_{Mg}), oxygen (ν_O), calcium (ν_{Ca}) and bound divacancies (ν_{MgO}) in MgO for the single jumps at 0 GPa. The same labels for the methods as in Table 1 are used.

	ν_{Mg} [THz]	ν_O [THz]	ν_{Ca} [THz]	ν_{MgO} [THz]	Method
This study	12.12	13.82	25.1	87.9	DFT GGA
Ita and Cohen (1997, 1998)	5.2	5.2	—	—	MD
Vočadlo et al. (1995)	15.95	8.55	—	—	LD
Harding et al. (1987)	23.15	—	—	—	ML
Sangster and Stoneham (1984)	32.9	—	—	—	ML

Table 3. Migration enthalpies of MgO at pressures P of the lower mantle. ΔH_{MgO} is the migration enthalpy for a divacancy (the higher of the two barriers for magnesium and oxygen hops).

	P [GPa]	ΔH_{Mg} [eV]	ΔH_O [eV]	ΔH_{MgO} [eV]
This study	5.3	2.06	2.2	2.81
	30.3	2.61	2.82	2.83
	136.6	3.88	4.27	2.67
Karki and Khanduja (2007)	20	3	2.9	—
	50	3.3	3.15	—
	150	4.3	3.95	—
Ito and Toriumi (2007)	20	2.59	2.66	—
	50	2.98	3.02	—
	140	2.12	2.31	—
Ita and Cohen (1997,1998)	20	2.34	2.55	—
	80	3.22	3.64	—
	140	3.99	4.31	—

Our results for MgO are shown in Figure 4. In order to compare our theoretical results with experiments, an estimate of the vacancy concentration in the experiments must be made. The Schottky-formation energy, $\Delta H_{S,}$ and Frenkel-formation energy, $\Delta H_{F,}$ have been calculated several times over the last 30 years and are given in Table 4 (the list is not exhaustive). For the charged defect correction, we adopted the value of the permittivity calculated by (Oganov et al. 2003). Formation energies continuously increase with pressure (Karki and Khanduja 2006b).

Our calculations and previous results find formation energies of Schottky and Frenkel-pair defects to be between 6.45-7.7 eV and 10.35-15.2 eV respectively. The equilibrium concentration of intrinsic magnesium vacancies is, therefore, small. However, the presence of heterovalent impurities will result in the formation of extrinsic vacancies in order to maintain charge neutrality. In fact, only a small concentration of impurities (much less than a few ppm at 2000 K) is sufficient for the number of extrinsic magnesium-vacancies to greatly exceed the number of intrinsic vacancies, and generally, the number of extrinsic magnesium-vacancies is assumed to dominate the number of defects in MgO by several orders of magnitude. It is possible, therefore, to constrain the experimental magnesium-vacancy concentration from their measured impurity concentrations. As shown in Figure 4, magnesium diffusion in MgO can readily be explained by our results using reasonable vacancy concentrations.

The experiments on oxygen diffusion are more difficult to explain than for magnesium. First of all oxygen diffusion is significantly slower than magnesium, and secondly, the different

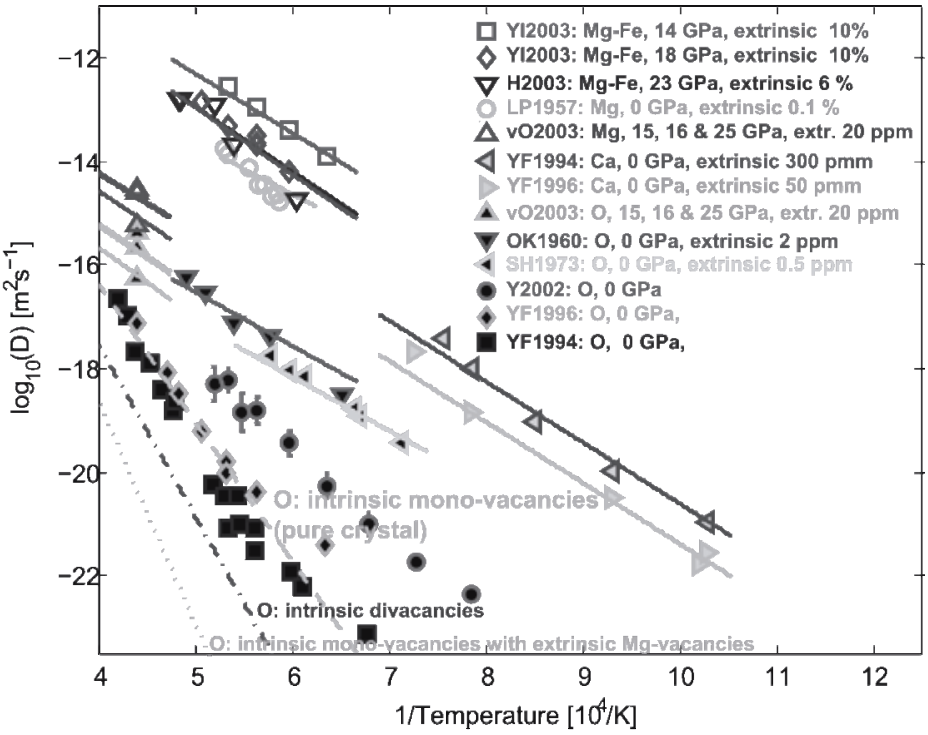

Figure 4. Lines are the results of our calculations using vacancy concentrations appropriate for the experiments. Empty symbols are magnesium (calcium) diffusion, filled symbols are for oxygen. In all experiments, magnesium diffusion can be readily explained assuming extrinsic vacancy hopping. YI2003: Yamazaki and Irifune (2003); H2003: Holzapfel et al. (2003); LP1957: Linder and Parfitt (1957); YF1996, YF1994: Yang and Flynn (1994, 1996); vO2003: van Orman et al. (2003); OK1960: Oishi and Kingery (1960); SH1973: Shirasaki and Hama (1973); Y2002: Yoo et al. (2002). The lowest oxygen diffusion data is not explained by theory: free oxygen vacancies are expected to be suppressed by extrinsic magnesium vacancies (for YF1994 and YF1996, they are constrained via Ca-diffusion data) resulting in the dotted line. Intrinsically formed divacancies are at least a magnitude too low (dash-dotted line). Intrinsically formed oxygen (mono-)vacancies could explain the Yang and Flynn data (dashed line) if no impurities (an extrinsic magnesium vacancy below 10^{-8}) are around for suppression (which is not the case).

Table 4. Theoretical Schottky ΔH_S and Frenkel ΔH_F defect formation energies in MgO at 0 GPa. The comment (bound) is used for the formation of divacancies and the same labels for the methods as in Table 1 are used.

	ΔH_S [eV]	ΔH_F [eV]	**Method**
This study	6.45 3.88 (bound)	14.21 (O)	DFT GGA
Gilbert et al. (2007)	5.97	10.35 (Mg) 12.17 (O)	DFT LDA
Karki and Khanduja (2006)	6.83	—	GGA LDA
Alfe and Gillan (2005)	7.5±0.53	—	QMC
Ita and Cohen (1997, 1998)	6.48 4.92 (bound)	—	MD
De Vita et al. (1992)	6.88	—	DFT LDA
Jacobs and Vernon (1990)	7.7 5.0	12.4 (Mg) 11.6 (O)	
Mackrodt (1988)	7.66	—	ML
Sangster and Rowell (1981)	7.72	—	MD
Mackrodt and Stewart (1979)	7.5 4.95 (bound)	11.9 (Mg) 15.2 (O)	ML

studies produce different slopes. The slowness is mostly due to the low concentration of oxygen vacancies in the experimental sample. The different slopes suggest that different mechanisms of migration and of intrinsic vacancy formation are at work. Some experiments have been thought to be in the intrinsic regime, where the measured activation energy also contains an activation energy of vacancy formation as well as migration (high slopes), and some are in the extrinsic regime, and so the measured activation energy is the migration energy only (low slopes). However, our results suggest that it cannot be intrinsic diffusion that is responsible for the higher slopes, but another, yet unknown, extrinsic diffusion mechanism.

The experiments of Oishi and Kingery (1960) as well as of Shirasaki and Hama (1973) are easiest to explain. They were performed on relatively impure samples, and the measured diffusion was assumed to be in the extrinsic regime. Plotted on the Figure 4 are our absolute diffusion rates, assuming an extrinsic vacancy concentration of about 2 ppm and 0.5 ppm respectively. These fit the experimental data well.

The experiments of Yang and Flynn (1994, 1996) are not as easy to interpret. The dashed line is our prediction for oxygen diffusion if we assume the oxygen vacancies are being formed intrinsically. The concentration of oxygen and magnesium vacancies is given by

$$C_{V_{\mathrm{O}}} C_{V_{\mathrm{Mg}}} = e^{\frac{-\Delta H_S}{kT}} \tag{6}$$

where, for no extrinsic vacancies, $C_{V_{\mathrm{O}}} = N_{V_{\mathrm{O}}}/N$ and $C_{V_{\mathrm{Mg}}} = N_{V_{\mathrm{O}}}/N$ are the oxygen and magnesium vacancy concentrations respectively. If we assume the oxygen and magnesium vacancies are charge balancing each other, then the diffusion coefficient is given as

$$D = N_V \frac{Z}{6} l^2 \nu^* e^{\frac{-\Delta H_M}{kT}} = N \frac{Z}{6} l^2 \nu^* e^{\frac{-(\Delta H_s/2 + \Delta H_M)}{kT}} \tag{7}$$

where the defect formation enthalpy, ΔH_S, the migration enthalpy, ΔH_M, and the effective jump frequency, ν^*, are all calculated from first principles. Although this fits the experimental data well, the good fit is, in fact, fortuitous. Yang and Flynn also measured Ca diffusion in the same MgO samples. These are also shown on Figure 4, and are very well described by an extrinsic vacancy diffusion mechanism (i.e., the slope is just the migration enthalpy), with an extrinsic cation vacancy concentration of about 50 to 300 ppm. The problem is that in samples with significant extrinsic concentrations of one of the Schottky pairs, Equation (6) above shows that the concentration of the other vacancy is proportionally reduced. For $C_{V_{\mathrm{Mg}}}$ of a few 10s of ppm, $C_{V_{\mathrm{O}}}$ is reduced to a tiny amount, and there are simply not enough oxygen vacancies to produce the diffusion coefficients shown in Figure 4. The oxygen diffusion coefficients for a sample containing 50 ppm magnesium vacancies are shown in Figure 4 (dashed line); it is many orders of magnitude too slow.

This problem with rationalizing the cation and anion diffusion results simultaneously was realized by Yang and Flynn, and they suggested that their diffusion experiments were actually measuring the diffusion of bound MgO vacancy pairs (or divacancies). The concentration of MgO divacancies is given, for the intrinsic case, by

$$C_{V_{\mathrm{MgO}}} = e^{\frac{-(\Delta H_S + \Delta H_B)}{kT}} \tag{8}$$

where ΔH_B is the energy of binding the two vacancies together (which is negative since they are opposite charge and, therefore, attractive). To calculate the mobility of the bound pair, we have calculated the migration enthalpies and frequency factors for the bound vacancies individually, and assumed that the slowest species limits the diffusion of the bound pair (see Tables 2, 3 and 4). The binding energy is about –2.6 eV and the effective migration energy for the slowest vacancy is 2.8 eV. Our theoretical absolute diffusion rates of the divacancies are

shown in Figure 4 (dashed-dot lines); they too are much slower than measured in experiments. To date, we are unable to constrain the oxygen diffusion mechanism for the experiments of Yang and Flynn (1994, 1996).

The recent measurement of oxygen diffusion by Yoo et al. (2002), revealed yet another activation energy, and much higher rates than the previous experiments. They suggest tentatively that their measured diffusion rates are actually for interstitial oxygen, although they acknowledge that these are unlikely to be in significant concentrations in MgO. Again, we have tested this by calculating the migration enthalpy for the oxygen interstitial and its formation energy. Interestingly, the migration energy for the interstitial is low: 0.7 eV. However, the formation enthalpy is, as expected, very large (~7 eV; half the Frenkel defect formation energy). Therefore, we conclude that there is not a significant concentration of oxygen interstitials in MgO. What the diffusion mechanism for the experiments of Yoo et al. (2002) is, also remains unclear.

Further complicating the assessment of the oxygen vacancy concentration and oxygen diffusion mechanism is the experimental finding that oxygen diffusion along dislocations (pipe-diffusion) has a similar activation energy (Narayan and Washburn 1973, Sakaguchi et al. 1992) as mono-vacancy diffusion. This has likely been observed by Yang and Flynn (1994, 1996) (and maybe also by Yoo et al. 2002) in their low temperature data of oxygen diffusion. At the same time, this might suggest that even the data of Oishi and Kingery (1960) as well as of Shirasaki and Hama (1973) represents pipe-diffusion instead of extrinsic oxygen diffusion as we have assumed here.

Although it is not possible to explain all the experimental results for oxygen diffusion in MgO, we are able to model successfully experiments where the migration mechanism is simple and unambiguous. For instance we very accurately model the direct vacancy hopping mechanism for cations when the vacancies are extrinsically controlled. Similarly, we can accurately model oxygen diffusion when it is in the extrinsic regime. In other words, there is good reason to expect that the migration barriers and frequency factors calculated via DFT are accurate to within a few tenths of an eV.

Results on $MgSiO_3$ perovskite

$MgSiO_3$ perovskite is the dominant phase in the Earth's lower mantle comprising up to 80% of its volume and it is thus of fundamental importance for understanding the thermochemical evolution of the Earth (e.g., Jackson 1998)

Computational studies of defect formation energies using the Mott-Littleton method suggest that the dominant defect in perovskite is the MgO partial Schottky defect (Price et al. 1989; Wright and Price 1993). Frenkel defects (interstitials) are energetically unfavorable. The same result has been found by first principles calculations (Karki and Khanduja 2006a, 2007). The high intrinsic formation energies (7.4 eV—MgO partial Schottky; 20.8 eV—full Schottky); rapidly increasing with increasing pressure) imply that vacancy concentrations in experiments and in the Earth's mantle are controlled extrinsically, i.e., by impurity content.

Magnesium and oxygen diffusion. We find that diffusion of both oxygen and magnesium in perovskite occurs via simple vacancy hopping. The migration enthalpies and jump frequencies are given in Tables 5 and 6. Figure 5 shows our predicted diffusion rates plotted against those found experimentally. The upper and lower bounds are those found from LDA and GGA respectively. In order to make this comparison, we need to estimate the vacancy concentrations in the experiments. For the oxygen diffusion experiments of Dobson (2003) this is relatively straightforward since he doped his sample with 0.6% Na in order to extrinsically control oxygen vacancies. Since each oxygen vacancy is charge balancing two Na^+ ions, this results in 0.1% vacancies (per unit cell). At high temperatures, a change in the conduction mechanism has been

Table 5. Migration enthalpies of all species in $MgSiO_3$ perovskite from experiments and theory. Our values are averages over the migration enthalpies of all different jumps (8 for oxygen, 3 for magnesium). For silicon our value is the maximum energy of the barrier of the six jump cycle.

	P [GPa]	ΔH_{Mg} [eV]	ΔH_{Si} [eV]	ΔH_O [eV]	Method
This study	24	3.81	3.64LDA	1.06	DFT GGA
	140	6.43	5.98LDA	2.23	
Karki and Khanduja (2007)	30	4.78	9.1	1.41	DFT LDA
	120	7.71	10.48	2.57	
Wright and Price (1993)	0	4.57	9.2	0.96	ML
	60	6.13	—	—	
	125	7.43	10.32	—	
Price et al. (1989)	0	4.6	—	0.8	ML
Holzapfel et al. (2005)	24	4.29±0.64	—	—	Mg-Fe interdiff.
Dobson et al. (2008)	25	—	3.6±0.76	—	
Yamazaki et al. (2000)	25	—	3.48±0.38	—	
Dobson (2003)	25	—	—	1.35±0.2	Na-doped
Xu and McCammon (2002)	25	—	—	1.47	Al-bearing

Table 6. Average attempt frequencies for magnesium and oxygen diffusion in $MgSiO_3$ perovskite. The attempt frequencies for the six jump cycle are shown in Figure 4.

P [GPa]	ν_{Mg} [THz]	ν_O [THz]
24	4.95	5.94
140	17.39	14.04

observed (probably from oxygen ionic to intrinsic electronic) and we subtracted this contribution from the experimental data in order to obtain the pure oxygen ionic conduction. Thereby our predicted diffusion rates for oxygen are only slightly lower than those found by Dobson (2003) but with a migration enthalpy almost exactly the same. Earlier studies of the conductivity of perovskite (Katsura et al. 1998; Xu et al. 1998; Xu and McCammon 2002) contained iron and hence the electrical conductivity is dominated by small-polaron electronic conduction. Nevertheless, at the highest temperature the study of Xu et al. (1998) showed a contribution from oxygen ionic conduction. Xu and McCammon (2002) analyzed this oxygen ionic component and found an activation energy in good agreement with our migration enthalpy.

For the Mg-Fe exchange experiments of Holzapfel et al. (2005) the concentration of magnesium vacancies is controlled by the amount of ferric iron. For an Al-free system, we can use the geochemical experiments of Lauterbach et al. (2000) and the expected oxygen fugacity in the multi-anvil experiments. Using the expression of Lauterbach et al. (2000), we estimate that the extrinsic concentration of magnesium vacancies should be about 0.2%. Using this concentration, our predictions for magnesium diffusion are in good agreement with the experiments.

Silicon diffusion. Silicon diffusion in $MgSiO_3$ perovskite, however, is complicated by the fact that we find that silicon diffusion does not occur via a simple vacancy method, where silicon jumps from one site directly into an adjacent vacancy, as with magnesium and oxygen. The lowest migration enthalpy for the direct jump is 5.2 eV, substantially higher than the values of ~3.6 eV obtained experimentally. Rather, we find that it occurs via a so-called

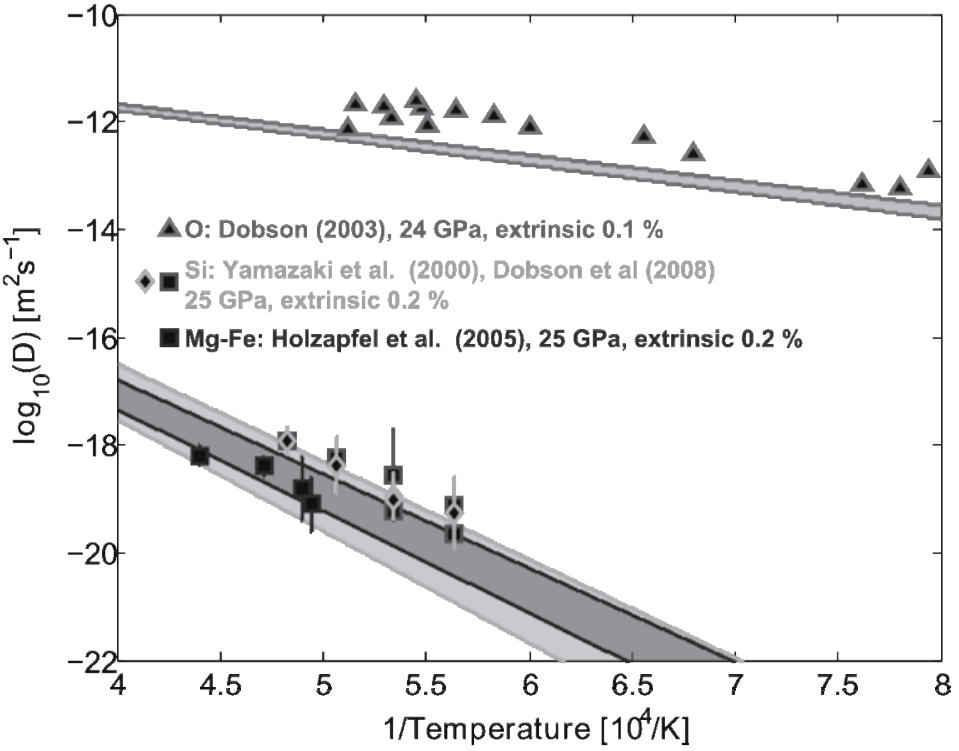

Figure 5. Comparison of experimental diffusion rates in $MgSiO_3$ perovskite with our theoretical calculations. Oxygen diffusion experiments in perovskite (Dobson 2003) had an estimated vacancy concentration of 0.1% (controlled via Na-content). We have subtracted the conductivity contributed by another mechanism in the high-temperature regime observed in the experiments. We calculated the vacancy concentration for the experiments (Holzapfel et al. 2005) of magnesium-iron interdiffusion in perovskite at 24 GPa at reducing conditions from the geochemical experiments of Lauterbach et al. (2000) to be 0.1-0.2%. Silicon vacancy concentrations in the experiments (Yamazaki et al. 2000; Dobson et al. 2008) have been estimated to be approximately 0.2% making reasonable assumptions (see text for details), however, they are not very certain.

six-jump cycle. This is common in some binary alloys (e.g., Elcock and McCombie 1957; Huntington et al. 1961; Debiaggi et al. 1996; Divinski and Herzig 2000; Duan 2006). The six jump cycle is shown in Figure 6. In a normal vacancy hopping mechanism, the migrating ion hops directly to an adjacent vacancy. But in the six-jump cycle, a magnesium ion jumps into the silicon vacancy, making an antisite defect and a magnesium vacancy. The adjacent silicon ion then jumps into the magnesium vacancy, leaving a new silicon vacancy. The situation then repeats itself, with a magnesium jumping into the new silicon vacancy, followed by the first antisite magnesium jumping into the vacated magnesium site. The silicon ion then jumps into the silicon vacancy from the magnesium site, and the cycle finishes with the magnesium on the silicon site jumping into the adjacent magnesium vacancy. The silicon vacancy has jumped to an adjacent site via six different intermediate hops, each with its own activation enthalpy. To analyze this complex diffusion process, we first have to consider what the effective activation energy of the six jumps is, and secondly, we have to consider how many times the cycle is broken by a vacancy hopping to a site that is not part of the cycle.

An analytical solution to the rate of the six jump cycle can be obtained using the approach of Arita et al. (1989). This method provides an effective jump-frequency, Γ, for the complete cycle. Also, by calculating the jump-frequency at different temperatures, it is possible to obtain an apparent activation (or migration) enthalpy for the cycle. It does, however, require the twelve individual jump-frequencies (obtained from Vineyard theory) and their migration energies. These are shown in Figure 6 for the fastest silicon cycle. The effective activation energy lies somewhere between the migration energy of the single largest jump, and the energy difference between the original site and the highest energy saddle point. As shown by Arita

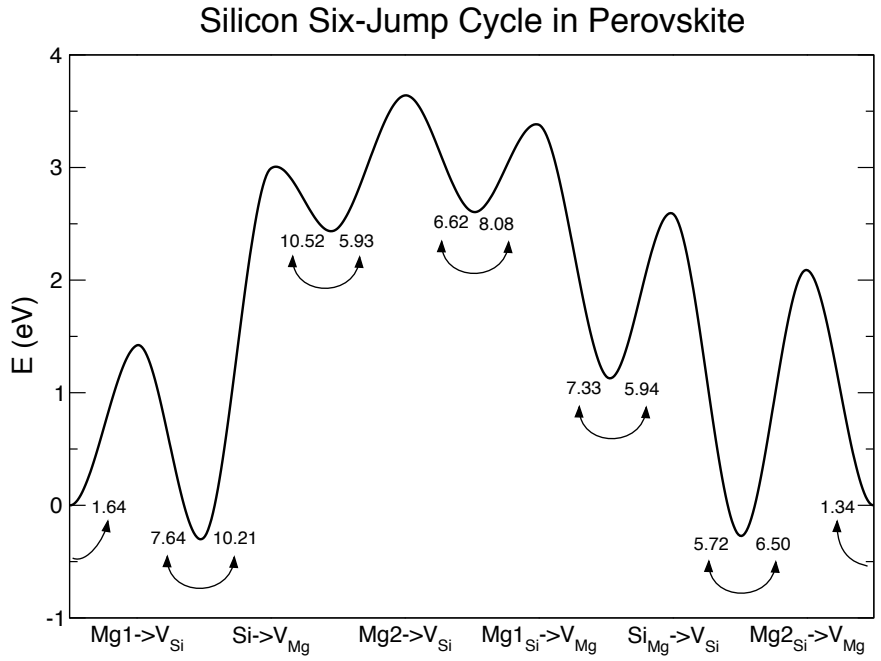

Figure 6. The energy barrier of the six-jump cycle for silicon diffusion in perovskite. The numbers are the attempt frequencies towards neighboring states as indicated by the arrows.

et al. (1989), the former is appropriate at high temperatures, while the latter is appropriate at low temperatures. The details depend on the particular system. We have used this approach for the cycle shown in Figure 6 and find that at all reasonable temperatures, the apparent migration energy is equal to 3.6 eV. This is the same as the maximum saddle point energy. The apparent migration enthalpy does decrease towards the largest single jump (3.3 eV for the silicon jumping into the magnesium vacancy), but only at very high temperatures. This is as expected since the maximum saddle-point energy (3.6 eV) is very similar to the single largest jump. This migration enthalpy agrees very well with the experimentally derived values of 3.61 eV and 3.5 eV obtained by Dobson et al. (2008) and Yamazaki et al. (2000) respectively. The entire cycle for one silicon vacancy to migrate can be described as a single Arrhenius process

$$D_V = \nu_a l^2 e^{\frac{-\Delta H}{kT}} = 3.5\times10^{12} l^2 e^{\frac{-3.6}{kT}} \tag{9}$$

Figure 5 shows the available experimentally obtained diffusion coefficients of silicon compared to our results. In order to make such a comparison, we have used a silicon vacancy concentration of 0.2%. This seems unexpectedly high for silicon vacancies, but it seems unavoidable that the experiments do indeed have very high concentrations of silicon vacancies. Using a nearest neighbor jump distance of 2.4 Å, a representative jump frequency of 10 THz, and the experimentally determined migration enthalpy of 3.6 eV, we can invert each of the experimental diffusion coefficients of Dobson et al. (2008) for the silicon vacancy concentration. These range from 0.35% to 0.075%. A similar range is found from the data of Yamazaki et al. (2000). The range is also in rough agreement with the defect calculations of Hirsch and Shankland (1991). So a vacancy concentration of about 0.2% is perfectly consistent with the fast measured diffusion rates.

Although the experimental diffusion rates can be explained by the six-jump cycle, there is an additional complication to be considered. At each step of the cycle there is a possibility that one of the vacancies takes a hop to a site not in the cycle. This, therefore, breaks the cycles until another vacancy comes along. For instance, the first step in the cycle produces a magnesium vacancy. The activation barrier for it to take the next step in the cycle is about 3.3 eV. However, the energy barrier for it to hop to one of the other neighboring magnesium

sites instead of the silicon site, is only between 3.6 and 4.1 eV (LDA and GGA respectively); there is, therefore, a non-negligible probability that it will take this jump. These processes of breaking the cycle must be taken into account when calculating silicon diffusion coefficients.

We can do this using Kinetic Monte Carlo (reviewed by Voter 2005). Given a set of rate constants (diffusion constants in this case), KMC is a way of propagating a dynamic system through a possibly complex set of paths (or phase space). If we image a vacancy at a certain position, it may have a number of possible paths. Normally it will take the one that is most probable (generally the lowest migration barrier), but sometimes it will take another. Once it has moved on, it is faced with another set of possibilities and associated probabilities. KMC provides a way of moving the system through the phase space and determining the overall rate constant (or diffusion constant). We could use this technique as an alternative to the analytic technique for obtaining the effective diffusion coefficient for the full cycle, ignoring possible breaks in the cycle; we do indeed get the same result using both methods. But KMC has to be used when a diffusing species has a choice of paths.

We are interested in how many times the six-jump cycle is broken. In order to use KMC to do this, we not only need the jump-frequencies for the possible first jumps off the cycle, we also need the next jumps in order to ensure that it doesn't jump back into the cycle. This rapidly becomes an impossibly large number of calculations, so we have restricted the calculation to the first two jumps off the cycle, after which we assume the vacancy is gone.

Our results show that the cycle is broken somewhere between about 1% and 20% of the time, depending on whether LDA or GGA jump-rates are used. This is mainly because of the change in the energy-barrier of the single jumps. LDA results in lower energy-barriers than GGA, however, the relative change of the energy barriers (from GGA to LDA) for the cycle-breaking jumps is smaller than the change in the cycle-barriers. The cycle is mostly broken at the second step. The migration energy for the magnesium vacancy to jump into the silicon site is about 3.3 eV; this is only slightly less than the migration energy of 3.6 eV for it to move into an adjacent magnesium site that is not in the cycle. The next jump is even lower in energy and the vacancy migrates away. The reason the cycle breaks can be easily understood: the silicon cycle starts with a silicon vacancy (charge −4), which is then occupied by a magnesium ion forming a magnesium on a silicon site (charge −2) and a magnesium vacancy (charge −2). The antisite and the magnesium vacancy have the same charge sign, and hence repel each other electrostatically. The energy of the reaction

$$Mg^{x}_{\mathrm{Mg}} + V^{''''}_{\mathrm{Si}} = V^{''}_{\mathrm{Mg}} + Mg^{''}_{\mathrm{Si}} \tag{10}$$

is only −0.3 eV when they are adjacent to each other, however, it decreases to about −2.2 eV (depending on the functional and the permittivity chosen for the charged defect correction) when the magnesium antisite and the magnesium are allowed to be infinitely separated. In other words, regardless of whether or not the cycle breaks, there should only ever be a vanishingly small concentration of silicon vacancies to begin with. This is completely at odds with the large number of vacancies required by fast diffusion coefficients observed experimentally.

One way to overcome the electrostatic repulsion of antisite and magnesium vacancy is to neutralize one of them; the most obvious candidates to do this are protons. We have, therefore, calculated the energy of the following reaction,

$$Mg^{x}_{\mathrm{Mg}} + 2H^{''}_{\mathrm{Si}} = V^{''}_{\mathrm{Mg}} + (Mg + 2H)^{x}_{\mathrm{Si}} \tag{11}$$

where, as with the previous reaction, the two species on the right-hand side are infinitely apart. We find that this reaction is strongly endothermic, with an energy of 2.44 eV. In other words, protons increase the concentration of silicon vacancies, something that has been suggested for other silicates such as forsterite (Brodholt 1997). Obviously the presence of protons may

change the jump frequencies, but jumps into sites inhabited with protons become substantially more complicated calculations and we have not attempted these yet.

At present we are able to explain the high silicon diffusion rates seen experimentally in two independent studies as a six-jump cycle with about 0.2% silicon vacancies stabilized by protons. The activation enthalpy of the direct jump is too high. So far, appreciable amounts of water have not been experimentally verified in perovskite, with some studies showing negligible water solubility (Litasov et al. 2003; Bolfan-Casanova 2005). Regardless of whether it is water, or some other extrinsic mechanism, the experiments are only consistent with high concentrations of silicon vacancies.

Other investigated silicon diffusion mechanisms

Previous studies (Wright and Price 1993; Karki and Khanduja 2007) on silicon migration barriers in perovskite found a decrease in the migration enthalpy in the presence of an oxygen vacancy. However, for our direct pathway (Ammann et al. 2009), the migration energy in the presence of a oxygen vacancy is increased to about 6.2 eV. This finding is not surprising as an oxygen-vacancy has the same charge-sign as the migrating silicon ion.

In many other silicates, silicon diffusion occurs via an interstitial mechanism and migration enthalpy and pre-exponential factor are linearly correlated (Béjina and Jaoul 1997) (compensation law). As observed by Béjina and Jaoul (2003), silicon diffusion in perovskite also satisfies this compensation law and they therefore suggested that silicon in perovskite diffuses via an interstitial mechanism. We find that there is a stable split interstitial configuration in which two silicon interstitials are located on opposite faces of the oxygen octahedron (slightly elevated above the centre of the triangle faces), around a vacancy at the centre of the octahedron. Split interstitials are very common in many materials and for various species—e.g., in forsterite (Walker et al. 2009; Béjina et al. 2009), quartz (Roma et al. 2001), various metals (Schilling 1978) and semi-conductors (Lee et al. 1998). However, our results indicate that also this split-interstitial mechanism cannot explain the experimental findings as the formation energy of this state is about 10 eV at 24 GPa.

Finally, we consider antisite migration. The idea is that the cation sublattice can be partially inverted, i.e., that magnesium ions occupy silicon vacancies and silicon ions occupy magnesium vacancies. The intrinsic generation of such an antisite pair, i.e., magnesium and silicon swap sites at the same time is energetically unlikely (12 eV at 24 GPa). The formation energy of such a bound antisite-pair is, however, only 3.1 eV (at 24 GPa) above the perfect crystal.

Silicon jumps, onto magnesium vacancies and vice versa, are the energetically most favorable cation jumps (among the ones investigated). We have found three mechanisms which make use of these antisites and are energetically feasible: I) the direct jump to second nearest neighbor vacancies in the presence of a magnesium vacancy, II) the antistructure bridge and III) the six-jump cycle.

(1) In order to migrate silicon efficiently through the crystal by the direct mechanism, magnesium vacancies need to be neighboring silicon vacancies. Unsurprisingly, this is not the case as they carry the same charge and thus repel each other.

(2) The antistructure bridge mechanism (also known in binary alloys, e.g., Duan 2006) starts with a silicon-vacancy plus a silicon-antisite atom. The antisite ion jumps into the vacancy effectively changing the type of the vacancy and a nearby silicon ion jumps from its silicon site onto the new magnesium vacancy creating again an antisite plus a silicon vacancy. The analogous process works for magnesium antisites. While we can expect to have quite some inversion for silicon vacancies (occupied with magnesium ions, formation energy ~-2.5 eV), there will be only very few silicon atoms occupying magnesium vacancies (formation energy ~8 eV). While this mechanism might well

contribute to magnesium diffusion, the resulting silicon diffusion rate would be much too slow compared with experiments. One could also envisage a situation in which a magnesium and a silicon swap their sites forming two neighboring antisites allowing a new mechanism. Such a pair would be electrostatically bound and could be moving via silicon and magnesium vacancy sites in a corporate manner. However, such pairs are rare as the formation energy is about 3.1 eV and the migration barrier is about 4.5 eV.

(3) The six jump cycle discussed above is the only mechanism we have found which can explain the experiments.

IMPLICATIONS FOR THE EARTH'S LOWER MANTLE

Viscosity of the lower mantle

We can use our absolute diffusion rates to estimate the viscosity of the lower mantle. At this point we assume that the volumetrically greatest phase, i.e., perovskite, controls its viscosity.

The lower mantle is probably deforming in the diffusion creep regime (Karato and Wenk 1995). Firstly, strain rates are low, temperatures are high, and grain sizes are thought to be small (Solomatov et al. 2002). Secondly, there is almost no evidence of shear-wave splitting in the lower mantle, which would be indicative of lattice preferred orientation developed in the dislocation creep regime. And thirdly, viscosity models from glacial rebound studies indicate a linear viscosity in the lower mantle, consistent with diffusion creep. We can estimate the viscosity of the lower mantle deforming via diffusion creep by using the Nabarro-Herring expression (Poirier 1985):

$$\eta = \frac{G^2 kT}{\alpha D_{eff} \Omega} \tag{12}$$

where G is the characteristic grain size, α is a geometrical factor, Ω is the molecular volume, and D_{eff} is the effective diffusion coefficient. The effective diffusion coefficient is simply the stoichiometrically averaged diffusion coefficients, D_i, of the individual ionic species

$$D_{eff} = \left(\sum_i \frac{n_i}{D_i} \right)^{-1} \tag{13}$$

where n_i is the stoichiometric factor for each species. The diffusion coefficient for each species should also contain a contribution from grain-boundary diffusion. Grain boundary diffusion is, however, small in both periclase and perovskite for large enough grains ($G > 500$ μm in periclase (van Orman et al. 2003) and $G > 10$ μm in perovskite (Yamazaki et al. 2000)). Therefore, for the expected grain size in the lower mantle (Solomatov et al 2002), grain boundary diffusion is negligible.

The viscosity profile of the lower mantle, using our absolute diffusion results, is shown in Figure 7. The upper bound corresponds to the product $G^2 N_V = 2\times10^{-5}$ mm^{-1}. In other words for a grain size of 1 mm and a vacancy concentration of 2×10^{-5}, or alternatively, a grain size of 0.1 mm and a vacancy concentration of 2×10^{-7}. The lower bound corresponds to the $G^2 N_V = 2\times10^{-3}$ mm^{-1}; that is a two orders of magnitude greater vacancy concentration than the upper bound (for the same grain size). The geotherm is taken from Stacey (1992). Superimposed on our predicted viscosity profile is that obtained by Mitrovica and Forte (2004) from a joint inversion of convection and glacial rebound data. The steep weakening seen at the base of the lower mantle is due to rapidly increasing temperatures in the thermal boundary layer. The agreement with the viscosity profile of Mitrovica and Forte (2004) is striking, especially when realizing that no experimental data have gone into the predicted viscosity.

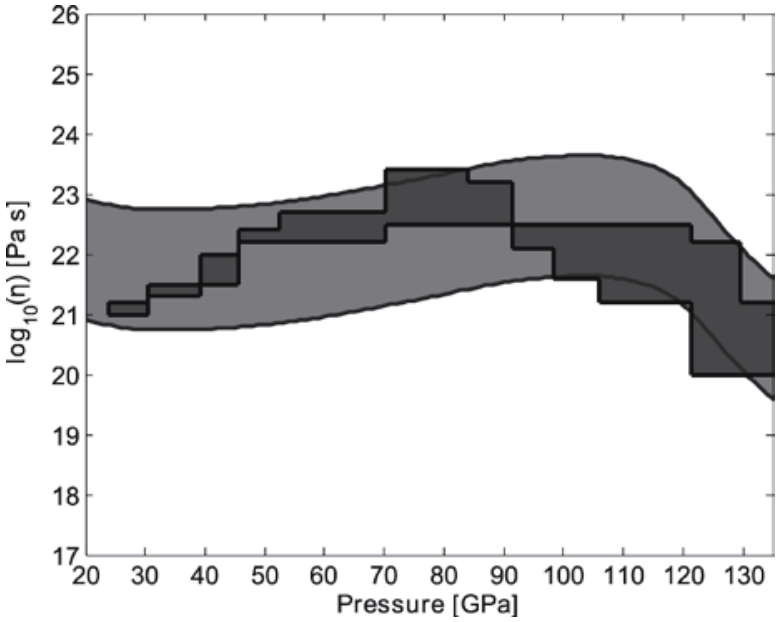

Figure 7. Viscosity of perovskite in the lower mantle deforming by diffusion creep. Calculated viscosity profile of the lower mantle with a composition of 100% $MgSiO_3$ perovskite (curved). Upper bounds correspond to either a grain size of G = 1 mm and a vacancy concentration of $N_v = 2\times10^{-5}$ or G = 0.1 mm and $N_v = 2\times10^{-7}$. Lower bounds correspond to either G = 1 mm and $N_v = 2\times10^{-3}$ or G = 0.1 mm and $N_v = 2\times10^{-5}$. Vacancy concentrations were assumed to be fixed throughout the entire lower mantle. Superimposed are the results of Mitrovica and Forte (2004) from inversion modeling.

It is clear that further work needs to be done in order to investigate the effects of impurities such as iron and alumina on the diffusion and therewith on rheology. However, the presence of impurities will result in an increased number of vacancies which should, therefore, lower the viscosity.

CONCLUSIONS

When the diffusion mechanism is simple, and when the concentration of vacancies in the experimental sample is reasonably clear, we have shown that we are able to predict from first principles the absolute diffusion in mantle minerals very accurately. For instance, we predict cation diffusion (magnesium and calcium) in all MgO experiments very well. We also predict oxygen diffusion in MgO, when the concentrations are extrinsically controlled. In perovskite we accurately reproduce the available experimental data on magnesium and oxygen diffusion as a simple vacancy hopping mechanism. Silicon diffusion in perovskite is more complicated since the direct jump does not seem to be energetically favoured. Rather we explain the data via the so-called six-jump-cycle. However, we are unable to explain why the concentration of vacancies in the experimental sample is so high. Our best explanation is that they are stabilized by water, as in other silicates.

ACKNOWLEDGMENTS

We are grateful to the EU for the Marie Cure “c2c” research-training network (Contract No. MRTN-CT-2006-035957). Computations were performed on HECToR, the UK national HPC facility, and on Legion, the UCL cluster.

REFERENCES

Alfè D (2009) PHON: A program to calculate phonons using the small displacement method. Comput Phys Commun 180:2622-2633, doi:10.1016/j.cpc.2009.03.010

Alfè D, Gillan MJ (2005) The Shottky defect formation energy in MgO calculated by diffusion Monte Carlo. Phys Rev B 71:220101:1-3

Ammann MW, Brodholt JP, Dobson DP (2009) DFT study of migration enthalpies in $MgSiO_3$ perovskite. Phys Chem Miner 36:151-158

Arita M, Koiwa M, Ishioka S (1989) Diffusion mechanisms in ordered alloys - a detailed analysis of six-jump vacancy cycle in the B2 type lattice. Acta Metall 37:1363-1374

Ball AJ, Murphy ST, Grimes RW, Bacorisen D, Smith R, Uberuaga BP, Sickafus KE (2008) Defect processes in $MgAl_2O_4$ spinel. Solid State Sci 10:717-724

Baroni S, de Gironcoli S, Dal Corso A, Giannozzi P (2001) Phonons and related crystal properties from density-functional perturbation theory. Rev Mod Phys 73:515-562

Béjina F, Blanchard M, Wright K, Price GD (2009) A computer simulation study of the effect of pressure on Mg diffusion in forsterite. Phys Earth Planet Inter 172:13-19

Béjina F, Jaoul O (1997) Silicon diffusion in minerals. Earth Planet Sci Lett 153:229-238

Béjina F, Jaoul O, Liebermann RC (2003) Diffusion in minerals at high pressure: a review. Phys Earth Planet Inter 139:3-20

Blanchard M, Wright K, Gale JD (2005) Atomistic simulation of Mg_2SiO_4 and Mg_2GeO_4 spinels: a new model. Phys Chem Miner 32: 332-338

Blöchl PE (1994) Projector augmented-wave method. Phys Rev B 50:17953-17979

Bolfan-Casanova N (2005) Water in the Earth's mantle. Mineral Mag 69:229-257

Braithwaite JS, Sushko PV, Wright K, Catlow RCA (2002) Hydrogen defects in forsterite: A test case for the embedded cluster method. J Chem Phys 116:2628-2635

Braithwaite JS, Wright K, Catlow RCA (2003) A theoretical study of the energetics and IR frequencies of hydroxyl defects in forsterite. J Geophys Res 108:2284

Brodholt J (1997) *Ab initio* calculations on point defects in forsterite (Mg_2SiO_4) and implications for diffusion creep. Am Mineral 82:1049-1053

Brodholt J (2000) Pressure-induced changes in the compression mechanism of aluminous perovskite in the Earth's mantle. Nature 407:20-622

Brodholt J, Refson K (2000) An *ab initio* study of hydrogen in forsterite and a possible mechanism for hydrolytic weakening. J Geophys Res 105:18,977-18,982

Catlow CRA, Corish J, Jacobs PWM, Lidiard AB (1981) The thermodynamics of characteristic defect parameters. J Phys C Solid State Phys 14:L121-L125

Cherry M, Islam MS, Gale JD, Catlow CRA (1995a) Computational studies of protons in perovskite-structured oxides. J Phys Chem 99:14614-14618

Cherry M, Islam MS, Catlow CRA (1995b) Oxygen ion migration in perovskite-type oxides. J Solid State Chem 118:125-132

De Vita A, Gillan MJ, Lin JS, Payne MC, Stich I, Clarke LJ (1992) Defect energetics in MgO treated by first-principles methods. Phys Rev B 46:12964-3322

Debiaggi SB, Decorte PM, Monti AM (1996) Diffusion by vacancy mechanism in Ni, Al, and Ni_3Al: calculation based on many-body potentials. Phys Status Solidi 195:37-54

Divinski S, Herzig C (2000) On the six-jump cycle mechanism of self-diffusion in NiAl. Intermetallics 8:1357-1368

Dobson DP (2003) Oxygen ionic conduction in $MgSiO_3$ perovskite. Phys Earth Planet Inter 139:55-64

Dobson DP, Dohmen R, Wiedenbeck M (2008) Self-diffusion of oxygen and silicon in $MgSiO_3$ perovskite. Earth Planet Sci Lett 270:125-129

Duan J (2006) Atomistic simulations of diffusion mechanisms in stoichiometric Ni_3Al. J Phys Condens Matter 18:1381-1394

Duclot M, Departes C (1980) Effect of impurities on cationic conductivity of magnesium-oxide single-crystals. J Solid State Chem 31:337-385

Elcock EW, McCombie CW (1957) Vacancy diffusion in binary ordered alloys. Phys Rev 109:605-606

Flynn CP, Jacucci G (1982) Dynamical corrections to rate theory. Phys Rev B 25:6225-6234

Gale JD (1997) GULP: A computer program for the symmetry-adapted simulation of solids. J Chem Soc Faraday Trans 93:629-637

Gale JD, Rohl AL (2003) The general utility lattice program (gulp). Mol Simul 29:291-341

Gibson A, Haydock R, LaFemina JP (1994) Stability of vacancy defects in MgO: The role of charge neutrality. Phys Rev B 50:2582-2592

Gilbert CA, Kenny SD, Smith R, Sanville E (2007) *Ab initio* study of point defects in magnesium oxide. Phys Rev B 76:184103:1-10

Harding JH, Sangster MJL, Stoneham AM (1987) Cation diffusion in alkaline-Earth oxides. J Phys C: Solid State Physics 20: 5281-5292
Harding JH (1989) Calculation of the entropy of defect processes in ionic solids. J Chem Soc Faraday Trans 2 85:351-365
Henkelman G, Uberuaga BP, Jónsson H (2000) A climbing image nudged elastic band method for finding saddle points and minimum energy paths. J Chem Phys 113:9901-9904
Hirsch LM, Shankland TJ (1991) Point defects in (Mg,Fe)SiO_3 perovskite. Geophys Res Lett 18:1305-1308
Hohenberg P, Kohn W (1964) Inhomogenous electron gas. Phys Rev 136:B864-B871
Holzapfel C, Rubie DC, Frost DJ, Langenhorst F (2005) Fe-Mg interdiffusion in (Mg,Fe)SiO_3 perovskite and lower mantle reequilibration. Science 309:1707-1710
Holzapfel C, Rubie DC, Mackwell S, Frost DJ (2003) Effect of pressure on Fe-Mg interdiffusion in (Fe_xMg_{1-x})O, ferropericlase. Phys Earth Planet Inter 139:21-34
Huntington HB, Miller NC, Nerses V (1961) Self-diffusion in 50-50 gold-cadmium. Acta Metall 9:749-754
Ita J, Cohen RE (1997) Effects of pressure on diffusion and vacancy formation in MgO from nonempirical free-energy integrations. Phys Rev Lett 79:3198-3201
Ita J, Cohen RE (1998) Diffusion in MgO at high pressure: implications for lower mantle rheology. Geophys Res Lett 25:1-4
Ito Y, Toriumi M (2007) Pressure effect of self-diffusion in periclase (MgO) by molecular dynamics. J Geophys Res 112:B04206, doi:10.1029/2005JB003685
Jackson I (1998) Elasticity, composition and temperature of the Earth's lower mantle: a reappraisal. Geophys J Int 134:291-311
Jacobs PWM, Vernon ML (1990) Defect energies for magnesium oxide and lithium. J Chem Soc Faraday Trans 86:1233-1238
Kantorovich LN (1999) Elimination of the long-range interaction in calculations with periodic boundary conditions. Phys Rev B 60:15475-15479
Kantorovich LN, Tupitsyn II (1999) Coulomb potential inside a large finite crystal. J Phys Condens Matter 11: 6159-6168
Karato S, Wenk HR (1995) Superplasticity in Earth's lower mantle: evidence from seismic anisotropy and rock physics. Science 270:458-461
Karki BB, Khanduja G (2006a) Computer simulation and visualization of vacancy defects in $MgSiO_3$ perovskite. Phys Rev B 61:8793-8800
Karki BB, Khanduja G (2006b) Vacancy defects in MgO at high pressure. Am Mineral 91: 511-516
Karki BB, Khanduja G (2007) A Computational study of ionic vacancies and diffusion in $MgSiO_3$ perovskite and post-perovskite. Earth Planet Sci Lett 260:201-211
Karki BB, Wentzcovitch RM, de Gironcoli S, Baroni S (2000) *Ab initio* lattice dynamics of $MgSiO_3$ perovskite at high pressure. Phys Rev B 62:14750-14756
Katsura T, Sato K, Ito E (1998) Electrical conductivity of silicate perovskite at lower-mantle conditions. Nature 395:493-495
Kohn W, Sham LJ (1965) Self-consistent equations including exchange and correlation effects. Phys Rev 140:A1133-A1138
Kotomin EA, Kuklja MM, Eglitis RI, Popov AI (1996) Quantum chemical simulations of the optical properties and diffusion of electron centres in MgO. Mater Sci Eng B 37:212-214
Kotomin EA, Popov AI (1998) Radiation-induced point-defects in simple oxides. Nucl Instrum Methods Phys Res B 141:1-15
Kresse G, Furthmüller J (1996a) Efficient iterative schemes for *ab initio* total-energy calculations using a plane-wave basis set. Phys Rev B 54:11169-11186
Kresse G, Furthmüller J (1996b) Efficiency of ab-initio total energy calculations for metals and semiconductors using a plane-wave basis set. Comput Mater Sci 6:15-50
Kresse G, Hafner J (1993) *Ab initio* molecular dynamics for liquid metals. Phys Rev B 47:558-561
Kresse G, Joubert J (1999) From ultrasoft pseudopotentials to the projector augmented wave method. Phys Rev B 59:1758-1775
Lauterbach S, McCAmmon CA, van Aken P, Langenhorst F, Seifert F (2000) Mössbauer and ELNES spectroscopy of (Mg,Fe)(Si,Al)O_3 perovskite: A highly oxidised component of the lower mantle. Contrib Mineral Petrol 138:17-26
Lee W-C, Lee S-G, Chang KJ (1998) First-principles study of the self-interstitial diffusion mechanism in silicon. J Phys Condens Matter 10:995-1002
Leslie M, Gillan MJ (1985) The energy and elastic dipole tensor of defects in ionic crystal calculated by the supercell method. J Phys C Solid State Phys 18:973-982
Lin J-F, Heinz DL, Mao H, Hemley RJ, Devine JM, Li J, Shen G (2002) Stability of magnesiowüstite in Earth's lower mantle. Proc Nat Acad Sci USA 100:4405-4408

Lindner R, Parfitt GD (1957) Diffusion of radioactive magnesium in magnesium oxide crystals. J Chem Phys 26:182-185
Litasov K, Ohtani E, Langenhorst F, Yurimoto H, Kubo T, Kondo T (2003) Water solubility in Mg-perovskites and water storage capacity in the lower mantle. Earth Planet Sci Lett 211:189-203
Lowitzer S, Wilson DJ, Winkler B, Milman V, Gale JD (2008) Defect properties of albite. Phys Chem Miner 35:129-135
Mackrodt WC (1988) Temperature dependence of lattice and defect properties of MgO and Li_2O. J Mol Liq 39:121-136
Mackrodt WC, Stewart RF (1979) Defect properties of ionic solids. III. The calculation of the point-defect structure of the alkaline-earth oxides and CdO. J Phys C Solid State Phys 12:5015-5036
Mackwell S, Bystricky M, Sproni C (2005) Fe-Mg interdiffusion in (Mg,Fe)O. Phys Chem Miner 32:418-425
Makov G, Payne MC (1995) Periodic boundary conditions in *ab initio* calculations. Phys Rev B 51:4014-4022
Mitrovica JX, Forte AM (2004) A new inference of mantle viscosity based upon joint inversion of convection and glacial isostatic adjustment data. Earth Planet Sci Lett 225:177-189
Mookherjee M, Stixrude L, Karki B (2008) Hydrous silicate melt at high pressure. Nature 452:983-986
Narayan J, Washburn J (1973) Self-diffusion in magnesium oxide. Acta Metall 21:533-538
Nevins D, Spera FJ, Ghiorso MS (2009) Shear viscosity and diffusion in liquid $MgSiO_3$: Transport properties and implications for terrestrial planet magma oceans. Am Mineral 94:975-980
Oganov AR, Gillan MJ, Price GD (2003) *Ab initio* lattice dynamics and structural stability of MgO. J Chem Phys 118:10174-10182
Oishi Y, Kingery WD (1960) Oxygen diffusion in periclase crystals. J Chem Phys 33:905-906
Parlinski K (2008) Software PHONON. *http://wolf.ifj.edu.pl/phonon/*
Perdew JP, Burke K (1996) Comparison shopping for a gradient-corrected density functional. Int J Quantum Chem 57:309-319
Perdew JP, Zunger A (1981) Self-interaction correction to density-functional approximations for many-electron systems. Phys Rev B 23:5048-5079
Perdew JP, Wang Y (1992) Accurate and simple analytic representation of the electron-gas correlation energy. Phys Rev B 45:13244-13249
Poirier JP (1985) Creep of Crystals. Cambridge University Press
Price GD, Wall A, Parker SC (1989) The properties and behaviour of mantle minerals: a computer-simulation approach. Philos Trans R Soc London A 328:391-407
Reich M, Ewing RC, Ehlers TA, Becker U (2007) Low-temperature anisotropic diffusion of helium in zircon: Implications for zircon (U-Th)/He thermochronometry, Geochim Cosmochim Acta 71:3119-3130
Roma G, Limoge Y, Baroni S (2001) Oxygen self-diffusion in α-quartz. Phys Rev Lett 86:4564-4567
Sakaguchi I, Yurimoto H, Sueno S (1992) Self-diffusion along dislocations in single-crystal MgO. Solid State Commun 84:889-893
Sangster MJL, Rowell DK (1981) Calculation of defect energies and volumes in some oxides. Philos Mag A 44:613-624
Sangster MJL, Stoneham AM (1984) Calculation of absolute diffusion rates in oxides. J Phys C Solid State Phys 17:6093-6104
Sheppard D, Terrell R, Henkelman G (2008) Optimization methods for finding minimum energy paths. J Chem Phys 128:34106:1-10
Schilling W (1978) Self-interstitial atoms in metals. J Nucl Mater 69-70:465-489
Sempolinsky DR, Kingery WD (1980) Ionic conductivity and magnesium vacancy mobility in magnesium oxide. J Am Ceram Soc 63:664-669
Shirasaki S, Hama M (1973) Oxygen-diffusion characteristics of loosely sintered polycrystalline MgO. Chem Phys Lett 20:361-365
Solomatov VS, El-Khozondar R, Tikare V (2002) Grain size in the lower mantle: constraints from numerical modeling of grain growth in two-phase systems. Phys Earth Planet Inter 129:265-282
Stacey FD (1992) Physics of the Earth. Brooksfield Press
Sushko PV, Shluger AL, Catlow CRA, Baetzold RC (1999) Embedded cluster approach: application to complex defects. Radiat Eff Defects Solids 151:215-221
Sushko PV, Shluger AL, Baetzold RC, Catlow CRA (2000a) Embedded cluster calculations of metal complex impurity defects: properties of the iron cyanide in NaCl. J Phys Condens Matter 12:8257-8266
Sushko PV, Shluger AL, Catlow CRA (2000b) Relative energies of surface and defect states: *ab initio* calculations for the MgO (001) surface. Surf Sci 450:153-170
Tsuchiya T, Tsuchiya J, Umemoto K, Wentzcovitch RM (2004) Phase transition in $MgSiO_3$ perovskite in the Earth's lower mantle. Earth Planet Sci Lett 224:241-248
Van Orman JA, Fei Y, Hauri EH, Wang J (2003) Diffusion in MgO at high pressures: constraints on deformation mechanisms and chemical transport at the core-mantle-boundary. Geophys Res Lett 30:28:1-4

Vineyard GH (1957) Frequency factors and isotope effects in solid state rate processes. J Phys Chem Solids 3:121-127

Vočadlo L, Wall A, Parker SC, Price GD (1995) Absolute ionic diffusion in MgO - computer calculations via lattice dynamics. Phys Earth Planet Inter 88:193-210

Voter AF (2005) Introduction To The Kinetic Monte Carlo Method. Springer, NATO Publishing Unit

Walker AM, Demouchy S, Wright K (2006) Computer modeling of the energies and vibrational properties of hydroxyl groups in α- and β-Mg_2SiO_4. Eur J Mineral 18:529-543

Walker AM, Woodley SM, Slater B, Wright K (2009) A computational study of magnesium point defects and diffusion in forsterite. Phys Earth Planet Inter 172:20-27

Wan JTK, Duffy TS, Scandolo S, Car R (2007) First principles study of density, viscosity and diffusion coefficients of liquid $MgSiO_3$ at conditions of the Earth's deep mantle. J Geophys Res 112:B03208, doi:10.1029/2005JB004135

Wright K, Price GD (1993) Computer simulation of defects and diffusion in perovskite. J Geophys Res 98:22.245-22.253

Wuensch BJ, Steele WC, Vasilos T (1973) Cation self-diffusion in single-crystal MgO. J Chem Phys 58:5258-5266

Xu Y, McCammon C (2002) Evidence for ionic conductivity in lower mantle $(Mg,Fe)(Si,Al)O_3$ perovskite. J Geophys Res 107: doi:10.1029/2001JB000677

Xu Y, McCammon C, Poe BT (1998) The effect of alumina on the electrical conductivity of silicate perovskite. Science 282:922-924

Yamazaki D, Irifune T (2003) Fe-Mg interdiffusion in magnesiowüstite up to 35 GPa. Earth Planet Sci Lett 216:301-311

Yamazaki D, Kato T, Yurimoto H, Ohtani E, Toriumi M (2000) Silicon self-diffusion in $MgSiO_3$ perovskite at 25 GPa. Phys Earth Planet Inter 119:299-309

Yoo H-I, Wuensch BJ, Petuskey WT (2002) Oxygen self-diffusion in single-crystal MgO: Secondary-ion mass spectrometric analysis with comparison of results from gas-solid and solid-solid exchange. Solid State Ionics 150:207-221

Vol 465|27 May 2010|doi:10.1038/nature09052

LETTERS

First-principles constraints on diffusion in lower-mantle minerals and a weak D′′ layer

M. W. Ammann[1], J. P. Brodholt[1], J. Wookey[2] & D. P. Dobson[1]

Post-perovskite $MgSiO_3$ is believed to be present in the D′′ region of the Earth's lowermost mantle[1–4]. Its existence has been used to explain a number of seismic observations, such as the D′′ reflector and the high degree of seismic anisotropy within the D′′ layer[5–8]. Ionic diffusion in post-perovskite controls its viscosity, which in turn controls the thermal and chemical coupling between the core and the mantle, the development of plumes and the stability of deep chemical reservoirs[9]. Here we report the use of first-principles methods to calculate absolute diffusion rates in post-perovskite under the conditions found in the Earth's lower mantle. We find that the diffusion of Mg^{2+} and Si^{4+} in post-perovskite is extremely anisotropic, with almost eight orders of magnitude difference between the fast and slow directions. If post-perovskite in the D′′ layer shows significant lattice-preferred orientation, the fast diffusion direction will render post-perovskite up to four orders of magnitude weaker than perovskite. The presence of weak post-perovskite strongly increases the heat flux across the core–mantle boundary and alters the geotherm[9]. It also provides an explanation for laterally varying viscosity in the lowermost mantle, as required by long-period geoid models[10]. Moreover, the behaviour of very weak post-perovskite can reconcile seismic observation of a D′′ reflector with recent experiments showing that the width of the perovskite-to-post-perovskite transition is too wide to cause sharp reflectors[11]. We suggest that the observed sharp D′′ reflector is caused by a rapid change in seismic anisotropy. Once sufficient perovskite has transformed into post-perovskite, post-perovskite becomes interconnected and strain is partitioned into this weaker phase. At this point, the weaker post-perovskite will start to deform rapidly, thereby developing a strong crystallographic texture. We show that the expected seismic contrast between the deformed perovskite-plus-post-perovskite assemblage and the overlying isotropic perovskite-plus-post-perovskite assemblage is consistent with seismic observations.

Figure 1 shows our calculated ionic diffusion rates in periclase and perovskite $MgSiO_3$ in comparison with available experimental data. Our results are in excellent agreement with the experiments for both phases and all three ionic species considered, throughout the pressure and temperature range in which they were measured. This provides confidence in our results on post-perovskite for which no data exist. Figure 2 shows our calculated diffusion coefficients for single vacancies, and the calculated diffusion creep viscosity, along a mantle geotherm. Oxygen in perovskite is the fastest-diffusing species throughout the lower mantle. We also find that oxygen, magnesium and silicon diffusion in perovskite are all essentially isotropic. Magnesium is the rate-limiting species in perovskite, in agreement with the conclusions of ref. 12. However, it should be noted that the rate-limiting species will depend on vacancy concentration, which may vary considerably in the mantle.

Considering post-perovskite, we find that silicon and magnesium diffusion is extremely anisotropic, with diffusivities varying by about eight orders of magnitude between the fastest direction, ⟨100⟩, and

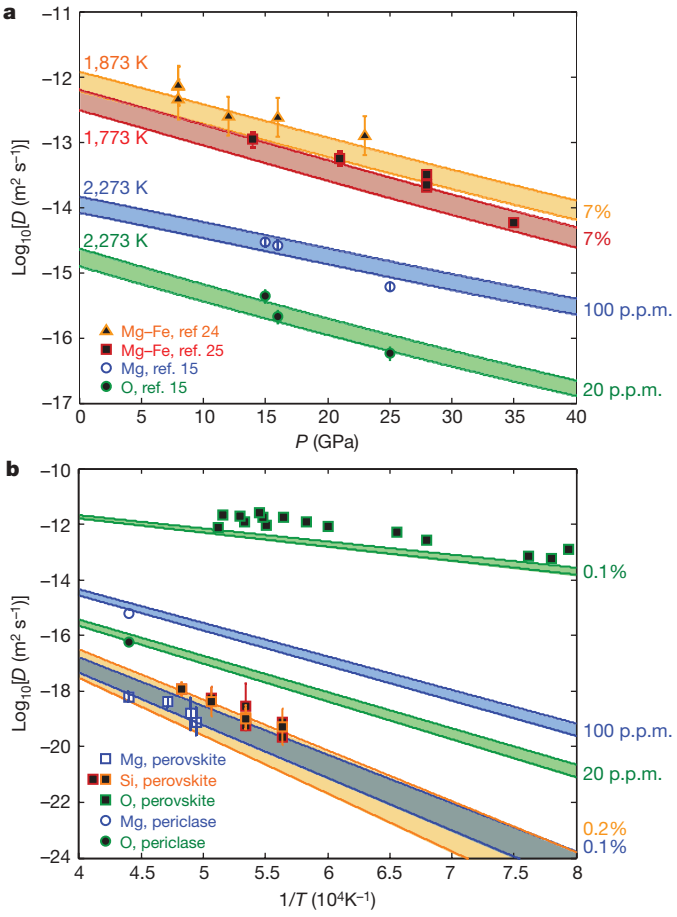

Figure 1 | Comparison of absolute diffusion rates with experiments. Our calculated diffusion rates, *D*, are shown as solid lines (upper limits show the local-density approximation (LDA) and lower limits show the generalized gradient approximation (GGA), both at the same cell volume; pressure was calculated from the GGA) and experimental data is shown as symbols. Values shown on the right-hand side indicate the vacancy concentrations estimated from experimental conditions (see Supplementary Information for details). **a**, Diffusion in periclase at different pressures, *P*, and temperatures, *T* (refs 15, 24, 25). **b**, Diffusion in perovskite and diffusion in pure periclase (same as pure periclase in **a**) at 25 GPa and varying temperature[12,16,26,27]. Where shown, the error bars represent the experimental error; the other experimental uncertainties are smaller than the symbol.

[1]Department of Earth Sciences, University College London, Gower Street, London WC1E 6BT, UK. [2]Department of Earth Sciences, University of Bristol, Wills Memorial Building, Queens Road, Bristol BS6 6LL, UK.

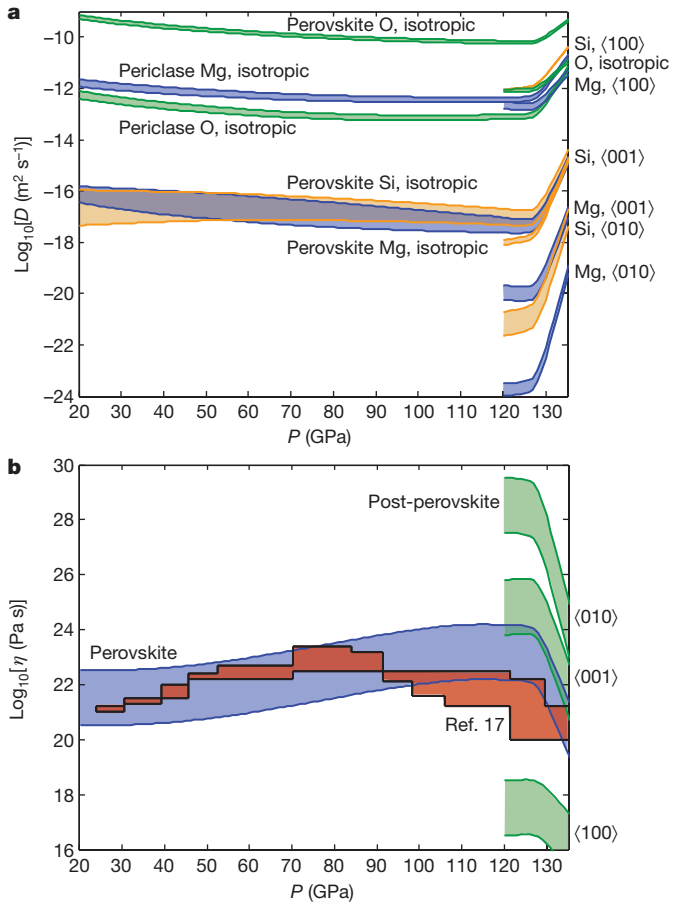

Figure 2 | Vacancy diffusion coefficients and viscosity in the lower mantle along a geotherm. **a**, Vacancy diffusion coefficients of periclase, perovskite and post-perovskite along a geotherm[28]. Upper bounds, LDA calculations; lower bounds, GGA calculations. **b**, Calculated viscosity profile, η, of perovskite $MgSiO_3$ deforming by diffusion creep, and endmember viscosities along the crystallographic axes of post-perovskite $MgSiO_3$. Grain size, G, and vacancy concentration, N_v, were varied such that $G^2/N_v = 0.01\ m^2$ for the lower bounds and $0.1\ m^2$ for the upper bounds. Vacancy concentrations for both minerals are assumed to be fixed throughout the entire lower mantle. Superimposed are the results from inversion modelling[17]. Except for highly aligned cases, post-perovskite deforming by diffusion creep is stiffer than perovskite as the bulk viscosity lies between the values of the ⟨010⟩ and ⟨001⟩ directions.

the slowest direction, ⟨010⟩. Magnesium and silicon diffusion rates in the fast direction are considerably faster than in perovskite, and are similar to those in MgO. Although some anisotropy may be expected as a result of the layered structure of post-perovskite, this is not the reason for this extreme anisotropy; magnesium and silicon diffusion in the ⟨010⟩ direction (across the layers) is similar to that in the ⟨001⟩ direction (parallel to the layers). The anisotropy is largely due to very fast diffusion in the ⟨100⟩ direction (see Supplementary Information for more details). Oxygen diffusion in post-perovskite is, however, essentially homogeneous. Even for the fast diffusion direction, the diffusion rates are too small to remove any chemical heterogeneities even over timescales of the age of the Earth (the characteristic diffusion length scale is less than 500 m for all species in all phases, assuming vacancy concentrations of 0.1%). Chemical exchange with the core would thus need to occur through grain boundary diffusion and chemical heterogeneities in the mantle could only be removed through mechanical mixing (stretching and thinning), grain boundary diffusion or fluid migration.

We now consider the effect of our calculated diffusion coefficients on mantle rheology. The absence of seismic anisotropy in the lower mantle, small grain size[13] and low stresses all argue for diffusion creep being the dominant creep mechanism through the majority of the lower mantle[14]. Moreover, viscosity models derived from glacial rebound indicate linear rheology for most of the mantle, which is again consistent with diffusion creep. We can therefore estimate the viscosity of the lower mantle using the Nabarro–Herring expression for diffusion creep (in the case of simple shear, this expression is multiplied by a factor of 2/5). Perovskite grain sizes in the lower mantle have been estimated[13] to be 0.1–1 mm, so we can neglect grain boundary diffusion creep for the major chemical species (magnesium, silicon and oxygen)[15,16]. Estimates of lower-mantle viscosity of between 10^{21} and 10^{24} Pa s, from post-glacial rebound, geoid anomalies and convection-related observables, are consistent with our results. Our calculated mantle viscosity also bounds the estimates from ref. 17 (Fig. 2b), consistent with diffusion creep being the dominant mechanism in the lower mantle. There is some mismatch in the D′′ layer, as post-perovskite is much stiffer than the modelled viscosity of ref. 17, suggesting that post-perovskite is deforming by a different mechanism such as dislocation creep. It is important to note that the quality of agreement can be improved, as the viscosity is strongly dependent on the geotherm, vacancy concentration and grain size.

The strong diffusion anisotropy in post-perovskite presents problems for predicting its viscosity in lattice diffusion creep. Averaging of the diffusivity tensor in an isotropic aggregate results in an effective viscosity of post-perovskite that is much larger than that of perovskite. This is because even small contributions from the slow and intermediate directions will dominate the diffusivity through the aggregate. An alignment of the [100] crystal axis in the shear direction may cause the aggregate to weaken substantially, becoming weaker than perovskite only for very highly aligned cases. It seems likely, however, that the D′′ region is not deforming in the diffusion creep regime. The high stresses accumulated at the edges of convecting cells and the observed seismic anisotropy in the D′′ layer both argue for deformation by dislocation migration at the base of the mantle. In the high-temperature case relevant to the D′′ layer, that of climb-assisted dislocation migration, the rate-limiting step is diffusion of the slowest species in the fastest direction. Our results predict that for climb-assisted dislocation creep, post-perovskite will be four orders of magnitude weaker than perovskite. This is supported by recent low-pressure analogue experiments which showed that post-perovskite was up to 50 times weaker than perovskite in the $CaIrO_3$ system[18]. We suggest, therefore, that post-perovskite in the D′′ layer will be significantly weaker than perovskite.

There are a number of implications of this weakening for the D′′ region. Recent experiments[11] have suggested that the transition from perovskite to post-perovskite in natural compositions is not sharp and might, in fact, extend over the whole of the lowermost 200 km of the lower mantle. Such a wide transition is inconsistent with post-perovskite being responsible for the seismic discontinuities observed at the top of the D′′ layer. If, however, post-perovskite is significantly weaker than perovskite, the system will show critical behaviour as the phase fraction of post-perovskite increases sufficiently for it to form an interconnected network; this is depicted in Fig. 3b. At the critical phase fraction, the rheology of the aggregate will switch from being dominated by perovskite to being dominated by post-perovskite. This implies that, although the phase fraction might increase monotonically, once the critical phase fraction is reached there will be a rapid weakening of the two-phase mixture and strain will partition preferentially into the post-perovskite-dominated region. Critical behaviour of this type was observed in rheological studies of $CaIrO_3$ during transformation from perovskite to post-perovskite[18], with the bulk of the weakening occurring at approximately 30% transformation. In the D′′ layer, this rapid weakening and strain partitioning will cause the texture of the mixture to change from isotropic to anisotropic over a short distance owing to the shear-induced lattice-preferred orientation (LPO). Experiments on analogue phases show that strong LPO can be generated in post-perovskite after relatively small strains. Figure 3 shows the effect that rapid generation

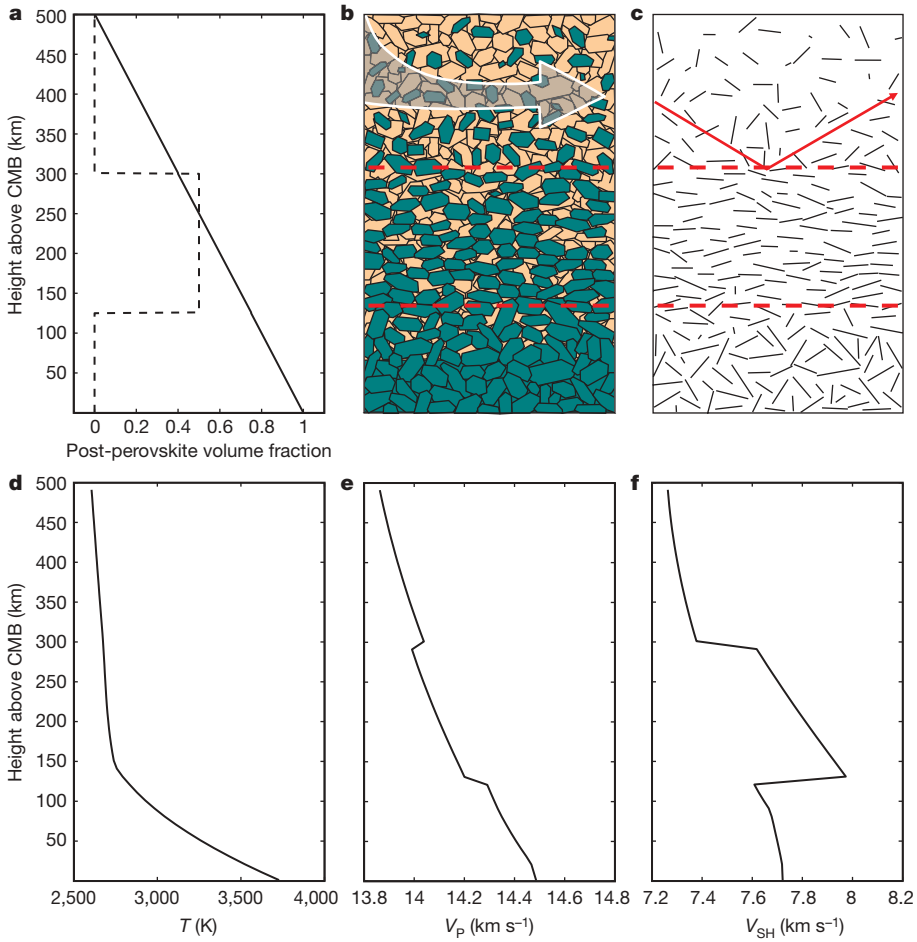

Figure 3 | Seismic speed as a function of depth for a gradual transformation to post-perovskite, with an abrupt change in deformation. **a**, Volume fraction of post-perovskite with depth (solid) and degree of alignment (dashed). **b**, Pictorial representation of the phase fraction (tan, perovskite; green, post-perovskite; arrow represents imposed deformation) and grain orientations. **c**, Orientation of (010) planes (planes perpendicular to ⟨010⟩) and the seismic reflector (arrow) due to flow parallel to the core–mantle boundary (CMB). The red dashed lines in **b** and **c** mark the region of LPO development. **d**, Geotherm[28]. For each point on the geotherm, we construct an aggregate elastic tensor comprising perovskite and post-perovskite in the modal proportions given by **a**, from *ab initio* calculated elasticities and gradients[4,6,29–32] (see Supplementary Information for details). **e**, **f**, P- and horizontal S-wave speeds, V_P and V_{SH}, that would be encountered by teleseismic PcP and ScS precursor reflections (epicentral distance, 60°) incident at 45° on the texture boundary; this is similar to the signal that has been measured for the lowermost mantle (see, for example, ref. 8).

of LPO in a gradually transforming mixture has on the observed seismic velocity for ray paths with low angles of incidence. If we assume that the critical phase fraction for post-perovskite-dominated rheology is 40%, we calculate (following ref. 7) an increase in shear speed of around 4%, which is sufficient to explain the observed D′′ discontinuity (Supplementary Information). The rapid development of LPO at the critical phase fraction might therefore be the cause of the D′′ seismic discontinuity, even if the transformation from perovskite to post-perovskite occurs over a wide depth range.

The broad region of phase coexistence suggested in ref. 11 is also inconsistent with a lower D′′ reflector seen in some regions as being the back-transformation of post-perovskite into perovskite[5,7]. We suggest, however, that the region immediately above the core–mantle boundary might be a region in which diffusion creep dominates owing to the steep thermal gradients in the thermal boundary layer and the free-slip condition that is imposed by the liquid outer core and results in a reduction of the shear stress immediately next to the core–mantle boundary. A transition in rheology at the very base of the D′′ layer would result in a change in the crystallographic texture across this deformation transition, possibly explaining the basal D′′ reflector (Fig. 3).

It is possible that that post-perovskite in the D′′ layer is deforming entirely within the diffusion creep regime. However, our results show that an isotropic mixture of post-perovskite would be very stiff, something that is inconsistent with geoid modelling and experiments on analogues. It would also be difficult to explain the observed seismic anisotropy in terms of diffusion creep. Diffusion creep may still occur if the grains are rotated such that their fast diffusion directions are parallel to the shear direction. This type of history-dependent rheology commonly leads to the development of shear zones, which could also bring regions of different anisotropies into proximity. Regardless of whether post-perovskite deforms by diffusion creep or, as is more likely, by dislocation creep, the observed sharp D′′ reflectors may be interfaces between regions of different anisotropies, and not the phase transition as is commonly assumed. It is also not necessary to invoke chemical heterogeneities or the presence of slabs to explain rapid changes in seismic properties[19,20]; rapid changes in post-perovskite texture can produce the same results.

In addition to providing an explanation for the observed D′′ seismic reflectors, a weak post-perovskite has other implications for the D′′ layer. It has been shown that a weak D′′ layer strongly increases the heat flux from the core and affects the geotherm[9]. If the viscosity is very low, small-scale internal convection may develop within the D′′ layer, further affecting heat flow from the core. The viscosity would also change laterally as the proportion of perovskite to post-perovskite varies owing to lateral temperature gradients. This is supported by recent geoid modelling, which requires colder regions of the deepest lower mantle to be weaker than hotter regions[10].

It is clear that the effects of a weak post-perovskite phase on the local seismic structure at the core–mantle boundary, on the transport of heat out of the core and on global geodynamics will require further careful examination. In addition, more work is required to understand creep and the effects of competing rheological mechanisms in a strongly anisotropic material. However, the present results provide a firm atomistic basis for strong weakening as perovskite transforms into post-perovskite, something that should also occur in the D'' region of the lowermost mantle.

METHODS SUMMARY

We calculated absolute diffusion rates for Mg^{2+}, Si^{4+} and O^{2-} in perovskite, post-perovskite and MgO using harmonic transition state theory. The minimum-energy migration pathways and saddle points were found using the climbing-image nudged elastic band method. Where they exist and where the paths are the same, our migration enthalpies are similar to those calculated previously[21,22]. We calculated phonon frequencies and all necessary energies using density functional theory. Calculations were performed at a constant volume using both the LDA and the GGA. Further computational and theoretical details are described elsewhere[23] as well as in Supplementary Information. We find that diffusion generally occurs in single jumps. However, silicon in perovskite and silicon and magnesium in post-perovskite diffuse across the silicon–oxygen octahedron layers by means of a so-called six-jump cycle on the magnesium–silicon sublattice. We investigated the rate of this mechanism using mean first-passage theory and the kinetic Monte Carlo method. The two methods yield equal rates if cycle-breaking jumps are ignored. However, as kinetic Monte Carlo computations revealed that cycles can eventually break up, the analytical solution obtained from mean first-passage theory is an upper limit for the final rate (see Supplementary Information for more details).

Received 17 January; accepted 26 March 2010.

1. Murakami, M., Hirose, K., Kawamura, K., Sata, N. & Ohishi, Y. Post-perovskite phase transition in $MgSiO_3$. *Science* **204,** 855–858 (2004).
2. Oganov, A. R. & Ono, S. Theoretical and experimental evidence for a post-perovskite phase of $MgSiO_3$ in Earth's D'' layer. *Nature* **430,** 445–448 (2004).
3. Tsuchiya, T., Tsuchiya, J., Umemoto, K. & Wentzcovitch, R. M. Phase transition in $MgSiO_3$ perovskite in the Earth's lower mantle. *Earth Planet. Sci. Lett.* **224,** 241–248 (2004).
4. Wentzcovitch, R. M., Tsuchiya, T. & Tsuchiya, J. $MgSiO_3$ postperovskite at D'' conditions. *Proc. Natl Acad. Sci. USA* **103,** 543–546 (2006).
5. Hernlund, J. W., Thomas, C. & Tackley, P. J. A doubling of the post-perovskite phase boundary and structure of the Earth's lowermost mantle. *Nature* **434,** 882–886 (2005).
6. Wookey, J., Kendall, J.-M. & Rümpker, G. Lowermost mantle anisotropy beneath the north Pacific from differential S-ScS splitting. *Geophys. J. Int.* **161,** 829–838 (2005).
7. Wookey, J., Stackhouse, S., Kendall, J.-M., Brodholt, J. & Price, G. D. Efficacy of the post-Perovskite phase as an explanation for lowermost-mantle seismic properties. *Nature* **438,** 1004–1007 (2005).
8. Hutko, A. R., Lay, T., Revenaugh, J. & Garnero, E. J. Anticorrelated seismic velocity anomalies from post-perovskite in the lowermost mantle. *Science* **320,** 1070–1074 (2008).
9. Čížková, H., Čadek, O., Matyska, C. & Yuen, D. A. Implications of post-perovskite transport properties for core–mantle dynamics. *Phys. Earth Planet. Inter.* (in the press).
10. Čadek, O. & Fleitout, L. Effect of lateral viscosity variations in the core–mantle boundary region on predictions of the long-wavelength geoid. *Stud. Geophys. Geod.* **50,** 217–232 (2005).
11. Catalli, K., Shim, S.-H. & Prakapenka, V. Thickness and Clapeyron slope of the post-perovskite boundary. *Nature* **462,** 782–786 (2009).
12. Holzapfel, C., Rubie, D. C., Frost, D. J. & Langenhorst, F. Fe-Mg interdiffusion in $(Mg,Fe)SiO_3$ perovskite and lower mantle reequilibration. *Science* **309,** 1707–1710 (2005).
13. Solomatov, V. S., El-Khozondar, R. & Tikare, V. Grain size in the lower mantle: constraints from numerical modeling of grain growth in two-phase systems. *Phys. Earth Planet. Inter.* **129,** 265–282 (2002).
14. Karato, S., Zhang, S. & Wenk, H. R. Superplasticity in Earth's lower mantle: evidence from seismic anisotropy and rock physics. *Science* **270,** 458–461 (1995).
15. Van Orman, J. A., Fei, Y., Hauri, E. H. & Wang, J. Diffusion in MgO at high pressures: constraints on deformation mechanisms and chemical transport at the core–mantle boundary. *Geophys. Res. Lett.* **30,** 1–4 (2003).
16. Yamazaki, D., Kato, T., Yurimoto, H., Ohtani, E. & Toriumi, M. Silicon self-diffusion in $MgSiO_3$ perovskite at 25 GPa. *Phys. Earth Planet. Inter.* **119,** 299–309 (2000).
17. Mitrovica, J. X. & Forte, A. M. A new inference of mantle viscosity based upon joint inversion of convection and glacial isostatic adjustment data. *Earth Planet. Sci. Lett.* **225,** 177–189 (2004).
18. Hunt, S. A. *et al.* Weakening of calcium iridate during its transformation from perovskite to post-perovskite. *Nature Geosci.* **2,** 794–797 (2009).
19. Lay, T., Hernlund, J., Garnero, E. J. & Thorne, M. S. A post-perovskite lens and D'' heat flux beneath the central pacific. *Science* **314,** 1272–1276 (2006).
20. Hutko, A. R., Lay, T., Garnero, E. J. & Revenaugh, J. Seismic detection of folded, subducted lithosphere at the core–mantle boundary. *Nature* **441,** 333–336 (2006).
21. Karki, B. B. & Khanduja, G. A computational study of ionic vacancies and diffusion in $MgSiO_3$ perovskite and post-perovskite. *Earth Planet. Sci. Lett.* **260,** 201–211 (2007).
22. Ammann, M. W., Brodholt, J. P. & Dobson, D. P. DFT study of migration enthalpies in $MgSiO_3$ perovskite. *Phys. Chem. Miner.* **36,** 151–158 (2009).
23. Ammann, M. W., Brodholt, J. P. & Dobson, D. P. Simulating diffusion. *Rev. Mineral. Geochem.* **71,** 201–224 (2010).
24. Holzapfel, C., Rubie, D. C., Mackwell, S. & Frost, D. J. Effect of pressure on FeMg interdiffusion in $(Fe_xMg_{1-x})O$, ferropericlase. *Phys. Earth Planet. Inter.* **139,** 21–34 (2003).
25. Yamazaki, D. & Irifune, T. Fe-Mg interdiffusion in magnesiowüstite up to 35 GPa. *Earth Planet. Sci. Lett.* **216,** 301–311 (2003).
26. Dobson, D. P. Oxygen ionic conduction in $MgSiO_3$ perovskite. *Phys. Earth Planet. Inter.* **139,** 55–64 (2003).
27. Dobson, D. P., Dohmen, R. & Wiedenbeck, M. Self-diffusion of oxygen and silicon in $MgSiO_3$ perovskite. *Earth Planet. Sci. Lett.* **270,** 125–129 (2008).
28. Stacey, F. D. & Davis, P. M. High pressure equations of state with applications to the lower mantle and core. *Phys. Earth Planet. Inter.* **142,** 137–184 (2004).
29. Oganov, A. R., Brodholt, J. P. & Price, G. D. The elastic constants of $MgSiO_3$ perovskite at pressures and temperatures of the Earth's mantle. *Nature* **411,** 934–937 (2001).
30. Stackhouse, S., Brodholt, J. P., Wookey, J., Kendall, J.-M. & Price, G. D. The effect of temperature on the seismic anisotropy of the perovskite and post-perovskite polymorphs of $MgSiO_3$. *Earth Planet. Sci. Lett.* **230,** 1–10 (2005).
31. Stackhouse, S. & Brodholt, J. P. in *Post-Perovskite: The Last Mantle Phase Transition* (eds Hirose, K., Brodholt, J., Lay, T. & Yuen, D.) 99–113 (AGU Geophys. Monogr. 174, American Geophysical Union, 2007).
32. Wentzcovitch, R. M., Karki, B. B., Cococcioni, M. & de Gironcoli, S. Thermoelastic properties of $MgSiO_3$ perovskite: insights on the nature of the Earth's lower mantle. *Phys. Rev. Lett.* **92,** 018501 (2004).

Supplementary Information is linked to the online version of the paper at www.nature.com/nature.

Acknowledgements The authors thank D. Prior and J. Wheeler for discussions. This work was funded by the European Commission through the Marie Curie Research Training Network c2c (Crust to Core) contract no. MRTN-CT-2006-035957. The authors acknowledge the use of University College London's Research Computing facility Legion and the use of HECToR, the UK national high-performance computing service, which is provided by UoE HPCx Ltd at the University of Edinburgh, Cray Inc. and NAG Ltd, and funded by the Office of Science and Technology through the Engineering and Physical Research Council's High-End Computing Programme.

Author Contributions J.P.B. and D.P.D. initiated the project. M.W.A. performed the calculations. J.W. performed the calculations of the seismic profile. M.W.A., J.P.B. and D.P.D. discussed the results and implications and wrote the paper.

Author Information Reprints and permissions information is available at www.nature.com/reprints. The authors declare no competing financial interests. Readers are welcome to comment on the online version of this article at www.nature.com/nature. Correspondence and requests for materials should be addressed to M.W.A. (m.ammann@ucl.ac.uk) or J.P.B. (j.brodholt@ucl.ac.uk).